A study of the performance of a nulling interferometer testbed preparatory to the Darwin mission

Pavel Gabor

To cite this version:

Pavel Gabor. A study of the performance of a nulling interferometer testbed preparatory to the Darwin mission. Astrophysics [astro-ph]. Université Paris Sud - Paris XI, 2009. English. NNT : . tel-00439669

HAL Id: tel-00439669
https://theses.hal.science/tel-00439669v1
Submitted on 8 Dec 2009

École Doctorale d'Astronomie et d'Astrophysique d'Île-de-France

THÈSE
présentée pour obtenir le grade de
DOCTEUR DE L'UNIVERSITÉ DE PARIS XI
spécialité : ASTROPHYSIQUE

par

PAVEL GABOR

ÉTUDE DES PERFORMANCES D'UN BANC INTERFÉROMÉTRIQUE EN FRANGE NOIRE DANS LE CADRE DE LA PRÉPARATION DE LA MISSION DARWIN

Soutenue publiquement le 22 septembre 2009 devant le jury :

Jean-Pierre Bibring,	Président
Peter Lawson,	Rapporteur
François Reynaud,	Rapporteur
Jonathan Lunine,	Examinateur
Daniel Rouan,	Examinateur
Alain Léger,	Directeur de thèse

Contents

Preface

You have worked hard for three years in the laboratory, you learned much, and you were even lucky enough to publish a few papers. Are the papers not enough? What is the point in wasting your time on a dissertation? Why not use the time you have more productively? Why do you not do more experimental work? You could obtain some publishable results...

While it is true that much of Chapters 4, 5, 6, and Appendix A has already been published elsewhere, I found that writing a dissertation is an eminently useful exercise. (And this is true not only because the dissertation gives me an opportunity to correct some extant errors in my papers...)

I set out to write a comprehensive and comprehensible introduction to SYNAPSE and NULLTIMATE which could be helpful to future adventurers (if any) who will enjoy working with them. Chapter 3 is, therefore, not just a description: it purports to be an explanation of the testbeds. I found that I spontaneously adopted a style where I try to explain things in simple terms. In order to do that I was often led to a deeper understanding of the subject matter.

Most of all, I am grateful for this opportunity to take a step back, and look at my work in a broader context, with a deeper understanding, and a better grasp of the network of details which is an experiment's fibre of being.

0.1 Teamwork

Ptolemy (*Almagest* IX, 2) mentions that Hipparchus refrained from formulating a definitive theory of planetary motion, providing a legacy of observations to future generations, whom Hipparchus invited to continue collecting data to the best of their ability. Ever since Hipparchus realised that one lifetime's worth of astronomical observations cannot provide empirical evidence of sufficient scope to decide certain scientific issues, astronomy has been the first discipline to become aware of itself as a collective effort (Špelda 2006, , p. 243) spanning generations. In recent decades, teamwork has become the rule in astronomy, especially when it comes to the construction of instruments, data acquisition and reduction.

0.2 Initiation

How does a humble adept become a part of this wonderful adventure? First, there is some schoolwork in order to acquire sufficient knowledge and a some skills. But I now view all of my years of study as mere preparation for the real challenge, the rite of passage called "PhD". Then he enters a cavern where the initiation takes place, labouring there not for nine days like the Greater Eleusinian Mysteries, but for three years!

My previous experience allowed me to realise the importance of being with good people. I am very grateful to Michael Heller, George Coyne, Pierre-Noël Mayaud, Pierre Léna, and Daniel Rouan who encouraged me and helped me choose the door on which to knock.

0.3 Work in a team: my acknowledgments

Then the door opened, allowing me to enter and participate in the Mysteries. I stepped over the threshold with trepidation. What frightful challenges would I have to face? Would I have to face them alone, struggling to overcome them surrounded by indifference or even hostility at the Temple called "Institut d'Astrophysique Spatiale"?

I am at a loss how to express how fortunate I feel to have found such a wonderful group of people there. Let me merely list the names (in the order in which I met them): Alain Léger, the paradigm of a physicist; Marc Ollivier, the brilliant experimentalist and nulling pioneer; Frank Brachet, the builder of SYNAPSE; Bruno Chazelas, the open-source wizard; Sophie Jacquinod, also known as Sophie Bond; Michel Decaudin, the star optician; Alain Labèque, the intrepid inceptor of SYNAPSE; Joël Charlet, the elusive electrician; Claude Valette, the cryogenic cameraman; Pascal Bordé, the moving spirit of the press review; Philippe Duret, the irreplaceable and imaginative Chagall of Shadoks; Vaitua Leroi, the friendly Martian; Peter Schuller, the fringe forebear/foreman; Benjamin Samuel, the Periodographic Nimrod; Thomas Laurent, who accompanied us on our obscure path but for a short while; and finally, Olivier Demangeon, my courageous successor.

I am truly sorry that I cannot list everybody, and I know this is not right. Let me at least mention two more categories of people. John S. Bell in one of his papers on quantum systems remarks that quantum measurements are interactions between microscopic sytems and macroscopic systems, the latter being difficult to delimit, and he asks whether the institute's administrative staff should also be counted as a part of the measuring apparatus. After my experience at the *Institut d'Astrophysique Spatiale* I have become convinced that all the "support" staff was very much a part of the team, and contributed significantly to our work.

Last but not least I would like to mention our colleagues from Nice, Cannes, Heidelberg, Liège, Delft, Grenoble, Pasadena — Yves Rabbia, Jean Gay, Marc Barillot, Ralf Launhardt, Olivier Absil, Pierre Kern, Peter R. Lawson, Bob Peters, Stefan Martin, Andrew Booth, Rob Gappinger, and all the nulling interferometrist around the world. May the light of nulling grow ever fainter!

Working as a team without reaching the expected performance parameters and results, we had to master our frustration, maintain good morale, perseverance and creativity. Regardless of how the optical experiment went, the sociological and psychological one was an extraordinary success.

In most of the text, I shall not even try to describe my contribution. More often than not the collective "we" does *not* stand for the author *but for the team.* An account of my personal efforts will be given in the last Chapter (7.2.1).

0.4 Goals and objectives

In distinguishing goals and objectives I am following a usage where "goals" are general teleological perspectives, whereas "objectives" are concrete performance parameters to be reached by a given date. The objectives were primarily imposed by outside commitments (an ESA contract). During the period of my graduate studies they evolved quite considerably. Just as an example, let me mention that at first we worked towards testing three achromatic phase shifter prototypes, by the end of 2008 this goal was practically no longer an objective (although it remained a goal – the difference being that there is no deadline set for the tests). I shall therefore not present our work against the background of these shifting objectives, but rather of the goals which remained unchanged throughout.

In this sense, the goals of this work are twofold. First, there are the science goals, namely, advancement of nulling interferometry in view of a future interferometric space mission capable of detecting biomarkers in spectral studies of Earth-like extrasolar planets. Second, there are pedagogical goals of the hands-on training in intrumental development. Although the pedagogical goals are, ultimately, the main purpose of post-graduate study, the dissertation is not the place to discuss them in any detail. Let me just say that I am very grateful that I worked in a small group where we had to develop many things from scratch and we knew that we simply had to take our time to do so. This meant that I did not feel like a small gear in a large result-producing machine but rather as if I had a three-year long practical.

The science goals outlined above in very broad terms can be described more specifically as:

- improving the performance of the SYNAPSE testbed,
- building the NULLTIMATE testbed as its successor,
- stabilising the SYNAPSE tested,
- testing the achromatic phase shifter prototypes.

In the conclusion of this dissertation I shall return to these goals, present a brief evaluation of what has been achieved so far, and indicate some pathways to be explored in the future.

0.5 Organisation of the dissertation

A French *résumé* is added at the very end of the volume, hopefully making it easier to find without a lot of page-turning.

The first two Chapters introduce the subject. The first (Chap. 1) gives a very brief overview of the issue of cosmic pluralism in the context of current scientific research. The second (Chap. 2) describes the principles of nulling interferometry. Chapter 3 is a description of the testbeds at *Institut d'Astrophysique Spatiale,* Orsay, called SYNAPSE and NULLTIMATE. Chapter 4 describes a stabilisation technique which we developed and used during our work on the testbeds. It closely follows the papers Gabor et al. (2008a,b). Chapter 5 is a report on the results obtained with SYNAPSE II, closely following the article Gabor et al. (2008c). (Readers who are familiar with these papers can skip Chapters 4, 5, and go directly to Chapter 6 which is a presentation of our work aiming to achieve a better understanding of the broadband null-depth limitation, performed on SYNAPSE II. Chapter 7 describes what was to be done, what was done, my personal contribution, what is to be done, i.e., future work to be carried out on the NULLTIMATE testbed, and some conclusions, including those regarding the broader context of spaceborne nulling interferometry.

Chapter 1

Astrobiology and Exoplanetology

Contents

1.1 Are we alone?

The question of cosmic pluralism has a long and complicated history, linked to its many interdisciplinary overlaps. Appendix A contains a study on the subject[1]. Speculation was the only possible approach for generations. The scientific community is currently developing observational techniques designed to bring the first quantitative answers. This dissertation is an account of a small part of these efforts.

1.1.1 What is life?

The speculation on humanity's uniqueness or mediocrity is doubtless fascinating in its own right but in order to explore all the possible scientific approaches we shall have to broaden the horizon of our investigation to include not only intelligent extraterrestrials but life in the Universe in general. Hence the question: "What is life?"

The discussion is ongoing. As the historian of science, James Strick, puts it:

> What is life? Is it the assemblage of the operations of nutrition, growth, and destruction, as Aristotle thought? Or is it organization in action, as French physician and biologist François-Xavier Bichat defined it? Or might it be the continuous adjustment of internal relations to

---

[1] Presented at the conference *Darwin's Impact on Science, Society, and Culture* held in Braga (Portugal), 9-12 September 2009.

> external relations, as the British philosopher and sociologist Herbert Spencer believed? (Strick 2003)

Let us make it quite clear from the outset that we are not going to discuss the question of the nature of life. It is by and large still an open issue with a captivating history and an even more confused historiography than cosmic pluralism.

We shall limit ourselves to an utilitarian approach, providing a rough outline of what exactly is meant by the extraterrestrial life that contemporary science seeks. We shall completely forego certain important chapters from the history of scientific thought, such as the theory of vitalism, in order to concentrate on the current position of the problem, starting with the Fermi Paradox, introducing Drake's Equation, and ending with a discussion of extremophiles, silicon-based life and spectroscopic biomarkers.

1.1.1.1 The Fermi Paradox

Stephen Webb presents the "canonical version" of the episode established by Jones (1985):

> Fermi was at Los Alamos in the summer of 1950. One day, he was chatting to Edward Teller and Herbert York as they walked over to Fuller Lodge for lunch. Their topic was the recent spate of flying saucer observations. Emil Konopinski joined them [... Then] there followed a serious discussion about whether flying saucers could exceed the speed of light. [...] The four of them sat down to lunch, and the discussion turned to more mundane topics. Then, in the middle of the conversation and out of the clear blue, Fermi asked: "Where *is* everybody?" His lunch partners Teller, York and Konopinski immediately understood that he was talking about extraterrestrial visitors. And since this was Fermi, perhaps they realised that it was a more troubling and profound question than it first appears. York recalls that Fermi made a series of rapid calculations and concluded that we should have been visited long ago and many times over. (Webb 2002, pp. 17-18)

A quantitative estimate of the number of space-worthy extraterrestrial civilisations in our own Galaxy, the Milky Way, led Enrico Fermi to the conclusion that there must be millions of them. Different authors after Fermi obtained different results, and it should be noted that Fermi's estimate is one of the more optimistic ones. Indeed, it would appear that over the last six decades sentiments among researchers have varied widely, and that some even find that pessimism and optimism have been coming and going in waves, an optimistic period succeeding a pessimistic one over the decades.

The discovery of extrasolar planets has, understandably, brought about a wave of optimistic estimates which is largely still upon us. Let us note, however, that (Santos et al. 2003) seem to indicate that our own planetary system, the Solar system, is rather unique since it would appear that giant planets migrate towards their stars in the early stages of the system's formation more often than not. The fact that Jupiter did not migrate through the habitable zone is very likely an important factor in the emergence of life on Earth. We shall not enter into the detail of this speculation: we believe more data are vitally needed in order to obtain a clearer picture of comparative planetology. Suffice it to say, that this study, as well as other convictions, led a number of researchers to adopt a more pessimistic view of cosmic pluralism in recent years. They would appear to be in a minority, nonetheless.

1.1.1.2 Drake's Equation

Ever since the 1960's, Fermi's estimate of the number of extraterrestrial civilizations in our Galaxy with which we might come in contact has been facilitated by the factorisation known as the Drake equation (Drake 1961; Drake and Sobel 1992). It permits us to quantify the individual factors intervening in the estimate:

$$n = R_* \times f_p \times n_e \times f_l \times f_i \times f_c \times L \tag{1.1}$$

where

- n is the number of civilizations in our galaxy with which we might expect to be able to communicate at any given time,
- R_* is the rate of star formation in our galaxy,
- f_p is the fraction of those stars that have planets,
- n_e is average number of planets that can potentially support life per star that has planets,
- f_l is the fraction of the above that actually go on to develop life,
- f_i is the fraction of the above that actually go on to develop intelligent life,
- f_c is the fraction of the above that are willing and able to communicate,
- L is the expected lifetime of such a civilization.

In this form, the temporal limitations are included as the product $R_* L$, i.e., the rate of star formation per unit of time multiplied by the lifetime of a civilisation. Another form of the equation is often used, determining the same temporal limitations taking the expression $N_* L/T_*$, where N_* is the number of stars in the Galaxy and T_* is a star's lifetime. This alternative form can thus be written as:

$$n = N_* \times f_p \times n_e \times f_l \times f_i \times f_c \times \frac{L}{T_*} \tag{1.2}$$

Contemporary empirical knowledge allows us to obtain estimates of some of these factors and of their uncertainties. Currently, the value of R_* is estimated as 7 per year (one also often encounters the older estimate of $R_* = 10$ per year). Using the alternative approach, the value of N_* can be estimated as $1.6\,10^{11}$, whereas T_* can be taken as equal to

$$T_* = \left(\frac{M_*}{M_\odot}\right)^{-2.5} 10^{10}\ \text{years}, \tag{1.3}$$

i.e., for stars with $M_* = 0.75 M_\odot$ we obtain

$$\frac{N_*}{T_*} = \frac{1.6\,10^{11}}{(M_*/M_\odot)^{-2.5} 10^{10}}\ \text{per year} = 8\ \text{per year}, \tag{1.4}$$

roughly the same number as our estimate for R_*.

The study of the extrasolar planets in the next two decades is likely to lead to good estimates for the values of f_p and n_e. The issue at hand is a better understanding of mechanisms behind the formation and evolution of planetary systems. The factor n_e is often understood as the number of planets per star which are in the so called "habitable zone", i.e. at such a distance from the star where liquid water can be found on their surface. Naturally, this is already a statement of a position regarding the physical and chemical conditions for life.

So far, we have little useful observational evidence for an assessment of the factor f_l. Indeed, considering how controversial and problematic a definition of "life" is, it is rather doubtful that a reasonable answer will be forthcoming in the next one or two generations.

However, if we restrict our notion of "life" somewhat, and make some presumptions about its biochemistry, we may be able to find a value of the factor f_l through spectroscopy of exoplanetary atmospheres.

1.1.1.3 Identifiable life

There are several assumptions that we can safely make about the chemistry of the life we want to search for. There are two aspects to this restriction. One has to do with feasibility and practicality: There may be other sorts of life but they would be even harder to identify. The other has more to do with our scientific understanding of the processes involved: It seems that it is easier for complex structures to form under certain conditions rather than under other conditions.

Two or three such assumptions stand out as an intersection of consensus among most researchers. Thus, we expect this “identifiable life” to

- be based on the chemistry of the element carbon simply because the alternatives (e.g., silicon) appear considerably less promising;
- have biomembranes defining the internal volume of the lifeform as opposed to its environment;
- use liquid water: this is mostly understood as “life in a liquid-water solution” but it could just mean that water is likely to play a rôle in the metabolic processes of all lifeforms.

Obviously, this still leaves a very broad space to explore. An interesting approach is based on the idea of hypothetically detecting terrestrial life from space. Studies (e.g., Kaltenegger et al. 2007) were conducted to see whether the presence of a biosphere on Earth could have been detected by remote sensing over our planet’s history. Spectroscopic methods may be able to detect the presence and mutual proportion of various chemicals in the planetary atmospheres.

1.1.1.4 Spectroscopic biomarkers

Supposing that sought-after extra-solar life is somewhat akin to the terrestrial biosphere, we may expect to observe its spectroscopically blatant impact on extra-solar planetary atmospheres. The possibility that O_2 and O_3 are ambiguous identifications of Earth-like biology, but rather a result of abiotic processes, has been considered in detail (Léger et al. 1999; Selsis et al. 2002). Various production processes have been evaluated, e.g., abiotic photodissociation of CO_2 and H_2O followed by the preferential escape of hydrogen from the atmosphere, cometary bombardment introducing O_2 and O_3 sputtered from H_2O by energetic particles. The conclusion is that a simultaneous detection of significant amounts of H_2O and O_3 in the atmosphere of a planet in the habitable zone presently stands as a criterion for large-scale photosynthetic activity on the planet. Future space missions like Darwin and TPF-I thus focus on the region between 6 μm to 20 μm, containing the CO_2, H_2O, and O_3 spectral features of the atmosphere.

Spectroscopic search for biological markers in exo-planets is therefore a goal to be achieved. The issue at hand is, “How?”

1.1.2 Current scientific approaches

We have introduced Drake’s equation and we mentioned the issue of identifying the presence of a biosphere on an exoplanet. Let us now take a step back and look at the panorama of current scientific approaches to the question: “Are we alone?”

1.1.2.1 SETI

Drake’s equation was inspired by the search for extraterrestrial civilisations rather than extraterrestrial life as such. We saw that some of the factors in the equation can be estimated by astrophysical observations. There is another avenue that is worth exploring, however. If there are extraterrestrial civilisations out there, they might produce artificial radiation in the domain of radio waves. In other words, they might be producing identifiable signals. And it would suffice to listen attentively in order to receive them. This programme is known as SETI, the Search for ExtraTerrestrial Intelligence.

1.1.2.2 Solar System exploration

The exploration of the Solar System is an ongoing endeavour with many different goals. One of them (arguably the oldest and most inspiring) is the search for life. Currently, four objects are under scrutiny.

Mars. The planet Mars has been one of the classic 19th-Century and early 20th-Century alien home worlds. Extensive research is being conducted from Mars orbit as well as on its surface. The main question today is whether, in its distant past when Mars had liquid water on its surface, any indigenous lifeforms formed there.

Europa. It is very probable that Europa, one of Jupiter's four moons discovered already by Galileo in 1609, possesses an internal global ocean under a crust of ice. A mission to explore this body is planned (EJSM: Europa Jupiter System Mission).

Titan. The largest of Saturn's moons, Titan, was the destination of the Huygens-Cassini space mission. The instruments reached Saturn's system in June 2004. The Huygens probe descended into Titan's atmosphere discovering a new and intriguing world where liquid methane plays a rôle analogous to water on Earth: there are vast lakes of methane, and methane rainfall. Cassini remains in orbit around Saturn updating our knowledge of the surface of Titan at every flyby. The most interesting point regarding Titan is this: If we find life there, based on methane as solvent, it becomes clear that life emerged independently twice in the Solar System. If it happened twice in one planetary system, it is very likely that life is ubiquitous in the Universe.

Enceladus. The Cassini mission discovered evidence that Enceladus, a natural satellite of Saturn, resembles Europa in having an ocean of liquid water under a crust of ice. Space mission proposals to study the Saturn system were submitted to the US and European space agencies (Titan Saturn System Mission, TSSM; Titan and Enceladus Mission, TandEM), and although a joint mission to the Jupiter system (EJSM) was selected in February 2009, the mission to Saturn's satellites will continue to be studied.

1.1.2.3 Exoplanetology

One of the most dynamic fields of astrophysical inquiry is exoplanet research. Its goals are

- a survey of planetary systems and a classification of their types,
- a census of exoplanets and their typology, morphology and geophysics,
- a better understanding of planet formation and the underlying mechanisms, and
- a study of the properties of exoplanetary atmospheres.

This list does not pretend to be exhaustive. Its purpose is to show that exoplanetology searches for answers that are of utmost pertinence to astrobiology.

1.2 Exoplanets

The direct observation of an exoplanet, in the sense of identifying and studying the photons emitted by an exoplanet, is very challenging. There are three major obstacles to be surmounted:

1. angular resolution: levels better than 0.1 arcsec are needed because there always is a very bright object at a very small angular distance, viz., the parent star around which the exoplanet revolves;

2. the contrast in brightness between the exoplanet and its star is such that even the starlight contained in the comparatively very dim outer diffraction pattern is still brighter than the planet; and
3. zodiacal and exozodiacal light, i.e., the environment of the Earth and of the observed exoplanet (as well as the intervening cosmic medium) contains sources of diffuse thermal emissions (gas and dust) at the same wavelength as those of the exoplanet.

1.2.1 Indirect detection

These challenges mean that direct observation of exoplanets cannot be performed so far. The information we have gained comes from indirect detection methods.

There are two types of effects of the exoplanet on the observation of its parent star:

1. **motion**: the orbital movement of the exoplanet influences the position of the observed star's photocentre;
2. **photometry**: the presence of the exoplanet may influence the brightness of the observed star.

The orbital motion of an exoplanet is coupled with an orbital motion of the star around a common centre of mass. Each of the bodies revolves on an elliptical path with the centre of mass in one of its foci. The semimajor axis a_* of the star's orbit can be expressed in terms of the semimajor axis of the exoplanet's orbit a_p and of the masses of the star and of the exoplanet, m_* and m_p, respectively, as follows:

$$a_* = \frac{m_p}{m_* + m_p}\, a_p. \tag{1.5}$$

This means that the star is in motion which is due to the orbital movement of the exoplanet. The star's velocity vector can be decomposed into the component along the line of sight from the Earth and into the two components in the plane tangent to the celestial sphere.

There are five methods based on these phenomena:

1. **Astrometry**: which observes the motion of the star on the celestial sphere. It provides an unambiguous measure of the planet's mass and orbital parameters.
2. **Radial velocimetry**: which measures the radial component of the star's velocity vector using spectroscopic methods. Using this technique, the planet's mass can be determined only indirectly as $m \sin i$ where i is the inclination of the planet's orbit with respect to the line of sight.
3. **Pulsar timing**: which also measures the radial component of the star's velocity vector, but applied to pulsars, this quantity can be deduced from the precise timing of the their pulses.
4. **Transits**: If the exoplanet passes in the line of sight between its parent star and the Earth, the star's light appears to decrease somewhat during the exoplanet's transit in front of the star's disc. This technique allows the planet's size to be estimated. In conjunction with radial velocimetry, it provides a measure of the exoplanet's density (the $m \sin i$ ambiguity is minimised by the fact that orbital planes of transiting exoplanets must be approximately aligned with the line of sight).
5. **Gravitational microlensing**: When a massive object lies between the observer and the observed object, the image of the latter can be deformed by the gravity of the lens, i.e., the intervening object. In a simple case, the lens amplifies the light of a faint star. If there is a favourably positioned exoplanet orbiting the star, then the lightcurve of the microlensing event contains a secondary peak due to the exoplanet. No follow-up observations of the objects detected by this technique are likely, and therefore the primary contribution of gravitational microlensing to exoplanetology is in statistical estimates of exoplanet populations.

1.2.2 Direct observation

Direct observations of exoplanets are defined by the separation of the photons emitted by the planet from starlight and exozodiacal light[2]. This can be achieved by several techniques which are under development.

Before we list them, it is good to realise that they must be regarded as sophisticated optical contrivances, that have to deal with a very challenging set of constraints even without having to deal with the distortion of optical path and absorption in the Earth's atmosphere. Let us, therefore, concentrate on space where the challenges of nulling interferometry as such are decoupled from the issues presented by atmospheric influence In this case, the solution can be found as a trade-off between diffraction and the star-planet contrast.

For a circular aperture of diameter D (e.g., the telescope's primary mirror) the diffraction pattern, known as the Airy pattern, has its first minimum at a radius of

$$r = 1.22\frac{\lambda}{D} \tag{1.6}$$

where λ is the wavelength. This means that working in the visible domain a telescope smaller (typically a few metres) than in the infrared suffices to overcome diffraction. In the infrared domain, a single telescope will not be practical.

At the same time it must be noted that the star-planet contrast is wavelength-dependent. Fig. 1.1 shows that the spectrum of the Earth contains three elements:

1. The reflected sunlight with its peak in the visible domain;

$$\lambda_{\max} = \frac{b}{T_{\text{eff}}} = \frac{2898\,\mu\text{m}\,\text{K}}{5778\,\text{K}} \approx 0.5\,\mu\text{m}; \tag{1.7}$$

2. Earth's thermal emission with the peak at

$$\lambda_{\max} = \frac{2898\,\mu\text{m}\,\text{K}}{300\,\text{K}} \approx 10\,\mu\text{m}; \tag{1.8}$$

3. absorption features of various molecules in the Earth's atmosphere.

The spectral region highlighted in Fig. 1.1 offers two advantages over the visible:

- It features essential biomarkers,
- the star-planet contrast is the least unfavourable.

As was already said, a single telescope in the infrared spectral range, would need to have a very large aperture because of diffraction. The alternative is to employ interferometric techniques. This leads us to the disadvantages of the infrared:

- Multiple space telescopes are needed, and
- they need to fly in formation.

Coronography. The approaches studied for exoplanet observation in the visible spectral range concentrate on coronography. There are two basic concepts:

- A single spacecraft with a sophisticated optical payload, including a substantial primary mirror (Fig. 1.2);
- A simple space telescope with another spacecraft at a distance of about 50 000 km whose rôle would be to carry an occulting screen (Fig. 1.3).

---

[2] Even though in some favourable cases the transit method can allow for such separation of the photons emitted by the planet itself from starlight, it is primarily an indirect detection method.

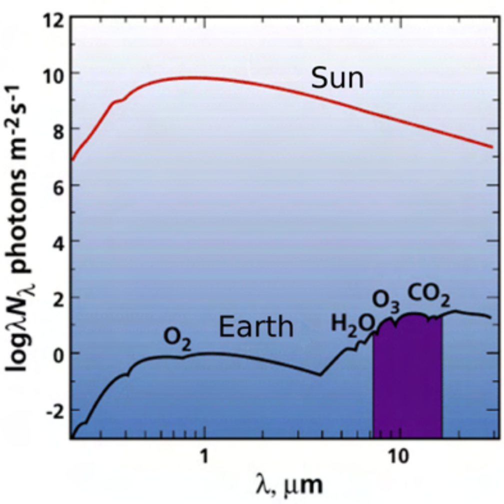

Figure 1.1 - Sun-Earth contrast observed from 10 pc with the main spectral features of O_2, O_3, H_2O, and CO_2 (Beichman et al. 1999).

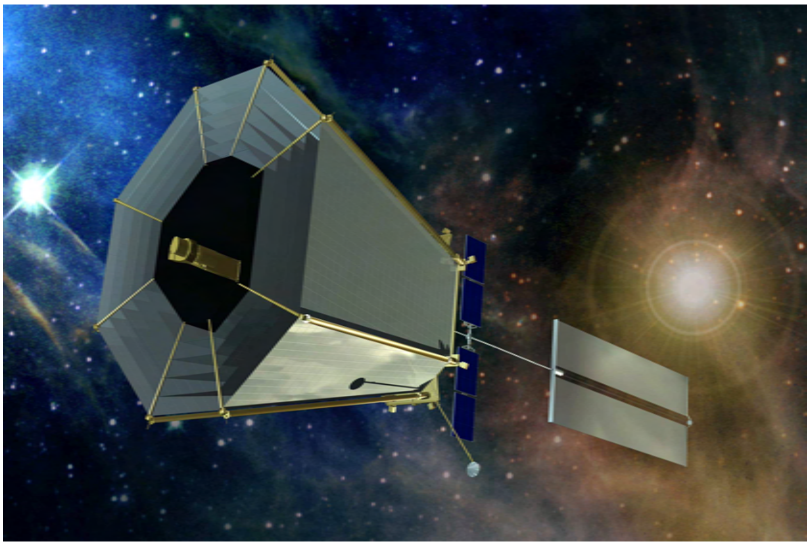

Figure 1.2 - Terrestrial Planet Finder Coronograph. An example of a single-spacecraft visible coronograph. The observed star with its planetary system is represented on the left. The Sun is on the right. The telescope is heavily shielded from sunlight. (Courtesy NASA/JPL.)

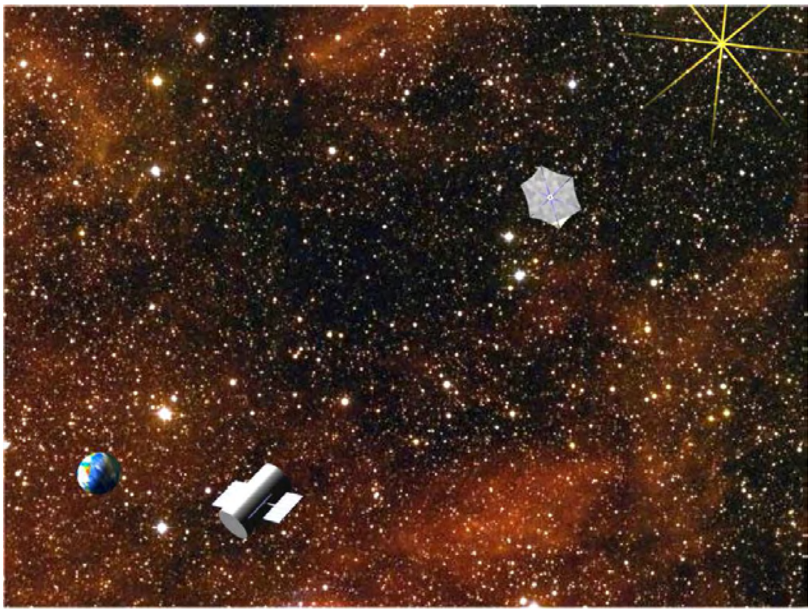

Figure 1.3 - New Worlds Observer. An example of a space occulter. There are two space vessels: a telescope and a screen-bearing spacecraft. (Courtesy W. Cash, University of Colorado.)

Interferometry is a technique introduced to enhance angular resolution. Bracewell (1978) proposed a variant where reduction of star-planet contrast is achieved applying a π phase shift between the light collected by two telescopes. A detailed discussion of the technique will be provided in the next Chapter (2).

Exoplanetary radio emissions. Apart from the Sun, the brightest radio object in our sky is the planet Jupiter. This fact leads radio astronomers to study the possibility of observing radio emissions of exoplanets (Lazio et al. 2009).

1.2.3 Step by step

After the discovery of giant planets, detection techniques are growing more and more efficient and will soon be able to detect planets of comparable size to the Earth's. Space missions will be needed to detect Earth-like planets in their stars' habitable zones, i.e., at distances of the order of the A.U. (SIM-Lite is the mission proposal most likely to succeed in this respect). Yet more powerful space observatories will be needed to observe these worlds, and to measure their spectra. The most promising mission proposal not only in terms of general observations and spectroscopy but also in terms of astrobiology is the *Darwin*/TPF-I project, a formation-flying nulling interferometer.

1.3 Formation-flying nulling interferometer

Léger et al. (1993) proposed the *Darwin* mission to the European Space Agency, a nulling interferometer comprising several telescopes and a combiner module flying in formation in space. A development (Angel and Woolf 1997) of this proposal was submitted to NASA. The American project is known as the Terrestrial-Planet Finder Interferometer (TPF-I).

It should be pointed out that although the primary aim of *Darwin*/TPF-I is clearly the search for life in the Universe, there are not a few other questions that the mission could elucidate. Indeed, all three main themes of exo-planet research (as identified in Perryman et al. (2005)) may benefit from it:

- characterising and understanding the planetary populations in our Galaxy;
- understanding the formation and evolution of planetary systems (e.g. accretion, migration, interaction, mass-radius relation, albedo, distribution, host star properties);
- the search and study of biological markers in exo-planets, with resolved imaging and the search for intelligent life as 'ultimate' and much more distant goals.

1.3.1 Design overview

Many improvements of the concept have been included over the years. By 2007 there was an agreement in design principles between the researchers at NASA and ESA, and the architecture for both TPF-I and *Darwin* converged (Lawson et al. 2007). Fig. 1.4 shows an artist's view of the space observatory which has to orbit the Sun with the same angular velocity as the Earth but at a distance 1.5 million km greater than the Earth, oscillating around the Sun-Earth L2 point. This positioning offers a number of advantages. Both the Earth and the Sun are always "behind" the spacecraft, facilitating cooling and observation planning. Less propellent is required for formation flying at L2 than in Earth orbit and even in an Earth-trailing orbit.

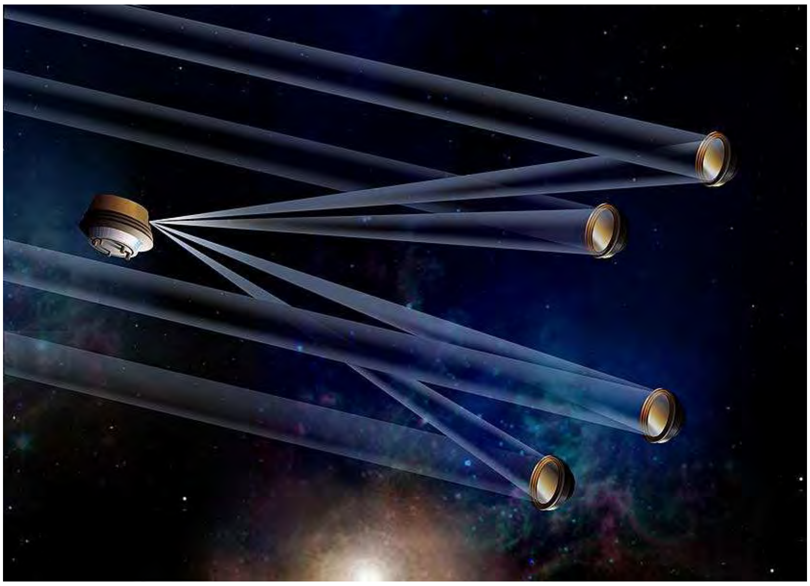

Figure 1.4 - *Darwin*/TPF-I space observatory. An artist's view of the Emma X-array configuration with four telescopes. Each points in the direction of and receives light from the star-planet system. The four beams are transmitted to the central beam combiner which also provides, together with the communication station, metrological reference for the required formation flying. (Courtesy Peter R. Lawson, NASA/JPL.)

Search for biomarkers is a major factor when considering the spectral band. The values found are 6–20 μm. Regarding the diameter and number of telescopes, photometric, interferometric, and technical considerations lead to a trade-off of four 2 m apertures arranged in the so called Emma X-array.

Fig. 1.5 (Lawson and Dooley 2005) shows the provenance of the photons detected by *Darwin*/TPF-I. The figure shows the intensity of the local and exo-zodiacal emission, the leakage from the nulled star, and the background from the 35 K telescope. The resultant signal-to-noise ratio is shown on the right-hand scale. At 7 μm, the largest part of the measured flux is due to the star, then to the exozodiacal light, closely followed by local zodiacal light. The signal emitted (or reflected) by the planet is several orders of magnitude smaller.

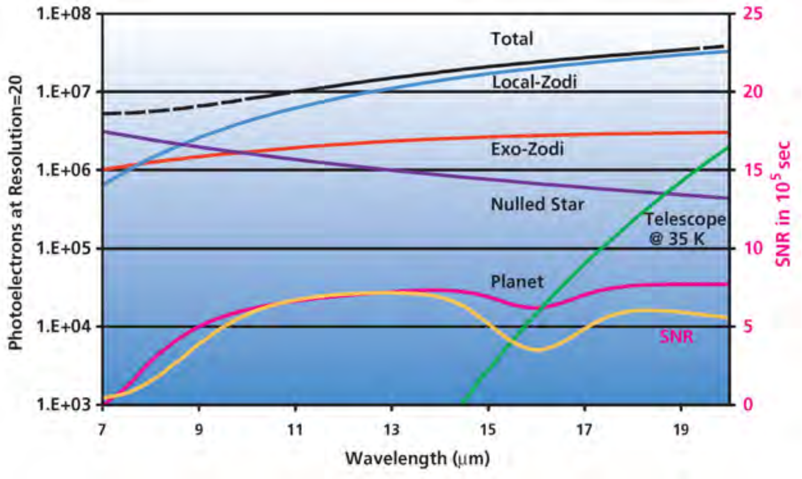

Figure 1.5 - The signal in photo-electrons in a 10^5 s integration period from an Earth-like planet observed through the 1 AU, 3.5 m version of TPF. The planet shows CO_2 absorption at 16 μm. The spectral resolution is R=20. Also shown are the other signals that contribute to the total photon shot noise. The bottom curve shows the signal-to-noise ratio (SNR) on the planet using the right-hand scale. (Beichman et al. 1999)

The typical star-planet contrast that the instrument will need to operate with is 10^7. First, the nulling must reduce the contrast by a factor 10^5.[3] The whole observatory must rotate around the line of sight, maintaing a stable nulling level (Fig. 1.6). A technique called *phase chopping* (or *internal modulation*) (Mennesson et al. 2005; Woolf and Angel 1997) is applied at the same time. The purpose of combining rotation and phase chopping is to distinguish between the centre-symmetric diffuse exozodiacal and the point-like planetary emissions (Fig. 1.7). Together with instrument stability which enables long exposure times to reduce the noise (Sec. 1.3.3), this yields another factor 100, reaching 10^7 star-planet contrast reduction. An additional factor 10 can be obtained using the technique of *spectral fitting* (Lay 2006).

1.3.2 Nulling ratio

The output of a simple interferometer at any given moment is a single intensity measurement. Changing the optical path length of one beam with respect to the other (Optical Path Difference, OPD) leads to variations of intensity, i.e., when the OPD is scanned, a pattern of interference fringes emerges. Interference can only occur between beams which are coherent with respect to each other. Even beams generated by the same source may not be coherent if the OPD is too great: there is a certain *coherence length* to consider. A fringe pattern is observable around zero OPD, spanning the coherence length. The minima and maxima of the fringe pattern correspond to OPD's of $k\lambda/2$ where k is even for the maxima and odd for the minima. The fringes can be circumscribed by an envelope symmetric around the zero OPD. The form of the envelope is given by a Fourier transform of the beam's spectrum. Classical interferometry combines two coherent beams constructively. In order to do this, the beams have to be in phase. Then the fringe pattern's global maximum is at zero OPD, and the fringes and the envelope have the same symmetry. Nulling interferometry inverses the fringes within the envelope, placing an interference minimum at its centre, i.e., at the zero OPD. This can be done by introducing a phase shift of π between the two interfering beams.

---

[3] This value is a result of a trade-off. Nulling reaches its nominal performance for on-axis light only, i.e., for light coming from a point-like source. On the other hand, there is the instrument's (here undesirable) ability to resolves the star. Cf. B.1.

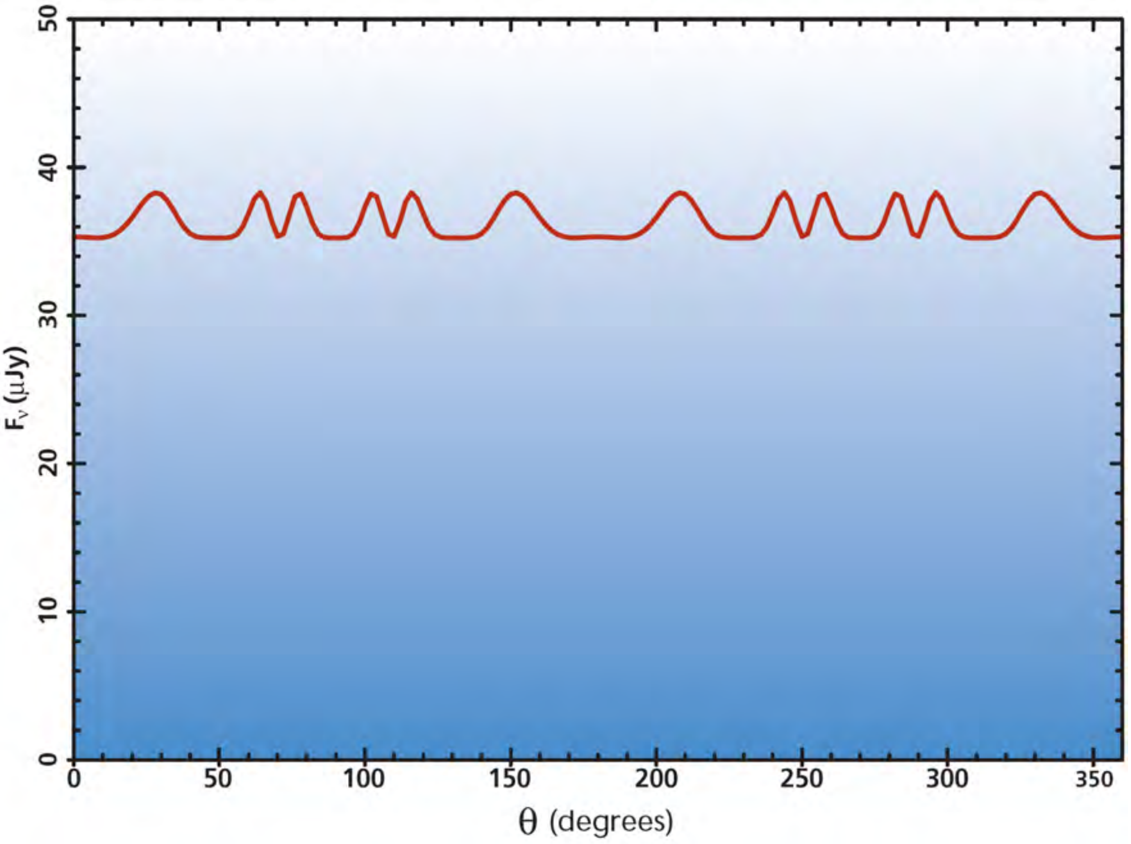

Figure 1.6 **-** As the interferometer rotates around the line of sight to a target star, the planet (a $3R_\oplus$ planet is shown for clarity in this TPF-I simulation) produces a modulated signal as it moves in and out of the interferometer fringe pattern. TPF would produce ≈ 20 such data streams, one for each of the observed wavelengths, that would be combined to reconstruct an image of the solar system and the spectra of any detected planets. (Beichman et al. 1999)

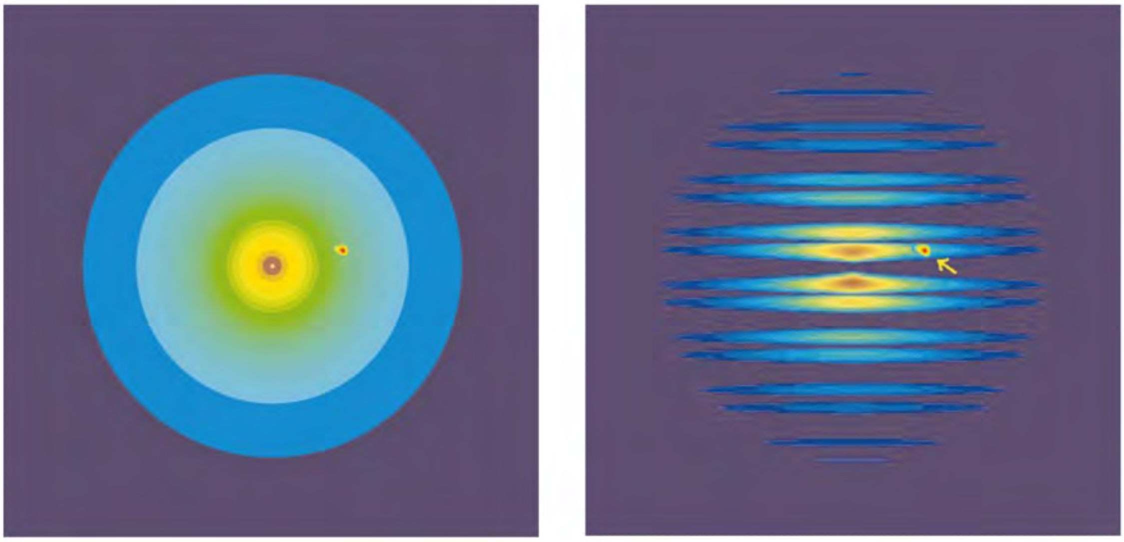

Figure 1.7 **-** The emission from a face-on exo-zodiacal dust cloud (left) with a single planet, and as it will be measured through the interferometer's transmission pattern (right). (Beichman et al. 1999)

The basic performance parameter of a nulling interferometer is the *nulling ratio*[4] *nl*,

$$nl(\lambda, \tau) = \frac{I_{\rm min}}{I_{\rm max}}, \tag{1.9}$$

where $I_{\rm min}$ and $I_{\rm max}$ are the minimum and maximum of the flux in fringe OPD fringe packet (cf. Sec. 2.2). $I_{\rm min}$ thus stands for the intensity of the on-axis dark fringe and $I_{\rm max}$ of the off-axis bright fringe. The nulling ratio is a function of the wavelength region, represented by λ, and of the integration time, τ.

We have already mentioned that the instrument needs to provide a nulling ratio of

$$nl = 10^{-5}, \tag{1.10}$$

and that this needs to be maintained with a high level of stability.

1.3.3 Stability

As already mentioned, because of the length of the planned exposure times during *Darwin*/TPF-I observations, instrumental stability must be regarded as a serious concern. Chazelas et al. (2006), referring to this fact as to the *variability noise condition*, analyse the problem, stating that instrumental stability is required regardless of telescope size and stellar distance.

We have seen that although the star-planet contrast is of the order of 10^7 (4×10^7 at 7 μm in the case of the Sun and the Earth), rotation & chopping techniques allow a reduction of the contrast by a factor 100, which means that the instrument has to provide a stable nulling ratio of 10^{-5} (Eq. 1.10). As pointed out by Lay (Lay 2004), this implies a high degree of null stability. Let us examine the contributions to the instability of the signal, i.e., to the noise of *Darwin*/TPF-I measurements.

Appendix B contains a discussion of these points because our work was to a large extent concerned with stability (Gabor et al. 2008a, cf. Chapter 4). Here, let us merely present the result (Eq. B.10)

$$\sigma_{\langle nl \rangle}(\lambda,\ 10\,\text{days}) \leq 2.5\,10^{-9} \left(\frac{\lambda}{7\,\mu\text{m}}\right)^{-3.37}, \tag{1.11}$$

which is expressed in terms of a quantity we shall define in Section 2.2. In broad terms it can be interpreted if we recall the well-known truth of photography: the longer the exposure time, the sharper the picture. This is only true if the noise is of a certain sort. It is called the *white noise*, and it decreases with exposure time τ as $\sqrt{\tau}$. The above *Darwin*/TPF-I requirement implies that the instrument noise has to be such that it allows for an improvement of the star-planet contrast over a period of 10 days.

---

[4] Sometimes also referred to as *stellar leakage* although this term refers more properly to stray starlight due to the fact a star is not a point source (Sec. B.1).

Chapter 2

Nulling Interferometry

Contents

In the previous Chapter (1), we saw that nulling interferometry is a promising approach in future research on exoplanets and astrobiology. We described, in very broad lay terms, the principle of *Darwin*/TPF-I. We listed the mission's main requirements imposed on the nulling interferometer itself (Eqs. 1.10, B.10), deriving the requirement Eq. B.10 in detail.

The purpose of this Chapter is to discuss two-beam nulling interferometers and their components.

2.1 Bracewell's principle

Interferometry is primarily a technique the purpose of which is angular-resolution improvement. Without having to resort to prohibitively large apertures, a classic two-aperture interferometer can increase angular resolution by separating two smaller telescopes by a certain distance, called base B. The beams collected by the individual apertures have to be combined under carefully controlled conditions. The interference pattern is then analysed and spatial or angular information about the target can be obtained. In order to obtain an image, it is necessary to perform a series of measurements with different lengths and orientations of the base, densely covering the parameter space.

Each measurement is done with the telescopes aligned and observing the same object. We ensure that the on-axis light from both telescopes arrives simultaneously, i.e., the two optical paths are equal, to the beam-combiner system where it merges on a single-element detector.[1] The output is therefore a single value. A set of such measurements for various values of Optical-Path Difference (OPD) forms an interference pattern. The zero OPD difference corresponds to the interference maximum, known as the white fringe. In theory, the white fringe does not have an intensity which would be just the sum of the intensities of the two interfering beams: its intensity is double the sum, i.e., four times the intensity of one interfering beam. This

---

[1] For the sake of simplicity, we shall refrain from discussing spectroscopic observations here.

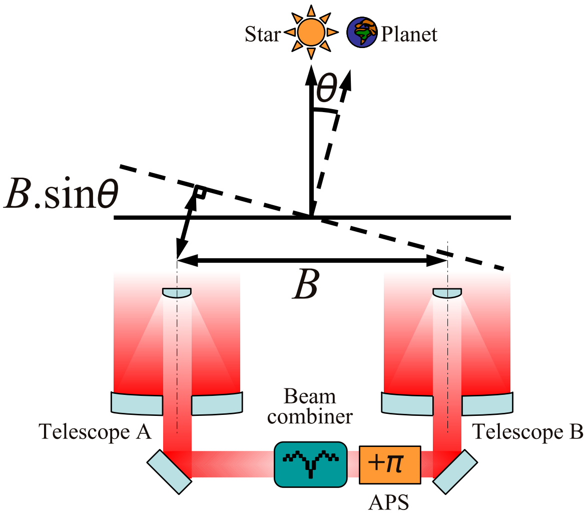

Figure 2.1 - Bracewell's nulling interferometer: two telescopes pointing in the direction of the star, the light of which is extinguished using an achromatic phase shifter ($+\pi$) so that the brightness contrast between the star and the planet is reduced.

is possible because in case of perfect interference of two monochromatic beams, there is strictly no flux at the interference minima. Thus the mean value of the flux is the expected sum of the two incident beams.

In the case of natural light (broad band), the white fringe, which corresponds to zero OPD, is still well defined, but the interference minima occur at different values of OPD for different wavelengths. This gives the interference pattern the characteristic shape of a packet of fringes: each successive fringe less and less pronounced.

A variant of this technique was proposed by Bracewell (1978). Instead of combining the beams constructively, he proposed to combine them destructively. The zero OPD corresponds to the interference minimum, known as the dark fringe. While this is trivial in the case of monochromatic light, natural light cannot be combined destructively unless an achromatic (wavelength-independent) phase shift is introduced. Supposing we have a perfectly achromatic phase shifter that shifts the phase of one of the beams by π, we obtain an inversion of the interference pattern. The dark fringe is symmetrically surrounded by imperfect white fringes, called grey fringes. The on-axis light is combined destructively. This property of the nulling interferometer makes it the instrument which can increase angular resolution and reduce the star-planet contrast.

In its simplest form (Fig. 2.1), a two-telescope nulling interferometer introduces a π phase-shift between the two apertures, resulting in destructive interference along the line of sight. At the same time, light at small off-axis angles from the line of sight will experience constructive interference, thus allowing a faint object close to a bright star to be discernible.

2.2 Performance parameters

Let us recall the quantities used in characterising the performance of nulling interferometers.

Nulling ratio was defined in Eq. 1.9 as

$$nl(\lambda,\tau) = \frac{I_{\text{min}}}{I_{\text{max}}}. \tag{2.1}$$

Rejection ratio is the inverse of the nulling ratio:

$$\rho(\lambda, \tau) = \frac{I_{\max}}{I_{\min}}. \tag{2.2}$$

Spectral band where the instrument operates is an inherent part of performance specifications. Both its absolute position in the electromagnetic spectrum and its width are important. The width is often expressed as a fraction (in per cent)

$$\frac{\Delta\lambda}{\lambda}. \tag{2.3}$$

Stability is a measure of how longer exposure times reduce star-planet contrast. For a set of values of nl, calculate the moving (or running) average with a window of the duration τ. Take this set of moving averages $\langle nl\rangle_\tau$, each averaged over exposure time τ, and calculate its standard deviation $\sigma_{\langle nl\rangle}(\tau)$. Now, repeat the procedure for a number of different windows widths τ, and inspect the dependence of $\sigma_{\langle nl\rangle}(\tau)$ upon τ. If it is consistent with $\tau^{-1/2}$ (i.e., white noise behaviour) up to a certain $\tau_{\max}$, then

$$\sigma_{\langle nl\rangle}(\tau = \tau_{\max}) \tag{2.4}$$

is a good expression of the nuller's stability.

Rudiments of interferometry. In the simplest, monochromatic case, we can represent a single wave with an amplitude of A as a function of the phase ϕ:

$$S_1 = A_1 e^{i\phi_1}, \tag{2.5}$$

and the corresponding intensity I_1 is:

$$I_1 = |A_1|^2. \tag{2.6}$$

Let us make two such waves interfere. The resulting complex sum is:

$$S = S_1 + S_2 = A_1 e^{i\phi_1} + A_2 e^{i\phi_2}, \tag{2.7}$$

and the intensity I is

$$I = |A_1|^2 + |A_2|^2 + 2|A_1||A_2|\cos(\phi_1 - \phi_2), \tag{2.8}$$

which can be expessed as

$$I = I_1 + I_2 + 2\sqrt{I_1 I_2}\cos(\phi_1 - \phi_2). \tag{2.9}$$

If $I_1 = I_2$, the interference pattern's maximum, $I_{\max}$, corresponds to $|\phi_1 - \phi_2| = 0$, i.e.,

$$I_{\max} = 2I_1 + 2I_1\cos(0) = 4I_1, \tag{2.10}$$

whereas the minimum, $I_{\min}$, corresponds to $|\phi_1 - \phi_2| = \pi$, i.e.,

$$I_{\min} = 2I_1 + 2I_1\cos(\pi) = 0, \tag{2.11}$$

hence the nulling ratio is

$$nl = \frac{I_{\min}}{I_{\max}} = 0. \tag{2.12}$$

Let us examine the behaviour of the nulling ratio close to this value, i.e., for $|\phi_1 - \phi_2| = \Delta\phi \ll 1$. In this case we obtain

$$nl = \frac{I_{\min}}{I_{\max}} = \frac{1 + \cos(\pi + \Delta\phi)}{1 + \cos(\Delta\phi)} = \frac{1 - \cos(\Delta\phi)}{1 + \cos(\Delta\varphi)} \tag{2.13}$$

$$nl \approx \frac{1 - 1 + \frac{\Delta\phi^2}{2}}{1 + 1 - \frac{\Delta\phi^2}{2}} \approx \frac{\Delta\phi^2}{4} \quad \text{for} \quad \Delta\phi \ll 1. \tag{2.14}$$

Let us now return to the situation where $|\phi_1 - \phi_2| = 0$, and examine what happens if $I_1 \neq I_2$. Supposing

$$I_2 = (1 + \epsilon)I_1, \tag{2.15}$$

where $\epsilon \ll 1$. This means that the relative flux flux mismatch $\Delta I / I$ is

$$\frac{\Delta I}{I} = \frac{I_2 - I_1}{I_1} = \frac{(1 + \epsilon)I_1 - I_1}{I_1} = \frac{\epsilon I_1}{I_1} = \epsilon. \tag{2.16}$$

The nulling ratio *nl* then is

$$nl = \frac{I_{\text{min}}}{I_{\text{max}}} = \frac{I_1 + I_2 + 2\sqrt{I_1 I_2}\cos(\pi)}{I_1 + I_2 + 2\sqrt{I_1 I_2}\cos(0)} = \frac{I_1 + I_2 - 2\sqrt{I_1 I_2}}{I_1 + I_2 + 2\sqrt{I_1 I_2}}, \tag{2.17}$$

$$nl = \frac{I_1 + (1 + \epsilon)I_1 - 2I_1\sqrt{1 + \epsilon}}{I_1 + (1 + \epsilon)I_1 + 2I_1\sqrt{1 + \epsilon}} = \frac{2 + \epsilon - 2\sqrt{1 + \epsilon}}{2 + \epsilon + 2\sqrt{1 + \epsilon}}, \tag{2.18}$$

developing $\sqrt{1 + \epsilon}$:

$$\sqrt{1 + \epsilon} = 1 + \frac{\epsilon}{2} - \frac{\epsilon^2}{8} + ... \tag{2.19}$$

$$nl \approx \frac{2 + \epsilon - 2(1 + \frac{\epsilon}{2} - \frac{\epsilon^2}{8})}{2 + \epsilon + 2(1 + \frac{\epsilon}{2} - \frac{\epsilon^2}{8})} = \frac{-2\frac{-\epsilon^2}{8}}{4 + 2\epsilon + 2\frac{-\epsilon^2}{8}}, \tag{2.20}$$

$$nl \approx \frac{\epsilon^2}{16}. \tag{2.21}$$

2.3 Achromatic Phase Shifters

One of the key components of the Bracewell interferometer is the Achromatic Phase Shifter (APS). It is an optical element designed to introduce a given difference in phase in a beam regardless of the wavelength.

Let us state clearly that in real life there are no perfect optical elements that would fulfil this function ideally. There are many workable solutions, however, always representing a compromise between the “neatness” of the phase shift (how well does the real phase shift correspond to the required value), and the width of the spectral band in which it is to be achieved.

For a given Optical-Path Difference (OPD) between the two optical paths, the corresponding phase difference $\Delta\varphi$ can be expressed as

$$\Delta\varphi = 2\pi\frac{\text{OPD}}{\lambda}, \tag{2.22}$$

where λ is the wavelength.

The phase shift therefore depends on the wavelength, $\Delta\varphi = \Delta\varphi(\lambda)$. In order to obtain a wavelength-independent phase shift of π at zero OPD, an APS has to be introduced into the setup.

There are alternative approaches, however. The “adaptive nuller” was tested at the JPL (Peters et al. 2008), and at Delft, polarisation and multi-axial nulling interferometry were studied (Spronck et al. 2006).

Many different concepts of achromatic phase shifters are available in the literature (Rabbia et al. 2001, 2000). The *Darwin* collaboration studied ten APS concepts (ESA 2002), promising $nl < 10^{-6}$. The spectral range was that of 6–20 µm, with 6–18 µm mandatory, the extension to 18–20 µm priority number 2, and that to 4–6 µm priority number 3. Their various merits will eventually need to be evaluated experimentally. Not all of these concepts are currently in the research and development process. Some, although promising

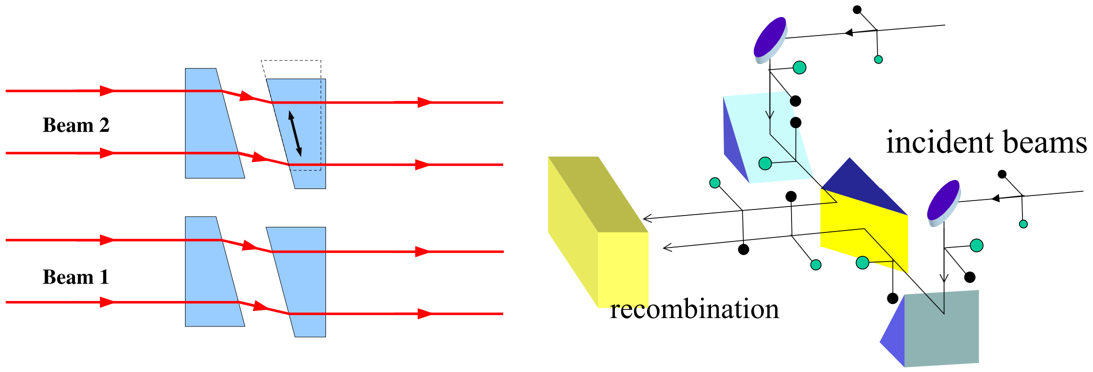

(a) Dielectric or Dispersive Prisms (b) Field Reversal or Periscope

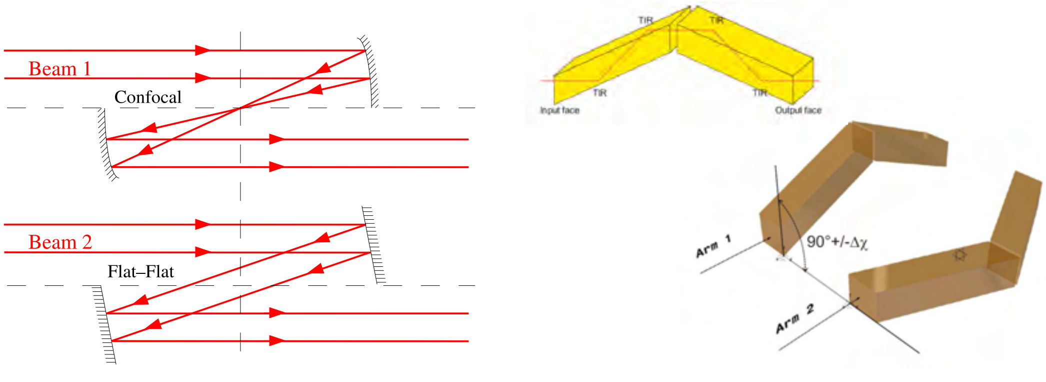

(c) Focus Crossing or Through Focus (d) Fresnel's Rhombs

***Figure 2.2* -** The four APS concepts investigated by ESA.

in the long run, require a substantial effort to overcome technical hurdles chiefly because of the novelty and of the required spectral range (e.g., integrated optics, zero order gratings).

Out of the ten, four APS concepts were selected for further study by ESA in recent years (Fig. 2.2):

1. Dielectric or Dispersive Prisms,
2. Focus Crossing or Through Focus,
3. Field Reversal or Periscope, and
4. Fresnel's Rhombs.

The SYNAPSE testbed uses two pairs of CaF_2 Prisms (Sec. 3.11) as a Dispersive Prisms APS and, at the same time, the prisms form an intrinsic part of the setup because they also function as a compensator balancing the cumulative thickness of dielectric in the optical path.

A Dispersive Prisms APS prototype with three pairs of prisms of three different materials was developed by Thales Alenia Space (Sec. 3.9.3). A Focus Crossing APS prototype was designed by the Observatoire de Côte d'Azur, Nice, France (Sec. 3.9.1). And, last but not least, a Field Reversal APS prototype was manufactured at Max-Planck-Institut für Astronomie in Heidelberg in collaboration with Kayser-Threde GmbH in Munich and the IOF Fraunhofer Institute for Applied Optics in Jena (Sec. 3.9.2).

2.4 The Dispersive Prisms APS

Let us now look in more detail at the Dispersive Prisms APS because it of its rôle in the SYNAPSE setup. This method is directly inspired by the practice of opticians who try to minimise chromatic aberrations in lens systems.

We shall examine one of the simplest cases when a pair of dispersive prisms is introduced into each arm of the interferometer. The beams thus propagate in two different media, viz., in air and in the dielectric. The refractive index n_{diel} of the dielectric varies with wavelength,

$$n_{\mathrm{diel}} = n_{\mathrm{diel}}(\lambda). \tag{2.23}$$

We shall consider air as not dispersive, i.e., its index n_{air} does not vary with wavelength

$$n_{\mathrm{air}}(\lambda) = 1. \tag{2.24}$$

Because of the presence of the dispersive elements, the phase difference $\Delta\phi$ between the two beams will vary with wavelength

$$\Delta\phi = \Delta\phi(\lambda). \tag{2.25}$$

It can be expressed as

$$\Delta\phi(\lambda) = \frac{2\pi}{\lambda}\left[n_{\mathrm{air}} \cdot (\mathrm{OPD} + e) - e \cdot n_{\mathrm{diel}}(\lambda)\right], \tag{2.26}$$

where e is the difference in thickness of dielectric encountered by the beams. Note that we can consider the total geometric length of the optical path constant, i.e., adding dielectric into the optical path reduces the air column in it by the same amount. We can thus write

$$\Delta\phi(\lambda) = \frac{2\pi}{\lambda}\left[\mathrm{OPD} \cdot n_{\mathrm{air}} + e \cdot (n_{\mathrm{air}} - n_{\mathrm{diel}}(\lambda))\right]. \tag{2.27}$$

Now we can impose

$$\Delta\phi(\lambda_1) = \pi, \tag{2.28}$$

$$\Delta\phi(\lambda_2) = \pi, \tag{2.29}$$

for two distinct wavelengths $\lambda_{1,2}$. This is a set of two equations with two unknowns, e and OPD,

$$\frac{2\pi}{\lambda_1}\left[\mathrm{OPD} \cdot n_{\mathrm{air}} + e \cdot (n_{\mathrm{air}} - n_{\mathrm{diel}}(\lambda_1))\right] = \pi, \tag{2.30}$$

$$\frac{2\pi}{\lambda_2}\left[\mathrm{OPD} \cdot n_{\mathrm{air}} + e \cdot (n_{\mathrm{air}} - n_{\mathrm{diel}}(\lambda_2))\right] = \pi. \tag{2.31}$$

For given two wavelengths there are values of e and OPD which correspond to a perfect $nl = 0$. If the material and the waveband are chosen appropriately, a Dispersive Prisms APS can provide nulling better than a specified value within the waveband (Fig. 2.3).

Let us look at the dual problem: How do we find the working point if we have the means to explore the parameter space (OPD, e)? Fig. 2.4 shows that there are many local minima, and thus we need to understand this space better in order to find the global minimum. Performing an OPD scan for a given value of e will yield a fringe packet. If the fringe packet is symmetric, we find a minimum (Fig. 2.5). It could be a local minimum, however. The ambiguity can be lifted by looking at neighbouring minima. Section 6.1.5 describes a practical application of this technique.

2.5 Wavefront filtering

Another important ingredient in nulling interferometry is wavefront filtering. Achieving high levels of destructive interference implies stringent requirements in terms of wavefront quality. These requirements can be reduced using a wavefront filter (Mennesson et al. 2002).

There are two techniques of wavefront filtering used in nulling interferometry:

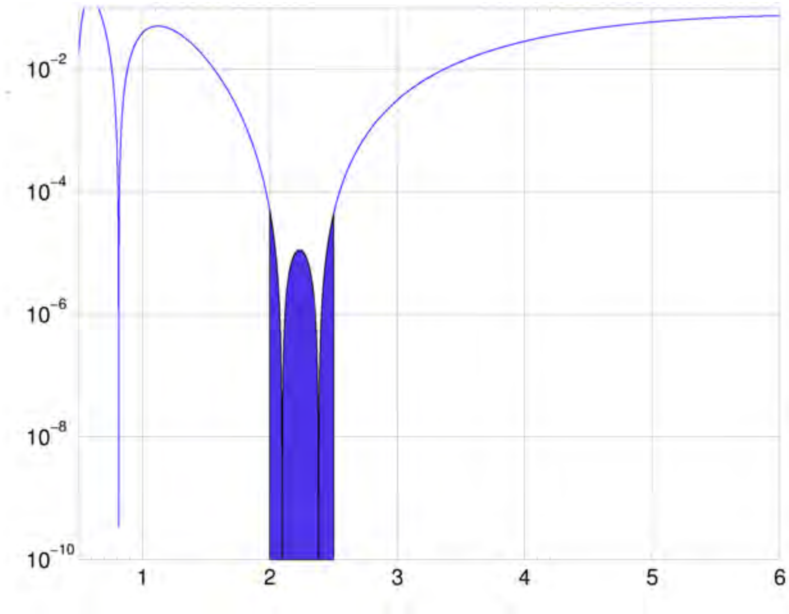

Figure 2.3 **-** Nulling ratio as a function of wavelength (in μm) produced by Dispersive Prisms APS with two thicknesses of CaF_2, one per beam. Appropriate selection of thicknesses ensures that in a given spectral band (highlighted) the nulling ratio is $nl < 10^{-4}$. This is possible because CaF_2 is dispersive, i.e., its refractive index varies with wavelength.

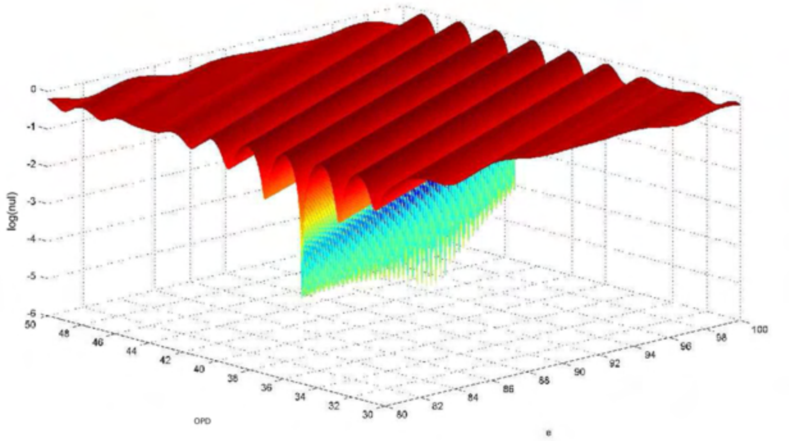

Figure 2.4 **-** Map of the (OPD, e) space. There are many local minima in the (OPD, e) parameter space. Nonetheless, the global minimum is unique.

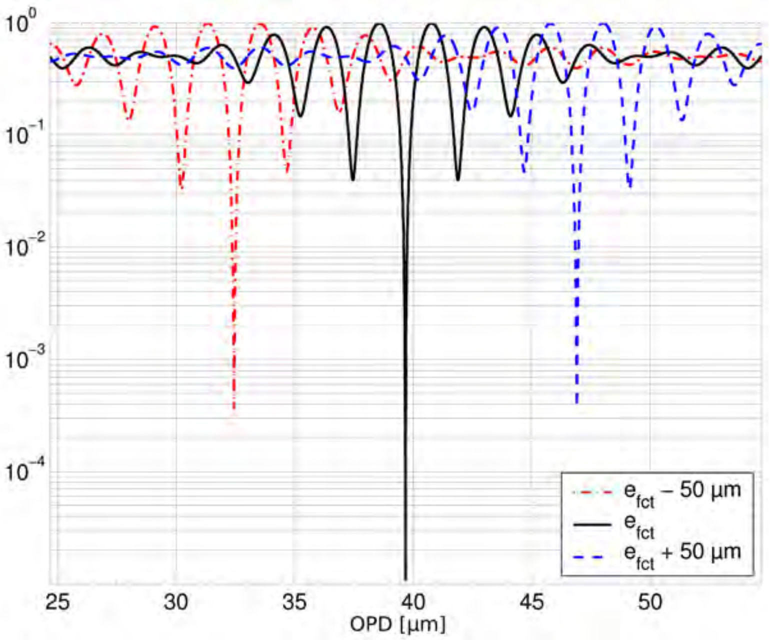

Figure 2.5 **-** Three OPD scans for different values of *e*. Performing an OPD scan for a given value of *e* will yield a fringe packet. If the fringe packet is symmetric, we find a minimum. It could be a local minimum, however. The ambiguity can be lifted by looking at neighbouring minima.

1. Pinholes, i.e., spatial filters;
2. Single-Mode optical Fibres (SMF's), i.e., modal filters.

A SMF is, effectively, a waveguide that transmits only one resonance mode. We can view the fibre as a resonance cavity with a single resonance mode in the given spectral band. This resonance mode is a solution of Maxwell's equations and is not confined to the internal volume of the fibre. In fact, it extends from both extremities of the fibre as lobes. Therefore, whatever the properties of the optical field incident upon the fibre head, the output of the fibre will be an extension of this proper mode.

Nulling interferometers require that the wavefront be without distortion to a level of $\lambda/1000$ if the nulling ratio *nl* is to be less than 10^{-5} (Sec. 3.3.6). The reason is easily seen when we realise that if there are defects in the wavefront, a part of the flux arrives at the point of interference out of phase. Without wavefront filtering, the $\lambda/1000$ requirement would be prohibitively strict because it implies that all the optical surfaces must be polished to that level of precision.

Unfortunately, the only way to estimate the quality of SMF's is to measure it with a specialised nulling interferometer (Ksendzov et al. 2007).

2.6 Stability

Experimental studies of nulling interferometer testbeds (Serabyn 2003; Schmidtlin et al. 2005; Ollivier et al. 2001; Vink et al. 2003; Alcatel; Brachet 2005) show that even in simple setups, the interference pattern is unstable, drifting with time. Even interferometers breadboarded on an optical bench in the relatively well-controlled laboratory environment (a priori simpler than the actual *Darwin*/TPF-I, with its multiple telescopes rotating in space) display drifts. Chazelas et al. (2006) give a quantitative summary of these effects, using data from Ollivier (1999); Alcatel; Vink et al. (2003).

We shall discuss this issue in detail in Chapter 4.

2.7 State of the art

Since 1999, several groups performed a number of experimental studies of nulling interferometry in the laboratory and on ground-based telescopes. In our bibliographical study we have drawn upon the summary table prepared by Chazelas (2007) and on Peter R. Lawson's null-vs-bandwidth plot (Lawson 2009). Our own updates are presented in Tab. 2.1 and Fig. 2.6.

Nulling interferometry is a new and challenging field of optics. By its very nature it is probably the most sensitive, and hence the most delicate, of optical experiments. This means that phenomena which are of the second or third order, and therefore rarely taken into consideration in optics, can stand out in nulling interferometry. It is a challenge, but it also is an opportunity to study them.

To summarise the current state of art in terms of demonstrating the feasibility of *Darwin*/TPF-I, the best progress was made at the Jet Propulsion Laboratory. The Adaptive Nuller demonstrated that $nl = 10^{-5}$ can be achieved in broadband (34 %) around 10 μm (Peters et al. 2008), and the Planet Detection Testbed demonstrated 4-beam nulling with $nl = 4 \times 10^{-6}$ and the detection of a simulated planet at a contrast level of 2×10^{6} (Martin et al. 2006).

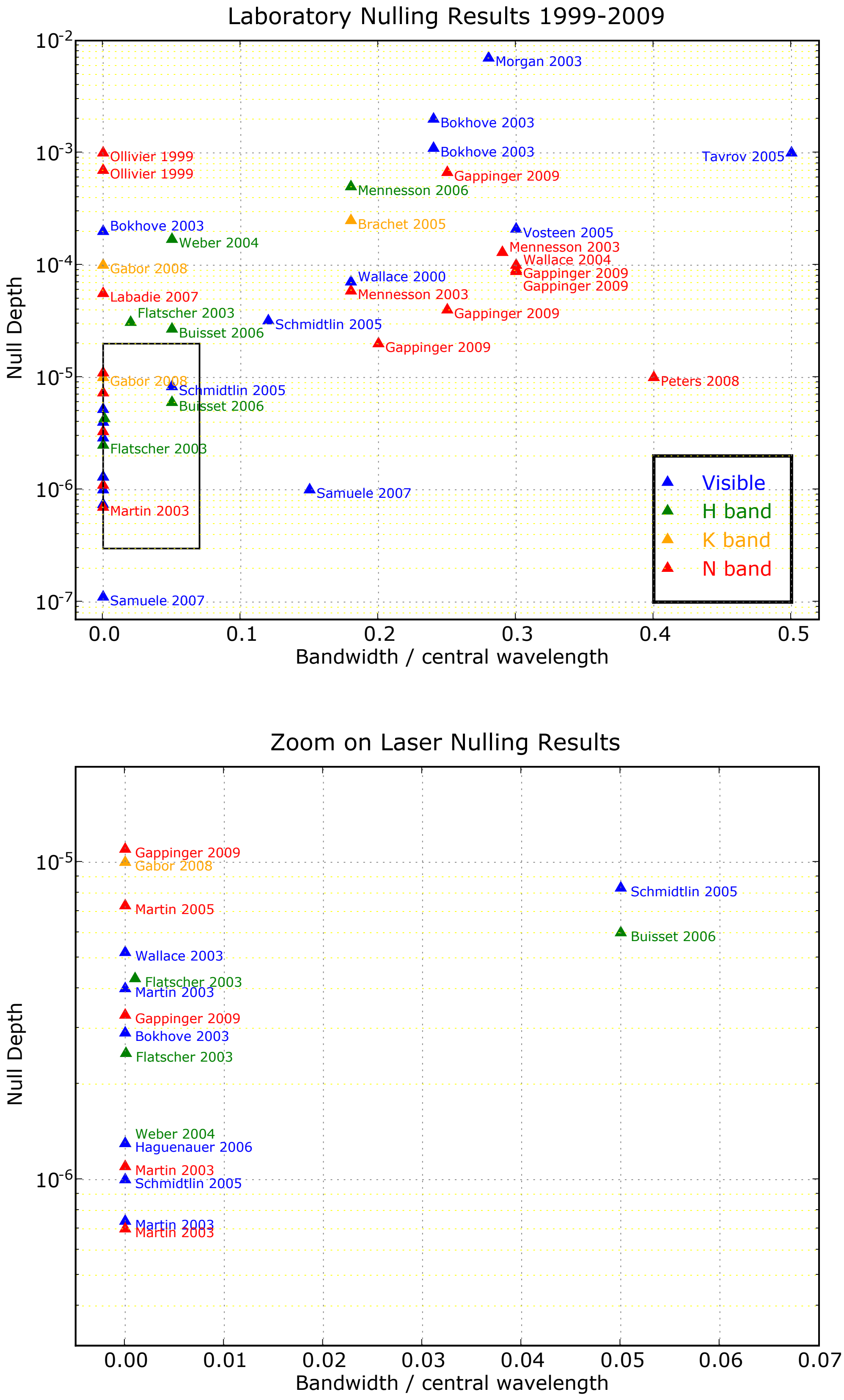

***Figure 2.6* -** Chart of nulling ratios achieved in laboratory experiments. The plot summarises the best results reported in the indicated papers, plotting the null depth against the bandwidth (given as a fraction of the central wavelength). The unabridged bibliographical references are provided in Table 2.1. Bottom plot provides a zoom on the narrow-band and laser experiment sector.

λ_{central}	$\frac{\Delta\lambda}{\lambda_{\text{central}}}$	**Null**	**Pol**	**Reference**	**Experiment**
600 nm	0.5	1×10^{-3}	–	Tavrov et al. (2005)	Tokyo
632.8 nm	3×10^{-6}	2×10^{-4}	–	Bokhove et al. (2003)	TNO TPD, Delft
632.8 nm	3×10^{-6}	2.9×10^{-6}	+	Bokhove et al. (2003)	TNO TPD, Delft
632.8 nm	3×10^{-6}	7.4×10^{-7}	+	Martin et al. (2003b)	Rot. Shear. Int., best
632.8 nm	3×10^{-6}	4×10^{-6}	+	Martin et al. (2003b)	Rot. Shear. Int., stab.
632.8 nm	3×10^{-6}	1.3×10^{-6}	–	Haguenauer and Serabyn (2006)	Fiber Nuller, JPL
635 nm	3×10^{-6}	5.2×10^{-6}	+	Wallace et al. (2003)	Opt. Pl. Det. Int., JPL
638 nm	3×10^{-6}	1×10^{-6}	+	Schmidtlin et al. (2005)	Opt. Pl. Det. Int., JPL
638 nm	3×10^{-6}	1.11×10^{-7}	–	Samuele et al. (2007)	Northrop, Redondo B.
650 nm	0.24	2×10^{-3}	–	Bokhove et al. (2003)	TNO TPD, Delft
650 nm	0.24	1.1×10^{-3}	+	Bokhove et al. (2003)	TNO TPD, Delft
650 nm	0.3	2.1×10^{-4}	–	Vosteen et al. (2005)	Delft; Friedrichshafen
650 nm	0.05	8.3×10^{-6}	+	Schmidtlin et al. (2005)	Opt. Pl. Det. Int., JPL
650 nm	0.12	3.2×10^{-5}	+	Schmidtlin et al. (2005)	Opt. Pl. Det. Int., JPL
650 nm	0.15	1×10^{-6}	–	Samuele et al. (2007)	Northrop, Redondo B.
650 nm	0.18	7.1×10^{-5}	+	Wallace et al. (2000)	JPL
700 nm	0.28	7×10^{-3}	–	Morgan et al. (2003)	Nulling B. Comb., JPL
1306 nm	8×10^{-5}	2.5×10^{-6}	–	Flatscher et al. (2003)	Astrium, Friedrichshafen
1.54 µm	3×10^{-6}	1.3×10^{-6}	+	Weber (2004)	MAII I, Cannes
1.545 µm	0.02	3.1×10^{-5}	–	Flatscher et al. (2003)	Astrium, Friedrichshafen
1.55 µm	0.05	2.7×10^{-5}	–	Buisset et al. (2007)	MAII II, Cannes
1.55 µm	0.05	6×10^{-6}	+	Buisset et al. (2007)	MAII II, Cannes
1.55 µm	1×10^{-3}	4.3×10^{-6}	–	Flatscher et al. (2003)	Astrium, Friedrichshafen
1.57 µm	0.05	1.7×10^{-4}	–	Weber (2004)	MAII I, Cannes
1.65 µm	0.18	5×10^{-4}	–	Mennesson et al. (2006)	Fiber Nuller, JPL
2.2 µm	0.18	2.5×10^{-4}	–	Brachet (2005)	Synapse I; IAS Orsay
3.39 µm	3×10^{-6}	1×10^{-5}	+	Gabor et al. (2008c)	Synapse II; IAS Orsay
3.39 µm	3×10^{-6}	1×10^{-4}	–	Gabor et al. (2008c)	Synapse II; IAS Orsay
9.5 µm	0.2	2×10^{-5}	+	Gappinger et al. (2009)	Achr. Nulling T., perisc.
9.5 µm	0.25	4×10^{-5}	+	Gappinger et al. (2009)	Achr. Nulling T., perisc.
9.5 µm	0.25	6.7×10^{-4}	–	Gappinger et al. (2009)	Achr. Nulling T., FC
9.5 µm	0.30	9.1×10^{-5}	–	Gappinger et al. (2009)	Achr. Nulling T., 2Prism
9.5 µm	0.30	8.8×10^{-5}	–	Gappinger et al. (2009)	Achr. Nulling T., 1Prism
10 µm	0.30	1×10^{-4}	–	Wallace et al. (2004)	Warm Nulling Testbed, JPL
10 µm	3×10^{-6}	3.3×10^{-6}	+	Gappinger et al. (2009)	Achr. Nulling T., perisc.
10 µm	3×10^{-6}	1.1×10^{-5}	–	Gappinger et al. (2009)	Achr. Nulling T., perisc.
10 µm	0.4	1×10^{-5}	+	Peters et al. (2008)	Adaptive Nuller T., JPL
10.6 µm	3×10^{-6}	1×10^{-3}	–	Ollivier (1999)	IAS Orsay; typ.
10.6 µm	3×10^{-6}	7×10^{-4}	–	Ollivier (1999)	IAS Orsay; best
10.6 µm	3×10^{-6}	1.1×10^{-6}	–	Martin et al. (2003a)	MMZ Nuller, JPL
10.6 µm	3×10^{-6}	7×10^{-7}	+	Martin et al. (2003a)	MMZ Nuller, JPL
10.6 µm	3×10^{-6}	7.3×10^{-6}	–	Martin et al. (2005)	Planet Detection T., JPL
10.6 µm	3×10^{-6}	5.6×10^{-5}	–	Labadie et al. (2007)	Grenoble
10.675 µm	0.18	5.9×10^{-5}	–	Mennesson et al. (2003)	Keck Nuller B. Comb., JPL
10.775 µm	0.29	1.3×10^{-4}	–	Mennesson et al. (2003)	Keck Nuller B. Comb., JPL

Table 2.1 - Main nulling-interferometry laboratory results, ordered according to spectral band (first column). The second column gives the bandwidth (as a fraction of the central wavelength), the third column give the best null achieved, the "Pol" column indicates whether polarisers were used at the output. The "Reference" and "Experiment" columns indicate the setup ("Achr. Nulling T." is the Achromatic Nulling Testbed at the JPL which had several phase shifter options: "perisc." was the periscope, "FC" was the through focus or focus crossing, "1Prism" was a setup with ZnSe dispersive prisms, "2Prism" was a setup with ZnSe and ZnS prisms).

Chapter 3

Description of SYNAPSE & NULLTIMATE

Contents

3.1 Introduction

3.1.1 The purpose of this Chapter

The purpose of this Chapter is to provide a detailed description of the two nulling testbeds currently operating at the *Institut d'Astrophysique Spatiale* in Orsay, France, namely the SYNAPSE and the NULLTIMATE instruments.

NULLTIMATE can be regarded as the successor of SYNAPSE: the know-how and insights we acquired while working on SYNAPSE went into the design of NULLTIMATE. This thesis is primarily a report on SYNAPSE. Nonetheless, since NULLTIMATE inherited many subsystems from SYNAPSE (certain light sources, detectors, single-mode fibres, etc.), it will not be too difficult to describe both testbeds.

What is more, our ambition is to provide an instructive text that future generations of students working with these testbeds would find useful. We shall, therefore, devote considerable space to the reasoning behind the design choices: and we hope that a parallel description of both testbeds will help us to achieve this goal.

3.1.2 General note

It must be noted that the two experiments are still a going concern. Their full potential has not been reached so far. If there were enough manpower, both experimental setups could be studied in parallel. We shall see that SYNAPSE is a more elegant optical design than NULLTIMATE which is more straightforward but also more robust. Certain aspects of SYNAPSE still need to be explained fully, and NULLTIMATE was designed to help in this regard. However, once a better understanding is reached with NULLTIMATE, it could be very satisfying to go back to SYNAPSE in order to verify the theory.

The fact that the experiments are ongoing does not merely mean that some set of goals has not been reached so far, but also that the objectives themselves are still evolving: not knowing the full potential of the testbeds, the work itself gradually brings forth the possible objectives to be reached. I am stressing this point because in the logical order of things the reader might expect that a description of an experiment should start with an account of its purpose. Should it not be the purpose that dictates the operational parameters and therefore the choice of means to achieve them? Should the work not have evolved linearly according to a predetermined plan, such as the one outlined below?

- Objective: compare the achromatic phase shifter performance in the K band.
- Since the theoretical limits of the phase shifter prototypes are to be expected at the null levels of $nl = 10^{-5}$, the testbed must reach at least $nl = 3 \times 10^{-6}$.
- In order to reach such null levels, and in view of other constraints (flux levels of available sources, quality and performance of optical elements including modal filters, precision of alignment procedures, sensitivity of available detectors, etc.) the setup has to have such and such an optical design.

Although there have certainly been elements of such linear planning present during the development of the testbeds in Orsay, neither SYNAPSE nor NULLTIMATE can be fully understood in such a framework. As with all pioneering projects, the testbeds can only be fully understood and appreciated as vehicles of discovery. Their ultimate purpose is not to reach certain predefined performance levels but *to learn in detail about phenomena hitherto known only by extrapolation.*

Figure 3.1 - A global view of the first nulling testbed at the *Institut d'Astrophysique Spatiale* (Ollivier 1999). It operated at ambient temperature in monochromatic polarised light at 10.6 μm and achieved $nl = 7 \times 10^{-4}$.

This is fundamentally the reason why this Chapter does not follow the classical, linear plan which would define the layout as a solution to the problem of reaching the objectives with available means. The choices were, naturally, dictated by considerations aimed at optimising performance. However, the process was not linear, and this Chapter would not benefit from attempts to follow the rationale behind each experimental choice. We shall, therefore, limit ourselves to a simple description of the equipment.

3.1.3 Historical background

3.1.3.1 Monochromatic 10.6 μm testbed

The *Institut d'Astrophysique Spatiale* in Orsay, France, has been involved in nulling interferometry since 1995 when Marc Ollivier started his thesis under Alain Léger's direction (Ollivier et al. 2001; Ollivier 1999). His testbed (Fig. 3.1) operated at ambient temperature in monochromatic polarised light at 10.6 μm and achieved $nl = 7 \times 10^{-4}$.

3.1.3.2 The SYNAPSE testbed

The second effort was the SYNAPSE[1] testbed (Fig. 3.2), again designed for operation at ambient temperature, but in polychromatic light in the K band, i.e., between 2.0–2.5 μm (Brachet 2005). The primary aim of this

---

[1] SYmmetric Nuller for Achromatic Phase Shifter Evaluation

Figure 3.2 **-** A view of the Synapse nulling testbed's interferometric setup (Brachet 2005, photograph taken in Sept. 2003).

apparatus was achromatic phase shifter testing. This purpose drove the optical design towards symmetry.

3.1.3.3 The Synapse II testbed

It soon became apparent that stability is a crucial issue in nulling interferometry, and an upgraded version of the Synapse testbed was implemented. It is known as Synapse II (Gabor et al. 2008c).

3.1.3.4 The Nulltimate testbed

In parallel with Synapse II, the team planned a new setup at 10.6 μm, this time in cryogenic conditions (Chazelas 2007). The project was called Nulltimate[2]. Considerable effort was dedicated to the cryogenic design (3.3) but in the end it was decided to postpone its realisation until the experimental technique is fully mastered at ambient temperature in the K band. This is why the Nulltimate testbed was finally designed for operational parameters very much like those of Synapse but with a different optical design (Fig. 3.4).

3.1.3.5 The Persee testbed

The IAS team is currently also involved in the Persee[3] testbed (Fig. 3.5) which was designed as a demonstrator for the Pegase mission proposal (Principal Investigator: Marc Ollivier). Persee is currently being installed at the Observatory of Paris in Meudon. The design and tests of several subsystems took place at IAS, however. The scope of our report must be limited, and we shall concentrate on two testbeds: Synapse and Nulltimate.

---

[2] NULling Low Temperature Interferometer for Multi Achromatic phase shifter TEsting

[3] Pegase Experiment for Research and Stabilization of Extreme Extinctions

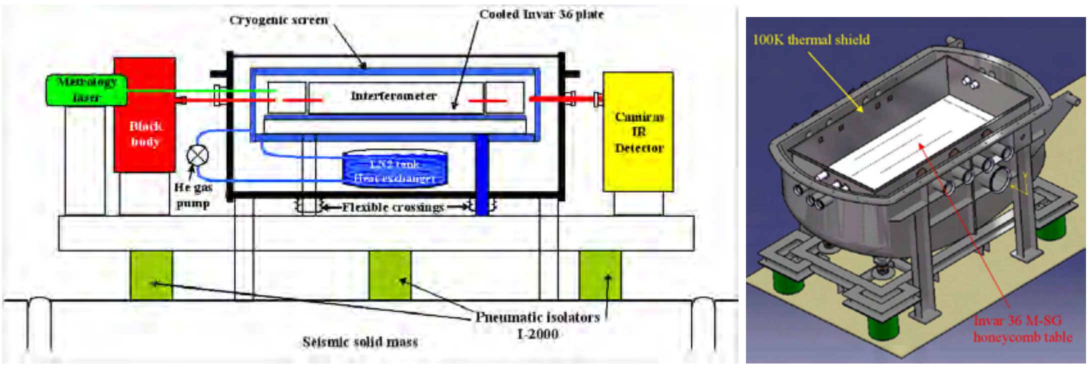

***Figure 3.3* -** The NULLTIMATE testbed was originally designed for cryogenic conditions (10^{-4} torr, 100 K) and $\lambda \approx 10$ µm (Chazelas 2007).

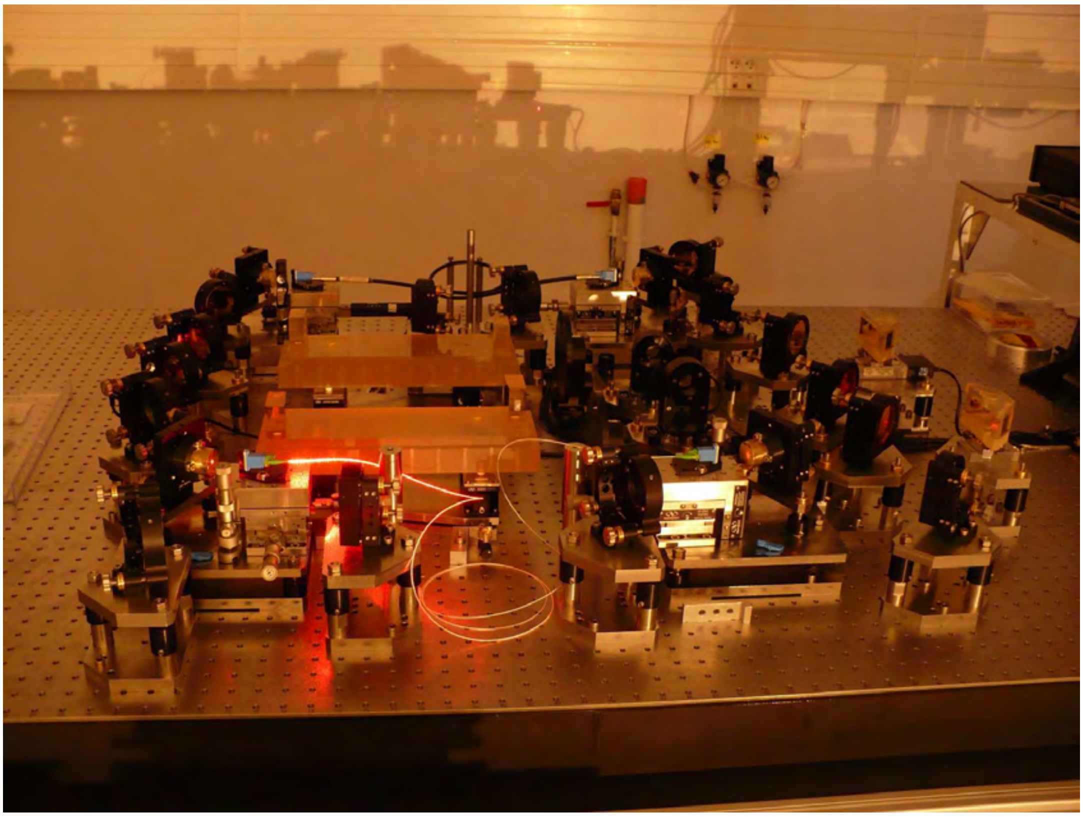

***Figure 3.4* -** General view of NULLTIMATE (during alignment).

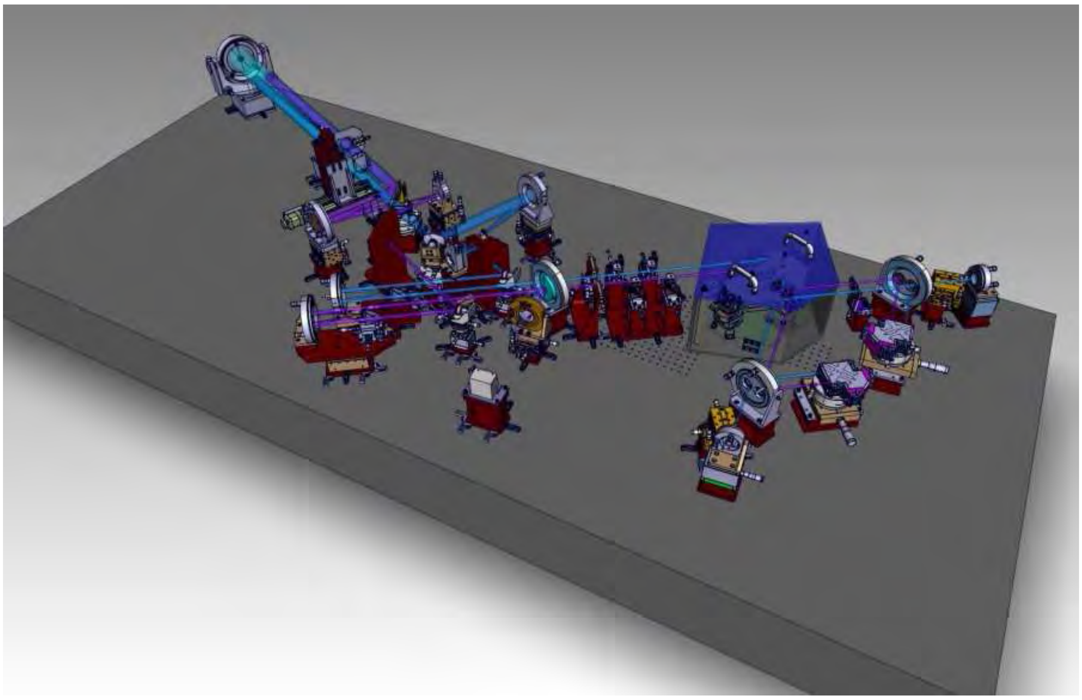

Figure 3.5 - A view of the PERSEE testbed.

3.2 General overview

3.2.1 An outline

The experimental setup contains the main optical chain of subsystems (the sources, the interferometer proper, the detectors), as well as a number of auxiliary subsystems (alignment instruments, experiment control electronics and software, data acquisition hardware and software, antivibration protection, thermal and accoustic insulation, temperature control). All of these will be described in detail after we first provide an outline of the whole.

The general purpose of both setups, SYNAPSE and NULLTIMATE, is to achieve high levels of stable nulling performance first in the K band (for our purposes defined as $\lambda \in [2.0, 2.5]\mu$m), and eventually at $\lambda = 10\ \mu$m. This means we need two identical beams, corresponding to the telescope apertures following the same field of view on the sky, we need to combine them interferometrically, and we need to detect the result. Both testbeds create the two identical beams by splitting a single beam into two. Combining the beams interferometrically means that the optical path of both beams must be of equal length. We therefore need to include delay lines and dielectric compensating plates or wedges to equate the optical paths of the two beams. Furthermore, polychromatic nulling requires that a phase shift of π be introduced between the two beams achromatically. And finally, when combined, the beams must be of equal flux and the wavefronts must be of adequate quality. An additional optical subsystem, namely two polarisers, one at each end of the interferometer, proved invaluable not only in providing additional information but in improving the performance.

The minimal list of optical subsystems can be outlined as follows:

- Source, generating a single beam.
- Beam splitting subsystem creating two identical beams.
- Delay lines and dielectric compensators.

- Achromatic phase shifters.
- Flux balance control.
- Wavefront filter.
- Polarisers.
- Beam combining subsystem.
- Detector subsystem.

There is also a number of auxiliary systems that need to be described:

- Alignment instruments.
- Temperature control.
- Antivibration protection.
- Thermal and accoustic insulation.
- Experiment control hardware and software.
- Data acquisition hardware and software.

Experiments are not fully determined by the instruments and their layout: the operational methodology is a crucial part of the whole process of experimental work. We shall, therefore, devote a part of this Chapter also to an outline of certain procedures, techniques and protocols, leaving a detailed discussion of some of them to the following Chapters (4 and 5).

3.2.2 General layout

Let us start with a general view of each of our two testbeds.

3.2.2.1 SYNAPSE

Whereas the interferometer proper is installed on a dedicated optical table, the sources as well as the detectors reside on their own optical benches, mechanically decoupled from the interferometer's primary bench (Fig. 3.6). These three tables are optically linked with optical fibres. Since we use single-mode fibres, the fibre linking the interferometer with the detector also serves as a modal filter. The interferometer with its dedicated optical table is insulated by a plexiglass enclosure with an optional imposed inverse heat gradient (Fig. 3.7).

3.2.2.2 NULLTIMATE

Fig. 3.8 shows the NULLTIMATE testbed with its protective casing. Here, the sources and the detectors are all installed on the same optical table as the interferometer proper. The interferometer is encased in a plexiglass enclosure, mechanically decoupled from the optical table. Again, single-mode optical fibres are used but, unlike in the case of SYNAPSE, they are not necessary to provide an optical link between the sources, the interferometer proper and the detector since these optical subsystems are all installed on the same optical table. Like in SYNAPSE, the purpose of the single-mode fibre linking the interferometer and the detector is modal filtering of the wavefront. The purpose of the fibre linking the sources with the interferometer proper is less crucial, however. It merely provides the same beam geometry regardless of which source is being used.

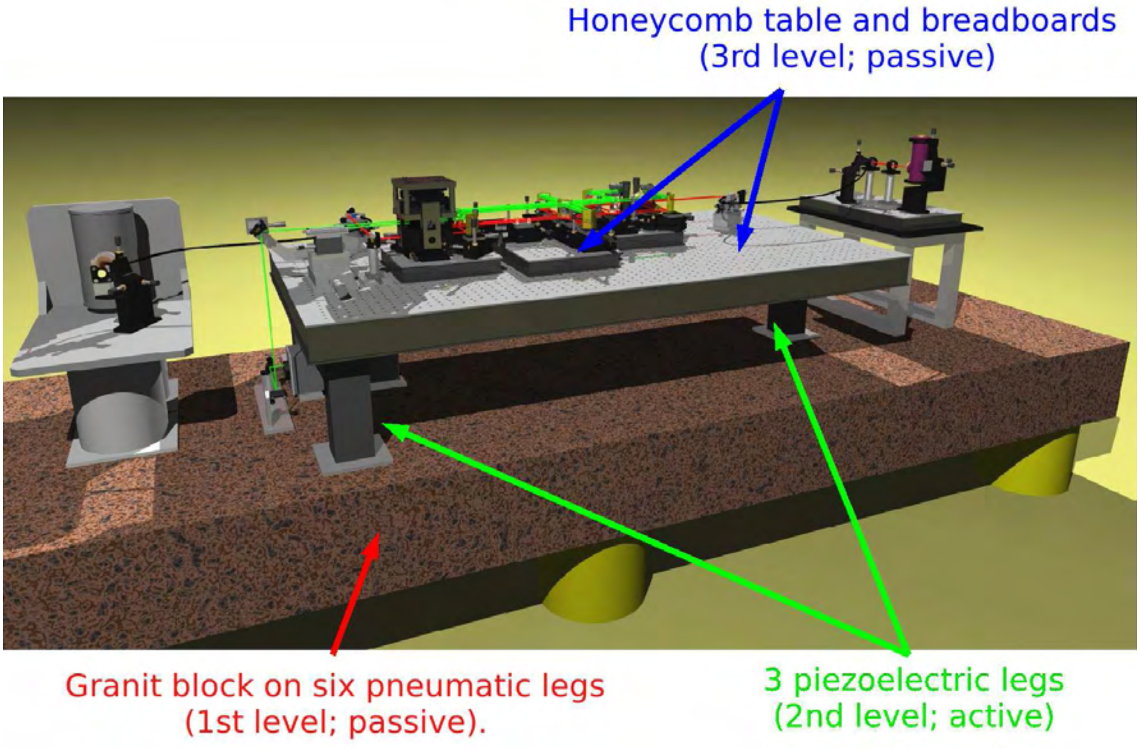

***Figure 3.6* -** SYNAPSE experimental setup: The interferometer itself is mechanically decoupled from the source and detector systems. The whole setup is installed on a granit block supported by six pneumatic legs (passive). Further, the interferometer's optical table stands on three piezoelectric active legs (Brachet 2005).

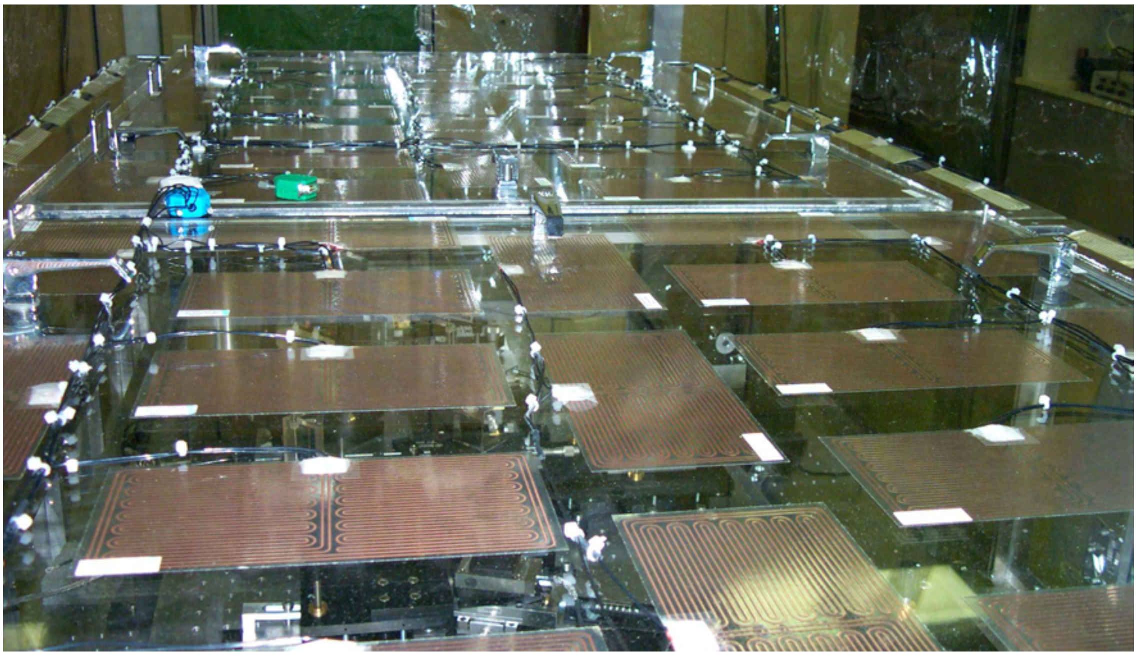

***Figure 3.7* -** The interferometer table of SYNAPSE is enclosed in a plexiglass enclosure. Its top can be heated in order to impose a thermal gradient to minimise air turbulence (Brachet 2005).

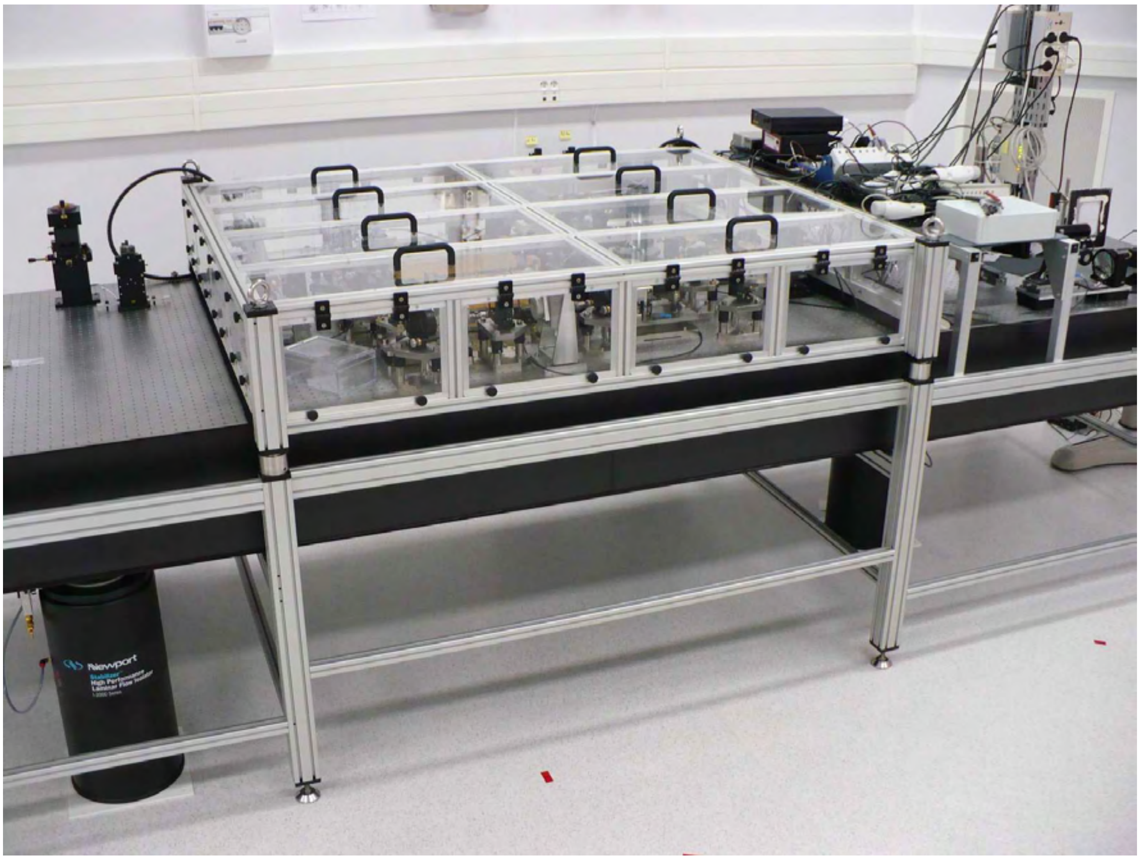

***Figure 3.8* -** NULLTIMATE on its optical table, with protective casing.

3.3 Purpose of the subsystems

We have already given a first glimpse of the the function, purpose and constraints of our setup in Section 3.2.1. In the present Section, we shall provide a qualitative description of the individual subsystems.

3.3.1 A point source observed by two apertures

As we have already said, the general purpose of the testbeds is to study nulling interferometry. This implies that we need to simulate a point source observed by two apertures and combined interferometrically in a destructive manner. The point source represents a star. (We do not simulate the planets orbiting our star.) The two apertures represent two telescopes observing the star. The rest of the setup corresponds to the combiner module of the future space observatory.

There are (at least) two possible approaches to the simulation of the point source observed by two apertures:

1. Create a large collimated beam (simulating an optical field generated by a point source), and sample it by two separate apertures. Only a small part of the flux can be utilised in this approach.
2. Create a collimated beam, and simulate the two apertures by splitting the beam into two equal beams. Practically all of the flux is sampled in this case, but the setup is more difficult to build.

The basic parameter we need to measure is the contrast between the two fluxes: one corresponding to the constructive interference, and the other to the destructive interference. This is the nulling ratio, *nl*, which we have discussed previously (Section 2.2). This means that one of the basic specifications our setups have to meet is the photometric budget. The two beams corresponding to the two apertures need to have a flux sufficient to provide adequate signal-to-noise in the measurement of the nulling ratio, i.e., the remnant flux at the “bottom” of the dark fringe needs to be sufficiently strong.

It turns out that it is not easy to generate infrared fluxes at the level we require, especially if we hope to measure deep nulling ($nl < 10^{-5}$). Therefore, both SYNAPSE and NULLTIMATE implement the second approach to simulating a point source observed by two apertures.

3.3.2 Three remarks on single-mode fibres

As we have already discussed in detail (Section 2.5), nulling interferometry is very sensitive to wavefront defects, and therefore requires modal filtering. This is performed by single-mode optical fibres (SMFs) placed at the output of the interferometer. Three design issues should be explained at this point.

3.3.2.1 Paired fibres

In principle, the modal filtering is performed at the output of the interferometer but we also use another fibre of identical properties at the interferometer’s input. The basic reason why both on SYNAPSE and on NULLTIMATE it is a good idea to use identical fibres at the input and at the output of the interferometer again has to do with the photometric budget: using fibres with identical core diameters coupled to identical collimating mirrors (off-axis parabolic mirros, see Section 3.3.3) minimises the flux losses at the output.

3.3.2.2 Intensity and phase

The second issue is a direct corollary of the purpose of the output fibre (if it works perfectly). The fibre reduces all the information about the injected optical field to two parameters only: the intensity and the phase. The incident flux will simply excite the proper mode with varying intensity and phase. We insist upon

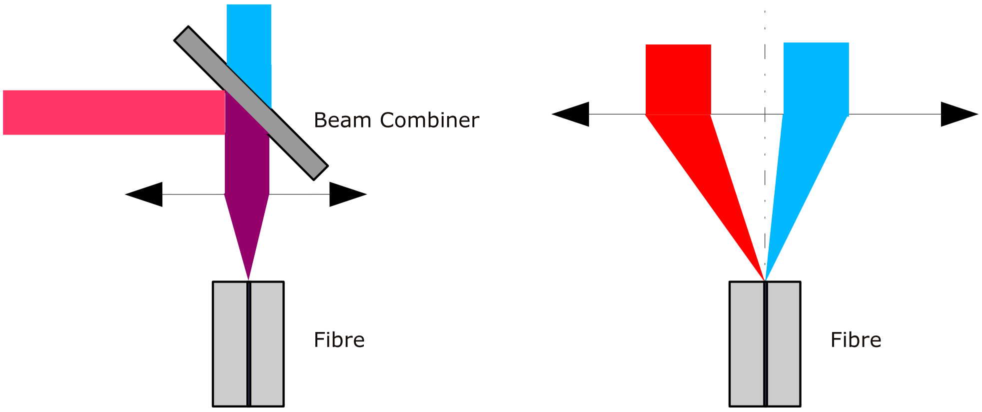

Figure 3.9 **-** Uni-axial (left) and multi-axial (right) beam combination. In order to couple both beams with the fibre identically (along the same axis) in the case of uni-axial beam combination, the beams need to be combined by a classic beam-combination element. In the case of the multi-axial beam combination, the beams non-ideally are coupled with the fibre.

these elementary observations only because it is important to remember that for all intents and purposes the relevant beam combination is going to occur upon the injection into the output fibre.

3.3.2.3 Uni-axial vs. multi-axial

The third issue is the choice of beam-combination method at the output of the interferometer. There are, generally speaking, two solutions available: uni-axial and multi-axial (Fig. 3.9). Let us take two beams which are to be combined interferometrically. In the multi-axial approach the fibre head is illuminated with the two beams that are to be combined coming from two different directions. Naturally, for each beam, the part of the incident flux which will be coupled with the fibre has to be within the acceptance lobe of the fibre. A more careful analysis of the injection shows that ideal coupling is possible only if the convergent incident beam and the acceptance lobe are identical (Appendix C.3). Since the two incident beams come from different directions, they cannot, in principle, both coincide with the acceptance lobe. Therefore, a part of the flux is lost.

The uni-axial approach is not ideal either. For simple geometric reasons, the two beams propagate through the interferometer on different paths. If they are to impact the fibre head coaxially, they have to be brought together by means of other optical devices, e.g., using a beam splitting plate. The simple presence of such an additional optical element is necessarily going to lead to flux losses. What is more, a typical beam splitter produces two complementary output beams at right angles, and only one of the two will be coupled to the output fibre. Unfortunately, even introducing another output fibre for the complementary output beam does not help, because the decisive process we need to measure is the injection into the first fibre, and the simultaneous injection into a different fibre is a different process without a direct, usable connection with the first.

Both SYNAPSE and NULLTIMATE use the uni-axial injection into the output fibre, and therefore require a classic beam combiner. This choice was motivated by the photometric budget as well as by the fact that uni-axial beam combination is the classical technique, whereas the limits of multi-axial techniques are under study.

3.3.3 Off-axis parabolic mirrors

This may be the appropriate point to include a discussion of another optical device employed on our testbeds. In both cases, i.e., on the SYNAPSE and NULLTIMATE testbeds, off-axis parabolic mirrors (OAPs) are used rather extensively.

1. Firstly, some of the sources effectively generate divergent beams, which then have to be collimated with OAPs. As we shall see in more detail in the next Section (3.4), this is the case of the ceramic black body, of the supercontinuum laser source, as well as of the laser diode.
2. Then, the collimated beams have to be injected into single-mode optical fibres through which they enter the beam-splitting setup used to generate the two beams ultimately destined to interfere at the end of the optical path. As we know, the testbeds simulate a star, the light of which they endeavour to eliminate interferometrically. The light beam produced at the output of this single-mode optical fibre simulates our "star".
3. At the output end of the star fibre, another OAP is used to generate a collimated beam, which then enters the beam-splitting subsystem generating the two beams which will pass through the testbed.
4. At the end of the bench, after the beam combiner, the combined beam is injected into the output single-mode optical fibre using another OAP.
5. And finally, at the output of the testbed's output fibre the last OAP is used to collimate the light exiting the fibre, and send it to the detector.

An OAP is (usually) an intersection of a paraboloid with a cylinder, their principal axes parallel. The angle between the principal axis and the radius r running from the paraboloid's focus to the central point of the OAP, is its angle α (Fig. C.1). It is one of the characteristics of a given OAP. The length of this radius r is

$$r = \frac{2f}{1+\cos\alpha}. \tag{3.1}$$

We provide description of Gaussian beams coupling to OAPs in Appendix C. Let us merely recall one non-intuitive property. One might think that the OAP is like a funnel, "pouring" photons into the fibre. Such a metaphor is misleading because, in fact, it implies that the whole of a "smaller" beam could be "poured" into a "larger" fibre. This is not the case. Fibre coupling is more like a resonance: the two optical fields are best coupled when they are of identical shape.

3.3.4 Symmetry

As we have already seen in connection with the coupling efficiency (Section 3.3.2.1, 3.3.3, C.3), symmetry of the design is one the key principles in our approach. In fact, the optical design of the SYNAPSE testbed can be seen as an exercise in symmetry. The beam splitting subsystem is designed in order to produce two identical beams, and the beam combiner is the beam splitter's exact counterpart.

In the case of the NULLTIMATE testbed, it was decided that symmetry would take second place after simplicity. Nonetheless, interferometry is impossible without a certain measure of symmetry. NULLTIMATE's two beams are not identical, but symmetry must be respected, and therefore the beam splitter is a mirror image of the beam combiner.

SYNAPSE implements a solution proposed by Serabyn and Colavita (2001) (Fig. 3.10, 3.11) which is symmetric by design. The dielectric plates need coatings so that the system produces beams of equal intensity.

The beam-splitter plates are plane-parallel which means that stray light, due to multiple internal reflections in the plate, has to be dealt with. The classic solution, which was implemented on NULLTIMATE, is to use slightly prismatic plates. SYNAPSE, however, uses a different approach where the stray light is deflected from contaminating the science beam's path by the shape and proportions of the plates. NULLTIMATE, with its classic solution, has to deal with beam dispersion on the prismatic beam splitter. An antisymmetrically oriented identical optical element, acting as a compensator plate, is placed as close to the beam splitter as possible.

In Section 3.3.7 we shall address the issue of balancing the thickness of dielectric in the two beams.

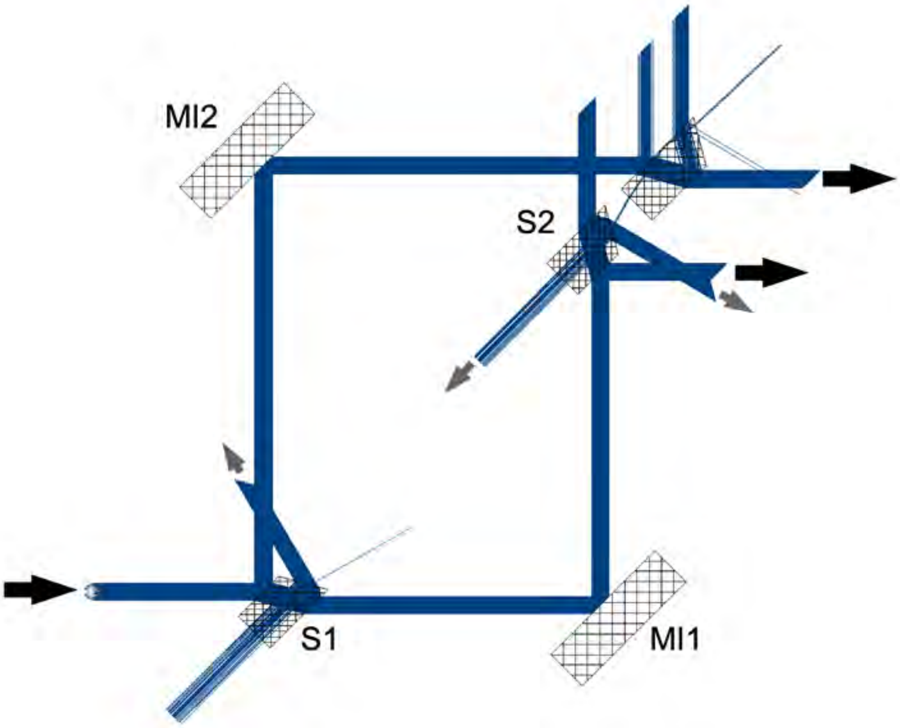

Figure 3.10 - Serabyn-Colavita modified Mach-Zehnder beam splitter.

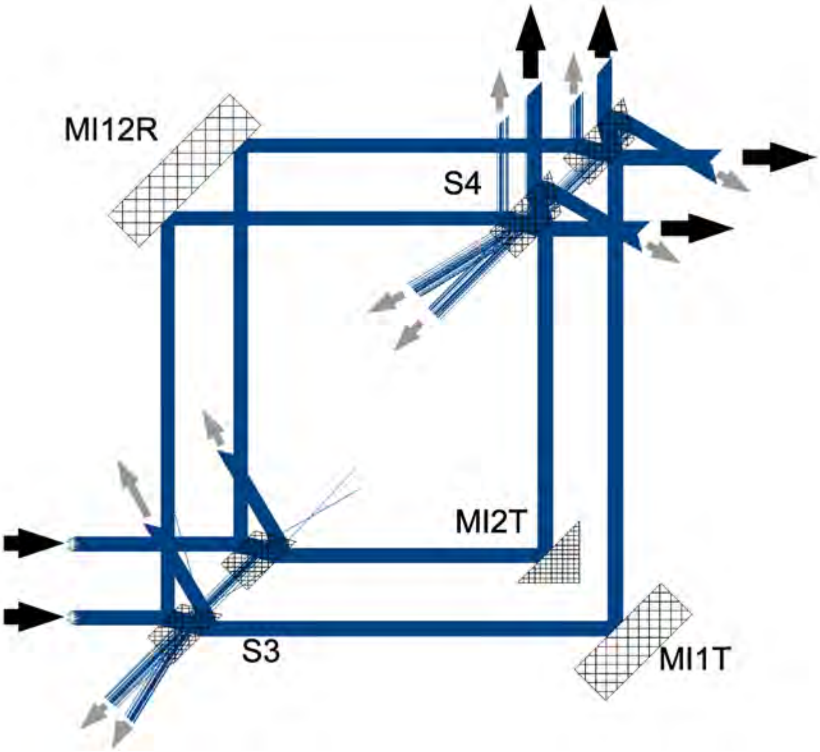

Figure 3.11 - Serabyn-Colavita modified Mach-Zehnder beam combiner.

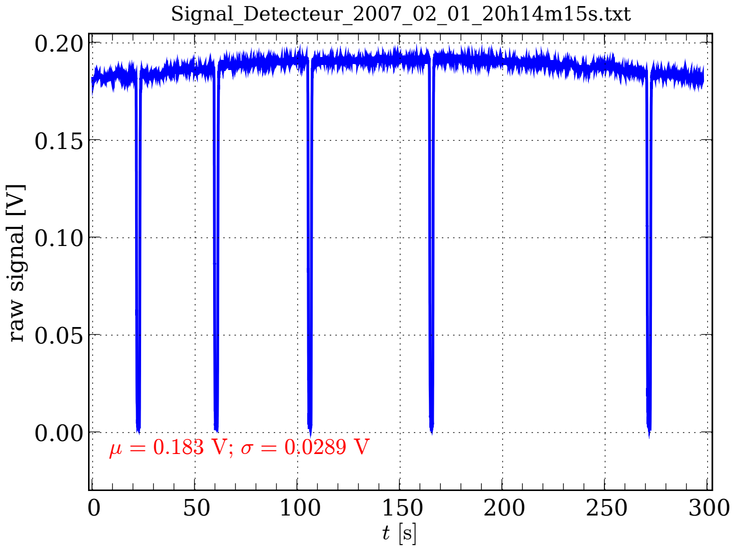

Figure 3.12 **-** Flux mismatch estimation

3.3.5 Flux balancing

As we have seen (Section 3.3.2.2), modal filtering of the interferometer output means that all the properties of the incident optical field are reduced to only two: phase difference and intensity mismatch. All interferometers need good control over flux balance but with our setup it is one of the two most crucial points.

3.3.5.1 Flux-mismatch estimation

When the flux-level is stable, estimating the mismatch is trivial. It suffices to measure flux in each beam and compare them. When the flux-level is unstable, however, such an expedient is not readily available. The flux is evolving during the measurement, and flux-mismatch estimation is no longer a simple matter of comparing two scalars.

Fig. 3.12 shows a series of measurements of one and the other beam (the shutter moves through a position where both beams are obscured) while the flux level is constantly changing. In order to estimate the flux mismatch reliably, we developed an algorithm based on the idea that the changes of the flux can be, under favourable conditions, considered linear. The algorithm acquires a series of measurements of the first beam, and tries to fit a line through the measured points. If successful, it procedes to the second beam, and repeats the procedure. In the ideal case, the algorithm produces two linear fits, roughly of the same inclination. The offset of one line with respect to the other then represents a good estimate of the flux mismatch.

3.3.5.2 Flux balancing

Several flux-balancing techniques were used on the SYNAPSE testbed over the years. We based our ideas on NULLTIMATE upon this experience.

Alignment. The first, used up to 2005[4], was based on the fact that the alignment of the bench as a whole was within 3 arcmin. Because of this and because the optics would often shift in position from one day to

---

[4] I have never used it myself.

another, tuning the orientation of several mirrors before each experimental session was not only considered acceptable: it was necessary. Flux optimisation and balancing was a natural part of the process.

Blades. With the improvement of alignment accuracy (within 10 arcsec), and especially after implementing the more solid mechanical design known as SYNAPSE II, it was no longer felt that touching the alignment was acceptable unless there was clear evidence of a shift in position. A dedicated flux-balancing device was therefore designed. It was based on two blade-bearing translation stages, one operated by a manual screw, while the other by a motorised one (Newport's "CMA-12PP" with a "SMC200" controller).

Injection into the output fibre. The coupling of each of the two beams with the output fibre is very sensitive to beam shear and tip-tilt. The relative situation of the beams is determined at the beam-combiner level. After that both beams encounter the same optical elements, viz., folding mirrors, the off-axis parabola and the output fibre. Our alignment procedures ensure that at the output of the beam combiner, the beam shear is

$$d \approx 0.1\,\mathrm{mm} \tag{3.2}$$

and the misalignment is

$$\delta \approx 5\,\mathrm{arcsec} \tag{3.3}$$

This means that if one beam is perfectly coupled with the fibre, the other necessarily is not. Fine movement of the folding mirrors can nonetheless always find a working point where both beams are equally well injected.

The procedure of flux balancing thus also fulfils the rôle of the last alignment procedure, compensating for the imperfection of beam superposition.

3.3.6 Stability

If it can be said that interference is the optical phenomenon which is the most sensitive to perturbations of all sorts, it is even more true in the case of nulling interferometry. This means that one of the guiding principles in the design of our testbeds was their mechanical and thermal stability.

Let us illustrate this point in terms of the optical path difference. If the nulling performance is to be maintained, e.g., below the level of $nl = 10^{-5}$, then (in the absence of other perturbations) the optical path difference must be maintained within

$$\frac{\Delta\phi^2}{4} < nl = 10^{-5} \tag{3.4}$$

$$\Delta\phi < 2\sqrt{nl} = 6.3 \times 10^{-3} \tag{3.5}$$

$$2\pi\frac{\mathrm{OPD}}{\lambda} < 2\sqrt{nl} = 6.3 \times 10^{-3} \tag{3.6}$$

$$\mathrm{OPD} < \frac{\lambda\sqrt{nl}}{\pi} = 10^{-3}\lambda \tag{3.7}$$

In the K band ($\lambda_{\min} = 2.0\,\mu\mathrm{m}$), therefore,

$$\mathrm{OPD} < 10^{-3}\lambda = 2\,\mathrm{nm} \tag{3.8}$$

Since we want to perform our nulling experiments in the K band, we need to make sure that we control the OPD to within nanometric levels. On such scales *everything* moves. We need to make sure, therefore, to make good use of all strategies available.

Before we outline our choices for testbed stabilisation, let us stress a point we already mentioned above (Section 3.1.2). Although the declared purposes of both Synapse and Nulltimate were tests of achromatic phase shifter prototypes, null stability, etc., the fundamental goal of these experiments is a better understanding of all the issues involved in nulling interferometry. The level of accuracy and stability required for nulling is such that it is only prudent to make sure that *all* potential perturbations are well known and under control.

The constraint of OPD being within $\lambda/1000$ is a formidable challenge in its own right. But our problem is much more daunting because it is perfectly clear that OPD control is by far *not the only* issue we have to deal with. In order to study all the perturbative effects, we need to be able to distinguish them, and that means making very sure that we indeed do have OPD under control so that we can study the impact of other parameters.

Let us now look at the available stabilisation techniques. They can be divided broadly into two categories: passive and active. The passive ones are based on the mechanical design of the optical table, the mounts, and the casing. The active ones are those employing servo loops.

3.3.6.1 Ambient conditions

From the very first picture of Synapse we have reproduced here (Fig. 3.6), it is clear that one of the chief concerns in its design was the issue of ambient conditions.

- We have *temperature* and *humidity* control (of varying quality) in both rooms where Synapse and Nulltimate are installed.
- What is more, the interferometers are installed in protective cases to minimise *air turbulence* and reduce acoustic perturbations.
- The Synapse testbed's protective case has a heating system which can introduce a temperature gradient in the volume of air, thereby *reducing uncontrolled convection.*
- The optical tables have *antivibration* features and are mechanically isolated from the floor.

We shall discuss the relevance and efficiency of all these measures in due course (Section 5.1.1).

3.3.6.2 Mechanics

The mounts of our optics likewise play a crucial rôle in the stability of the setup. The criteria to be considered concern not only their rigidity but also their practicality during alignment procedures in terms of precision, repeatability, and sensitivity. The technical solutions adopted in the initial design of Synapse were not very satisfactory. Hence, an improved version was implemented under the name of Synapse II. A different approach was taken in the making of the Nulltimate testbed. The details of the solution are included in due course (Sections 3.11).

An alternative, or rather complementary, approach is widely used, e.g., at the Jet Propulsion Laboratory, Pasadena, Ca. Servo systems may provide beam shear (lateral position) and tip-tilt (direction) control. Neither Synapse nor Nulltimate use such devices.

3.3.6.3 OPD control

No mechanical solution can guarantee the level of stability required. In the case of the most sensitive parameters, it is therefore necessary to implement active stabilisation techniques, i.e., servo systems. A possible control system can maintain the correct OPD according to continuous metrology measurements. As we have mentioned, other servo mechanisms could control the beam tip-tilt and shear. Yet another system can maintain a perfect flux balance of the two beams. Another popular option is fringe tracking.

Our colleagues implemented it on the Persée testbed in Meudon demonstrating that it also permits flux balancing (Houairi et al. 2008; Houairi 2009).

The original architecture of the Synapse testbed was designed with a metrological OPD control in mind. This system was never commissioned satisfactorily. The fundamental problem was very probably the conjunction of two facts: (1) the mounts were not sufficiently stable, and (2) the metrology beams were led about 2 cm above the science beams (using the same optical elements, but not the same points of incidence). These two observations can explain why the amplitude of required corrections exceeded the servo system's capacity. The result was that a different approach, based on OPD dithering, was pursued.

In the final months of the operation of the original Synapse it was demonstrated that OPD dithering can succeed where the original metrology control system did not. OPD dithering is an algorithm based on cyclic measurements of the scientific signal while creating small OPD changes with the delay line. The same principle was implemented in the control software of the improved Synapse II testbed as well as on Nulltimate.

3.3.6.4 Flux balance

Another parameter liable to change spontaneously during measurements is the flux balance. Experiments on Synapse have shown that this parameter is less unstable than the OPD.

In our experience, both in the case of Synapse and Nulltimate, the first hurdle is to obtain a good estimate of the flux balance. As a direct implication of what was mentioned above (Section 3.3.2), it is impossible to obtain a measurement of the flux coming into the output single mode fibre from one branch of the interferometer simultaneously with measuring its analogue coming from the other branch. And, *a fortiori*, it is impossible to perform interferometric experiments while measuring the fluxes coming from either of the two branches, unless integrated optics are used (e.g., Fluor combiner on Iota Coude Du Foresto et al. 1998, or Vinci on VLT-I). This simple fact can make it quite difficult to obtain a fast and reliable estimate of the flux balance.

The original Synapse testbed did not have a dedicated flux-balancing subsystem. Later in the setup's evolution, blades were used to reach flux balance. And finally, the latest version of Synapse II as well as Nulltimate balance the fluxes by tweaking the the injection into the output fibre (Section5.2.5.1).

An automated servo system, analogous to the OPD dithering, may be implemented on Nulltimate in the future (Section 7.3.4) in order to reach and maintain the flux balance.

3.3.7 Optical path

The optical path of the two branches of the interferometer has to be equal, i.e., the integrated geometric length of the branches A and B, weighted with the local refractive index has to be equal (s being the geometric path):

$$\int_A n(s)\mathrm{d}s = \int_B n(s)\mathrm{d}s \tag{3.9}$$

We consider that the beams propagate through two distinct media which simplifies the integrals, as we take $n(s) = n_1$ or n_2 where $n_{1,2}$ are constant refractive indices generically describing the two media[5]:

$$n_1 s_{1,A} + n_2 s_{2,A} = n_1 s_{1,B} + n_2 s_{2,B}. \tag{3.10}$$

The reason why there are at least two media is due to the fact that we opted for creating our beams using a beam splitter and combining them using a beam combiner. One medium is therefore air, while the other it the dielectric of the beam splitters and beam combiners.

---

[5] The reality is, naturally, somewhat more complicated, and the variations of the refractive index along the optical path reflect the local inhomogeneities, temperature, presure, humidity, etc.

If the experiments were to be performed in monochromatic light, the Equation 3.10 would mean that we could compensate the potentially unequal thickness of the dielectric in the two branches, $s_{\mathrm{dielectric},A} \neq s_{\mathrm{dielectric},B}$ with an appropriate column of air (easily implemented by moving the delay lines). In the polychromatic case, however, this approach is inadequate because the dielectric medium is, in principle, dispersive[6]. It is, therefore, necessary to replace the condition 3.10 with the two conditions:

$$s_{\mathrm{air},A} = s_{\mathrm{air},B} \tag{3.11}$$

$$s_{\mathrm{dielectric},A} = s_{\mathrm{dielectric},B} \tag{3.12}$$

This implies that we need to ensure that the thickness of the dielectric in the two branches of the instrument be equal (Eq. 3.12). In other words, either we make sure that all of our dielectric plates are plane-parallel and of equal thickness (if they were prismatic, we would have to make sure that the beam passes exactly homologous regions of the prisms), or we need to include a compensating device, *chromatism compensator*, into our testbed's design. SYNAPSE uses plane-parallel plates but they are not necessarily of equal thickness. The CaF_2 Prisms act as a chromatism compensator. NULLTIMATE uses prismatic beam splitters and dispersion compensators (Sec. 3.3.4) one of which can slide perpendicular to the beam, varying the thickness of the dielectric in the optical path.

3.4 Sources

The light sources were acquired at different points of the experimental work, and over the years were used in the case of the two optical testbeds. In this Section, we shall provide a list of the sources; whereas their usage in actual experiments will be made clear in the Chapters 4, 5, and 6.

3.4.1 Ceramic black body

This black body source consisting of a LaCr hollow cylinder (20 mm diameter, 20 cm length; Fig. 3.13) with a 5 mm hole on the side, conducting a current of ≈ 17 A, emits visible and thermal radiation closely approximating a black body at 2000 K. The radiation is filtered using interference filters, focused with an off-axis parabola, and injected into a single-mode optical fiber (Section 3.5.1). In order to avoid thermal and mechanical perturbations of the interferometer, the source subsystem, as well as the detector subsystem, are decoupled from the optical table.

The theoretical power output can be estimated from Planck's law. By integrating $B_\lambda(T)$ over our spectral band we obtain the flux F

$$F(T) = \int_{\lambda_{\min}}^{\lambda_{\max}} B_\lambda(T)\,\mathrm{d}\lambda = \int_{\lambda_{\min}}^{\lambda_{\max}} \frac{c_1}{\lambda^5} \frac{\mathrm{d}\lambda}{e^{\frac{c_2}{\lambda T}} - 1}. \tag{3.13}$$

Taking $\lambda_{\min} = 2.0\ \mu\mathrm{m}$, $\lambda_{\max} = 2.5\ \mu\mathrm{m}$, $T = 2000$ K, we obtain

$$F = 4 \times 10^4\ \mathrm{Wm^{-2}sr^{-1}}. \tag{3.14}$$

For a somewhat differently defined K band, viz., with $\lambda_{\min} = 2.08\ \mu\mathrm{m}$, and $\lambda_{\max} = 2.40\ \mu\mathrm{m}$, we have

$$F = 2.85 \times 10^4\ \mathrm{Wm^{-2}sr^{-1}}. \tag{3.15}$$

The étendue $S\Omega$ of our beam is limited by the optical fibre which we use (Section 3.5.1)

$$S\Omega \approx \left(\frac{\lambda_{\min} + \lambda_{\max}}{2}\right)^2 \approx 4.88 \times 10^{-12}\ \mathrm{m^2sr} \tag{3.16}$$

and therefore the available power is

$$P \approx 1.39 \times 10^{-7}\ \mathrm{W}. \tag{3.17}$$

---

[6] The dispersion of the air is much less pronounced.

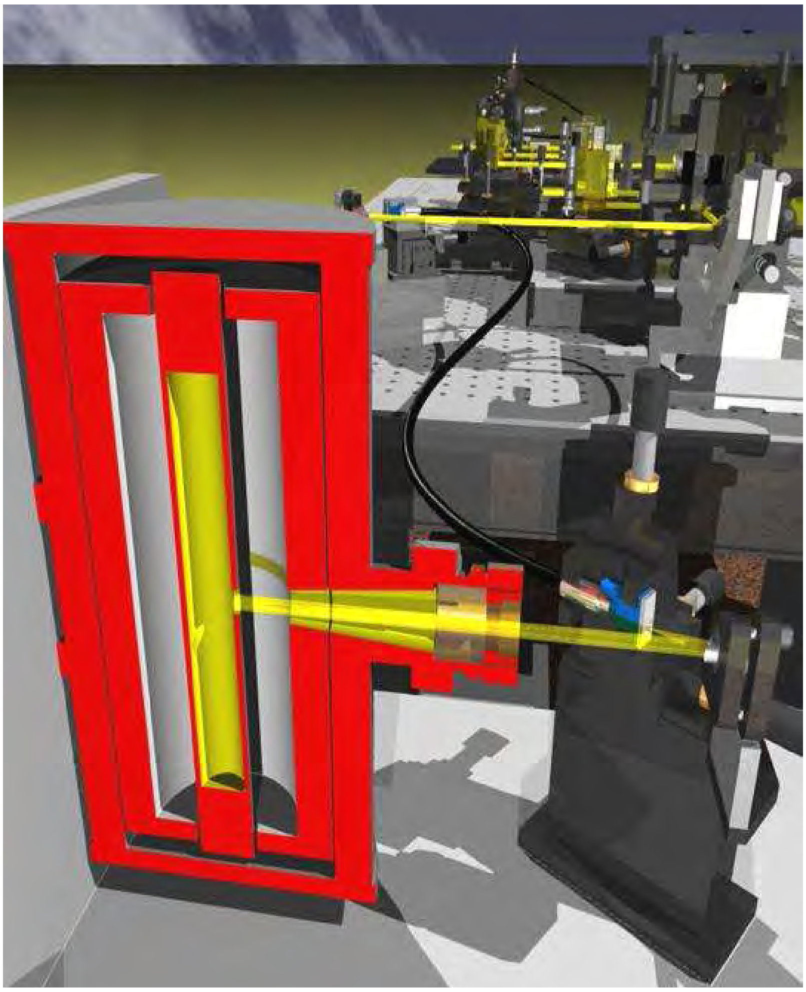

Figure 3.13 - Ceramic black body (a cross-section).

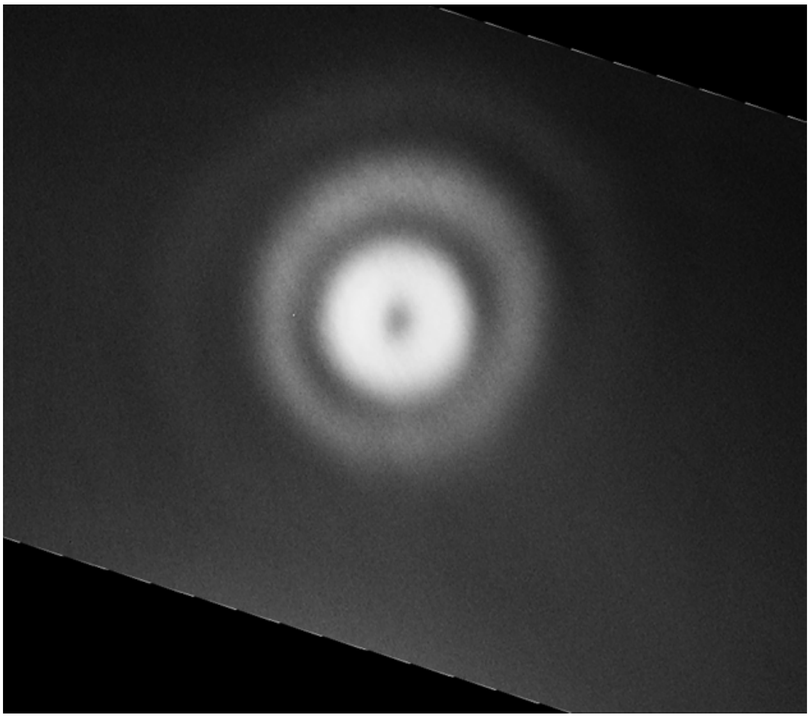

Figure 3.14 - Structure of the 1.15 µm laser beam

3.4.2 3.39 µm HeNe laser

Research Electro-Optics supplied us with a HeNe infra-red laser. It can operate at two wavelengths: 1.15 and 3.39 µm. Since we cannot easily image the 3.39 µm beam, we sometimes use the 1.15 µm for alignment purposes because we can observe it through an infra-red visor. We discovered that the beam has an unexpected structure (Fig. 3.14). This behaviour remains unexplained by the producer, which makes us wary of accepting the provided data sheet on face value.

The furnished documentation contains the following values:

- beam diameter = 1.55 mm;
- beam divergence = 2.78 mrad = 9.55 arcmin.[7]

If we consider the given "beam divergence" to be the half-angle divergence, we obtain a better accord with our observations than if it were the full-angle divergence.

The nominal power of the 3.39 µm beam is given as 3 mW. We verified this value with a calorimeter, and concluded that it is a good approximation. The available power is

$$P \approx 2\,\mathrm{mW}. \tag{3.18}$$

3.4.3 Supercontinuum laser source

Fianium supplied a "white laser" or *supercontinuum* source based on a non-linear, photonic crystal optical fibre. It produces about 2.7 mW/nm in the spectral range of 400–2500 nm.

The time averaged power of our source is $\approx$ 2 W, when integrated over the whole spectral band. A typical spectrum of such a source is given in Fig. 3.15. Unfortunately, we do not have the spectrum of our source. We estimate that out of the total 2 W, about 10 % goes to the K band.

---

[7] One may ask how is the producer able to determine these values with such accuracy...

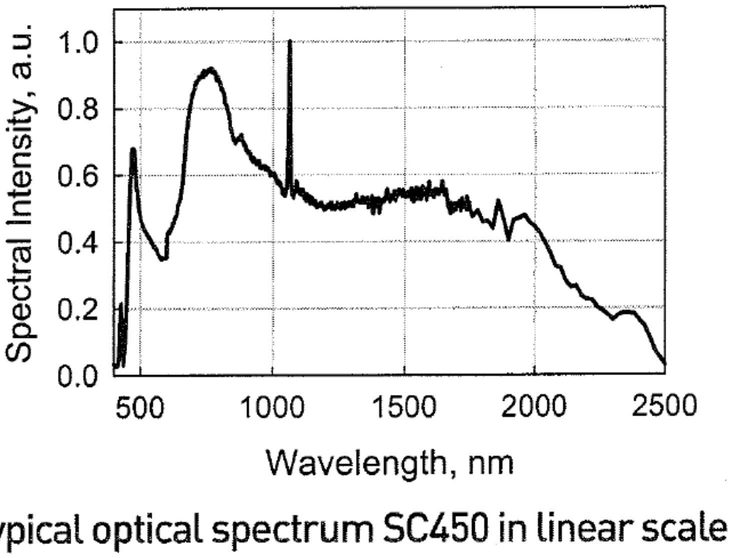

Figure 3.15 - Spectrum of a supercontinuum laser source.

The effective temperature $T_{\rm eff}$ of the source can be estimated. This is the temperature of a black-body source that would emit the same flux with the same étendue ($S\Omega = \lambda^2$). We find that our source (over the whole spectral range between 400 and 2500 nm) is the equivalent of a black body with the impressive effective temperature of

$$T_{\rm eff} = 140\,\mathrm{MK}. \tag{3.19}$$

Looking up the values for the photonics crystal fibre used in the Fianium supercontinuum source (the fibre itself is made by Crystal Fibre), we found a plot of the MFD (mode-field diameter; MFD = $2w_0$; cf. Section 3.5.1) as a function of wavelength covering the wavelength range from 400 to 1700 nm. The variation is rather weak, going from MFD $\approx$ 3.83 µm at 400 nm to MFD $\approx$ 4.20 µm at 1700 nm. We graphically extrapolated, finding

$$\mathrm{MFD} = 2w_0 \approx 4.4\,\mu\mathrm{m} \tag{3.20}$$

at $\lambda = 2.2$, which gives

$$\theta = 0.32, \tag{3.21}$$

and therefore a parabola of $f = 33\,\mathrm{mm}, \alpha = 30°$ (cf. Section 3.3.3) produces a collimated beam of $D = 22.5\,\mathrm{mm}$. Using a parabola with $f = 12.7$ mm, and $\alpha = 90°$, gives a beam with $D = 16.2$ mm.

3.4.4 2.32 µm laser diode

We also purchased a spectrally single-mode laser diode with single-mode fibred optical output from NanoPlus. The available power is $\approx$ 2 mW.

As for the fibre, NanoPlus provided the information that it was a Corning SMF 28 (9/125 µm) fibre. Its cutoff wavelength is 1260 nm, and the MFD's are given for 1310 and 1550 nm, viz. 9.2 and 10.4 µm, respectively. Using the given values of the index difference, 0.36 %, and the core index n_c at 1310 and 1550 nm, which are given as $n_c = 1.4675$ and 1.4681, respectively, we obtained an extrapolated value of $n_c(\lambda = 2.32\,\mu\mathrm{m}) = 1.4700$, and NA = 0.125.[8] Using the value NA = 0.125, we obtained $w_0/a = 1$. The core diameter is given as $2a = 8.3\mu\mathrm{m}$, which means that $w_0 = 8.3/2\mu\mathrm{m}$.

---

[8] Two of the documents mention that "NA was measured at the one percent power angle of a one-dimensional far-field scan at 1310nm", one listing the value as NA = 0.13, while the other document gives the measured value NA = 0.14.

We obtain therefore

$$\theta = 0.178, \tag{3.22}$$

which means that for $f = 13$ mm, and $\alpha = 35^\circ$, the beam diameter is $D = 5.1$ mm.

3.5 Modal filters

We discussed the importance of wavefront filtering in nulling interferometry in Section 2.5. While SYNAPSE always used SMF's, NULLTIMATE, originally aiming for 10 µm, is provided with a set of pinholes, and also benefited from the R&D on silver halide fibres at the University of Tel Aviv (prof. Abraham Katzir). We are not working at 10 µm, however.

3.5.1 Fluoride-Glass Single-Mode Fibres

We have five SMF fibres from Verre Fluoré:

- two 1-metre K-band fibres with cutoff wavelength $\lambda_{\mathrm{co}} = 1.95$ µm, and core diameter $2a = 6.5$ µm,
- three 2-metre K-band fibres, $\lambda_{\mathrm{co}} = 1.95$ µm, $2a = 6.5$ µm, and
- one 2-metre L-band fibre, $\lambda_{\mathrm{co}} = 2.85$ µm, $2a = 11$ µm.

The transmission of the fibres is shown in Figs. 3.16, 3.17.

Our K-band single-mode fibre (SMF) has a numerical aperture (NA) of 0.23. This is given by the physical properties of the materials used, namely

$$NA = \sqrt{n_{\mathrm{core}}^2 - n_{\mathrm{cladding}}^2}. \tag{3.23}$$

The waist $w_0 = 3.9$ µm, core diameter $2a = 6.5$ µm and normalised frequency $V = 2.135$ at $\lambda = 2.2$ µm.

Using

$$\theta = \frac{\lambda}{\pi w_0} \tag{3.24}$$

we obtain

$$\theta = 0.18\,\mathrm{rad} = 10.3^\circ \tag{3.25}$$

for the far-field angular radius (half-angle divergence) of the Gaussian TEM_{00} beam at $1/e^2$.

3.5.2 Fibre output aperturing

An interesting option for the improvement of the modal-filtering performance of our fibres is output aperturing (Lawson et al. 2008). With certain fibres (e.g., the silver halide fibres), pinholes may be installed relatively easily on the exit fibrehead. Another approach is to collimate the output beam and use an iris in the image plane.

3.6 Spectral filters

We are equiped with a set of interference filters furnished by Northumbria Optical Coatings:

- two K filters with central wavelength of 2.21 µm and full width at half maximum of 0.33 µm, i.e., 2.045–2.375 µm; bandwidth of 15 % (Fig. 3.18);

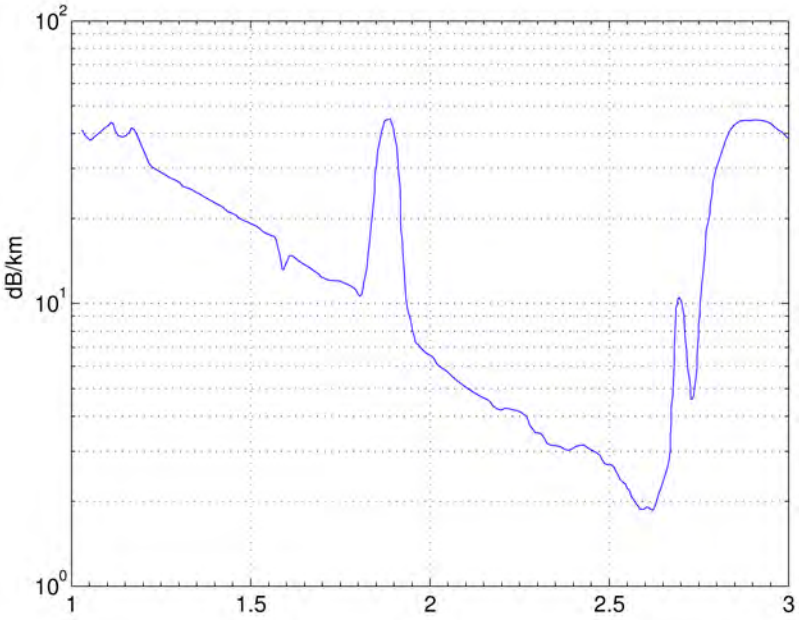

Figure 3.16 - Transmission of the K-band single-mode fibre (in dB/km) vs. wavelength (in μm; courtesy VerreFluoré).

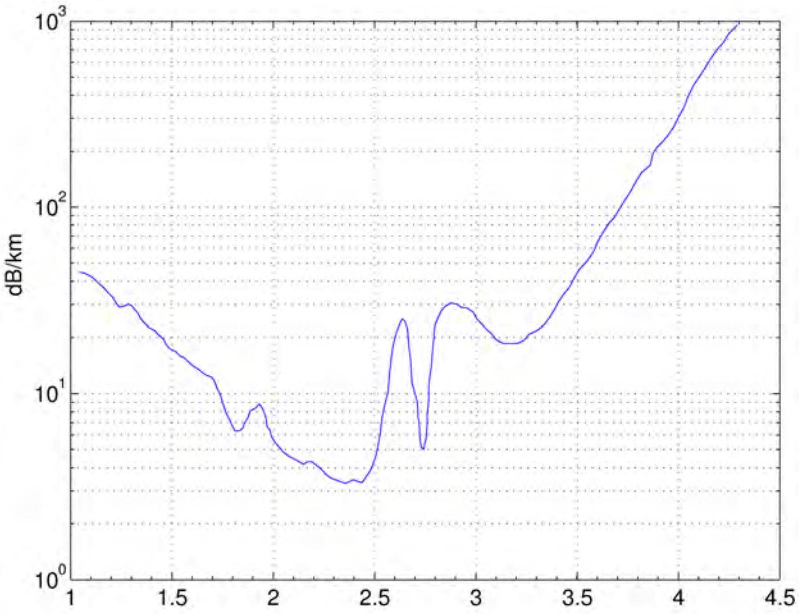

Figure 3.17 - Transmission of the L-band single-mode fibre (in dB/km) vs. wavelength (in μm; courtesy VerreFluoré).

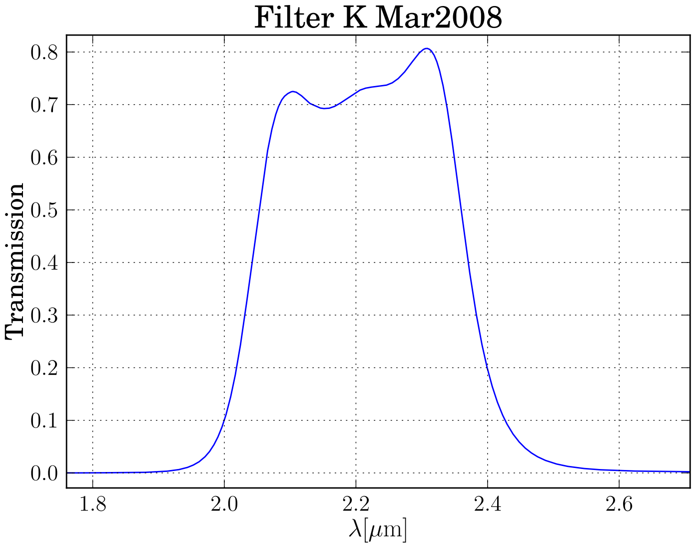

Figure 3.18 **-** Transmission curve of the interference filter with central wavelength of 2.21 µm and full width at half maximum of 0.33 µm.

- a K filter with a passband of 2.21–2.41 µm, i.e., bandwidth of 8.7 % (Fig. 3.19);
- an L filter with a passband of 3.25–3.75 µm,i.e., bandwidth of 14 % (Fig. 3.20); and
- a filter with 16 nm FWHM at 2.344 µm (i.e., bandwidth of 0.7 %; Fig. 3.21) .

3.7 Polarisers

We have two P03 polarisers from InfraSpecs. The transmission curves are in Fig. 3.22. They are realised as a line grid of gold wires with a thickness of ≈ 1 µm, and spacing of ≈ 1 µm. A rough estimate based on the knowledge of the production process allows to deduce that the wire diameter may vary within one grid by ≈ 5 %. In order to prevent the wires from touching each other, there are spacing rods between the wires. The spacing rods are of similar thickness as the wires, with a spacing of ≈ 50 µm.

3.8 Detectors

3.8.1 Array detector

CIRCUS is an astronomical camera system previously used on the Canada-France Hawaii Telescope. It uses a solid-nitrogen cooled cryostat, and, since 1990, it has a 128x128 pixel InSb array, called AMBER 128. Useful pixel size is $40 \times 40\ \mu\text{m}^2$.

3.8.2 Single element detector

Electro-Optical Systems supplied a commercial, liquid-nitrogen cooled, InSb detector. Its active surface is 0.25 mm in diameter, and its Noise Equivalent Power is

$$\text{NEP} = 6 \times 10^{-14}\,\text{W}\,\text{Hz}^{-1/2}, \tag{3.26}$$

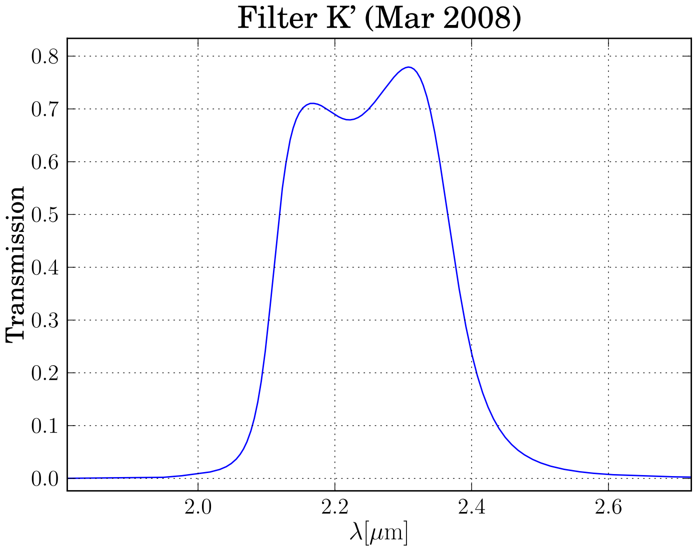

Figure 3.19 **-** Transmission curve of the interference filter with a passband of 2.21–2.41 μm.

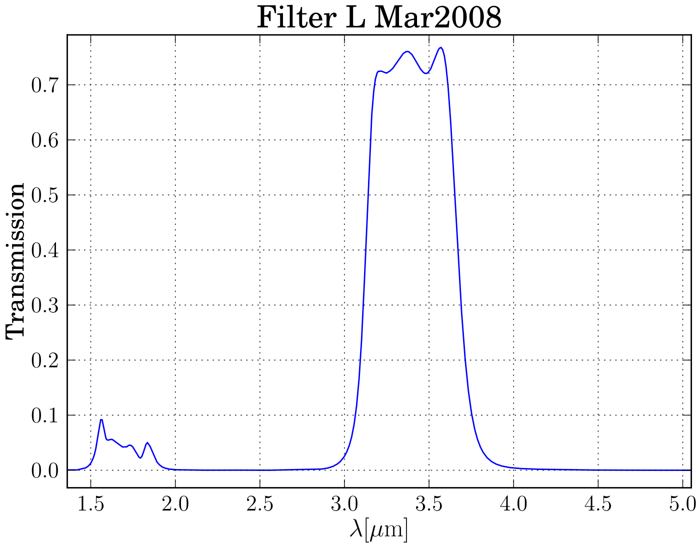

Figure 3.20 **-** Transmission curve of the interference filter with a passband of 3.25–3.75 μm.

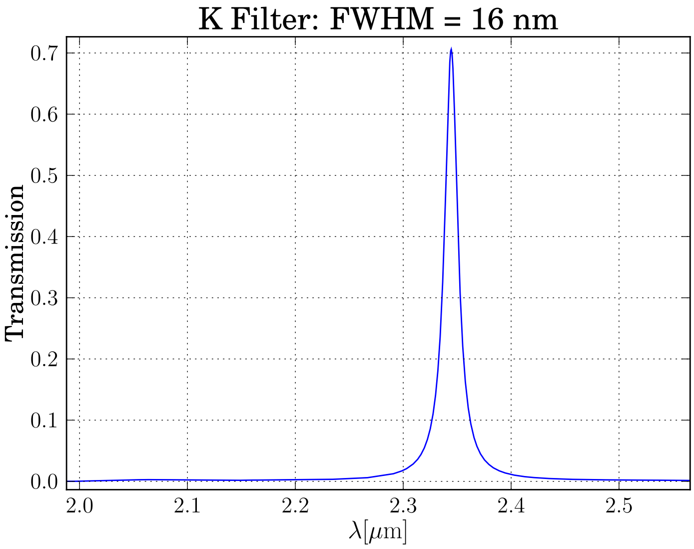

Figure 3.21 - Transmission curve of the interference filter with central wavelength of 2.344 μm and full width at half maximum of 16 nm.

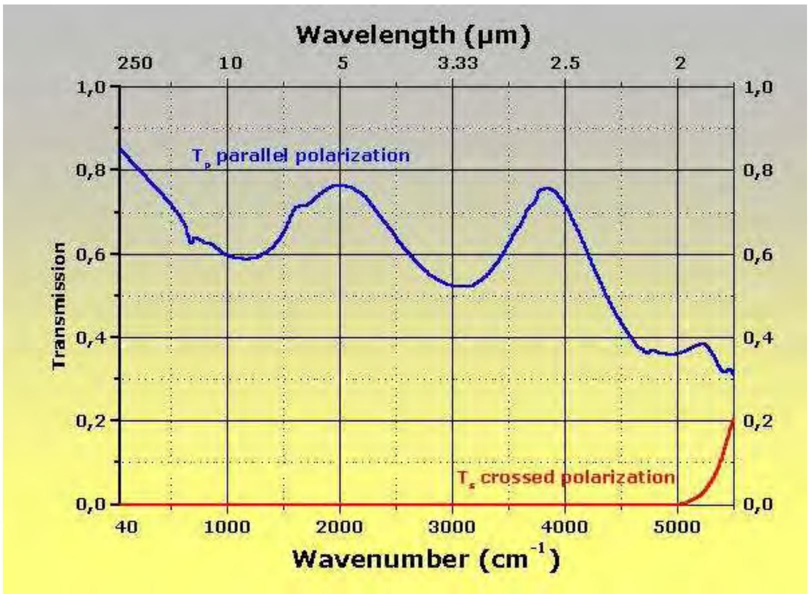

Figure 3.22 - Transmission curves of P03 polarisers. (Courtesy InfraSpecs)

Figure 3.23 **-** Focus Crossing APS prototype

i.e., its specific detectivity D^*, considering $D^* = \sqrt{A}/\mathrm{NEP}$, where A is the active area,

$$D^* = 4 \times 10^{11}\,\mathrm{cm\,Hz^{1/2}\,W^{-1}}. \tag{3.27}$$

3.9 Phase shifter prototypes

We have discussed the Achromatic Phase Shifters (APS) in Section 2.3. In the context of an ESA study, we have three APS prototypes in addition to the $\mathrm{CaF_2}$-prisms forming an APS/chromatism compensator which is an intrinsic part of the SYNAPSE testbed (cf. Sec. 2.4).

3.9.1 Focus Crossing or Through Focus

A Focus Crossing APS prototype (APS FC; also known as Through Focus APS) was developed by the Observatoire de Côte d'Azur, Nice, France (Fig. 3.23). The APS FC is based on the so-called Gouy effect where light undergoes a phase shift of π when crossing a focus. The phenomenon is independent of wavelength (Gouy 1890; Boyd 1980). The principle of this approach is similar to the one of the Achromatic Interfero-Coronagraph (Gay and Rabbia 1996; Baudoz et al. 2000a,b; Rabbia et al. 2006).

APS FC comprises two modules, one bearing two confocal half-parabolic off-axis mirrors, the other, two flat mirrors. The "confocal" module produces an achromatic π-phase shift, a pupil rotation by π and an extra optical path (twice the focal length of a paraboloid), while the role of the "flat-flat" module is to balance this pathlength and to reproduce the beam geometry of the confocal module. At beam combination, the resulting amplitude is nulled for an on-axis point-like source, provided the wavefronts are perfectly cophased. If not, nulling is incomplete and a residual flux remains.

3.9.2 Field Reversal or Periscope

A Field-Reversal APS prototype (APS FR; also known as Periscope APS) is shown in Fig. 3.24. The system again comprises two modules, but, unlike the APS FC where the flat-flat module is for reference purposes only, here both modules are needed to create the π phase shift. Each module is composed of three flat mirrors. Two reflections per beam are necessary to induce the phase shift, the third reflection merely flips the beams so that the outgoing beams are parallel to the incoming beams.

Two reflections, arranged in such a way that s and p polarisation components are successively permuted, flip the field vectors, inducing an achromatic phase shift, as well as a pupil rotation of π. Suitably applied to a couple of beams, a couple of periscopes generates an intrinsically achromatic phase shift of π (opposed field vectors). Then a modified constructive interferometer provides two nulled outputs by suitably mixing the beams.

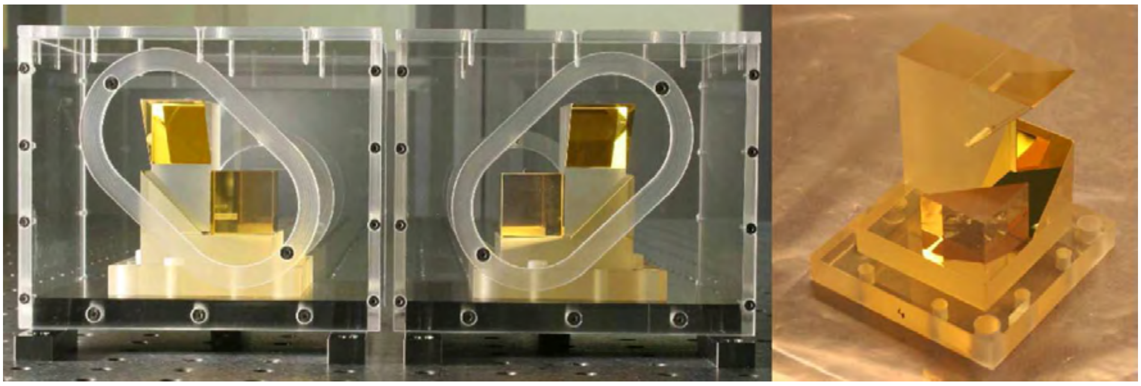

Figure 3.24 **-** Field Reversal APS prototype

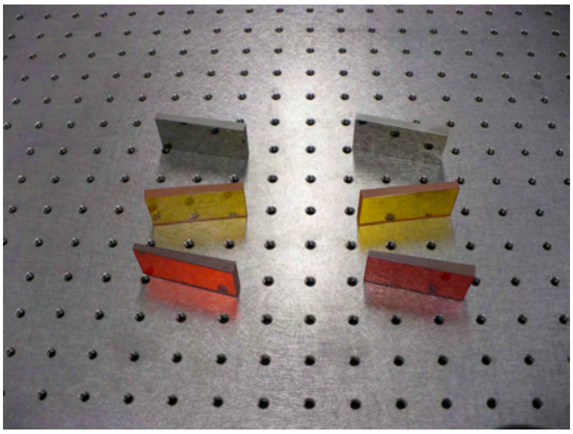

Figure 3.25 **-** Dispersive Prisms APS prototype

A prototype APS FC was developed at Max-Planck-Institut für Astronomie in Heidelberg in collaboration with Kayser-Threde GmbH in Munich and the IOF Fraunhofer Institute for Applied Optics in Jena (Launhardt 2008).

3.9.3 Dispersive prisms

The principle of this method consists in introducing dielectric plates into each arm of the interferometer. Their number, composition and thickness are optimised, together with the OPD, so that the chromaticity of the resulting phase shift in a given spectral band is below a specified level. The description of Synapse (Sec. 3.11) mentions that a simple APS using two prisms of the same material in each arm of the interferometer is an integral part of the setup. A model with three prisms of three different materials per interferometer arm is under development by Thales Alenia Space. A set of three pairs of Dispersive Prisms was developed by Thales Alenia Space (Fig. 3.24). The materials are Germanium, KRS5, and ZnSe.

3.10 Electronics & Software

We have already mentioned (Section 3.8.2) the lock-in amplifier which is a fast and sensitive Analog-Digital Converter (ADC) with a precision oscillator and a computer running sophisticated software. But we shall not go into the details of the commercial hardware with its built-in software. Rather, we shall concentrate on the custom software used in experiment control and data acquisition.

Figure 3.26 - Stanford Research Systems SR830 Lock-In Amplifier.

3.10.1 Lock-in amplifier

3.10.1.1 Data sampling or transfer?

The Stanford Research Systems SR830 Lock-In Amplifier (Fig. 3.26) operates digitally, i.e., after it digitises the input signal all of its further operation is digital. The data output stream is accessible via a GPIB port. A digital-analog converter is built in to provide an optional analog output, coding the output data as a voltage. Its main *raison d'être* is backwards compatibility: lock-in amplifiers' operation used to be analog, and it was therefore natural to use an analog output port. With a fully digital lock-in amplifier this does not make sense.

The argument for keeping with the analog output is that the digital data transfer is too slow. This line of thought ignores the fact that there is a fundamental difference between the data output of an analog and a digital lock-in amplifier. In the days of analog lock-in amplifiers the output was a raw stream, and it was up to the user to treat it. A fully digital lock-in amplifier, on the other hand, provides a clean digital output that does not have to be faster than, typically, the time constant τ. It does not make sense to acquire data at a frequency higher than $1/\tau$ because the output data stream does not require any processing (fast sampling, averaging, etc.): all that has already been done by the lock-in amplifier much more cleanly than whatever the user can do playing with the re-analogised voltage. What happens between the lock-in amplifier and the experiment-control computer is data transfer, not data sampling. Sampling is done by the lock-in amplifier's analog-digital converter operating on the input signal.

The original SYNAPSE architecture uses the old way of thinking about lock-in amplifiers. It is only the latest system, which we implemented on the NULLTIMATE testbed in 2008/2009, that uses the digital output directly. SYNAPSE II therefore uses the re-analogised lock-in amplifier output sampled by an external analog-digital converter (we use commercial products of the *National Instruments* Corporation).

3.10.1.2 "Dark current"

The lock-in amplifier's output is a complex value represented as two real numbers. This ordered pair of numbers is provided either in its native Carthesian form, viz., as X and Y, or converted into polar co-ordinate system, as R and θ. The lock-in amplifier represents the data in the Carthesian form, and provides the conversion to polar co-ordinates as an optional step. It is therefore faster (albeit marginally) to work with X and Y.

When the lock-in amplifier operates with a chopper wheel (as in our case), it receives alternatively the background flux alone and the signal with the background. Its output can be naturally viewed as a result of a sophisticated method of subtracting the background from the signal. Contrary to many experimenter's reflexes, it is therefore unnecessary to subtract a "dark current". It has already been done by the lock-in amplifier.

Another way of looking at this issue has to do with the behaviour of the co-ordinate θ. It has two regimes of behaviour:

1. When there is a signal (when there is a consistant difference between the voltage acquired when the chopper wheel leaves the beam path open, and when it shuts it) then θ fluctuates around a determined value with an amplitude of, typically, a degree.

2. When there is no signal (no consistant difference between the situations when the chopper wheel opens and closes the beam path) then the value of θ is uniformly distributed over 2π.

Naturally, the value of R has a different physical interpretation in the two cases. In the first instance, it is a good estimate of the signal (unless the signal-to-noise ratio is very poor, e.g., < 2). In the second instance, it is the modulus of two random variables, X and Y, which are both supposed to have zero mean values, $\langle X \rangle = \langle Y \rangle = 0$. What we would really like to know is not R, but rather we would like to verify that indeed $\langle X \rangle = \langle Y \rangle = 0$, and to determine the standard deviations σ_X, σ_Y. Measuring R can merely provide an upper limit on these values.

3.10.2 Software

As with the testbeds themselves, our custom software went through several stages of development. The first system, implemented on the Synapse testbed, was developed by Frank Brachet. It was entirely implemented using the *National Instruments* LabView software (for more details see Brachet (2005)). The perceived priority in the design of this system was the integration of the metrology feedback loop, requiring fast, real-time operation with high data transfer rates.

Once it was realised that the metrology system will no longer be a concern, other issues came to the forefront. The main weakness of the Frank Brachet's system was that new functions were difficult and tedious to implement. Therefore, a more flexible architecture was desired.

This second stage of software development was based on the system implemented on the Sesame testbed at the Observatory of Paris in Meudon. The basic issue this system set out to address in Meudon was remote operation: the laboratory being relatively far from the offices of the experimentators, an efficient method of running the setup remotely became a priority. The solution was to create a simple server that would receive commands via ethernet. The server was implemented using LabVIEW, while the commands were sent (and responses were received) through shells running IDL, Yorick, MatLab, etc.

The Sesame architecture was adapted at IAS by Bruno Chazelas and myself, the one major difference being that the user interface shell was written in Python.

The third stage is an upgrade of the previous Sesame-based design. There are two key differences. Firstly, the data acquisition via the lock-in amplifiers was overhauled, making it purely digital. And secondly, the concept of remote operation shifted.

The original Sesame design had the server software running on a computer in the laboratory and the user interface running on a computer in a distant office. Over time we started relying more and more on VNC[9], i.e., on remote desktop sharing software. We would run both the server and the user interface software on the same computer in the experiment's control room, bringing up this computer's desktop remotely via VNC on any computer connected to the network. The obvious advantage of this solution is that the user interface software needs to be installed and kept up-to-date only on one computer, which facilitates tweaking of the software.

This changed mode of operation brought about a change in the division of labour between the server and user interface software.

---

[9] Virtual Network Computing

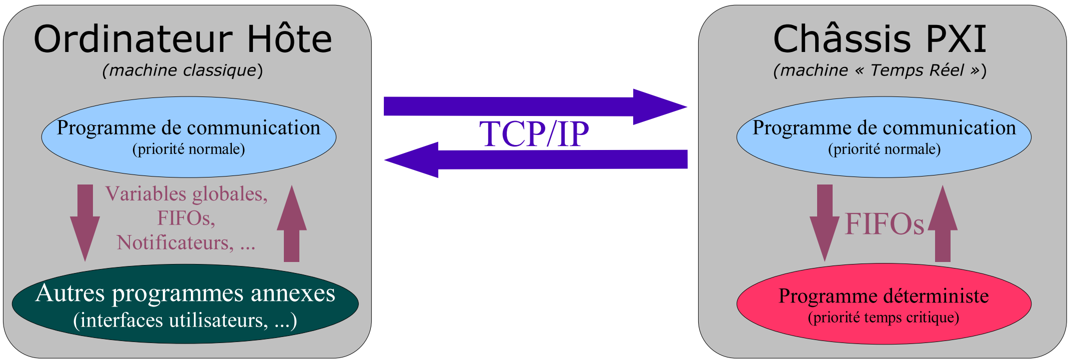

Figure 3.27 **-** The first software system. General architecture of the "real time". (Brachet 2005)

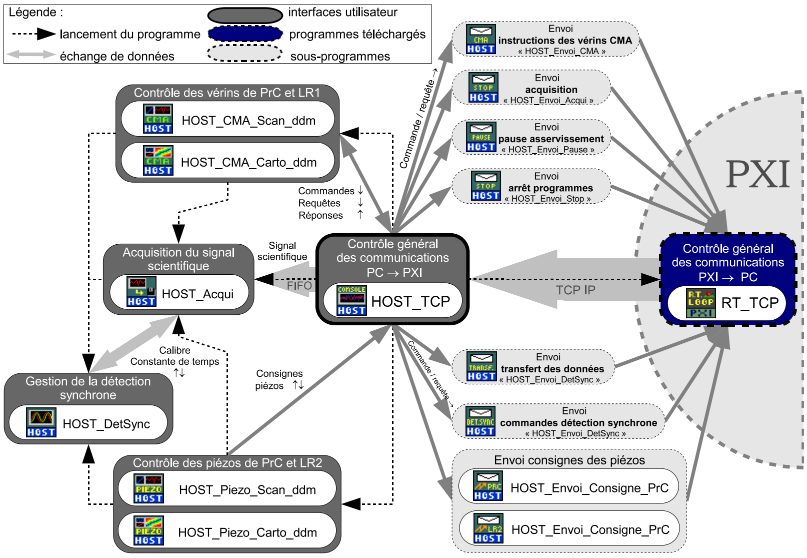

Figure 3.28 **-** The first software system. Overview of the LabView *vi's* running on the PC. (Brachet 2005)

The first software system. In order to manage the information flow of the metrology system with adequate efficiency, the software runs on two different platforms simultaneously: on a dedicated *National Instruments* PXI computer, and on a standard *Intel* Pentium based personal computer. Both computers are interacting with the hardware but the PXI does so at constant rate of 4 kHz, whereas the PC sends instructions to or receives information from the hardware only when needed. It may be said that the packages running on the PC serve primarily as a user interface to whatever is happening in "real time" controled by the PXI. The communication protocols used are summarised in Fig. 3.27.

In order to perform, e.g., a null stability measurement, the user runs interface software from the PC (Fig. 3.28). The main user interface is the HOST_TCP *LabView* Virtual Instrument (*vi*). It ensures communication (via TCP/IP) with the PXI, and allows the possibility of running scientific measurement applications: from simple data acquisition, through setting the positions of the delay lines and of one phase shifter prism, to optical delay line or dispersive prisms phase shifter scans (stepping the actuators in moving the optics to modify the optical delay line length or the position of one of the prisms of the phase shifter, while acquiring the measured signal a preset number of times at each stop).

A closer look "under the hood" is required (Fig. 3.29). There are two main packages running on the PXI. The first (called RT_TCP) ensures communication with the PC (via TCP/IP), and the second (TCL_Agilent)

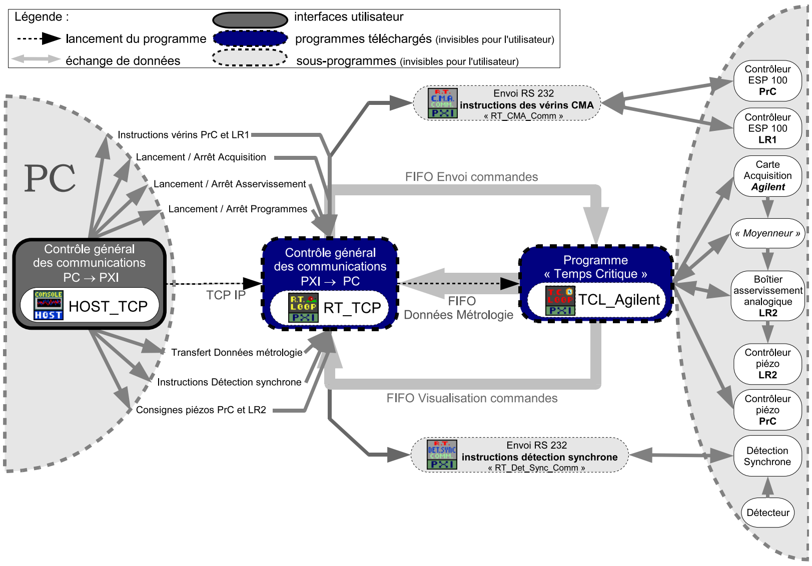

***Figure 3.29* -** The first SW system. Overview of the LabView *vi's* running on the PXI. (Brachet 2005)

is the "real-time" loop designed for the *Agilent* metrology control system. The loop has many operating modes (represented by different CASEs in the *vi*) which are selected, according to the information coming from the user interface.

The metrology loop was an essential element of the TCL_Agilent, and was running permanently whenever the software was on. Nonetheless, the loop could run without actually effecting any changes in the position of the delay lines. In this case, the loop was merely monitoring the metrology signal, opening the possibility of recording the OPD information. As we have already mentioned (Section 3.3.6.3), this setting was the only viable option because the metrology beams passed above the science beams, and therefore the metrology was following the mechanical vibrations of the optics at inappropriate points of incidence. In fact, simple geometrical considerations give credibility to the opinion that the vibration amplitude at the two levels must have been different (viz., roughly twice larger at the metrology level than at the science beam level).

The first version of the OPD dithering algorithm (see Chapter 4) was implemented under this system, in a subset of the CASEs mentioned above.

The second software system. Inheriting the *National Instruments* PXI industrial computer with all of the input/output operations from/to the testbed being handled by the PXI's cards, meant that the new SESAME server (introduced in Section 3.10) had to be installed on the PXI. These machines, however, are designed with a different mode of operation in mind, viz., they are furnished with a minimalist operating system the sole purpose of which is to run compiled LabVIEW programmes, loaded via ftp. It was decided to make our PXI double boot, i.e., adding the option of running Windows XP for more flexibility.

The SESAME server LabVIEW vi (*virtual instrument*) runs a loop waiting for messages sent to it via ethernet (TCPIP, Fig. 3.30). Each message is decoded as a string of characters. If the first eight characters correspond to one of the implemented instructions (see Table 3.1), the appropriate code is executed and a response (if any) is sent out again as a string of characters via ethernet.

The framework of the server was taken from the SESAME software but the commands were implemented from scratch.

At this stage, the philosophy of the server LabVIEW vi closely copied that of our colleagues in Meudon: the user was not to use the server's front end directly, but rather interact with a shell (written in a scripting

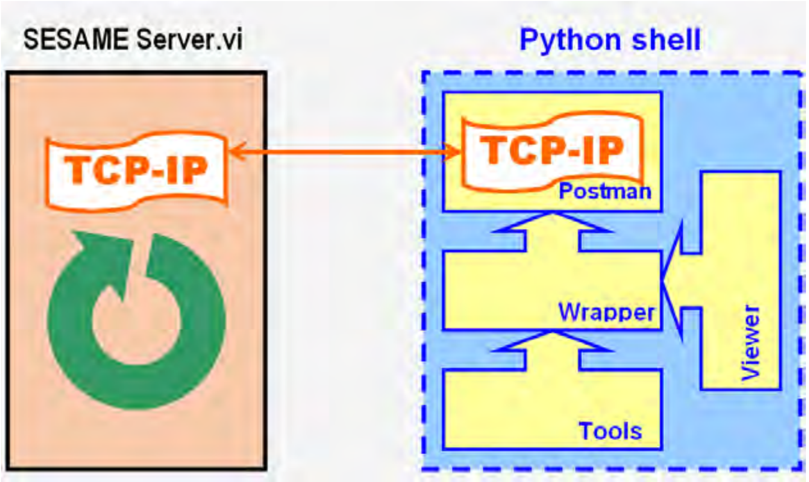

Figure 3.30 **-** The second software system. The server LabVIEW *virtual instrument*, based on the loop designed for the Sesame testbed at the Observatory of Paris in Meudon (left), runs on a dedicated PXI industrial computer hard-connected to the systems of the testbed. It receives commands and sends out answers via TCP-IP to and from a Python shell (right) implemented on any user computer. The server itself does not provide direct data output.

Command	Description
CMDSR830	General communication with the lock-in amplifier.
LIA_MMSR	Versatile measurement with lock-in amplifiers.
MSR_REG1	An acquisition of the lock-in amplifier data output.
GET_DETS	Get lock-in amplifier's gain.
SET_DETS	Set lock-in amplifier's gain.
GET_OFLT	Get lock-in amplifier's time constant.
SET_OFLT	Get lock-in amplifier's time constant.
ADJ_DETS	Adjust lock-in amplifier's gain to a given voltage.
SRC_DETS	Adjust lock-in amplifier's gain to the signal.
CMND_SMC	General communication with the SMC commander.
NSC_CMND	General communication with the NSC commander.
ROT_SHUT	Open or close one or both interferometer branches.

Table 3.1 **-** The second and third software system. List of commands implemented in the Sesame server (a sample).

language), sending commands, receiving and visualising the testbed's response in the shell environment.

The shell Bruno Chazelas and myself implemented, is written in Python. Its basic module deals with the communication via TCP-IP with the server LabVIEW vi. Another module wraps the server's eight-character commands, generating the appropriate strings (comprising the command and its arguments) to be sent to the server, providing default arguments, screening the user input for invalid argument values, and decoding the server's response, converting the incoming string of characters into appropriate variables. The third module is a collection of scripts calling the commands, wrapped by the previous module, in order to perform more sophisticated operations (e.g., flux mismatch estimate, which requires alternate measurements of the flux in each branch of the interferometer).

The fact that our work is *research* in the ethymological sense, made itself manifest also in the process of software development. In fact, with time it became clear to us that our practice comprises three stages:

1. First we would try a new experimental procedure sending out commands one by one, manually typing them in through the shell.
2. Once we had a good grasp of an algorithm we would write a Python script and include it as a method, usually, in the "tools.py" module.
3. After a while we might find that it would be better to implement the same function directly as one of the commands of our SESAME LabVIEW server.

A good example of this process is the procedure providing an estimate of intensity mismatch (Section 3.3.5).

The OPD dithering algorithm was implemented in this version of the software as a separate program thread, comprising a loop, initially running "dry" (without performing any action) and accepting three different commands: (1) start dithering or restart it after a pause, (2) pause dithering, and (3) stop dithering closing down the thread. Each of these commands took additional arguments defining the duration of the individual stages of the dithering cycle, etc.

The third software system. The third software system can be called a consequence (if somewhat belated) of fast networking. It took us a while to realise the obsolescence of the SESAMEan philosophy, which solved the conundrum of remote experiment control by running a server and a shell on two different computers linked via TCP-IP. Fast networking makes it easy to run both the server and the shell on the same machine, which the user interacts with via a remote desktop session (including work from off-campus home computers).

The advantage of this system is very practical: The original SESAME system was a little cumbersome to develop because software versions had to be carefully correlated between the dedicated PXI and the user machines running the Python package. It required additional work to keep track of the development and co-ordinate the work. What is more, the "viewer" module, providing graphics output in the Python shell, was liable to platform-related and installation-related instabilities. With both the server and the command shell running on the same machine, all of these problems were eliminated.

Working via remote desktop also had some other implications, the main one being that the graphics output could be implemented directly on the LabVIEW server level. This is clearly a more logical solution because there is no need of data transfer via the TCP-IP protocol[10].

3.11 SYNAPSE

Fig. 3.32 shows the interferometer with the science and metrology beams. It is set up on an optical table with passive vibration protection, and protected from acoustic and thermal perturbations by a plexiglass box (Section 3.3.6.1). The optical bench itself comprises two modified Mach-Zehnder interferometers serving

---

[10] The transfer is internal to the same computer but it still passes through the ethernet card.

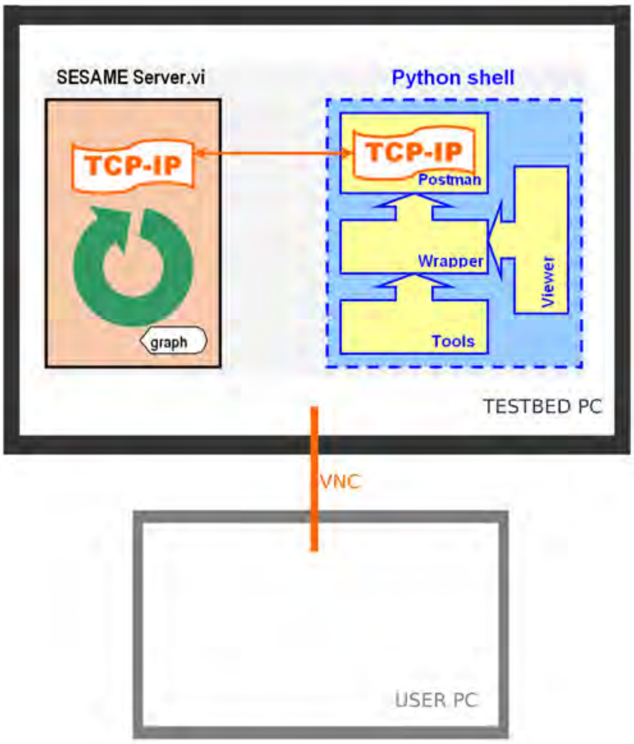

Figure 3.31 - The third software system. The server LabVIEW *virtual instrument*, based on the loop designed for the SESAME testbed at the Observatory of Paris in Meudon (top left), runs on a dedicated computer hard-connected to the systems of the testbed. It receives commands and sends out answers via TCP-IP to and from a Python shell (top right) implemented on the same computer. The server also provides direct output of data in graphic form. The user communicates with the system via remote desktop (VNC; bottom).

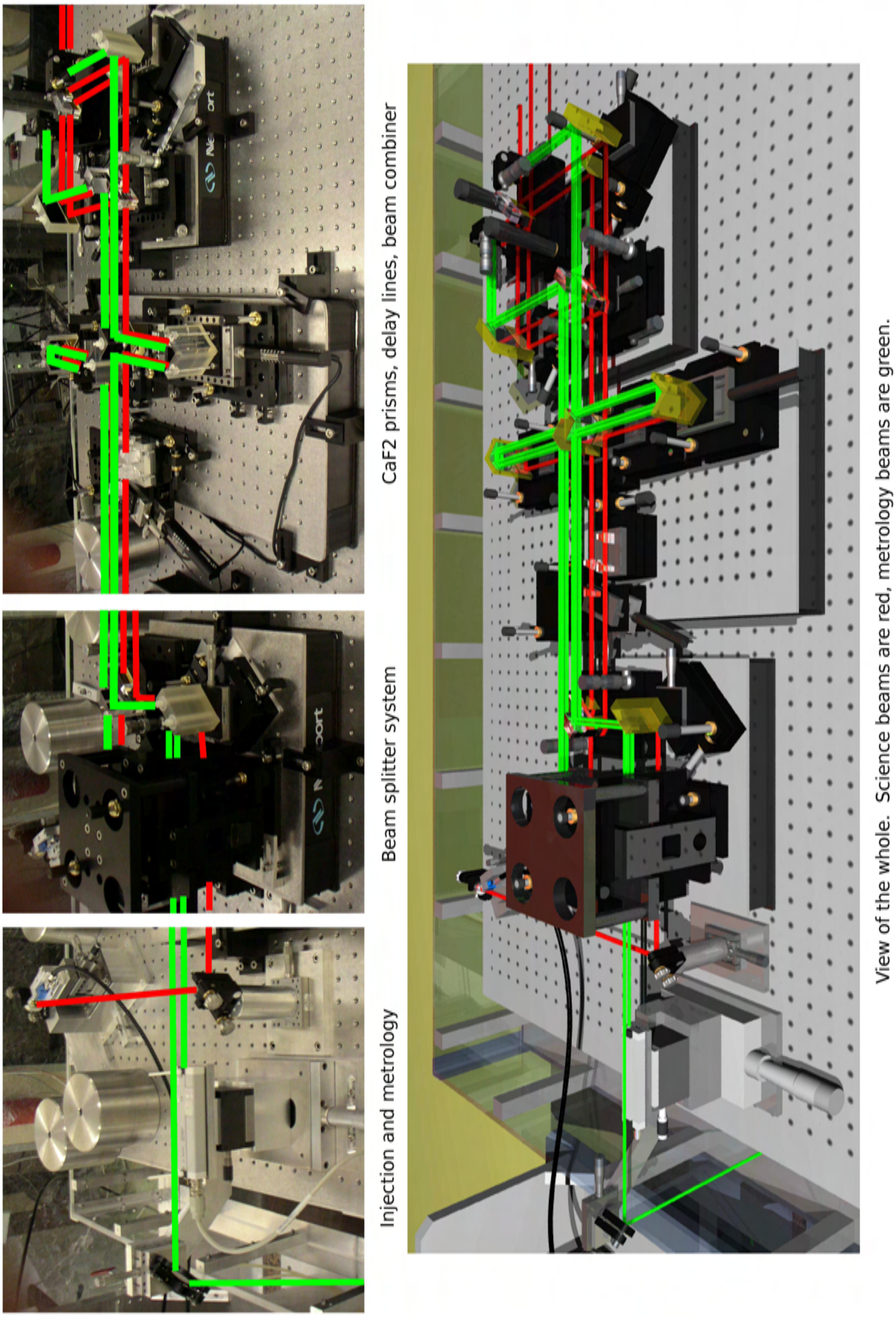

CaF2 prisms, delay lines, beam combiner

Beam splitter system

Injection and metrology

View of the whole. Science beams are red, metrology beams are green.

Figure 3.32 **-** Images of Synapse overlaid with science and metrology beams

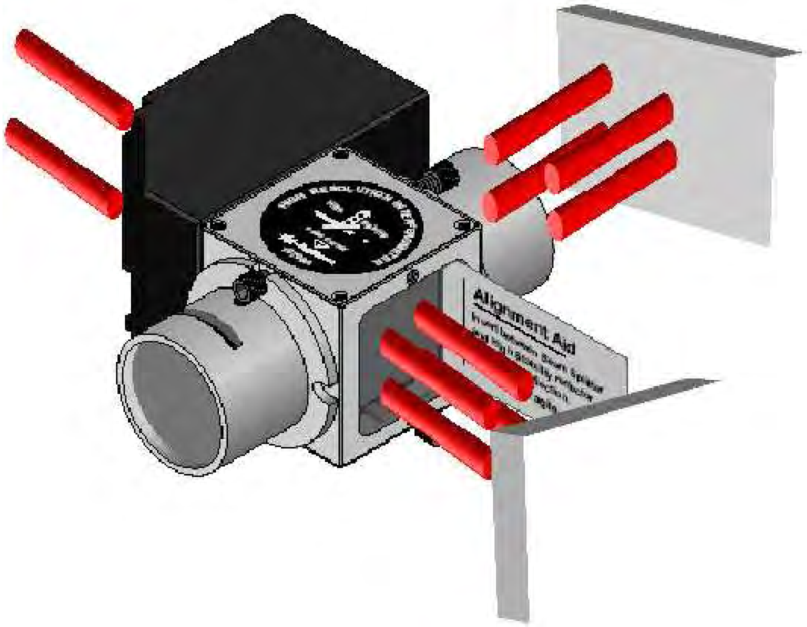

Figure 3.33 - Metrology beam splitter.

as beam-splitting and beam-recombination devices (Serabyn and Colavita 2001), creating the two identical beams (Section 3.3.4), delay lines, and a simple APS with two CaF_2 Prisms in each interferometer arm.

The beam-splitter and beam-combiner systems use parallel CaF_2 plates. Their thickness is not guaranteed to be identical to the required accuracy, and therefore a compensator needs to be included in the design. The bench's intrinsic APS, comprising two CaF_2 prisms in each interferometer arm, fulfills this role. As an APS, it can introduce any given phase shift, and reduces the chromaticity in the K or L band so that the resulting theoretical nulling performance is better than $\approx 10^{-5}$.

The metrology beam (Section 4.2) is generated by a laser (under the optical table) and split by a dedicated beam splitter (Fig. 3.33) which is suspended from the top of the tower also housing the first beam-splitting plate (Fig. 3.32, the tower is in the bottom-left corner of the beam-splitter's breadboard).

Both delay lines, based on rooftop mirrors, are motorised:

- one with a stepper motor running 25 mm (i.e., optical path of 50 mm) at 0.1 μm reproducibility,
- and the other with a piezoelecric actuator running 15 μm at a reproducibility better than 0.5 nm.

Since the bench (if well aligned) is symmetric by design, the flux of the two arms can be balanced using simply injection into the exit SMF, tweaking the orientation of the folding mirror illuminating the off-axis parabola (Section 3.3.5). The better the superposition of the two beams, the easier the balancing.

3.12 SYNAPSE II

The functional outline of the SYNAPSE II testbed is given in Fig. 3.34. It is very similar to the original SYNAPSE, differing only in four aspects:

- the external-metrology system was dismounted,
- there was extensive work done on the mechanics (e.g., the optical table was changed, the tower on the

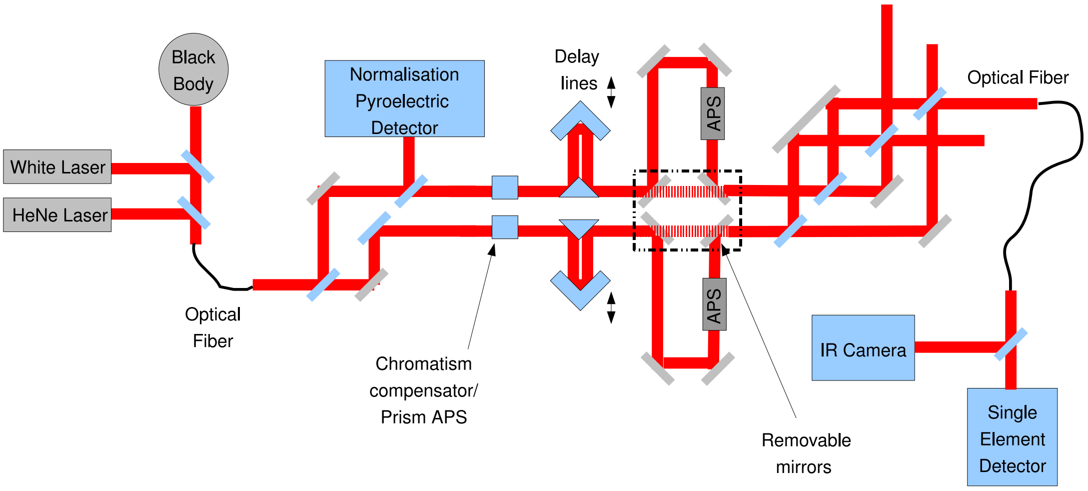

Figure 3.34 - SYNAPSE II (from left to right): Sources (three options), SMF, beam-splitter subsystem, CaF_2 prisms (chromatism compensator and/or APS), optical switch, APS prototype modules, beam-combiner subsystem, SMF, detectors (two options).

beam splitter's breadboard was disassembled, the beam combiner was placed on a new breadboard), enabling us to improve the alignment,

- the Focus Crossing APS prototype was mounted, and
- new sources were coupled to the input fibre (SYNAPSE originally used only the Ceramic Black Body).

For the tests of the FC APS prototype, a translation stage with folding mirrors acts as an optical switch to insert the prototype into the optical path.

3.13 NULLTIMATE

The general optical layout of NULLTIMATE (Fig. 3.35) is that of a simple Mach-Zehnder interferometer, rather than a double one as is the case with SYNAPSE. The number of optical surfaces has been reduced. The optics are ZnSe. The beam splitter and the beam combiner are prismatic (1° opening angle) and require compensators (Section 3.3.4). One of the compensators is also a chromatism compensator (Section 3.3.7). The mechanical design uses a line-point-plane on all optical elements (Fig. 3.36).

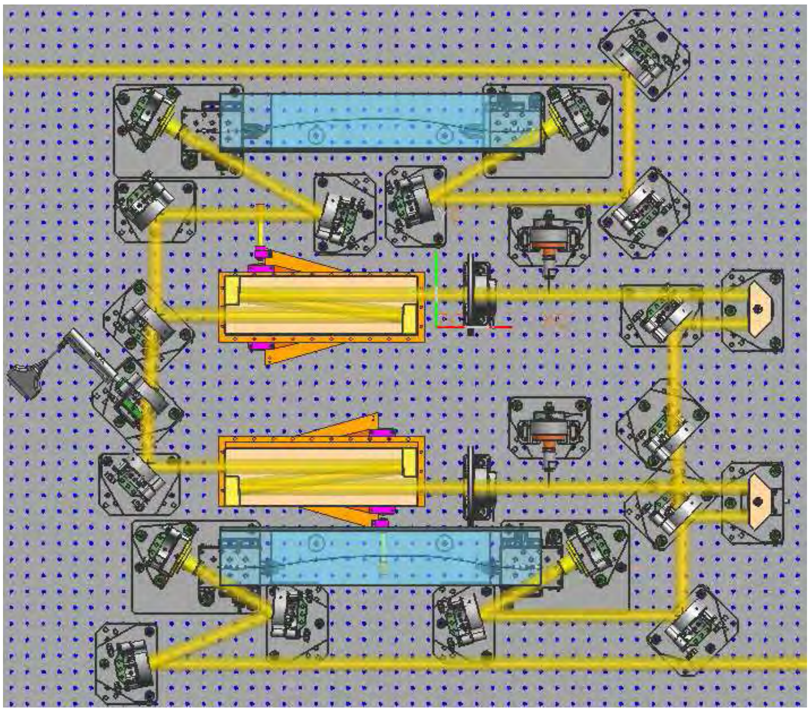

Figure 3.35 - NULLTIMATE: outline of the optical layout. The beam arrives from bottom right, going left towards two folding mirrors and a parabola which injects it into the input fibre. The beam leaves the diagram at top left.

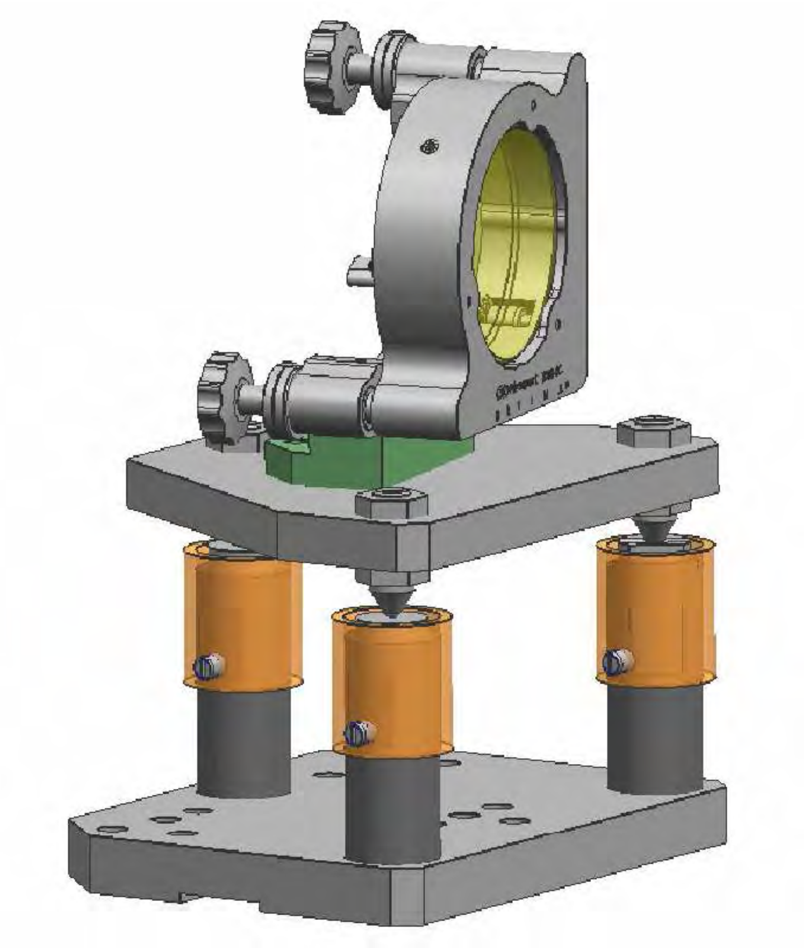

Figure 3.36 **-** NULLTIMATE. The line-point-plane system is implemented on all optical elements.

Chapter 4

Stabilisation

Contents

4.1 Introduction

We have seen (Sec. 2.6) that stability is crucial for nulling interferometry. Testbed studies suggest that it is not easy to achieve.

OPD is one of the first quantities that needs to be controlled in an interferometric setup. Several strategies may, and in fact, should be applied simultaneously. One approach uses a separate metrological servo system, based on a laser beam following the path of the beam whose behaviour is actually under study ("scientific beam") as closely as possible. The strong points of such systems include high accuracy, monitoring as well as servo functions, high-frequency servo control, etc. The disadvantages have to do with the fact that metrology always uses monochromatic lasers whereas the scientific beam ultimately has to be a polychromatic one. Moreover, the metrological laser is very often at a wavelength outside of the working band of the experiment, which means that the OPD's and the flaws seen by the two systems may be different.

An alternative approach is dither stabilisation, implementing a servo mechanism based on the scientific beam itself. A classical form of this technique has been investigated by Ollivier et al. (2001), although this first experiment was inconclusive. More recently, Schmidtlin et al. (2005) have demonstrated the potential of dithering in a sequential way, obtaining good levels of stabilisation with nulling ratio around $8\,10^{-7}$ with a laser diode at 638 nm. It was this work that provided our team with decisive inspiration.

4.2 Metrology

In the original concept of Synapse, a dedicated metrology system was to monitor and control OPD. The metrology system is a Michelson interferometer based on a commercial product (HP Agilent 10716A) operating with visible laser beams (HeNe 633 nm) that run four times through the setup. This ensures a precision of 0.3 nm. The drawback is that the metrology beams cannot easily follow exactly the same path as the science beams (mainly because of the fundamental difference between a Mach-Zehnder and a Michelson setup). Fig. 3.32 shows the metrology beams running about an inch above the science beams. The optical path comprises 16 reflections and 19 transmissions in each arm; and the metrology beams pass through them four times.

4.2.1 Setup and operation

The electric signal produced by the metrology detector is digitised by the electronics of a commercial PCI card. The output of the card is a 32-bit channel at 10 MHz. Each of these 2^{32} steps corresponds to 0.3 nm. The system is thus capable of measuring distances of about 1.3 m with a resolution of 0.3 nm.

Since the optical properties of the testbed are not likely to change on timescales of $1/10\text{MHz} = 0.1\,\mu\text{s}$, the output is too fast. What is more, the piezzoelectric actuator of the Fine Delay Line which is in the servo loop, is not designed to operate at such timescales. The PCI card's output, therefore, is averaged by custom electronics before entering the computer that runs the 4-kHz control loop .

4.2.2 Results

In 2005 Synapse in this setup reached $nl = 3 \times 10^{-4}$ in the K band. It also became clear that there was a significant OPD drift.

Let us reproduce the results of two typical acquisitions without stabilisation. The first (Fig. 4.1, left) shows an acquisition of about 200 s with a mean nulling ratio $\langle nl \rangle = 2.7\,10^{-4}$ with a considerable standard deviation $\sigma_{\langle nl \rangle} = 6\,10^{-5}$. The second (Fig. 4.1, right) is a slightly longer recording, of about 10 minutes with a nulling ratio $\langle nl \rangle = 2.5\,10^{-4}$ during the first 100 seconds (with $\sigma_{\langle nl \rangle} = 6\,10^{-5}$), showing the effects of significant drift, probably due to OPD instability.

Applying metrology stabilisation did not help, unfortunately. Fig. 4.2 shows a data acquisition obtained with the metrology running. A drift quite clearly persists.

4.3 Optical Path Difference Dithering

4.3.1 Introduction

Dithering is a standard technique in control engineering defined as “the modification of the low-frequency properties of an unstable nonlinear system by the application of a high-frequency signal in order to stabilise the system” (Gelb and Vander Velde 1968).

The present algorithm, however, departs in two ways from the classical system described by the quoted definition (the very formulation of which is reminiscent of analog electronic signal processing). First, the goal of the classical dithering method is to obtain a deconvolved signal: the dithered parameter is changing continuously, and the measured signal is a convolution of the variations due to the dithering as well as due to the studied system.

In our case, the experimental setup displays good stability on intermediate time scales ($t < 100\,\text{s}$), and we only have to fight against long-term drifts. Our approach was, therefore, to reach and maintain a delay-line position x_0 corresponding to the best null simply by moving the delay line every few seconds, rapidly measuring the flux at positions $x_0 \pm \varepsilon$, and moving the delay line to a new position based on the information

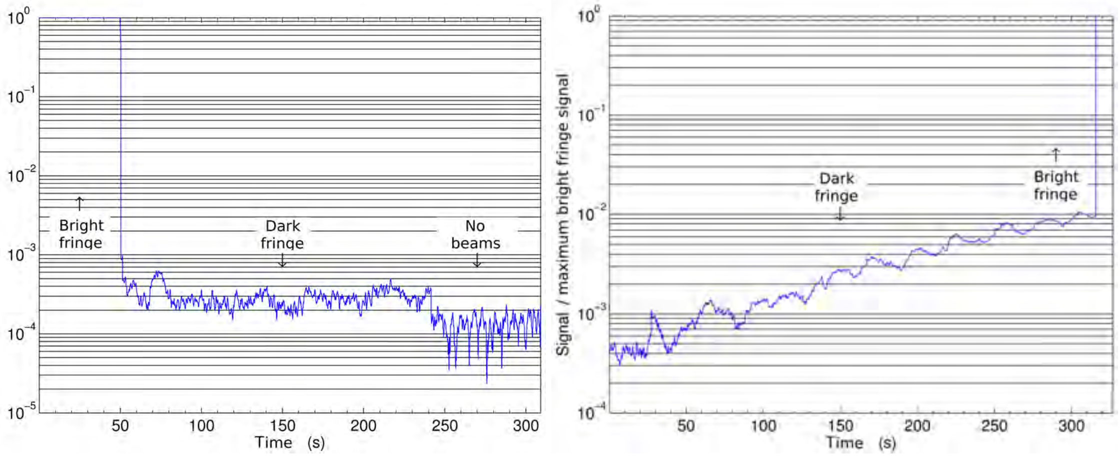

Figure 4.1 - Synapse measurements in the K spectral band. Left: The transition between the bright fringe (the first 50 seconds) and the dark fringe (between 50 s and 240 s) was performed manually by modifying the length of the delay line. The last part of the curve shows the dark current (the detector being covered). The mean rejection factor is about 2.4 times greater than the dark current of the detector. Right: Same measurement with a significant drift.

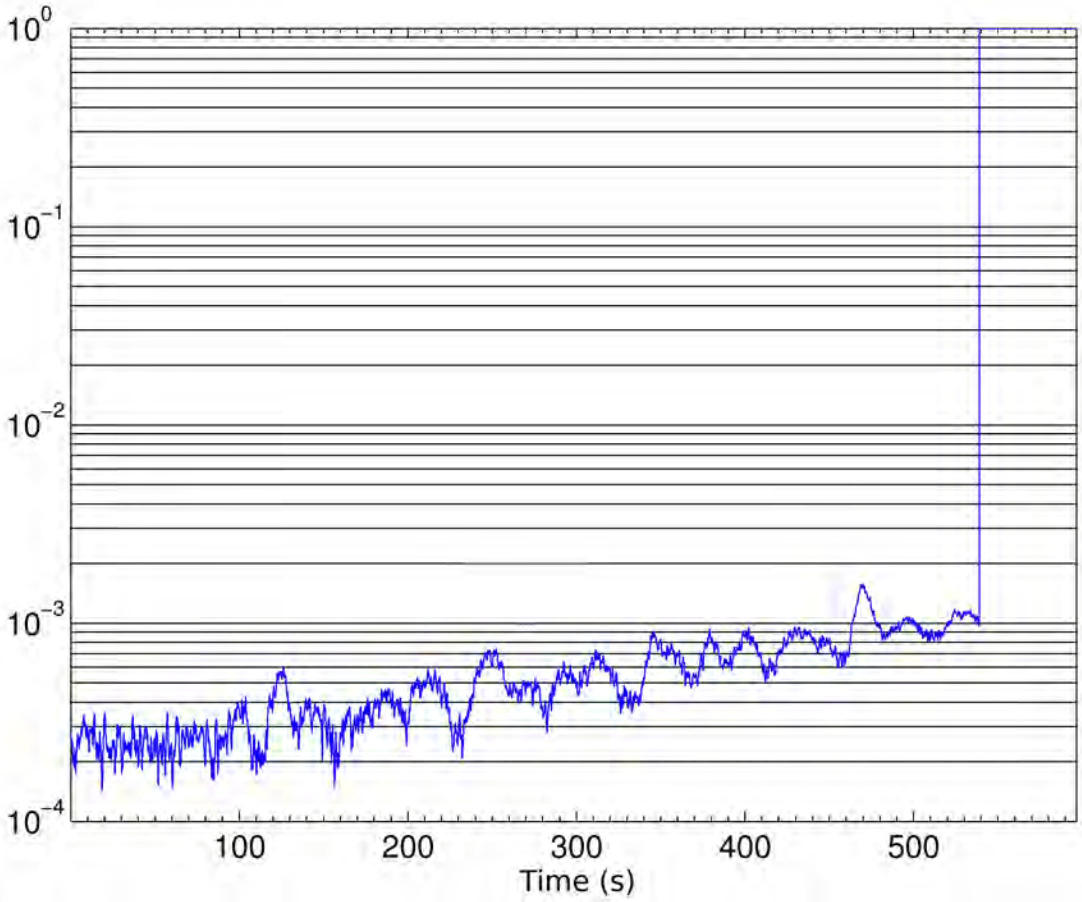

Figure 4.2 - Synapse measurement in the K band with the external metrology system running. A drift is clearly present.

obtained during these excursions. Unlike Schmidtlin et al. (2005) who record data throughout the dithering cycle (i.e., their recorded data contain points measured during delay-line movement and point measured at $x_0 \pm \varepsilon$), we chose to investigate a slightly different approach and to record data only during the final stage of each dithering cycle (i.e. at x_0), corresponding to the best null.

Thus, the second difference between our procedure and the classical definition of dithering is that we do not have to perform any post-acquisition signal deconvolution. Our version of dithering simply helps to maximise the amount of time the system stays in its optimal setting; i.e. employing the dithering only when needed, with relatively long periods of unperturbed data acquisition.

4.3.2 Principle

The nulling ratio in the vicinity of the dark fringe's centre, with other parameters constant, can be described as a function of the phase shift $\Delta\varphi$ (Eq. 2.14):

$$nl = \frac{I_{\min}}{I_{\max}} = \frac{1+\cos(\pi+\Delta\varphi)}{1+\cos(\Delta\varphi)} = \frac{1-\cos(\Delta\varphi)}{1+\cos(\Delta\varphi)} \tag{4.1}$$

$$nl \approx \frac{1-1+\frac{\Delta\varphi^2}{2}}{1+1-\frac{\Delta\varphi^2}{2}} \approx \frac{\Delta\varphi^2}{4} \quad \text{for} \quad \Delta\varphi \ll 1. \tag{4.2}$$

Bracewell's method uses achromatic phase shifters (APS) to produce a π phase shift independent of wavelength (within a given band). The phase shift can be translated into the OPD between the two arms of the interferometer

$$\Delta\varphi(\lambda) = 2\pi\frac{x}{\lambda} \tag{4.3}$$

where x is the OPD. The signal during an OPD scan can be described as tracing a parabola around the point where the nulling ratio reaches its minimum versus λ ($x \ll \lambda$)

$$I = ax^2 + bx + c. \tag{4.4}$$

The vertex of the parabola corresponds to the deepest null obtainable at a given moment adjusting the delay line, i.e. the centre of the dark fringe. The drift in nulling performance due to OPD instability can therefore be represented as a shift of the parabola and of its vertex.

With the empirical knowledge of three points of a parabola we can calculate the position of its vertex unambiguously. Since measurement of three points of the parabola is required, the OPD has to be modified deliberately. In our experimental setup the speed of operations is limited by the speed of the delay line actuators and by the integration time required to get a sufficient signal-to-noise ratio. This allows for compensation of slow drifts (observable on time scales of a few tens or hundreds of seconds).

If data are acquired at three different OPD's, e.g. at x_0, $x_0+\varepsilon$, and $x_0-\varepsilon$, then the position of the dark fringe, i.e. of the vertex x_v of the parabola, can be calculated as

$$x_v = x_0 - \frac{I_+ - I_-}{2(I_+ + I_-) - 4I_0}\,\varepsilon \tag{4.5}$$

where I_0, I_+, and I_- are the signal values measured at x_0, $x_0+\varepsilon$, and $x_0-\varepsilon$, respectively. This formula represents a simple recipe that can be directly implemented (Fig. 4.3).

4.3.3 Cycle parameters

The choices of dithering-cycle parameters are a result of several trade-offs.

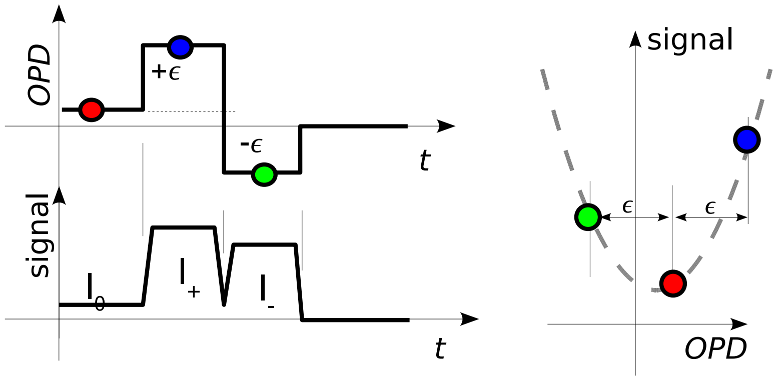

Figure 4.3 - OPD dithering cycle. The top curve shows schematically the position of the delay line whereas the bottom curve is an idealised representation of the corresponding detected signal. From an initial position the dithering alters the OPD value by $+\varepsilon$(OPD) with respect to the initial position. A measurement of the flux is performed. During the next stage, the dithering algorithm again alters the OPD, this time by $-\varepsilon$(OPD) with respect to the initial position. Another measurement is performed. We thus know three points, defining a parabola (right), which allows us to calculate and reach a new working position of the OPD (the vertex of the parabola).

4.3.3.1 Waiting times

A limitation is imposed by the delay line's movement. The piezzoelectric actuator reaches a position close to the desired one very rapidly, but then its controller takes some time, proportionate to the movement's amplitude ε, to stabilise the system at the new position:

$$\tau_{DL} \approx \left(90 + 6\,\frac{\varepsilon}{\text{nm}}\right)\ \text{ms}. \tag{4.6}$$

For ε of 5 nm, each dithering cycle therefore implies a waiting time of:

$$3\,\tau_{DL}(\varepsilon = 5\,\text{nm}) \approx 360\ \text{ms} \tag{4.7}$$

4.3.3.2 Dithering amplitude

As for the dithering amplitude ε itself, we accepted a limitation imposed by the gauge of the data acquisition system. We used a lock-in amplifier (Section 3.10.1) and, since changing its gauge requires time, we maintained the same gauge for all measurements: at x_0, $x_0 \pm \varepsilon$ and x_v, alike.

The flux $I_\pm(\varepsilon)$ measured at $x_0 \pm \varepsilon$ can be approximated as

$$I_\pm(\varepsilon) \approx I_{\max}\,\frac{\Delta\varphi^2}{4} = I_{\max}\left(\frac{\pi\varepsilon}{\lambda}\right)^2, \tag{4.8}$$

whereas the flux at x_v, expressed as

$$I_{\max}\,nl, \tag{4.9}$$

is due to a residual flux mismatch between the two arms of the interferometer, polarisation issues, and other factors contributing to nulling degradation. On the whole, we found that

$$\varepsilon = 5\,\text{nm} \tag{4.10}$$

$$\Delta\varphi = 1.5\,10^{-2}, \tag{4.11}$$

was well suited for our purposes.

4.3.3.3 Integration time

The dithering cycle with a duration of τ_{cyc} can be regarded as comprising:

- integration time τ_v at x_v, and
- time $\tau_{cyc} - \tau_v$ when dithering actions are performed.

The noise (assuming it is white noise in the relevant frequency band), measured by the standard deviation σ, decreases with the square root of the integration time. The scaling factor for σ is therefore

$$\sqrt{\frac{\tau_{cyc}}{\tau_v}}. \tag{4.12}$$

If $\tau_v/\tau_{cyc} = 2/3$, the noise will increase by 22 %. If $\tau_v/\tau_{cyc} = 9/10$, the noise will increase by 5 %. Therefore, in our experiment we did not consider it a strong priority to increase τ_v/τ_{cyc} beyond $\approx 2/3$.

4.3.3.4 Integration time at auxiliary points ($x_v \pm \varepsilon$)

There are two possible upper limits for the integration time $\tau_\pm$ of the flux $I_\pm$ measurements at $x_v \pm \varepsilon$.

- One is given by the fact that there is no reason for the corresponding SNR to be better than that of the flux I_v measurements at x_v. This can be expressed as (assuming white noise only):

$$\tau_\pm \leq \tau_v I_v / I_\pm = \tau_v \, 4nl/\Delta\varphi^2 \tag{4.13}$$

- The second upper limit for $\tau_\pm$ to be considered is given by the time τ_{DL} taken up by delay-line movements.

As a rule of thumb, since it takes τ_{DL} to reach a position, there is little practical gain in reducing $\tau_\pm$ to values less than τ_{DL}, which leads to $\tau_\pm \leq \tau_{DL}$. In practice, it is this latter upper limit that will be more applicable.

4.4 Results

We have tested this method on the Synapse testbed, and found it very convenient to use. It is highly efficient in finding the physical dark fringe (within one or two iterations; Fig. 4.4, left) and reliable, driving the OPD back to its optimal value in spite of artificial perturbations (Fig. 4.4, right).

4.4.1 K band

We performed three long dithering-stabilised data acquisitions, two of more than 6 hours each, and one of 2 hours 20 minutes. All three were performed with comparable settings: 1.25 s per stage, i.e., $\tau_\pm = \tau_v =$ 1.25 s, and 6.25 s per cycle[1]; dithering amplitude $\varepsilon = 5$ nm, i.e., $\Delta\varphi = 1.5\,10^{-2}$; lock-in amplifier's time constant at 100 ms.

The fluxes in the two arms of the interferometer were balanced before the acquisition (using an adjustable semi-planar knife-edge) with an accuracy better than 0.5 percent.

Fig. 4.5 presents one of the 6-hour data acquisitions, together with data taken immediately before the stabilisation was turned on and after it was turned off. Drifts are quite clearly present without the stabilisation.

---

[1] At this point the dithering cycle could not be optimised, the control software allowing only for stages of equal duration (cf. Gabor 2006).

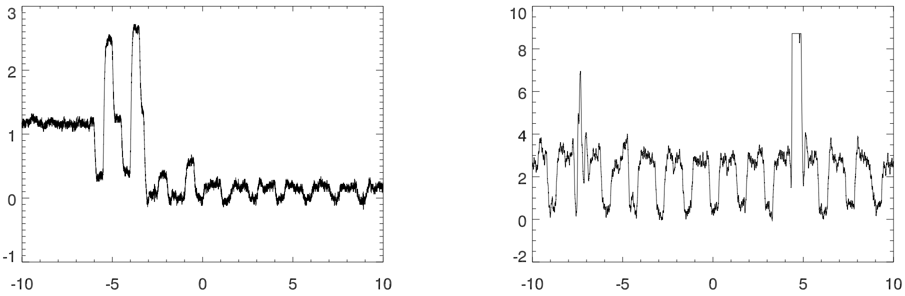

Figure 4.4 - Oscilloscope measurements.

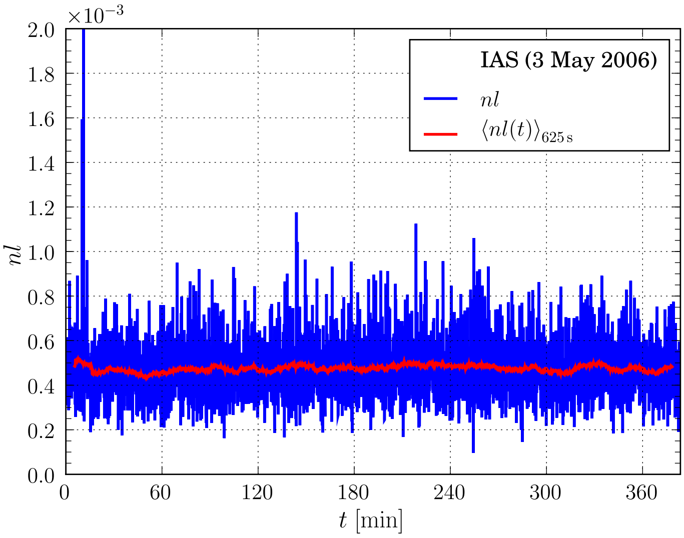

(a) Nulling ratio *nl* from a 6 hour-long OPD dither-stabilised data acquisition

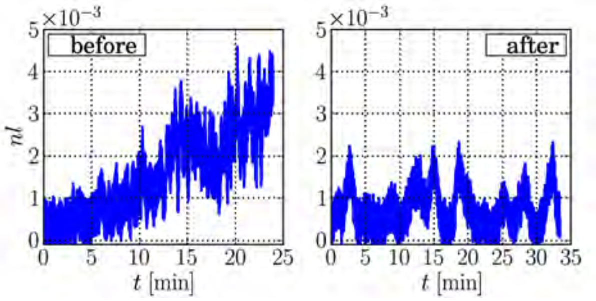

(b) Data acquisition with no stabilisation taken before and after the long stabilised run

Figure 4.5 - (a) Nulling ratio (or stellar leakage) $nl(t)$ as a function of time (blue plot), with the moving average calculated over 625 seconds $\langle nl(t)\rangle_{625\mathrm{s}}$ overplotted (red). (b) Data acquisitions with no stabilisation taken immediately before and after the long stabilised run.

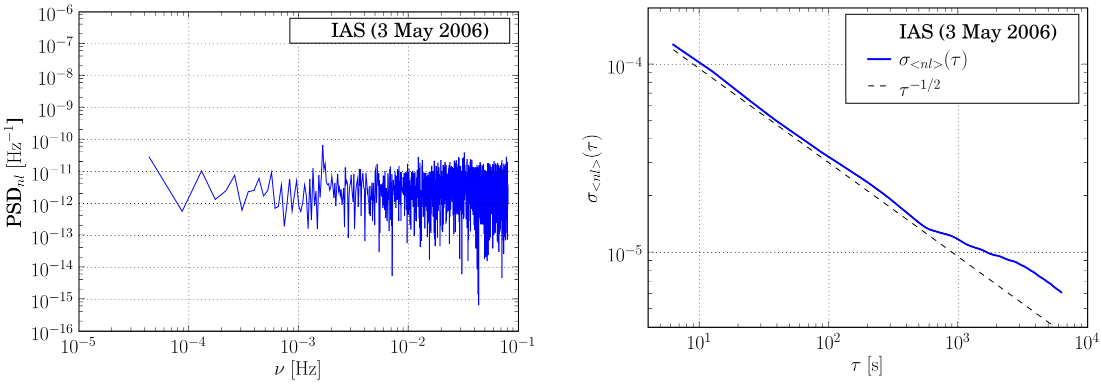

Figure 4.6 **-** Left: Power spectrum density of the nulling function, PSD(nl). Note that $1/f$ component is negligible. Right: Standard deviations of the running average of the nulling function over the time interval τ, $\sigma_{\langle nl \rangle}(\tau)$ (curve above). A (displaced) $\tau^{-1/2}$ function is shown for comparison (line below). Note that up to $\tau \approx 500$ s, the experimental curve is consistent with the $\tau^{-1/2}$ behaviour, with $\sigma_{\langle nl \rangle}(500\,\mathrm{s}) \approx 1.5\,10^{-5}$.

With no beams, the lock-in amplifier's θ output was random, and the mean values of the X and Y outputs

$$\langle X \rangle \approx \langle Y \rangle \approx 0 \tag{4.14}$$

This means that the measurement chain was well set up. Since the standard deviations of the X and Y outputs

$$\sigma_X \approx \sigma_Y \approx 0.2\,\mu\mathrm{V}, \tag{4.15}$$

the acquired R output was more than 10 times greater, and therefore this output can be considered to represent the measured flux directly (without "subtracting the dark current"; cf. Section 3.10.1.2).

The bright-fringe signal was thus

$$I_{\max} = (8.4 \pm 1.0)\,\mathrm{mV} \tag{4.16}$$

and the dark-fringe signal was

$$I_{\min} = (4.0 \pm 1.1)\,\mu\mathrm{V} \tag{4.17}$$

The mean nulling ratio nl was, therefore

$$\langle nl \rangle = (4.7 \pm 1.4) 10^{-4} \tag{4.18}$$

In order to evaluate the nulling ratio's variability, we looked at its Power-Spectrum Density (PSD) and at the standard deviation as a function of integration time. Fig. 4.6 (left) shows the power-spectrum density of the nulling function, PSD(nl), while Fig. 4.6 (right) shows the standard deviation of the mean value of the nulling function over the time interval τ, $\sigma_{\langle nl \rangle}(\tau)$.

Let us now briefly list the results of this analysis. We shall discuss them in due course (Section 4.5). Note, however, that there is no significant $1/f$ component in the PSD plot (Fig. 4.6), and the standard deviation decreases with integration time as $\tau^{-1/2}$ up to $\tau \approx 600$ s. (Fig. 4.6).

The main result can therefore be stated in terms of the standard deviation of the mean nulling ratio averaged over $\tau = 600$ s (analysing a set of mean values for the integration time of $\tau = 600$ s where these means correspond to a moving window[2]):

$$\sigma_{\langle nl \rangle}(\tau = 600\,\mathrm{s}) \approx 1.5 \times 10^{-5}. \tag{4.19}$$

---

[2] This type of statistics is called the *moving* or *running average.*

	Black Body (K band)			
T_{total}	6 hrs			
T_{opt}	6 hrs			
$\langle nl \rangle$	4.7×10^{-4}			
σ_{nl}	1.4×10^{-4}			
$\sigma_{\langle nl \rangle}(\tau = 600\,\text{s})$	1.5×10^{-5}			
	K band		7 µm	
	1 s	10 days	1 s	10 days
$\sigma_{\langle nl \rangle}(\tau, \lambda)$	$3.7{\cdot}10^{-4}$	$4.0{\cdot}10^{-7}$	$7.5{\cdot}10^{-6}$	$8.1{\cdot}10^{-9}$
$\sigma_{\langle \text{OPD} \rangle}(\tau, \lambda)$	13 nm	440 pm	3.0 nm	10 pm

Table 4.1 - Stabilisation results with a ceramic black body source in the K band (2.0–2.5 µm). The stabilisation followed the dark fringe over a total time T_{total} of 6 hours and over the whole period maintained the nulling ratio at the same level, $\langle nl \rangle = (4.7 \pm 1.4)10^{-4}$, with white noise only ($\tau^{-1/2}$ behaviour) up to $\tau = 600$ s. The mean nulling ratio averaged over windows of the duration τ had the standard deviation $\sigma_{\langle nl \rangle}(\tau = 600\,\text{s}) \approx 1.5 \times 10^{-5}$. This result is scalable and the bottom part of the table gives its extrapolations to $\tau = 1$ s and 10 days in the K band and at 7 µm. Corresponding values in OPD are also included.

In order to be able to compare this value with other experiments, let us also calculate the same quantity for $\tau = 1$ s and 10 days (1 s representing a unit of time and 10 days being the required stability timeframe for *Darwin*/TPF-I). We thus extrapolate the $\tau^{-1/2}$ scaling law, and obtain:

$$\sigma_{\langle nl \rangle}(\tau = 1\,\text{s}) \approx 3.7 \times 10^{-4}, \tag{4.20}$$

$$\sigma_{\langle nl \rangle}(\tau = 10\,\text{days}) \approx 4.0 \times 10^{-7}. \tag{4.21}$$

We may also want to extrapolate from the K band to 7 µm, using the scaling law Eq. B.10:

$$\langle nl \rangle_{\tau = 10\,\text{days}}\,(7\,\mu\text{m}) \approx 1 \times 10^{-5} \tag{4.22}$$

$$\sigma_{\langle nl \rangle}(\tau = 10\,\text{days}, 7\,\mu\text{m}) \approx 8 \times 10^{-9}. \tag{4.23}$$

These values can also be expressed in terms of the standard deviation of mean OPD, i.e., in units of length. All of these expressions of the main results (Eq. 4.18, 4.19) are presented in Table 4.1.

4.4.2 Laser light

Working with monochromatic light, at 3.39 µm, produced by a HeNe laser we reached

$$\langle nl \rangle = (1.0 \pm 0.8)10^{-5} \tag{4.24}$$

OPD-stabilised long-duration measurements were performed[3]. The dithering cycle was 3 s long, out of which 1 s was integration time at x_v.

The OPD dithering was able to follow the dark fringe over a period > 11 hrs. However, at this level of nulling, instabilities that cannot be fully controlled with OPD manifested themselves. Fig. 4.7 shows the PSD and $\sigma_{\langle nl \rangle}(\tau)$ obtained from the data taken during the first 10 min of the run. This period represented

---

[3] This time with upgraded the software which enabled more control over the OPD cycle parameters

	Laser 3.39 µm			
T_{total}	11 hrs			
T_{opt}	10 min			
$\langle nl \rangle$	1.0×10^{-5}			
σ_{nl}	0.8×10^{-5}			
$\sigma_{\langle nl \rangle}(\tau = 10\,\text{s})$	5×10^{-7}			
	3.39 µm		7 µm	
	1 s	10 days	1 s	10 days
$\sigma_{\langle nl \rangle}(\tau, \lambda)$	$1.6{\cdot}10^{-6}$	$1.7{\cdot}10^{-9}$	$1.4{\cdot}10^{-7}$	$1.5{\cdot}10^{-10}$
$\sigma_{\langle \text{OPD} \rangle}(\tau, \lambda)$	1.4 nm	44 pm	830 pm	27 pm

Table 4.2 - Stabilisation results with a 3.39 µm monochromatic laser source. The stabilisation followed the dark fringe over a total time T_{total} of 11 hours, and maintained the nulling ratio at the level of $\langle nl \rangle = (1.0 \pm 0.8)10^{-5}$ for typically 10 min, with white noise only ($\tau^{-1/2}$ behaviour) up to $\tau = 10$ s. The mean nulling ratio averaged over windows of the duration τ had the standard deviation $\sigma_{\langle nl \rangle}(\tau = 10\,\text{s}) \approx 5 \times 10^{-7}$. This result is scalable and the bottom part of the table gives its extrapolations to $\tau = 1$ s and 10 days at 3.39 µm and at 7 µm. Corresponding values in OPD are also included.

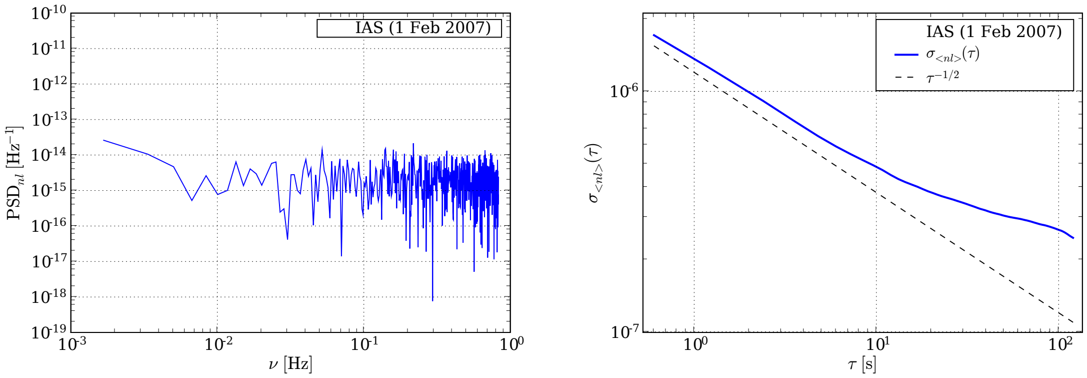

Figure 4.7 - Measurements with a HeNe laser at 3.39 μm. Left: Results of an OPD scan in terms of the nulling ratio *nl*. Right: Results of a 10-minute OPD-stabilised acquisition of the signal at the “bottom” of the dark fringe presented in terms of standard deviations of the running average of the nulling function over the time interval τ, $\sigma_{\langle nl \rangle}(\tau)$. A (displaced) $\tau^{-1/2}$ function is shown for comparison (line below).

the time during which the system remained at the "bottom" of the dark fringe (best nulling-ratio values), with $nl \approx 10^{-5}$. After that drifts deteriorated nulling performance, with $nl \approx 4 \times 10^{-4}$.

The plot of the standard deviations of the running average of the nulling ratio against the width of the averaging window (Fig. 4.7, right) exposes deviations from the $\tau^{-1/2}$, i.e., white-noise, behaviour. The "scalable" result (analogous to Eq. 4.19) is

$$\sigma_{\langle nl \rangle}(\tau = 10\,\mathrm{s}) \approx 5 \times 10^{-7}. \tag{4.25}$$

Tab. 4.2 contains all the values derived from this.

4.5 Comparison with some other experiments

Courtesy of our colleagues (Ollivier 1999; Alcatel; Vink et al. 2003; Brachet 2005), we were able to analyse their nulling-experiment data[4]. Unfortunately, in all cases, the power spectral density (PSD) of the null output displays a strong peak at low frequencies, i.e., a $(1/f)^{\alpha}$-type behaviour, with $\alpha \geq 1$ (Fig. 4.8). Consequently, none of these experiments show a $\tau^{-1/2}$ decrease in the standard deviation of the integrated null value, which means that the required performance cannot be obtained during very long integrations.

Let us compare our Figs. 4.6 and 4.7 with Fig. 4.8. It is clear that the power-spectrum density of the nulling function, PSD(nl), in the former case shows little or no $1/f$ component. *It must be emphasised that these three experiments in Fig. 4.8 had the goal of achieving a low null value but not maintaining its stability.* Similar conclusions can be drawn by examining the standard deviations of the mean value of the nulling functions over the time interval τ, $\sigma_{\langle nl \rangle}(\tau)$. The efficiency of OPD dithering in stabilising the setup stands out. This corresponds to an improvement of nulling stability with integration time. *It must be stressed, however, that we start from modest nulling ratios in comparison to our colleagues,* e.g., the Astrium group (Flatscher et al. 2003) reached $\sigma_{\langle nl \rangle} \approx 2\,10^{-7}$ during 100 s.

4.6 Discussion

These results have to be regarded as preliminary because, as we shall see in the next two Chapters, SYNAPSE has not reached its designed potential so far, and the technique has not been fully tested. It is all the more impressive that under these conditions OPD dithering proved to be a great help in studying the performance of our setup, providing a method of obtaining comparable results.

It is a promising method not only for laboratory use but also for space application. It does not require dedicated hardware, and represents an interesting option to setup stabilisation. A comparison with the *Darwin*/TPF-I requirements (Sec. 2.6, Chazelas et al. 2006): $\langle nl \rangle = 10^{-5}$ and $\sigma_{\langle nl \rangle}(10\,\mathrm{days}) = 3 \times 10^{-9}$ after a 10-day integration is optimistic. As shown in Tables 4.2 and 4.1, our K-band results extrapolate to *Darwin*/TPF-I conditions as

$$\langle nl \rangle\,(10\,\mathrm{days}, \lambda = 7\,\mu\mathrm{m}) = 8 \times 10^{-9}, \tag{4.26}$$

our 3.39 μm-laser results extrapolate as:

$$\langle nl \rangle\,(10\,\mathrm{days}, \lambda = 7\,\mu\mathrm{m}) = 2 \times 10^{-10}. \tag{4.27}$$

It remains to be shown that the method works at the required *Darwin*/TPF-I nulling level of 10^{-5} in broadband.

In the meantime, we would like to stress that we found the technique very practical in experimental work. We used it not only to reach and maintain the optimal OPD as we have seen, but also to perform "tweaking" experiments where the impact of small changes in interferometer geometry, passband and other settings on the nl and OPD can be monitored (Sec. 5.2.5.1).

---

[4] This work was done at the *Institut d'astrophysique spatiale* while preparing the article Chazelas et al. (2006)

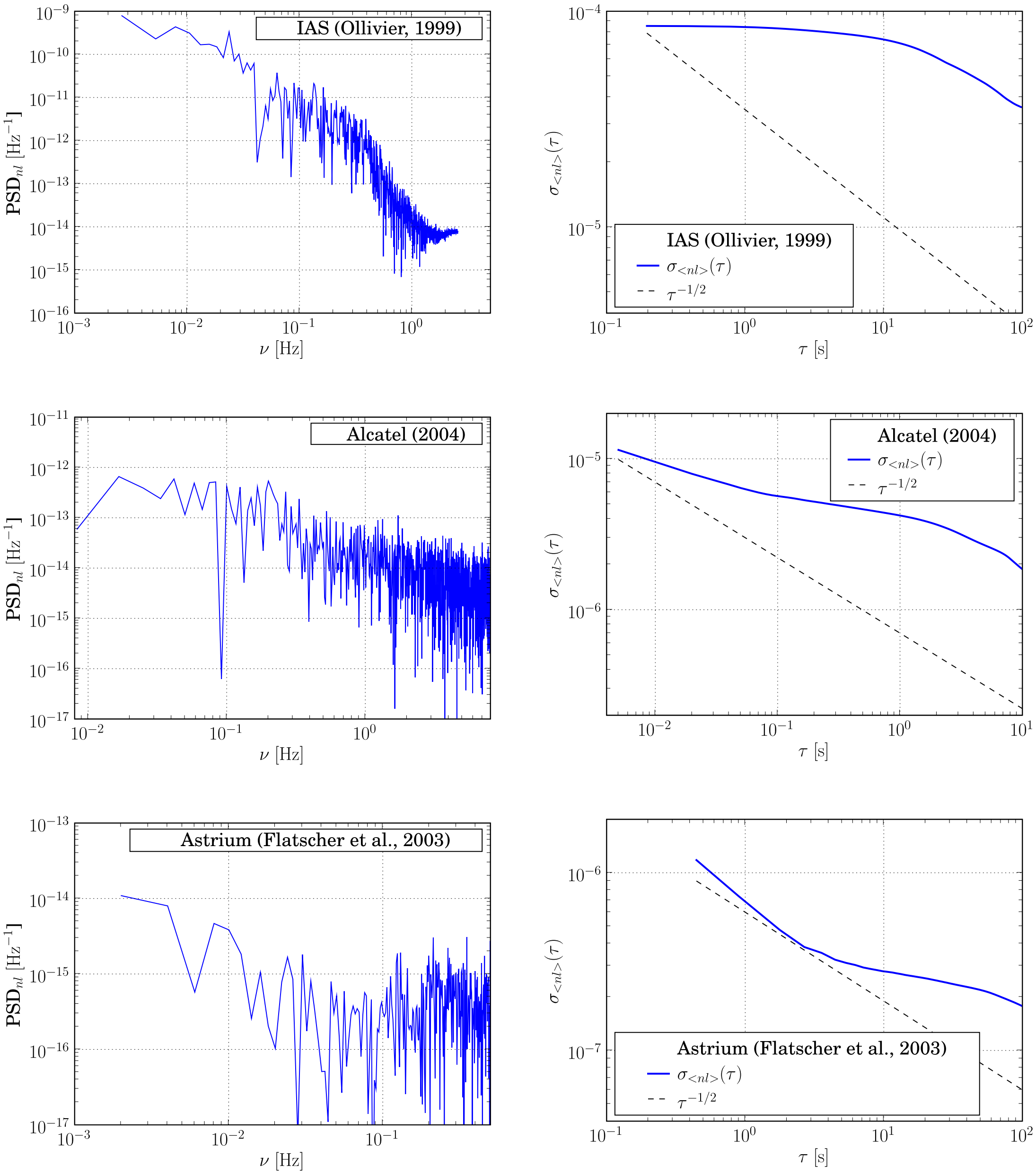

Figure 4.8 - Comparison with three other experiments. Left column: Power spectrum distributions. Right column: Standard deviation of the running average of *nl* over time τ, $\sigma_{\langle nl\rangle}(\tau)$. Top: Results from Ollivier's nulling experiment (Ollivier 1999; Ollivier et al. 2001). Centre: Results from the Alcatel nulling experiment (Alcatel), using a laser diode at $\sim 1.57\mu$m and an integrated optics recombiner (courtesy Alcatel Space Industry; now Thales Alenia Space). Bottom: Astrium results (Flatscher et al. 2003) (courtesy Astrium, Germany).

In our setup, we can balance the fluxes of the two interferometer arms by modifying the orientation of a folding mirror which sends both beams onto the exit fiber's off-axis parabola. Since the beams are not perfectly superimposed (they are parallel to within 10 arcsec but laterally shifted by about 0.1 mm), changing the point of impact on the parabola has an influence on flux mismatch. Therefore, a good example of a tweaking experiment consists in using OPD dithering to reach and maintain the dark fringe, and then tweak the folding mirror orientation in order to minimise the dark-fringe flux.

And finally, another practical point should be mentioned. It is true that the next step towards full stabilisation has to involve control of intensity mismatch between the interferometer arms. In order to perform tests of APS prototypes at $nl = 10^{-5}$, however, OPD stabilisation suffices in providing reliable and reproducible results.

Chapter 5

SYNAPSE results update

Contents

The purpose of this Chapter is to provide an overview of the results obtained with SYNAPSE up to 2008. This moment in time was not chosen arbitrarily. We shall see that some of the results still remain to be interpreted. We tried many different approaches and by mid 2008 we started running out of ideas. At the same time, new laboratory space was commissioned for the NULLTIMATE testbed. In Autumn 2008, we gradually turned our attention to this new setup. This was necessary. Because of our limited manpower we are unable to operate two testbeds in parallel. What is more, we hope NULLTIMATE brings some insights on our SYNAPSE results. In fact, NULLTIMATE's design was, in many respects, inspired by our desire to learn from our experience with SYNAPSE and to decipher its puzzling performance. This is why NULLTIMATE is a simpler optical design with a better signal-to-noise ratio. Some indication about future NULLTIMATE experiments will be given in Chapter 7.

The previous Chapters (3, 4) provided a description of the experimental setup, of the software systems for the running of the experiments, as well as of the testbed stabilisation techniques employed and the stabilisation performance achieved. Here, we shall describe the measurement techniques developed for the testbeds, and give an overview of the results obtained. The following Chapter (6) will provide a discussion of these results.

5.1 Preliminaries

5.1.1 Thermal and mechanical instability

We saw (Section 3.3.6.1) that the issue of ambient conditions was a major concern in the design of SYNAPSE. Day to day experimental work validated some of the concerns and the adopted solutions while showing that others were to be re-evaluated.

The piezoelectric active dampening proved impractical and ultimately not useful. It was difficult to operate because it required balancing the weight on the table, carefully distributing balast. After 2005 it was never turned on, and the piezo legs were used as a passive element only. As such, they proved very valuable. This was clearly shown when there was a mechanical short-circuit, and the granit block was directly linked with the optical table. The fringe pattern became unstable.

The passive pneumatic legs under the granite block were likewise essential to the nulling performance.

Opening one of the two lids of the plexiglass case briefly and then closing it left the fringe pattern disturbed for up to 2 hours. Opening one of the small side doors was usually much less disruptive, and measurements without major OPD drifts were often possible within 10 minutes after the door was closed.

The thermal gradient was never imposed on the air volume in the interferometer's housing after the initial tests with the ceramic black body source (Section 3.4.1) which did not appear to influence the nulling level of $nl \approx 3 \times 10^{-4}$ in the K band (we shall see this value very often in this Chapter). The subsequent monochromatic measurements with the 3.39 μm HeNe laser (Section 3.4.2) reached $nl \approx 10^{-5}$ without the imposed thermal gradient.

The air conditioning in the laboratory is noticeably noisy. Therefore, we performed a nulling experiment with the air conditioning off. It did not improve the nulling level in the K band beyond the very reproducible value of $nl \approx 3 \times 10^{-4}$.

5.1.2 Detector calibration

The InSb single-pixel detector (Section 3.8.2) with the lock-in amplifier SR830 (Section 3.10.1) was calibrated (Brachet 2005, pp. 151-153). The average gain was

$$g \approx 2.4 \times 10^{6}\,\mathrm{V/W} \tag{5.1}$$

which means that

$$1\,\mathrm{V} \mathrel{\hat{=}} 420\,\mathrm{nW}. \tag{5.2}$$

5.1.3 Transmission

Theoretical estimates of the transmission of the individual elements of SYNAPSE for the K band can be found in Brachet (2005, pp. 127-131). We reproduce them in the left half of Table 5.1.

The table also lists measured values. They are given first in the form of transmission coefficients of individual elements (except for the 83 % which correspond to the transmission of two elements in series: of the CaF_2 Prisms *and* the delay lines). Values for the MMZs represent one beam only. The measured power in W is given after the input and after the output fibre.

In most cases, there is only a slight discrepancy between the theoretical estimate and the measured value. This is quite consistent with the view that the measured values must be considered to suffer from a

After	theoretical transmission per element	theoretical transmission cumulative after input fibre	measured transmission per element	measured transmission cumulative after input fibre
input fibre	56 %		7.9 nW	
beam splitter MMZ	21 %	21 %	23 %	23 %
CaF_2 Prisms	88 %	18 %		
delay lines	92 %	17 %	83 %	19 %
beam combiner MMZ	11 %	1.9 %	10 %	1.9 %
output fibre	78 %	1.5 %	45 %	0.9 %
total	0.8 %		0.7 nW	

***Table 5.1* -** Photometry of Synapse in the K band (Brachet 2005). Theoretical estimate and measured values. These are given after each optical element (the measurement after the MMZ's correspond to one beam only; the 83 % after the delay lines correspond to the transmission of the CaF_2 Prisms *and* the delay lines). The measured power in W is given after the input and after the output fibre. The measured values must be considered to suffer from a relative error of 10 %, while the theoretical estimate can be inaccurate as to coatings' properties.

relative error of 10 %, and the theoretical estimate can be inaccurate as to coatings' properties. The only measured value which is clearly less than the theoretical expectation is the flux at the output of the output fibre. This is typical of the experimental reality, however: the nulling was rarely performed with optimal coupling at the output fibre.

5.2 Techniques

Several measurement techniques have been studied for Synapse:

5.2.1 Zero optical path difference and the CaF_2 Prisms

For each position of the CaF_2 Prisms a fringe pattern can be obtained with a Long Delay Line scan. We spoke about the theory in Section 2.4, and we shall see an example in Section 6.1.5.

5.2.2 Fringe dispersion

Let us briefly mention a technique studied by Chazelas (2007, pp. 143-145) as well as by Boffety and Drugeon (2006). Placing an array detector with a dispersive prism at the exit of the bench while scanning the OPD, provides a series of low-resolution spectra (Fig. 5.1). In an ideal case the resulting pattern would contain a straight dark fringe. Its deviation from the ideal form yields a measure of phase-shift chromaticity (Chazelas 2007).

The chief advantages of this approach is that it is inherently independent of flux mismatch, and that it works even when the signal-to-noise ratio does not allow for a direct measurement of *nl*. Nonetheless, we have not implemented this approach. One difficulty has to do with OPD drifts (which would have to be stabilised using external metrology), and the other is practical: our array detector is much more difficult to use than the single-element detector.

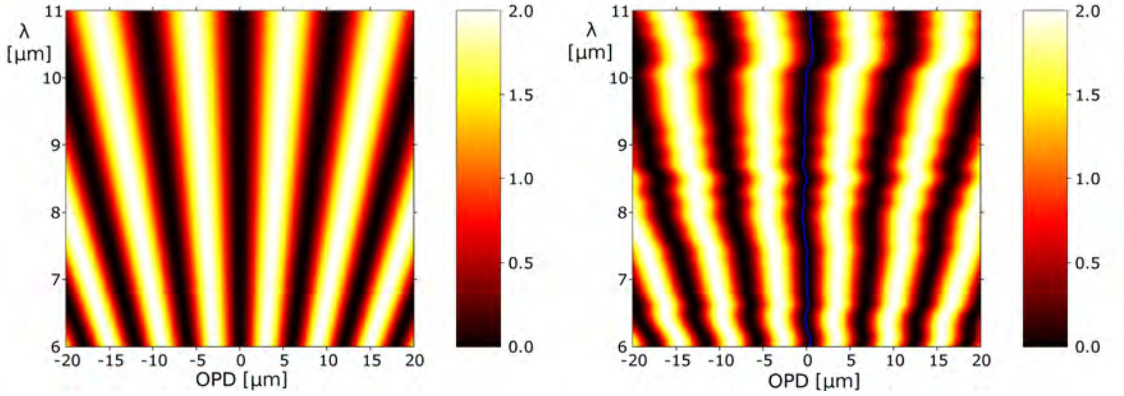

(a) (b)

Figure 5.1 **-** Evaluation of nulling by fringe dispersion. (a) A perfectly achromatic phase shifter. (b) An imperfectly achromatic phase shifter. The central fringe is distorted. Its deviation from a straight line corresponds to residual phase defects. (Chazelas 2007)

5.2.3 Fourier transform

Another technique which is under study is the Fourier transform of OPD scans with the Long Delay Line (Chazelas 2007, p. 133). The beams are recombined in a SMF which also provides modal filtering, and the flux is measured using a single element detector. The Fourier transform method gives workable results regardless of low signal-to-noise ratio for the dark-fringe signal, and regardless of chromatic flux mismatch. Unfortunately, tests show that SYNAPSE's Long Delay Line is not sufficiently smooth and its motor does not move uniformly enough for the purposes of this technique. It may eventually be implemented on NULLTIMATE which was designed with this option in mind.

5.2.4 Direct nulling measurements

We shall use the expression "Direct Nulling Measurement" as a technical term denoting a measurement of the bright and dark fringe intensity with a single pixel detector at the output of the interferometer. This is generally regarded as the most straightforward measure of the nulling performance.

Most of the results presented in this thesis were obtained with the single pixel detector and the lock-in amplifier (Section 3.10.1) measuring the interferometric output of the testbed. In Section 3.10.1.1 we described two data acquisition methods. All of the measurements reported in this Chapter were performed using the first one; the second one was first implemented on the NULLTIMATE testbed.

5.2.5 Experimental protocol

The direct nulling measurements were performed following an experimental protocol which will be summarised below. Let us briefly note that, as with so many other aspects of this work, the protocol should be considered as under development. It can be said, nonetheless, that its basic outline has remained operative since SYNAPSE's beginnings.

Note that OPD stabilisation is used not only to reach and maintain the optimal OPD (and therefore enabling reproducible measurements of nl and σ_{nl}) but also tweaking experiments where the impact of small changes in flux balance, CaF_2 prism position, monochromator prism orientation, etc., on the nl and OPD can be monitored and optimised.

- Check position of optical switch: experiment with or without FC APS.
- Check CaF_2 prism and long delay-line position.
- Start optimising injection into the exit fiber by maximising Beam 1 flux with motorised folding mirrors.
- Switch to Beam 2. Remove residual flux mismatch by tweaking folding mirror orientation (aiming for $\Delta I/I \approx 0.5\%$).
- Perform OPD scan with the fine delay line. Find current dark fringe position and the first *nl* value.
- Repeat OPD scan, focusing on the dark fringe. Obtain a measure of *nl*.
- Start OPD-stabilised DAQ, monitoring the flux and OPD position.
- Perform tweaking experiments.

5.2.5.1 Parameter tweaking experiments

A notable innovation of the protocol came with the realisation that OPD stabilisation allows for experiments (Section 4.6).

- tweak folding-mirror position in order to monitor/minimise the impact of flux mismatch on *nl*;
- while monitoring its impact on *nl*, tweak CaF_2 prism position in order to fine-tune the prism APS.

5.2.5.2 Flux balancing

One of the preliminary procedures in our protocol is flux balancing. We described its two elements (intensity-mismatch estimation and flux balancing) in Section 3.3.5. Here, we shall only say that patience was needed in order to perform the procedure successfully on Synapse (it only rarely took less than half an hour) but *we never performed measurements unless we made sure that intensity mismatch was less than 1 %,*

$$\frac{\Delta I}{I} < 1\,\%, \tag{5.3}$$

which corresponds to a nulling ratio (in the absence of all other perturbative factors; Eq. 2.21):

$$nl < 2.5 \times 10^{-5}. \tag{5.4}$$

5.2.5.3 Dark current subtraction

As we have seen (Section 3.10.1.2), nulling experiments often have to face the frustrating fact that the better the nulling performance the more likely it is to be measured with poor signal-to-noise ratio. Being close to the sensitivity limits of the detector system leads to the natural temptation to “subtract the dark”. Indeed, when the beams are stopped, the lock-in amplifier shows a $\langle R \rangle > 0$ (Fig. 5.2). Subtracting $\langle R \rangle$ from the dark-fringe signal can improve the nulling ratio as much as twofold.

We have shown (Section 3.10.1.2) that this temptation must be resisted, and that the adequate procedure (unless a more careful analysis is warranted) with a well set-up measurement chain is merely to verify that θ varies randomly when the beams are stopped. *No “dark current” was subtracted from the dark-fringe flux.*

5.3 Nulling levels reached with Synapse

This Section describes the evolution of nulling measurements on the Synapse testbed, starting in 2004.

5.3.1 The 2000 K black body

The first experiments with the Synapse testbed were Simple Nulling Measurements (Section 5.2.4) using a setup where:

- the source was the 2000 K ceramic black body (Section 3.4.1),
- the spectral band was defined by the "K" interference filter (Section 3.6),
- the bench contained only its generic achromatic phase shifter (CaF_2 Prisms),
- the metrology system (Section 4.2) was sometimes used for optical path difference stabilisation, and
- a thermal gradient was sometimes imposed on the air volume inside the optical bench's protective case (Section 3.3.6.1).

This work was performed and reported by Frank Brachet (2005). It has brought to light two features of the Synapse nulling performance in the K band (2–2.5 µm). The first being the best value of the nulling ratio of

$$nl = 3 \times 10^{-4}. \tag{5.5}$$

The second parameter observed was the degree of nulling performance stability (cf. Chapter 4). Let us reproduce the results of a typical acquisition (Fig. 5.2). It is an acquisition of about 200 s with a mean nulling ratio $\langle nl \rangle = 3 \times 10^{-4}$ with a considerable standard deviation

$$\sigma_{nl} = 6 \times 10^{-5}. \tag{5.6}$$

5.3.2 First effective stabilisation

We reported about our implementation and testing of an effective OPD stabilisation system in the previous Chapter (4.3). We saw that in the K band, at the nulling level of

$$nl = (4.7 \pm 1.4)10^{-4} \tag{5.7}$$

the system tracked the dark fringe for > 6 hrs, and over the whole period maintained the nulling ratio at the same level. White noise only ($\tau^{-1/2}$ behaviour) was demonstrated for acquisition times up to $\tau = 600$ s. The mean nulling ratio averaged over windows of duration τ had the standard deviation

$$\sigma_{\langle nl \rangle}(\tau = 600\,\mathrm{s}) \approx 1.5 \times 10^{-5}. \tag{5.8}$$

Implementing this approach, we have succeeded not only in stabilising the nulling performance, but also gained a powerful instrument for bench optimisation (cf. Sec. 5.2).

5.3.3 3.39 µm HeNe laser and polarisers

In order to find ways of improving the nulling performance of the testbed, we started working with monochromatic light, at 3.39 µm, produced by a HeNe laser (Section 3.4.2). The first results were limited to

$$\left\langle nl_{\mathrm{unpolarised}} \right\rangle = 6 \times 10^{-5}. \tag{5.9}$$

Introducing polarisers has led to

$$\left\langle nl_{\mathrm{polarised}} \right\rangle = 10^{-5}. \tag{5.10}$$

An OPD scan is shown in Fig. 5.3. This result seems roughly consistent with our theoretical studies (Chazelas 2007) of the effects of polarisation mismatch (primarily due to residual alignment errors) on the nulling performance. Let us mention that this apparent accord with the theoretical model will have to be discussed in more detail in the following Chapter (6). We felt justified, however, in wanting to re-align our optics carefully. In fact, we found that this was only possible if some improvements were made to the mechanics of the testbed. The upgraded setup became known as Synapse II.

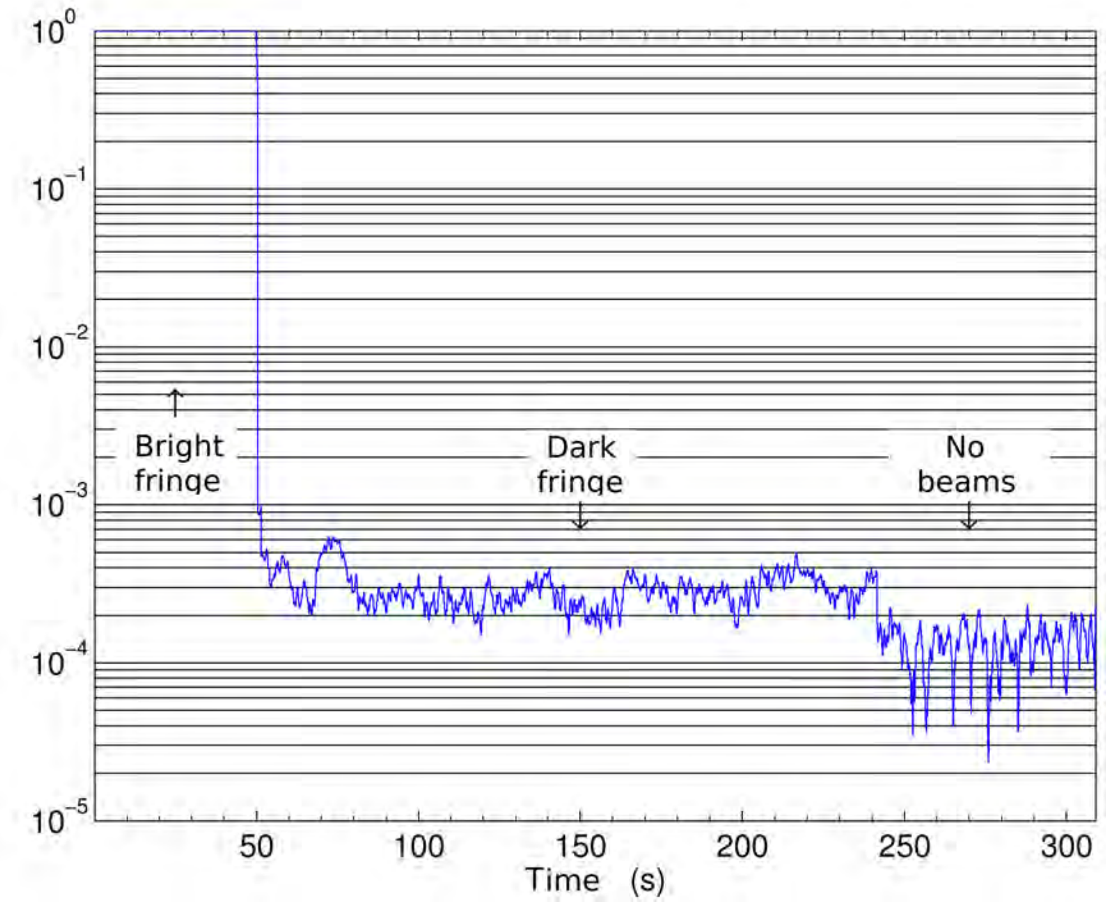

Figure 5.2 - SYNAPSE measurements of recombined flux in the K spectral band, normalised dividing by the mean bright fringe flux. The transition between the bright fringe (the first 50 seconds) and the dark fringe (between 50 s and 240 s) was performed manually by modifying the length of the delay line. The last part of the curve shows the lock-in amplifier's module output *R* when the detector was covered, illustrating that measurement chain was well set up.

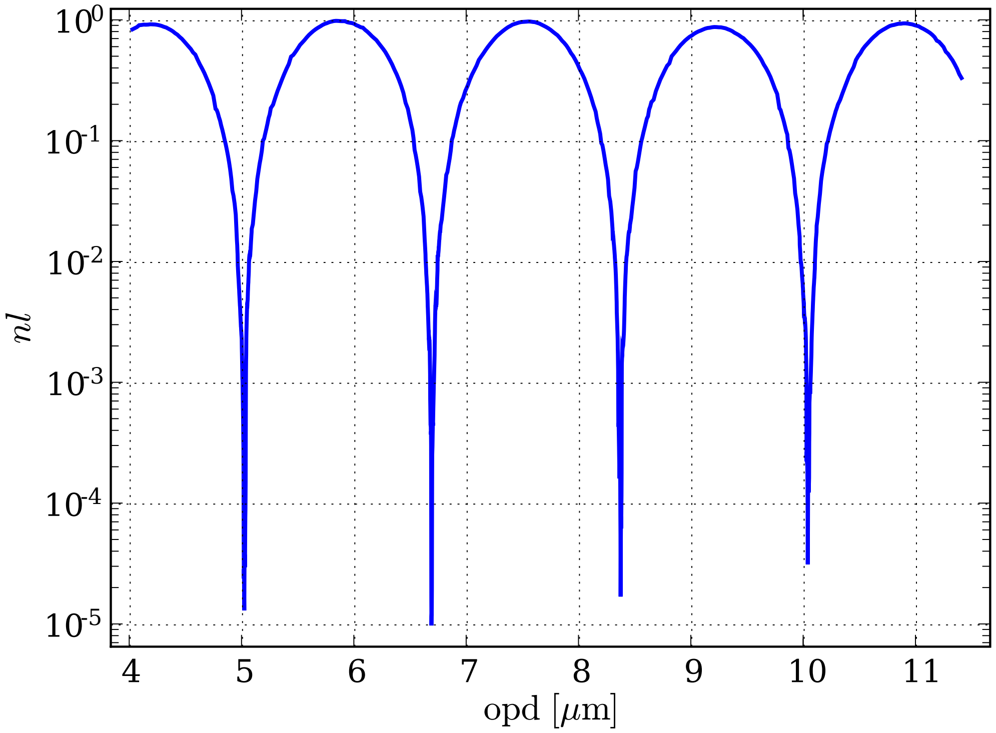

Figure 5.3 - Measurements with a HeNe laser at 3.39 μm. Results of an OPD scan in terms of the nulling ratio *nl*. The fact that the fringes do not seem to be of equal depth is attributable to the scan's step (10 nm; which is too coarse).

λ	polarisers without	polarisers with
K band	5×10^{-4}	3×10^{-4}
3.39 μm	5×10^{-5}	1×10^{-5}

***Table 5.2* -** Nulling performance of SYNAPSE II.

5.3.4 SYNAPSE II: Improved mechanics and alignment

After these encouraging results with monochromatic light we concentrated our efforts on improving the level of null in broad band. From the results of monochromatic measurements we deduced that the factor limiting nulling levels of the test bench could not be thermal and mechanical (vibrations) stability. Such phenomena would also deteriorate monochromatic nulling performance.

We have also seen that improving bench alignment (to within < 10 arcsec as opposed to the previous < 3 arcmin) may help reduce polarisation mismatch, greatly facilitating flux balancing of the two interferometer arms. Performing direct nulling measurements with and without polarisers in this improved setup has demonstrated a surprising consistency with the results obtained with the first version of SYNAPSE (Tab. 5.2).

As we have seen in the previous Chapter (4.4.2), OPD-stabilised long-duration measurements (the OPD dithering was able to track the dark fringe over a period > 11 hrs, maintaining the nulling ratio at the level of

$$\langle nl \rangle = (1.0 \pm 0.8)\, 10^{-5} \tag{5.11}$$

for typically 10 min, with white noise only ($\tau^{-1/2}$ behaviour) up to $\tau = 10$ s. The mean nulling ratio averaged over windows of the duration τ had the standard deviation

$$\sigma_{\langle nl \rangle}(\tau = 10\,\mathrm{s}) \approx 5 \times 10^{-7} \tag{5.12}$$

Conclusion. From these measurements we had to conclude that improving the alignment, although very useful as regards practical aspects of experimental work, *did not alter overall nulling performance.*

5.3.5 Supercontinuum source

The previous measurements, especially those taken with the polarisers, had a relatively small signal-to-noise ratio. The noise can be quantified as, typically, $\sigma_N = 0.5\,\mu$V whereas the dark fringe fluxes were typically a few μV.

In order to improve the situation, as well as to gain new experimental possibilities (we shall see one in Section 5.3.7), we upgraded our setup and acquired a supercontinuum source (Section 3.4.3). It provides a usable flux of about 200 mW in the K band (about a million times more than 0.17 μW, which is the flux available from the ceramic black body).

Even with this new light source, the nulling performance did not improve, and remained at the previously reported levels.

5.3.6 Focus crossing APS

SYNAPSE II was also designed to permit measurements of the Focus Crossing (or Through Focus) APS prototype (Section 3.9.1). It was initially built to work in the spectral range of 6–18 μm (proposed range for *Darwin*/TPF-I), and its optimal designed nulling performance is

$$nl_{\mathrm{FC\ APS}}(\mathrm{optimal}) \leq 10^{-6}, \tag{5.13}$$

λ	with polarisers
K band	3×10^{-4}
3.39 μm	1×10^{-5}

***Table 5.3* -** Nulling performance of Synapse II with the Focus Crossing APS prototype.

	without	with
λ	FC APS	
narrow band	3.4×10^{-4}	3.4×10^{-4}

***Table 5.4* -** Nulling performance of Synapse II with the narrow passband filter (16 nm FWHM) centred around 2.3 μm.

depending on the bench configuration. In the working conditions of Synapse the expected value is

$$nl_{\text{FC APS}}(\text{expected}) \leq 10^{-5}. \tag{5.14}$$

Using the CaF_2 Prisms as chromatism compensators (Section 3.3.7), we tested the FC APS prototype with polarisers. Both in the K band and with the monochromatic 3.39 μm laser we once again obtained the same values (Tab. 5.3) as without the FC APS prototype and the CaF_2 Prisms used as an APS.

Conclusion. The expected performance ($nl = 10^{-5}$) was demonstrated with laser light at 3.39 μm. Rejection performance of the FC APS in the K band (2.0–2.5 μm) was limited by the performance of the Synapse II testbed itself.

5.3.7 Narrow band centred at 2.3 μm

The high flux of the supercontinuum source in conjunction with an interferometric filter with a narrow passband (16 nm FWHM) centred around 2.3 μm, enabled us to perform a number of decisive experiments (we shall discuss their implications in the following Chapter 6). The results are summarised in Tab. 5.4.

5.3.8 Fibre curvature

In order to explore the possibility that Synapse nulling performance is limited in non-monochromatic light by the quality of modal filtering, we performed tests with our single-mode fibres. Twisting the fibre around a 40 mm diametre cylinder (3 or 8 full turns) was suggested as a means for improving secondary-mode rejection.

These direct nulling measurements were performed in the K band (2.0–2.4 μm) with the polarisers but without the FC APS. The measured nulling ratio

$$nl = 1.9 \times 10^{-4} \tag{5.15}$$

demonstrated some improvement. No reproducible difference was observed between setups with 3 and 8 full turns of the fibre.

5.3.9 L band

One of our experiments to explore the possibility that Synapse nulling performance is limited in non-monochromatic light by our modal filters was performed in the L band (3–4 μm). The setup was otherwise unchanged. Although we have L-band single-mode fibres, in this case we used the ones designed for the K band, i.e., with a cutoff wavelength of $\lambda_c = 1.95\,\mu\text{m}$. Taking fibres designed for the K band and using them in the L band reduces the throughput but may improve modal filtering properties.

These direct nulling measurements were thus performed in the L band (3–4 μm) with the polarisers but without the FC APS. The measured nulling ratio

$$nl = 2.1 \times 10^{-4} \tag{5.16}$$

again indicated some improvement. This value was obtained with a poor signal-to-noise ratio, however, and should be regarded as an upper limit.

5.4 Summary

An overview of our progress in terms of *nl* and stability (when available) is given in Tab. 5.5. Three points stand out:

1. Focus-Crossing APS prototype's nulling ability was validated with the 3.39 μm laser to the level of 10^{-5}. The performance of the setup in the K band was not limited by the prototype.

2. Polarisation. The presence of polarisers clearly improves the nulling ratio. In all configurations where we tested the nulling performance with and without polarisers, the setup with polarisers provides better nulling ratios. We shall see (Sec. 6.1.3) that this effect is not fully explained by the available theoretical models.

3. Particularity of 3.39 μm**-laser light?** What stands out is a discrepancy between the nulling ratios achieved with the 3.39 μm laser source and with all other tested configurations. If it were an issue of chromatism, we would expect to see a difference between K-band results and the results obtained with the narrow (16 nm FWHM) filter at 2.3 μm (Sec. 5.3.7). Perhaps it is an issue of the Single-Mode Fibres. The last two tests, viz., twisting the SMF (Sec. 5.3.8) and using the K-band SMF in the L band (Sec. 5.3.9), seem to suggest that this may be the case.

The last two issues will be discussed more closely in the next Chapter (6).

	λ	polarisers	APS FC	nl	stability
Nov '05	K band	–	–	3×10^{-4}	
May '06	K band	–	–	5×10^{-4}	$\sigma_{\langle nl \rangle}(600\,\mathrm{s})$ $= 1.5 \times 10^{-5}$
Jan '07	$3.39\,\mu$m	–	–	10^{-4}	
Jan '07	$3.39\,\mu$m	+	–	6×10^{-5}	$\sigma_{\langle nl \rangle}(10\,\mathrm{s})$ $= 5 \times 10^{-7}$
Feb '08	3.39 µm	+	–	10^{-5}	
Feb '08	3.39 µm	+	+	10^{-5}	
Feb '08	K band	–	+	4×10^{-4}	
Feb '08	K band	+	+	4×10^{-4}	
May '08	2.3 µm (16 nm FWHM)	+	–	3.4×10^{-4}	
May '08	K band (SMF twist)	+	–	1.9×10^{-4}	
Jun '08	L band (K-band SMF)	+	–	$< 2.1 \times 10^{-4}$	

***Table 5.5* -** An overview of progress on SYNAPSE in terms of *nl* and stability (when available) expressed in terms of the standard deviation of the nulling-ratio means averaged over windows of the duration τ, $\sigma_{\langle nl \rangle}(\tau)$ (these values are scalable as $\tau^{-1/2}$ because there is white noise only).

Chapter 6

Error budget

Contents

The purpose of this Chapter will be twofold: (1) to discuss the setup's error budget and therefore the expected performance levels, and (2) to list and describe all the avenues we explored while trying to understand our results. As we have seen in the previous Chapter (5), some of results we obtained so far on SYNAPSE II, must be regarded as preliminary until we reach a full understanding of the underlying phenomena. The two observations that require special attention are

1. polarisation: there seems to be a discrepancy between the theoretical predictions and our observations;
2. why are the nulling ratios achieved with the 3.39 µm-laser light better than those obtained in other configurations?

6.1 Tests and models

6.1.1 Detector nonlinearity

The accuracy of nulling measurements depends on the detection system's linearity. The nulling ratio is calculated from two measurements: of the bright fringe, and of the dark fringe. Since the whole purpose of nulling experiments is that these two measurements differ by several orders of magnitude, it is clear that the detection system must have a linear response curve (as a function of flux intensity).

The PhD thesis of Christophe Buisset (2007) contains a detailed study of the response curve of a detection system very similar to our own, comprising a single pixel detector (InGaAs) and a lock-in amplifier (Stanford Research 830). He used two polarisers to modulate the measured intensity over six orders of magnitude. He concluded that the non-linearity of the detection system induces an inaccuracy of less than 7 % in the nulling ratio.

After a discussion with Christophe's director, Yves Rabbia, we decided to try a different approach, in order to obtain an independent estimate ourselves, but mainly to confirm that our detection system does not significantly deviate from linearity. While we use the same lock-in amplifier model, our single pixel detector is not identical to the type Christophe used (ours is InSb, produced by *Electro-Optical Systems*).

We demonstrated (App. D) that our detector system is linear within an error of $\approx$ 10%. The method we applied is not sensitive enough to provide a better constraint, probably because of the geometric factor close to the detector. A better approximation of a point source would be advisable.

Conclusion. A non-linearity within the measured limits ($\approx$ 10 %) does not explain our observations.

6.1.2 Beam path

We have already mentioned (Section 3.12) that the better quality of the mechanics and of the alignment in Synapse II clearly improved the setup in terms of solidness and reproducibility of measurements. Realigning the bench and the measurements performed on the occasion, also allowed us to eliminate certain hypotheses that, if true, might have offered insights into our results:

- vignetting,
- mismatched and/or non-Gaussian beam profiles.

We verified whether there were any obstructions in the optical path in the visible with cameras, taking pictures of the beam, and in the infrared with pinhole scans (Fig. 6.1).

Conclusion. The measured beam profiles were consistent with the Gaussian spatial distribution. We thus verified that neither vignetting nor other beam profile mismatch is a factor in our setup.

6.1.3 Polarisation

Our colleagues in Nice (Weber 2004; Buisset 2007), as well as Bruno Chazelas (2007) studied the issue.

Bruno Chazelas (2007) concludes that if all the surfaces of Synapse are aligned with a tolerance of ±46 arcsec, the nulling ratio in the K band should be better than 10^{-6}. At the wavelength of 3.39 μm, the alignment tolerance necessary for $nl < 10^{-6}$ is slightly less stringent, viz., ±43 arcsec.

Conclusion. The improved alignment of Synapse II is within ±10 arcsec. The fact that nulling-ratio measurements in monochromatic light without polarisers were five times worse than with polarisers seems to indicate that the theoretical models do not account for the observed results.

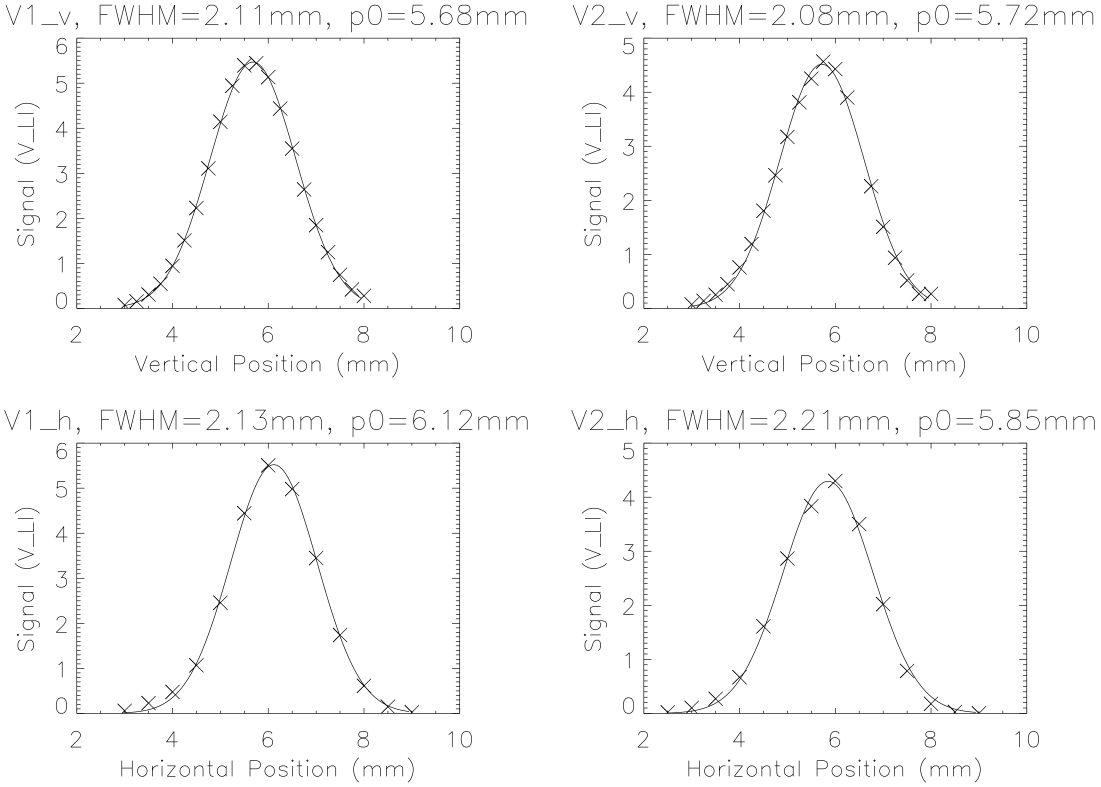
V1_v, FWHM=2.11mm, p0=5.68mm

V2_v, FWHM=2.08mm, p0=5.72mm

V1_h, FWHM=2.13mm, p0=6.12mm

V2_h, FWHM=2.21mm, p0=5.85mm

Figure 6.1 - Beam profiles obtained with pinhole (1.5 mm) scans in the infrared. The scans on the left represent beam 1, those on the right, beam 2. The scans on top were performed vertically, those on bottom, horizontally. Error of each point ≈ 0.2 %.

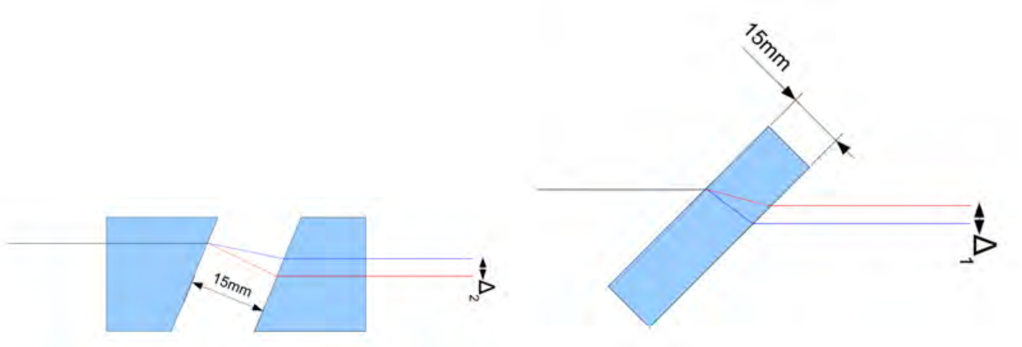

Figure 6.2 - Lateral dispersion due to CaF_2 Prisms (left) and beam splitters (dielectric plane parallel plates).

6.1.4 Chromatic shear and other dispersive effects

6.1.4.1 Chromatic shear

SYNAPSE uses two types of dielectric elements: (1) plane-parallel plates as beam splitters, and (2) prisms in the intrinsic compensator / achromatic phase shifter (Section 3.11). All of these dielectric elements are made of CaF_2. Chromatic shear introduced by their presence (Fig. 6.2) between the flux at $\lambda = 2.1\ \mu\text{m}$ and that at 2.4 μm is $\Delta_1 = 9.4\ \mu\text{m}$ in the case of the plane-parallel plates, and $\Delta_2 = 11.9\ \mu\text{m}$ in the case of the prisms (Laurent 2008). Overall, $\Delta = 2\Delta_1 - \Delta_2 = 6.9\ \mu\text{m}$

Each beam is, therefore, laterally dispersed. If the two are not perfectly superimposed, the flux coming from one interferometer branch and coupled with the output fibre differs chromatically from the coupled flux coming from the other branch, while maintaining an overal flux balance.

We measured the shear of the beams, and found it to be about 0.1 mm. In our calculations we will work with an upper limit of 0.5 mm.

We performed numerical simulation of the coupling. We disregarded the flux balance issue, supposing that imperfect coupling was compensated for by other effects, and thus did not influence flux balance. We thus supposed beam 1 perfectly injected but having less flux than beam 2. Our calculation used $I_1/I_2 = 0.95$. With this flux mismatch, the lateral dispersion of 6.9 μm, and beam shear of 0.5 mm, the nulling ratio should be 1.2×10^{-7}. Under these conditions for a nulling ratio to be 4×10^{-4}, the lateral dispersion would have to be at least 100-times greater than 6.9 μm.

6.1.4.2 Angular dispersion

Supposing that inner surfaces of the moving couple of CaF_2 Prisms are not perfectly parallel, there would be an angular dispersion between 2.1 and 2.4 μm which we estimated using a Zemax model of the setup. Since the alignment of beams is within 10 arcsec, we find that the maximum dispersion is 0.04 arcsec.

We can compare this value with the chromatic shear discussed above. On the one hand we can consider the ratio of the chromatic shear (6.9 μm) to the beam radius (2.51 mm),

$$\frac{6.9\ \mu\text{m}}{2.51\ \text{mm}} = 2.7 \times 10^{-3} \tag{6.1}$$

and on the other hand we can consider the 0.04 arcsec in relationship to the mirror's focal length $f = 13\ \text{mm}$ and the fibre's core radius $a = 4.1\ \mu\text{m}$

$$\frac{0.04 \times 5 \cdot 10^{-6}\ \text{rad} \times 13\ \text{mm}}{4.1\ \mu\text{m}} = 6.3 \times 10^{-4} \tag{6.2}$$

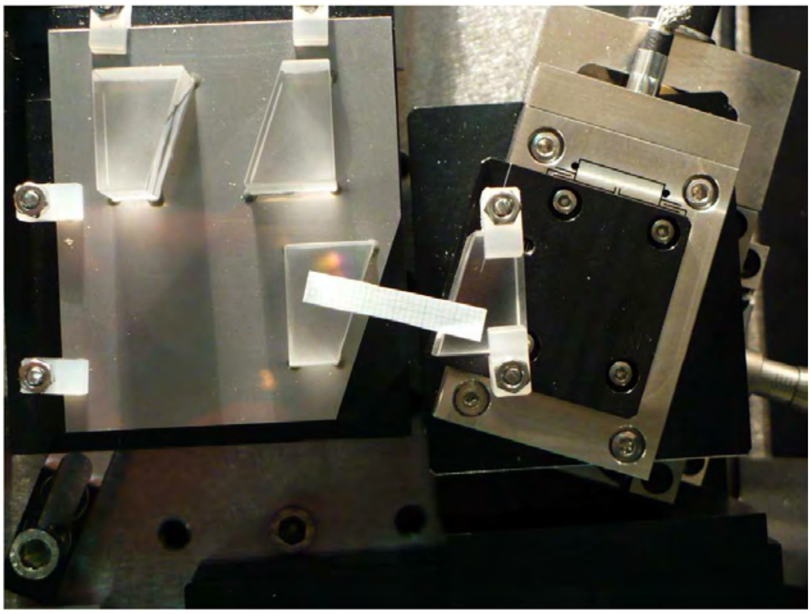

Figure 6.3 - Verification of the equality of air colums between the two pairs of CaF_2 Prisms. The fixed pair's separation is 15 mm.

Therefore, the angular dispersion is even less of a problem than the worst-case chromatic-shear scenario.

6.1.4.3 Unequal air columns in CaF_2 Prisms

Another possible chromatic effect arises from unequal air colums between the two pairs of CaF_2 Prisms. These values were verified to be equal to within 0.1 mm (Fig. 6.3). Calculations show that if the difference is 0.1 (worst case), then the expected nulling ratio should be

$$nl = 5 \times 10^{-6}, \tag{6.3}$$

again integrating between $\lambda_{\min} = 2.1\,\mu\text{m}$ and $\lambda_{\max} = 2.4\,\mu\text{m}$.

6.1.4.4 Off-axis parabola defects

Supposing that the two beams impact two distinct regions of the injection off-axis parabola in front of the output fibre, further supposing that in one of these regions the parabolic mirror would be perfect whereas the other one would have severe defects, the effects on two beams would be that they would become out of phase, and that their coupling with the output fibre would be unequal, i.e., there would be an intensity mismatch. The phase defect would not be an issue because it would be corrected by the delay lines. The flux mismatch, however, needs to be considered a little more closely.

In our worst-case-scenario model, the defects of the off-axis parabola are causing a flux mismatch which is fully compensated for by other means (e.g., knife edges). In our calculations we consider two monochromatic beams, one at 2.125 µm, and the other at 2.325 µm. We find that in order to limit $nl = 3 \times 10^{-4}$, the surface of the parabolas would have to be at $\lambda_v/5$ RMS or $\lambda_v/1.7$ PTV (if the relationship between RMS and PTV is as in the sinusoidal case). These numbers appear less than an order of magnitude greater than what we would expect from manufacturer's specifications. Let us look at the flux mismatch that would have to be compensated for by the aforementioned "other means". It turns out to be 36 %. This cannot be the case because there simply are no knife edges in the beam path.

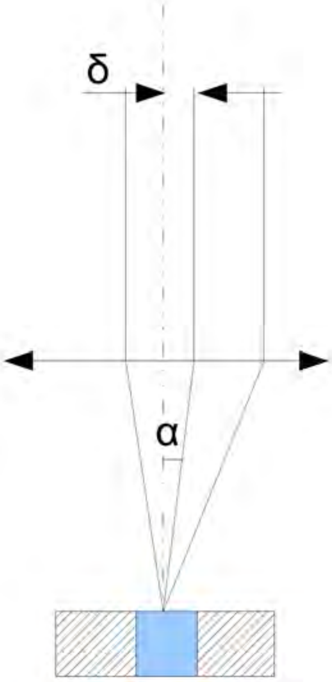

Figure 6.4 - Injection shear. The axis of the fibre intersects the Off-Axis Parabola (OAP; represented here as a convex lens) at a certain point. The axis of the beam intersects the OAP at a different point. The distance between these two points is the injection shear, δ. It corresponds to the angle $\alpha = \delta/r$, where $r = 2f/(1+\cos\theta)$, f being the focal length of the OAP, and θ its angle (Sec. 3.3.3).

6.1.4.5 Narrow passband filter

After careful study of the chromatic shear and other dispersive effects (which lasted a couple of months) we found that none of them can account for our observed K-band nulling ratio. What is more, we then discovered that we had a narrow passband interferometric filter (Sec. 3.6), centred around 2.3 μm and with a FWHM of only 16 nm. Reducing the passband from $\lambda/\Delta\lambda$ of 7.5 (the values we used in our calculations were 2.1 and 2.4 μm) to 150, i.e., by a factor of 20, typically reduces the expected chromatic effects by the same factor. As was reported in the previous Chapter (5.3.7), the measurements with the narrow passband filter yielded approximately the same nulling ratios as with the K band filter (3.4×10^{-4} and 4×10^{-4} respectively).

Conclusion. These chromatic effects do not explain the measured nulling ratios. SYNAPSE is not limited by the chromatic shear, and other considered dispersive phenomena.

6.1.5 CaF$_2$ Prisms: multiple working points

When searching for the working point of SYNAPSE, there are two parameters that need to be tuned: the differential thickness *e* of the dielectric represented our CaF$_2$ Prisms, and the optical-path difference OPD realised by our delay lines (Sec. 2.4). It could be that we did not choose the optimal working point in this two-dimensional parameter space. OPD scans may show similar fringe patterns corresponding to phase shifts of $(2n-1)\pi$, but the optimal (in terms of providing the best nulling performance) working position is unique. With a degraded null it is possible to mistake *a* working point for *the* working point.

We verified this by a series of measurements shown in Fig. 6.6, examining nulling ratios at working

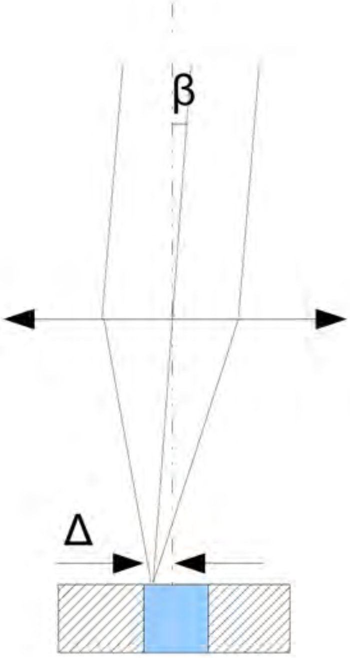

Figure 6.5 **-** Injection tip/tilt. The proper mode of the fibre is collimated by the Off-Axis Parabola (OAP; represented here as a convex lens). The axis of this putative collimated beam is shown by the dotted line. It is at an angle β to the incident beam. This means that the beam does not impact the fibrehead at its centre but at a point which is at the distance Δ from the centre of the fibre.

points ranging from -11π to $+11\pi$.

Conclusion. We verfied that the interferometer was at the optimal working point in the two-dimensional space defined by the parameters of OPD and differential dielectric thickness.

6.1.6 Coatings

SYNAPSE beam splitters bare coatings (Sec. 3.11). If these coatings were unequal, there could be a chromatic difference between the two arms of the interferometer.

Using McLeod software, we simulated a 10 % difference in the thickness of our coatings, and obtained

$$nl < 10^{-6} \tag{6.4}$$

Conclusion. Simulations suggest that differences in thickness between beam splitters cannot limit the testbed's nulling ability to the observed degree.

6.1.7 Inhomogeneities

Similarly, the dielectric substrate of the beam splitters and of the prisms was checked interferometrically for inhomogeneities by our optics supplier when they started working with it. The material was homogeneous to a degree which would enable us to measure

$$nl < 10^{-6} \tag{6.5}$$

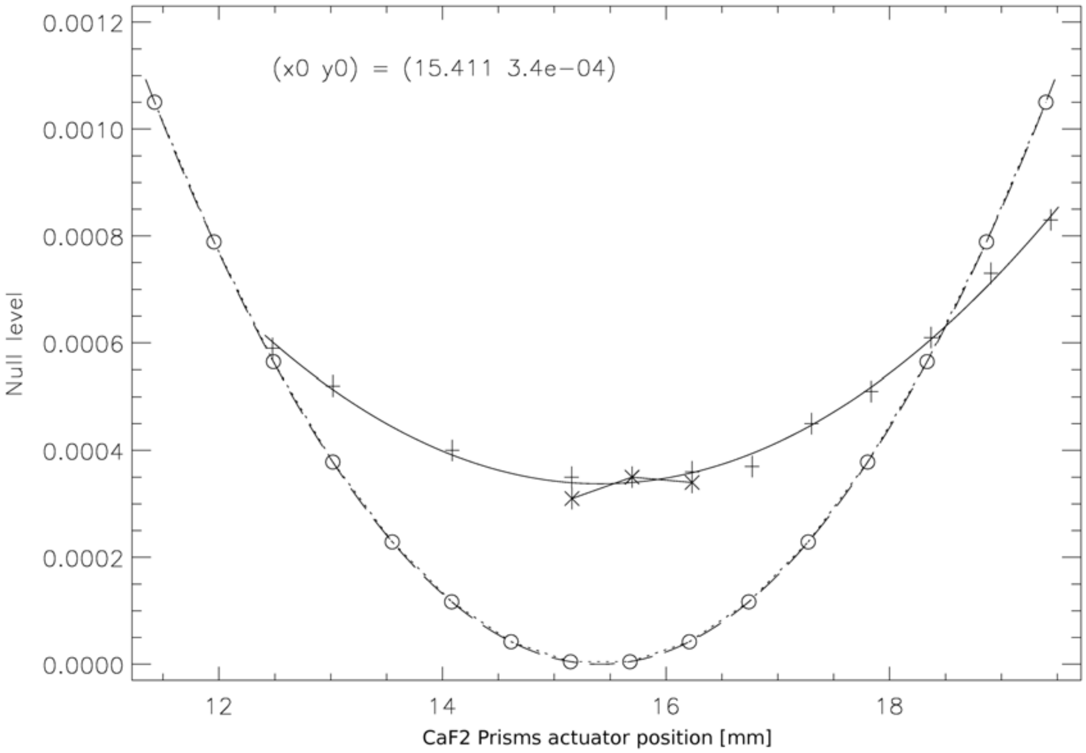

***Figure 6.6* -** Nulling measurement at different CaF$_2$ working points. Crosses represent a series of measurements, ranging from -11π to $+11\pi$. Stars are another series of measurements, the difference between the first and second series being an indicator of the measurement's uncertainty. The full line is an parabolic fit of the data (first series of measurements only). The circles and the dotted line represent the theoretical model.

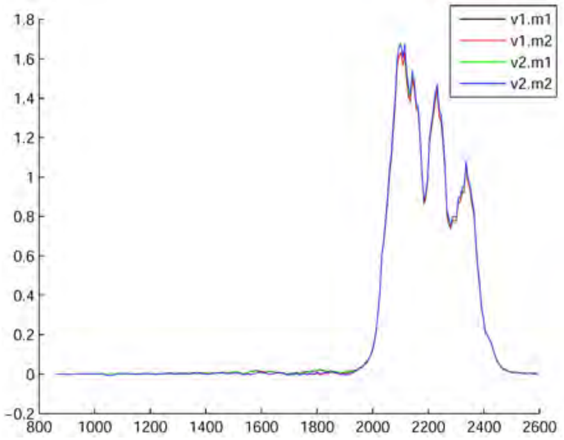

Figure 6.7 - Verification of the spectral mismatch between the two beams. Two measurements per beam were made. "v1" and "v2" designate the two beams. (Intensity in arbitrary units vs. wavelength in nm.)

Conclusion. The homogeneity of the CaF_2 used in our optics should allow Synapse to reach nulling levels that we have not observed.

6.1.8 Spectral mismatch

If the two beams were not perfectly matched spectrally, the nulling ratio would suffer. Therefore, we performed a series of spectral measurements of the light emitted at the exit of the output fibre. The spectrometer had 256 channels between 858.68 and 2595.46 nm. It operated at -10 °C (with a Pelletier system). We measured each beam twice. Each of the four measurements comprised 50 scans, each scan being an average of 10 integration periods of 10 ms.

The results are presented in Fig. 6.7. The differences between the two beams are of the same order as the differences between the individual measurements of each beam. This is consistent with the hypothesis that the observed differences between the two beams are due to measurement noise.

We calculated the nulling ratio corresponding to the situation when the observed spectral differences would be only due to real spectral mismatch between the two beams (worst-case scenario). Our estimate is

$$nl = 3.8 \times 10^{-5}. \tag{6.6}$$

Conclusion. Even if the measured spectral variations were dominated by a real spectral mismatch between the two arms of the interferometer, the corresponding nulling ratios are an order of magnitude better than the observed values in the K band.

6.1.9 Wavefront quality

We recalled the importance of wavefront quality in nulling interferometry, and the influence of modal filtering with single-mode fibres (Section 2.5). As reported in Sections 5.3.8 and 5.3.9 we performed some experiments aimed at improving secondary-mode rejection. They were performed with relatively low levels of flux, and their results cannot be regarded as fully reliable. They do, nonetheless, seem to indicate that more study is needed on the performance of our SMFs.

The last experiments performed on Synapse II (July 2008) before we concentrated on Nulltimate aimed at determining the quality of the injection into the fibres.

Since we could not easily examine the output fibre, we decided to perform a series of experiments on the input fibre. In the previous experiments, the 3.39 μm-laser beam was focused on the fibrehead with an OAP ($f = 13$ mm, $\alpha = 35°$), whereas the supercontinuum source used a dedicated setup to couple its photonic-crystal fibre with the testbed's input SMF. For the new experiments we modified our injection system in the case of the supercontinuum source. With another OAP, we generated a collimated beam which we then injected into the testbed's input SMF via the same OAP that the laser used. Now, both sources were injected into the testbed's input fibre via the same OAP ($f = 13$ mm, $\alpha = 35°$). We performed nulling measurements with both sources, obtaining

$$nl = 10^{-5} \quad \text{with } 3.39\ \mu\text{m laser}, \tag{6.7}$$

$$nl = 4 \times 10^{-4} \quad \text{with supercontinuum.} \tag{6.8}$$

We also performed scans of the optical field at the injection point by translating the fibrehead vertically. We found roughly Gaussian distributions with

$$\text{FWHM} = 37\ \mu\text{m} \quad \text{with } 3.39\ \mu\text{m laser}, \tag{6.9}$$

$$\text{FWHM} = 12\ \mu\text{m} \quad \text{with supercontinuum.} \tag{6.10}$$

This result was unexpected. We hoped to find the exact opposite. In that case we would have concluded that indeed there is a problem with cladding modes in the case of the supercontinuum source. What we found did not allow us to draw any conclusions. Does the FWHM = 37 μm in the case of the laser mean that we are injecting some flux in the cladding? It is possible that it does not limit the nulling ratio because the laser beam is monochromatic and highly coherent. On the other hand, the supercontinuum beam also should be coherent, and while its FWHM is three times smaller, it is still about twice as large as the SMF's acceptance lobe.

Once again we realised that we faced a dilemma: Either perform careful diagnostics on our equipment, or procede without delay towards our objectives (in this case APS prototype testing, and the commissioning of NULLTIMATE). We opted for the latter, hoping that NULLTIMATE will either provide a good nulling performance, or allow us to conduct better tests, mainly thanks to the higher level of flux.

6.2 Testing on NULLTIMATE

As we have concluded in the previous Section (6.1.9), we chose to abandon the tests on SYNAPSE and concentrate on NULLTIMATE. We have worked hard to achieve very high levels of flux with NULLTIMATE, and the preliminary measurements seem to indicate that we will be able to work with fluxes that were beyond our reach with SYNAPSE (perhaps by a factor 10^3). This is important because some of the experiments we are planning to perform are impossible without good flux. The planned experiments include:

- **Monochromatic and narrow passband**: compare high signal-to-noise (SNR) nulling ratios obtained with the 2.32 μm laser diode and with the 16 nm FWHM narrow passband filter;
- 2.32 μm **and** 3.39 μm **laser sources**: compare high SNR nulling ratios obtained with two truly monochromatic sources, emitting at different wavelengths, both within the SMF's interval between its cutoff wavelength λ_{co} and $2\lambda_{\text{co}}$;
- **Polarisation**: perform high SNR nulling experiments in polarised light, i.e., obtain a reproducible nulling ratio with the s and p polarisations (as defined by the 45° incidence on most of our optics).

6.3 Error budget

Following Serabyn (2000), it has become customary to list the contributors that degrade the null (Buisset et al. 2007; Gappinger et al. 2009) in an overview, summing the individual terms. We shall endeavour to provide a similar error budget in Table 6.1, bringing together the elements already discussed in the previous pages.

Parameter	Null Allocation	
	K band	Laser 3.39 μm
Intensity mismatch $(\Delta I/I)^2/16 = 0.5$ %	1.6×10^{-6}	1.6×10^{-6}
Spectral intensity mismatch	3.8×10^{-5}	0
Path length control	1.5×10^{-5}	5×10^{-7}
Dielectric thickness mismatch	1×10^{-6}	0
Pupil rotation	1×10^{-9}	1×10^{-9}
Broadband source size (SMF, i.e., point source)	0	0
Sum total (single polarisation)	5.6×10^{-5}	2×10^{-6}
Polarisation phase delay	4.8×10^{-5}	4.8×10^{-5}
Sum total (both polarisations)	1×10^{-4}	5×10^{-5}

Table 6.1 - Broadband error budget considering perfect single-mode fibres.

Our Table closely follows that presented by Gappinger et al. (2009). The first line refers to the intensity mismatch, giving the typical value achieved during our measurements.

The second line completes, in the broadband case, the information provided in the first line of the Table where we consider the flux integrated over the whole spectral band, which means that a chromatic intensity mismatch may be hidden by the flux-balancing procedure. Earlier in this Chapter, we discussed a number of possible causes of such an effect. Section 6.1.4 contains several estimates obtained from measurements of the quality of beam superposition and other alignment tolerances. The value included in the second line is based on the very conservative estimate obtained in Section 6.1.8 as a result of direct measurements of the spectra of our two beams.

The third line reproduces the results discussed in Chapter 4, viz., Eqs. 4.19 and 4.19. These values represent the “scalable” results for $\sigma_{\langle nl \rangle}$.

The fourth line concerns the dielectric thickness mismatch, which is applicable only to the broadband case. As we have seen, the chromatism compensator is designed to deal with the issue of the possible unequal thickness of CaF_2 elements in the setup. We verified its setting (Sec. 6.1.5), deducing that differential CaF_2 thickness is not a limiting factor. Another possible source of dielectric thickness mismatch are the coatings. We have seen (Sec. 6.1.6) that a conservative estimate of such a mismatch represents a cotribution of 1×10^{-6} to the error budget.

The fifth line of the Table is only included because it is present in our Table’s model (Gappinger et al. 2009). Differential pupil rotation of α_{rot} represents a null allocation of $(\alpha_{\mathrm{rot}})^2/4$. Considering 10 arc sec as a conservative estimate of the misalignment of Synapse II (Sec. 6.1.3), we obtain:

$$\frac{(\alpha_{\mathrm{rot}})^2}{4} \approx 1 \times 10^{-9} \tag{6.11}$$

The sixth line is also included merely for the sake of completeness. The contribution due to source size is zero by definition because we are working with collimated beams.

The Table provided by Gappinger et al. (2009) contains also an estimate of the null allocation due to polarisation phase delay. Gappinger et al. (2009) reports a measurement of phase delay between the s and p polarisations represented by a dark fringe position shift. The bottom part of our Table presents an estimate of such a contribution to the error budget. We know (Table 5.2) that during our experiments with the 3.39 μm laser, introducing polarisers led to a considerable improvement of the null depth, viz., from a level of 5×10^{-5} without the polarisers to 1×10^{-5} with polarisers. From this, and from the estimates of the quality of the alignment of Synapse II, we can deduce that 5×10^{-5} corresponds to the sum total of terms limiting the null depth. If 5×10^{-5} is the sum total and 3×10^{-6} is an estimate of the sum of all other contributions, then the polarisation phase delay term can be estimated as $5 \times 10^{-5} - 3 \times 10^{-6} = 4.7 \times 10^{-5}$. This value also contributes in the broadband case. We can also use it to derive the amplitude of the polarisation phase delay $\Delta\Phi_{s-p}$. If $(\Delta\Phi_{s-p})^2/4 = 4.7 \times 10^{-5}$, then $\Delta\Phi_{s-p} = 1.4 \times 10^{-2}$ rad, and $\mathrm{OPD}_{s-p} = 5$ nm.

A similar reasoning can lead us to an estimate of the contribution of the single-mode fibres to the error budget. If we consider the broadband null depth of 3×10^{-4} (with polarisers), and the estimated sum total of all other contributions to the error budget which we find to be 5.6×10^{-5} in the K band (with polarisers), we can deduce that the single-mode fibres contribute 2.4×10^{-4} to the error budget in the K band (with polarisers). This would mean that they reject incoherent light at a ratio of 4000:1.

6.4 Summary

We examined a large spectrum of phenomena that could affect SYNAPSE's broadband nulling performance. Theoretical models preclude a certain number of them from being considered as the possible cause. Others were eliminated by experimental results (e.g., $nl = 3.4 \times 10^{-4}$ with the 16 nm FWHM passband filter). We decided to suspend this effort, and concentrate our forces on the preparation of a new experimental setup, the NULLTIMATE testbed.

Chapter 7

Conclusions and perspectives

Contents

We shall first recall the goals of our team's work, we shall present a brief summary of what was achieved, enumerating my personal contributions, then we shall indicate some of the future work, and finally we shall situate our endeavours in the context of the preparation of a spaceborne nulling interferometer like the *Darwin*/TPF-I space mission.

7.1 What was to be done

In the Preface we outlined the science goals of our work, listing four points:

- stabilising the SYNAPSE tested,
- improving the performance of the SYNAPSE testbed,
- building the NULLTIMATE testbed as its successor,
- testing the achromatic phase shifter prototypes.

Let us recall that by the end of its commissioning, in late 2005, it was clear that the SYNAPSE testbed was suffering from drifts and that its performance in terms of the nulling ratio was limited to a level which was a factor 300 less than the designed value. The drifts made it difficult to perform reliable diagnostics on the testbed, and therefore the first order of business was to find an efficient way of conducting reproducible measurements.

The second goal was then to see what could be done to improve the performance and bring it up to the expected levels, identifying the causes of the unexpectedly large broadband nulling ratio.

The third goal was to build another testbed, NULLTIMATE. The original purpose of the project was similar to that of the SYNAPSE testbed, viz., achromatic phase shifter prototype testing. Unlike SYNAPSE, the new bench was to be cryogenic and, ideally, work in the band 6–18 μm. By the time I joined the team at the *Institut d'Astrophysique Spatiale* it was clear that NULLTIMATE could be cryogenic only if we understood why there was a problem with SYNAPSE.

The fourth goal, often presented (to the funding agencies) as the only one, was to test the prototypes of achromatic phase shifters constructed by our colleagues in Nice, Cannes, Heidelberg, and Liège. By the end of my first year, the latter (Liège) was dropped, and its testing was to be done elsewhere.

7.2 What was done

The first goal was achieved quite satisfactorily by implementing an optical-path difference stabilisation algorithm (OPD dithering; Chap. 4). In addition to it being an interesting technique that may prove useful even in the context of a space mission, it is thanks to this system that we were able to conduct reproducible measurements of SYNAPSE's nulling performance.

We found that the 3×10^{-4} nulling ratio minimum was not due to OPD drifts. In order to study the origin of this limit we tested the stability of SYNAPSE with the 3.39 μm laser, finding a surprising improvement of the nulling performance especially once we started working with polarised light. This indicated that the testbed was poorly aligned. We decided to undertake a major overhaul of the mechanics and a new alignment of the testbed. New electronics were installed and new software was developed. The improved testbed, SYNAPSE II, aimed at the second goal listed above. The new setup did not solve the problem of the 3×10^{-4} nulling levels broadband, and a series of tests were performed in order to identify the limiting factor.

In August 2008, the effort was put on standby and we concentrated on the NULLTIMATE testbed. It was designed in the period of several months, spanning Winter, Spring, and early Summer 2008. NULLTIMATE was built, aligned and its preliminary tests started in November 2008, leading to some design modifications (installing polarisers; building a new coupling device in order to switch between sources more readily). The commissioning of the definitive design began in August 2009. It may be said that the third goal was reached. A discussion of NULLTIMATE's future is included in the next Section.

The fourth goal remains to be reached. The prototype that we tested so far was the Focus Crossing, and we concluded that it did not limit the performance of the testbed at the level at which it operates so far. More tests are to be conducted in the future (cf. next Section).

7.2.1 My contribution

As I stressed in the Preface, the work was that of a team, the discussions and decisions were those of a team. In a dissertation such as this, it is important nonetheless to indicate what was the student's own contribution. One indicator of the way I was integrated in our team is that I wrote up the three papers (App. E) reporting on our activities. The following list suggests the areas where I was the most useful. Let me say once again that none of these points was an individual effort.

- I developed the OPD dithering algorithm, performed stability measurements of several hours with the black-body source as well as with the 3.39 μm laser both on SYNAPSE I and SYNAPSE II.

- I coupled the 1.15/3.39 μm laser to the input fibre, developing the mechanics and an injection procedure observing the laser's beam emitted at 1.15 μm with an infrared visor.

- I implemented a technique of intensity balancing by positioning of the exit fibre and exploiting the residual imperfections in beam alignment.

- I contributed to the conception, realisation and alignment of SYNAPSE II, performing most of its commissioning.
- I wrote most of the software for SYNAPSE II.
- I carried out a considerable number of the tests described in Chapters 5 and 6.
- I contributed some ideas to the optical design of the NULLTIMATE testbed (arguing for a simple Mach-Zehnder, i.e., a design minimising the number of optical elements; arguing against optical coatings; motorising the delay lines).
- I designed, realised and programmed NULLTIMATE's driving and data acquisition system (essentially upgrading the system implemented on SYNAPSE II).

7.3 Perspectives

7.3.1 NULLTIMATE

In the last months, our work has been concentrating on the installation of the new testbed, NULLTIMATE. As the photographs in Figs. 3.4 and 3.8 show, all of the elements are now in place. The optics have been aligned, and large flux levels were reached. The work under way can be called debugging.

In the months to come, the basic operational parameters (detector calibration, transmission, flux stability) will be measured and the first nulling results (nulling ratio and its stability) will be obtained with the Focus Crossing (also called Through Focus) Achromatic Phase Shifter prototype (Section 3.9.1).

NULLTIMATE being of simpler layout, using more stable mechanics, and having better transmission than SYNAPSE, it was designed to provide some answers to our questions (Section 6.2). Working with the new setup, especially during the alignment, makes us believe that it indeed *is* mechanically more stable. The first tests indicate that it provides a much higher luminous flux than SYNAPSE. We feel, therefore, that the new testbed will live up to our expectations.

We hope that within the next year or two, we will be able to obtain some results and share them with the scientific community. The following Sections provide a brief enumeration of experiments that are scheduled to be performed on the NULLTIMATE testbed, and which are likely to be of general interest to those who work in nulling interferometry.

7.3.2 Polarisation

If NULLTIMATE is as stable as we hope, and if there is sufficient flux, nulling measurements can be performed in linearly polarised light not only oriented parallel to the testbeds polarisation plane of maximum transmission but also perpendicular to it. Such an experiment could be the first direct demonstration, in the context of nulling interferometry, of the difference in optical path length between the two polarisations. As we have seen (Section 6.1.3), theoretical models (e.g., Chazelas 2007) do not seem to account for all of the observed phenomena. A better understanding of the rôle that polarisation states play in nulling interferometry is a necessary part of basic research in this field.

7.3.3 Tests of achromatic phase shifters

The best tests of achromatic phase shifters to date were recently performed at the Jet Propulsion Laboratory (Gappinger et al. 2009). We are confident that NULLTIMATE will provide more conclusive results especially because we will be using better quality prototypes (Section 2.3). NULLTIMATE is being set up with the Focus Crossing (also called Through Focus) Achromatic Phase Shifter prototype (Section 3.9.1) and is ready for the installation of a Field Reversal (Periscope) APS prototype (Section 3.9.2), both of which are single block designs and therefore likely to provide more reproducible and conclusive results than the tests mentioned above.

7.3.4 Flux-balance stabilisation

The optical path difference stabilisation system successfully tested on Synapse will be also implemented on Nulltimate. In addition, Nulltimate will eventually have an analogous system (employing dithering; cf. Section 3.3.5) controlling flux balance. Thus, Nulltimate may directly demonstrate that nulling ratio stability can reach the levels required in the future *Darwin*/TPF-I space mission, viz., $\sigma_{\langle nl \rangle}(10\,\mathrm{days}) < 3 \times 10^{-9}$ at the nulling ratio of $\langle nl \rangle \approx 10^{-5}$.

7.3.5 Experiments around 10 μm

If the transmission of single-mode optical fibres at $\lambda = 10\,\mu\mathrm{m}$ continues to increase (cf. Section 3.5), Nulltimate will be able to operate with powerful laser sources at $\lambda = 8.9$ and $10.6\,\mu\mathrm{m}$. Work with these sources will provide a possibility to validate the modal-filtering qualities of the fibres, as well as marking a passage to the *Darwin*/TPF-I waveband. Using either of the two laser sources could lead to interesting results on stabilisation, and using both in conjunction may provide a means of testing the phase shifter prototypes.

7.4 Towards a flagship space mission

This is perhaps the best point at which to consider our work in the context of preparation for the *Darwin*/TPF-I space mission. It is clear to us that a flagship space mission with the purpose of searching for spectroscopic biosignatures will be launched eventually. So far, it seems very likely that it will be an infrared formation-flying nulling interferometer. Let us reiterate the objectives that need to be successfully reached before such an ambitious space mission can be considered feasible. It has to be said that there are three fields to be investigated, and each one of them is a major technological challenge:

- Cryogenics/cooling of optics and detectors: work carried out in the context of other projects (Herschel/Planck, James Webb Space Telescope, etc.);
- Formation flying to within ≈ 10 cm: laboratory demonstrator experiments (Formation Control Testbed at the JPL), space precursors (Prisma, Proba-3), including work carried out in the context of other missions (Simbol-X, Lisa);
- The payload, i.e., the nulling interferometer itself.

While the former two are important, it is the latter one which is truly critical because it is specific to this mission. If laboratory tests demonstrate conclusively that a nulling interferometer can be built to the *Darwin*/TPF-I specifications, then the increased motivation for development in the former two fields will surely lead to effective solutions.

Such payload demonstrator experiments need to be conducted on several fronts:

- Modal filters operating in the waveband of 6–20 μm, with a throughput of 50% or better and with a 25 dB modal suppression of non-fundamental modes (Lawson et al. 2008);
- Achromatic nulling in the waveband of 6–20 μm with the nulling ratio of $\langle nl \rangle < 10^{-5}$ and stability of $\sigma_{\langle nl \rangle}(10\,\mathrm{days}) < 3 \times 10^{-9}$;
- Four-beam nulling and planet detection with internal modulation (also called phase chopping) and spectral filtering, i.e., simulation of a star and of a planet (with a realistic contrast) and the detection of the simulated planet.

Let us stress that work in preparation for other projects based on nulling interferometry (designed for the Large Binocular Telescope, or considered for installation in Antarctica; or the space mission proposals FKSI and PEGASE) does not need to reach *Darwin*/TPF-I specifications, and therefore is unlikely to do so. We believe that the only way to demonstrate the feasibility of *Darwin*/TPF-I is to conduct a dedicated experimental programme.

Important milestones have already been achieved but more work needs to be done. The approach we adopted in the SYNAPSE, and NULLTIMATE testbeds is to first master nulling in the K band (2.0–2.5 μm) and only then go on to the mid-infrared. The reasons for this are twofold:

- Single-mode spatial filters are not available for the mid-infrared so far, at least not for the whole waveband of 6–20 μm, and not with a satisfactory transmission (this issue is linked to the problem of sufficiently bright broadband sources);
- Work in the K band is, in principle, more challenging as to wavefront quality, stability, etc., because wavelengths are about four times shorter, and perturbations are inversely proportional to wavelength; and so it can be said that if *Darwin*/TPF-I performance levels (in terms of nulling ratio and its stability) are reached in the K band, once single-mode spatial filters are available for the mid-infrared, transposition of the results from the K band to longer wavelength will be easier.

It would seem that development of a future formation-flying nulling interferometry mission is not at its highpoint at the moment. In this context, apart from its scientific merit, our work on stabilisation and the preparation of the NULLTIMATE testbed has acquired an additional dimension. It has become a contribution to the much-needed continuity of research in this field: without continuity, know-how is often lost.

7.5 Summary

Three years ago we set out with the four goals in mind: stabilise SYNAPSE, improve its performance, build NULLTIMATE, and perform tests of achromatic phase shifter prototypes. We implemented an improved method of optical path difference (OPD) stabilisation based on the science beam itself, dithering around the delay-line position corresponding to the deepest null (Section 4.3). We were able to demonstrate its efficiency and share the results with the scientific community (Gabor et al. 2008a,b).

We overhauled the testbed creating SYNAPSE II. Working on the SYNAPSE II testbed we gained some understanding of the factors limiting its performance (Gabor et al. 2008c) and, in order to overcome them, we built a new testbed, NULLTIMATE. This promising experimental setup is likely to produce interesting results in the years to come.

If we were to summarise what we learnt in terms of a message regarding the future formation-flying nulling interferometer observatory, we would stress that both external (metrology with dedicated auxiliary beams) and internal (working with the science beams) stabilisation systems should be implemented.

Appendices

Appendix A

Cosmic Pluralism

One of the few constants in the life of generations of human beings, maybe even before the dawn of our own biological species of Homo sapiens, was the fact that there are stars overhead. For millenia this sight filled people's hearts with wonder and I am sure it must have been very long ago that someone, maybe a child, asked the Question: "Are we alone in this vast Universe or do the stars tell us of distant worlds where there are other beings like ourselves?" For generations countless minds who pondered this issue found no path to a real answer. We are privileged to live in a time when a new avenue of promise is opening before our eyes.

A.1 Millennia of speculation

Steven J. Dick (1996) has stressed the intimate connection between cosmological views in the broadest sense of the word and attitudes toward extraterrestrial life. Indeed, our Question is the point where philosophical cosmology meets philosophical anthropology. What is at stake is one of the very basic issues of human reflection: "Who am I?" The (possible) existence of many inhabited worlds in the Universe is unseparable from the issue of our place in the world, and hence of our own identity.

"Are we alone?", the question of cosmic pluralism, touches upon some of the fundamental issues regarding our view of the world and of our place in it. It has been around for millennia. Who was the first author on record to reflect upon it? Simplicius of Cilicia (c. 490 – 560 A.D.) claims (Fragment Phys. opin. 4, 7) that it entered the historical scene in connection with the Greek philosopher Anaximander (c. 610 – 546 B.C.). This claim remains somewhat isolated (Kahn 1960). We should also note that even if Anaximander was the one who introduced the question, he was more likely to have taken up a position against cosmic pluralism.

In any case, whoever among the pre-Socratic philosophers opened the debate, the important and lasting influence must be attributed to the atomists, Leucippus (first half of the 5th century B.C.) and Democritus of Abdera (c. 460 – 370 B.C.), and especially to the Epicureans who adopted their cosmological heritage and developed it until the end of Antiquity.

A.2 Links and implications

If we were to indulge in a serious discussion of cosmic pluralism we would also have to reflect upon its links to other problems of philosophical cosmology with significant implications. This is not our present purpose, however. We shall, nonetheless, at least give an overview of these avenues of inquiry.

Cosmic pluralism is closely linked with the question of whether we are exceptional or banal. This issue is often discussed as the Anthropic Principle or the Principle of Mediocrity, and seems to lead to intriguing paradoxes. Our study of the Universe is based on the assumption that our own region of it, including the laws of physics that we can study in laboratory here on Earth, is typical of the whole. This would seem to imply that the emergence of life would occur wherever there are favourable conditions. Since the Mediocrity Principle (sometimes also called the Copernican or the Cosmological Principle) logically views the Earth as a banal planet orbiting an unexceptional star, should we not have already observed signals produced by extraterrestrial civilisations? Or indeed, if we consider the temporal version of the Mediocrity Principle, the so called Doomsday Argument, should we not have long ago been contacted by civilisations more advanced than ours? This paradox is often refered to as the Fermi Paradox.

Another interesting avenue of inquiry would be epistemological. As we have noted at the very beginning, we are singularly placed to witness, in the case of the cosmic pluralism issue, the transition from millennia of pure speculation to development of quantifiable observational and experimental approaches. I believe it is legitimate to regard this transition as an instance of the long-term programme of mathematised science. The effort of generations of researchers painstakingly, but always with quantifiable knowledge of its own limitations, strives for a “natural philosophy”[1].

All these questions are interconnected and they have profound philosophical and even theological implications. As we have said, this is not the place to discuss them. It is noteworthy, however, that we have often observed yet another paradox in this context, namely that for many professional philosophers and theologians the topic seems to be of little interest; an attitude in complete contrast to that of the general public.

A.3 Historical notes

Cosmic pluralism has a long history, as we have already seen. Recently, it has become subject of several enlightening studies. Let us just mention the informal trilogy by Dick and Crowe (Dick 1984; Crowe 1999; Dick 1996), which may be considered as *the* reference of the day.

A.3.1 Three forms of cosmic pluralism

Let us first note that, historically, the cosmic pluralism had at least three different forms. The term “cosmic pluralism” itself can be understood as implying either the belief that (A) there are many “cosmoses” (whatever is meant by a “cosmos” in this context), or that (B) there are many inhabited worlds in the one universe we know.

The list of the three forms described below is not a systematic classification with a well-defined discriminating criterion. Rather, it gives an overview of the main forms of cosmic pluralism that we encounter in the history of western thought.

1. In the oldest version of cosmic pluralism, as represented, e.g., by Epicurus (341–270 B.C.) and his followers, a “cosmos” is a separate whole with its own Earth, “planets” (including some very bright ones, e.g., the Sun or the Moon) and a starlit firmament.
2. The second version, attributable to Nicolas of Cusa (1401–1464), considers the Earth as a “star”, i.e., a celestial body. Consequently, it is claimed that all “stars” are habitable worlds like the Earth, be it the “wandering stars”, i.e., planets within the Solar system, or the “fixed stars”. Cusanus himself, and most of his followers, e.g., Johannes Kepler, maintained that these worlds not only can be inhabited, but that they indeed *are* inhabited by intelligent creatures, which were more often than not considered more noble than Earthlings.
3. The third version, which may be due to Giordano Bruno (1548–1600), differs from the previous variant only in one point. Whereas Cusanus claimed that the Earth was a celestial object, the next

---

[1] Here we use the term “natural philosophy” in the strong sense, designating a philosophy based on mathematical reflection of nature. A captivating recent study of the subject was published by Gaukroger (2006).

> step was to propose that the “fixed stars” were like our Sun. Since the Sun is clearly giving light and heat to the planets in its vicinity, it can also be imagined that each of the “fixed stars” is similarly the source of radiation for a set of planets analogous to our own planetary system. The novelty of this variant of cosmic pluralism was the claim that there are other planets forming planetary systems beyond our own.

It is indeed intriguing that all three of these philosophical positions have a well-defined and even well-argued counterpart in contemporary science.

Epicurean or multiple-universe cosmic pluralism. Regarding the first one, the Epicurean variant of cosmic pluralism, it is clear that the operative notion of the universe in the original form of this hypothesis was very limited in comparison to our own Standard Model of cosmology. It is equally clear, however, that the Epicurean cosmic pluralism is akin to the contemporary theory of multiple universes because it understands cosmic pluralism as the belief in multiple wholes that have to be considered as sister entities which are not directly observable.

We shall, therefore, tend to refer to it as to the Multiple Universe Hypothesis. Let us note that in the current debate on fundamental physics, it is often invoked as an answer to the enigmatic Anthropic Principle (let us evoke Susskind’s recent Cosmic Landscape hypothesis; Susskind 2006).

The leading professional historian studying the extraterrestrial life debate, Michael J. Crowe, reminds us, however, that

> the basis of Epicurean pluralism lay not in direct observation but in the metaphysical materialism and atomism of its philosophy. Other worlds must exist because some of the chance conglomerations of infinite atoms in an infinite universe must form worlds, all things being possible. (Crowe 1999)

Such an infinity of universes, however awe-inspiring, does not provide the least hope of communication or travel among the inimaginably vast expanses of space. Although we would not be alone in the strict sense, our existence would nonetheless be lonely.

Cusanus’ plurality of inhabited worlds within our Universe. This view is still very much present not only in popular thought (albeit with the extraterrestrials of superior intellect to our own being often perceived as a threat), but also in the scientific mind as the motivating principle for such endeavours as the search for life on Mars. Historically, Cusanus did not propose any hypothetical bodies beyond those known from Antiquity, and that is why we shall regard his version of cosmic pluralism as the inspiration for Solar system exploration.

Bruno’s cosmic pluralism. The extension of cosmic pluralism to other planetary systems than our own has become a guiding principle of empirical research in two ways. Firstly, it brought us the SETI (Search for ExtraTerrestrial Intelligence) programme in radioastronomical observation and signal analysis. And secondly, scarcely two decades ago, the field of exoplanetology became a reality. The first planets orbiting a star similar to our Sun were detected in 1995, and as of June 2009, the hunt for exoplanets has brought to light the existence of about 350 objects.

The latter two versions of cosmic pluralism, Cusanus’ and Bruno’s, both lead to a clear answer as to our question of whether we are alone in the Universe: No, we are not alone. There is a difference, however. Whereas the second hypothesis places our cosmic cousins well within the reach of man-made probes even in our pioneering age, the third position leaves open a broad range of possibilities regarding the distance to the nearest inhabited world. Our closest neighbours may be orbiting some of the closest stars, i.e., only several light-years away, or perhaps not even in our own Galaxy. Because of the great intergalactic distances (the Andromeda Galaxy, M31, is approximately 2.5 million light-years away) two-way communication would be impossible unless the light-speed barrier can be overcome.

A.4 Ideology and historiography

The story of western science has long served as an example to support various progressist, positivist, anti-clerical, and generally ideological agendas. Perhaps the most inspiring author who pointed out the ideologisation of the historiography of science was Polanyi (1958). He was more concerned with a representation of important developments in modern science where fidelity to the actual historical evidence was very often sacrificed on the altar of a particular view of what "should have happened" if the scientists followed the established theory of scientific discovery.

A.4.1 "Pre-Socratic light"

There were worse excesses, however, regarding older history. The second half of the 19th century produced a positivist view of history where humankind progressed from explanations of phenomena in terms of myths to metaphysical and finally to scientific explanations. In this context, scientific advances were considered as symptoms of humanity's progress, moving inexorably from darkness to light. It is from this period, comparatively recent, that we have inherited such "wonders" as the idea that the Middle Ages believed that the Earth was flat and that Columbus had to prove its sphericity. Such a proposition is so preposterous that I find it disturbing that certain academic circles at the time could traffick such blatant fabrications without any concern for truth, undoubtedly believing that "anything goes" when it comes to supporting the "true" representation of reality as they understood it, i.e., in terms of their particular variant of positivistic ideology.

The history of cosmic pluralism was particularly distorted by 19th-century ideological historiography. Many scientists writing on the subject of cosmic pluralism, repeat the story fabricated mostly by positivist historians.

> Since the dawn of history, man has speculated about the possibility that intelligent life may exist on other worlds beyond the Earth. This idea probably originated from the often unsuccessful attempts of primitive religions to give meaning to those aspects of the environment which had no simple explanations. [...] As astronomy developed, the concept of the existence of life on other worlds began to acquire some scientific bases. Most of the early Greek philosophers, both the materialists and the idealists, thought that our Earth was not the sole dwelling place of intelligent life. Considering the limitations of science at that time, these early philosophers displayed great originality and ingenuity. [...] Anaximander asserted that worlds are created and destroyed. Anaxogoras, one of the first proponents of the heliocentric theory, believed the moon to be inhabited. He also maintained that invisible "seeds of life," from which all living things originated, were dispersed throughout the universe. In later eras, similar concepts of "panspermia" (ubiquitous life) were propounded by various scientists and philosophers. This idea was incorporated into Christianity soon after its inception. The Epicurean school of materialist philosophy taught that many habitable worlds, similar to our Earth, existed in space. The Epicurean, Metrodoros, maintained: "To consider the Earth the only populated world in infinite space is as absurd as to assert that in an entire field sown with millet only one grain will grow." It is of interest that the proponents of this doctrine considered that not only the planets, but also other heavenly bodies in the vast reaches of space, were inhabited. [...] For fifteen hundred years after the birth of Jesus of Nazareth, Christian cosmology influenced by the theories of Ptolemy, taught that the Earth was the center of the universe. The concept of life on other worlds seemed to be incompatible with this philosophy. (Shklovskii and Sagan 1966, p. 3)

This inconsistent[2] collection of half-truths closely follows Auguste Comte's ridiculous "Law of Three Stages", which is based on the conviction that the chief business of religion, philosophy, and science is to provide an explanation of the natural phenomena. Within this framework, three stages of the development

---

[2] If panspermia was supposedly "incorporated into Christianity soon after its inception", why would "the concept of life on other worlds" be "incompatible with its [Christianity's] philosophy"?

can be identified in the history of thought, progressing inexorably from the most primitive to the most advanced. The most primitive stage is that of mythical explanations, which includes most of religious convictions. The following stage is metaphysical, represented by thinkers who were struggling to see the truth in spite of the pervasive religious superstition of their time. Finally, the one and only valid explanation was reached with the advance of positive science.

The fact that this perfectly philistine view was accepted by people who were supposed to be seaking for the truth, is an illustration of the bitterness of 19th-century ideological strife. Let us note that already in Plato's Academy philosophers in training were taught that the value of myths is not in providing explanations of natural phenomena, but rather that they have an irreplaceable function inspiring and guiding in the spiritual, moral, ethical and societal sphere. As for the explanations of natural phenomena, they were to be sought (if at all), with mathematics.

Let us briefly examine the above excerpt from Shklovskii and Sagan (1966). The beginning nicely demonstrates that they subscribe to the "Law of Three Stages". The next part repeats another popular prejudice. The authors glorify early Greek philosophy, erroneously claiming that "most" of these thinkers (commonly called pre-Socratic) subscribed to cosmic pluralism. They do not mention that the most influential philosophical schools of Antiquity were clearly against any such concept. They even go as far as to purport that Anaxagoras peopled the Moon as if this were an established and undisputed opinion.[3] The purpose of this is to make all the more stark the contrast between the "original and ingeneous" Greeks and the rigidity of "fifteen hundred years" of authoritarianism and obscurantism brought about by Christianity. Yet, progress cannot be stopped for ever, and inexorably did truth re-establish itself thanks to brave thinkers who had to overcome terrible opposition, often dying for their convictions at the stake...

We do not pretend to be able to reconstruct the long and complicated history of the idea of cosmic pluralism. It is clear to us, however, that nothing can be gained by first creating a theory of what happened and then carefully selecting those tidbits of evidence that seem to support our claim while rejecting those that do not seem to fit into our preconceived story.

A.4.2 "Medieval darkness"

The first form of cosmic pluralism as we defined it in Section A.3.1 was fundamentally a philosophical position in the context of one of Antiquity's great schools of philosophy, the Epicureism. Philosophical schools at the time were ultimately concerned with the question of how to live wisely. The representations of the physical world they cultivated, can only be understood as a part of an harmonic whole guided by the principle of unity between the macrocosm and microcosm, i.e., between the world and the individual. Ethical behaviour is determined by perceived values, and therefore the view of the physical reality fostered by a given school of philosophy naturally corresponded to its system of values. Epicureans believed that life, and the world is a passing chance with no purpose: a chaotic dance of atoms in an endless void. This view harmonised with their ethics which was founded upon two basic principles: sustainably minimise your suffering and value your friends.

Philosophical schools based on Plato's and Aristotle's heritage found Epicureanism unacceptable because of what they perceived as its lack of depth, its inability to inspire higher aspirations, etc. Platonists and Aristotelians of all hues consider the world as fundamentally One. The goal of ethical effort is to reach a wholeness of one's self reflected in the One, the Principle of the Universe. A fragmented, irreconciliably multiple world of the Atomists and Epicureans was of necessity rejected by these schools. And this was,

---

[3] Simplicius quotes Anaxagoras as saying:

> Since these things are so, it is right to think that there are many different things present in everything that is being combined, and seeds of all things, having all sorts of forms, colors, and flavors, and that humans and also the other animals were compounded, as many as have soul. Also that there are cities that have been constructed by humans and works made, just as with us, and that there are a sun and a moon and other heavenly bodies for them, just as with us, and the earth grows many different things for them, the most valuable of which they gather together into their household and use. I have said this about the separation off [NB. "separating off" is a key process in Anaxogoras' physics], because there would be separation off not only for us but also elsewhere. (Fragment B4a)

It is not at all clear what is meant by elsewhere. According to the The Stanford encyclopedia of philosophy (2007), no ancient sources discuss this. Simplicius himself, after quoting the fragment, is puzzled by it, and argues for a metaphysical interpretation.

naturally, also the case of the cosmic pluralism.

Platonist and Aristotelian influences have been crucial in the development of Christian thought. It was only natural that the cosmic pluralism of the first sort had been considered incompatible with Christianity until 1277. This was the year when Etienne Tempier, Bishop of Paris, condemned 219 propositions which seemed to take the then fashionable Aristotelian thought too far.

Rational speculation inspired by Aristotle was leading some of the 13th-century Parisian intellectuals to the conclusion that even God was not free from the constraints of logic, and since cosmic pluralism was considered absurd by Aristotle, God could not have created multiple worlds. Let us note that this rejection of cosmic pluralism was formally similar to Aristotle's own way of arguing, but it also was fundamentally different from Aristotle who used logic to construct a harmonised worldview but who considered, as all philosophers of Antiquity, that Philosophy was primarily concerned with the wisdom of living a good life, whereas many already in the 13th century subscribed to the modern view of philosophy which is considered primarily as an intellectual exercise.

Proposition number 34 among those condemned in 1277, therefore, reads:

> that the First Cause cannot make many worlds

After 1277 many authors attempted to reconcile Aristotelian inclinations with God's freedom in creating multiple worlds. It was not until Nicolas of Cusa's *De docta ignorantia* of 1440 that cosmic pluralism was affirmed.

A.4.3 Nicolas of Cusa

Cusanus is the undisputed author of what we called the second form of cosmic pluralism, writing:

> Life, as it exists on earth in the form of men, animals and plants, is to be found, let us suppose, in a higher form in the solar and stellar regions. Rather than think that so many stars and parts of the heavens are uninhabited and that this earth of ours alone is peopled – and that with beings, perhaps of an inferior type – we will suppose that in every region there are inhabitants, differing in nature by rank and all owing their origin to God, who is the centre and the circumference of all stellar regions. [...]
>
> Of the inhabitants then of worlds other than our own we can know still less, having no standards by which to appraise them. It may be conjectured that in the area of the sun there exist solar beings, bright and enlightened denizens, and by nature more spiritual than such as may inhabit the moon – who are possibly lunatics – whilst those on earth are more gross and material. [...]
>
> And we may make parallel surmise of other stellar areas that none of them lack inhabitants, as being each, like the world we live in, a particular area of one universe which contains as many such areas as there are uncountable stars.

We may only suspect that the reason why so many texts on the history of cosmic pluralism do not mention Cusanus has to do with the fact that his existence does not conform with the positivistic fable outline above. Cusanus affirmed that the Earth was not at the centre of the Universe. He affirmed that the Universe could be infinite. He affirmed that the Earth was of the same nature as the "stars". He affirmed that there was no perfection in the physical universe, and therefore, that the planetary motions were not following perfect geometrical figures, and that celestial spheres, could not be perfectly spherical. He affirmed that the "stars" were habitable and that there were many non-human extraterrestrial beings inhabiting the "stars" we observe in the night sky.[4]

If the positivistic story of cosmic pluralism were true, Cusanus would have been persecuted. As Crowe puts it:

---

[4] Let us note again that Cusanus' peopling of celestial objects with intelligent beings, was in all probability not linked with the idea of our Sun being a star, and therefore of planets orbiting other stars than our Sun. Curiously, even though Cusanus represents giant leap, this further development required an additional step.

> A superficial knowledge of the extraterrestrial life debate, including belief in the myth that Giordano Bruno was martyred for his pluralistic convictions, might lead one to suspect that these claims of Cusanus reveal a person with little sense of the politically acceptable, if not a man destined for imprisonment or burning at the stake. (Crowe 1999, p. 8)

But the facts do not follow this logic. Nicolas of Cusa was made a Cardinal in 1448, eight years after publishing *De docta ignorantia.*

A.4.4 Giordano Bruno

However, we have yet to discuss the most crucial episode in the positivistic story about cosmic pluralism, viz., the teachings and martyrdom of Giordano Bruno. The version one finds perpetuated in all the standard texts written by scientists can be exemplified by the following very recent brief account:

> Believing Copernicanism to be true, Giordano Bruno enlarged it to a vision of an indefinite multiplicity of solar systems, which anticipated the modern conception of stellar spaces. Fifty-seven years after the death of Copernicus, Bruno was burnt alive for his convictions. (Polanyi 1958, p. 146)

As before, although both of the above statements are mostly true, their implied connection is unlikely to be founded upon historical evidence. Michael Polanyi was one of the first to point out that history of science should not be used instrumentally just to prove ideological points, and yet, here he repeats an established half-truth. Therefore, if even the very advocate of critical historiography of science fell for the “myth” (as Crowe refers to it) so dear to positivists, we should not judge harshly those who perpetuate it even today.[5]

Contrary to the “myth”, it is not clear what exactly happened at Bruno’s trial (and much less what went on behind the scenes). The main problem is that the files of the Roman trial against Giordano Bruno (1548-1600), once kept in the archives of the Holy Office, are lost. The only official documentation we have is a summary, which derives from the originals (on the margins of the document you often find citations of the pages of the lost trial). Some abstracts of Giordano Brunos works, his interrogations, some of the records of his Venetian trial in 1592 and some other documents copied from the original files converged in the summary, which was probably used by the Assessor of the Holy Office.

The lack of proper sources is very frustrating. To illustrate the point, let us mention just two tantalising issues. Firstly, it is very strange that his trial lasted for nearly eight years, whereas usual proceedings of the Holy Office typically took several weeks, rarely as much as one year. Why the delay?

The second, perhaps even more intriguing question is that of the actual accusation. The crucial moment in the trial came when he was asked to recant eight propositions prepared by the Cardinals Bellarmine and Commisario. Unfortunately, the text of these propositions is lost:

> What were the eight propositions? It is of course almost impossible to say, but [a possible list could cover] propositions as to (1) the distinction of persons in God; (2) the Incarnation of the Word; (3) the nature of the Holy Spirit; (4) the Divinity of Christ; (5, 6, and 7) the necessity, eternity, and infinity of Nature; (8) the Transmigration of Souls. (McIntyre 1992, p. 90)

It is unlikely that these propositions included the mobility of the Earth, or other Copernican views.[6] A good argument for this assertion can be deduced from the development of the Copernican and Galilean contro-

---

[5] A recent textbook on planetology says: “An example of the conflict between the formal teachings of the Catholic Church of the 16th century and astronomy is the execution of Giordano Bruno (1548–1600 AD) by burning at the stake on February 17 of 1600 in Rome. Bruno had openly advocated the heliocentric model of the Universe proposed by Copernicus and had stated that the Earth moves around the Sun. In addition, he claimed that the Universe is infinite. During his trial, which lasted seven years, he refused to retract these and other heretical ideas he had published in his turbulent life. Finally, Pope Clement VIII declared him to be an impenitent and pertinacious heretic. When he was sentenced to death on February 8 of 1600, he is reported to have told the judges of the inquisition: Perhaps your fear in passing judgement on me is greater than mine in receiving it.” (Faure and Mensing 2007)

[6] “His [Bruno’s] sources, including Lucretius, Cusanus, Palingenius, Paracelsus, Copernicus, and the Hermetic writings, seem to have been more numerous than his followers, at least until the eighteenth- and nineteenth-century revival of interest in Bruno as a

versy in Rome up to 1633. In the extensively documented trials of Galileo there is no reference to these "eight propositions", which would be surprising if they contained an official position on Copernicanism.

A second issue that still remains to be adequately clarified is Bruno's influence on the extraterrestrial life debate during his lifetime and in the decades after his death. Unfortunately, even the most recent books on Bruno tend to concentrate on other things, leaving these questions unanswered. Writing about the latest Brunonian monograph (Rowland 2008), Anthony Gottlieb is rather caustic:

> Although Rowland would like us to see Bruno as a martyr to science, his [Bruno's] work comes across more as theologically inspired science fiction. He was a poetic speculator, not an empirical or systematic investigator. Thus it is still not clear what the great master of memory should be remembered for. (Gottlieb 2008)

It would be good to know what part did Bruno's writings play in the formation of René Descartes' version of cosmic pluralism. Cartesian views, expressed in his *Principia philosophiae* (Descartes 1644), had a large impact, also thanks to the popularity of Bernard le Bovier de Fontenelle's (1657–1757) *Entretiens sur la pluralité des mondes* (Fontenelle 1686), where Giordano Bruno is not mentioned once. What is more, Bruno may have, paradoxically, done a disservice to Copernicanism. It is not impossible that many 17th-century intellectuals found Bruno's exalted visions too disturbing, and rejecting them, rejected also heliocentrism:

> Copernicus held that not just the solar system but the entire universe was heliocentric, and Kepler denied that the stars have planetary systems. The first person to make explicit the idea of a large - indeed, an infinite - number of other worlds in orbit about other suns seems to have been Giordano Bruno. But others thought that the plurality of worlds followed immediately from the ideas of Copernicus and Kepler and found themselves aghast. In the early seventeenth century, Robert Merton contended that the heliocentric hypothesis implied a multitude of other planetary systems, and that this was an argument of the sort called reductio ad absurdum, demonstrating the error of the initial assumption. (Sagan 1980, p. 164)

In order to have a clearer view of this open field of inquiry, a broader perspective is of essence. The period from Cusanus to Newton witnessed a profound "transformation of cognitive and intellectual values", a "redefinition of the nature and goals of enquiry", in short the "emergence of the scientific culture" (Gaukroger 2006, p. 3). Many different currents of thought were arising and interacting at the time, and historiography has mostly perceived Bruno's contribution without sufficient attention to the emergence of the science as a whole. A brief attempt to situate his work in this context can be found in recent Gaukroger's monograph on the genesis of modern science:

> After Bruno, the naturalist tradition collapsed in natural philosophy, not so much because of the dreadful death inflicted upon him by the Roman Inquisition in 1600, but because he cut natural philosophy loose from virtually all its traditional bearings, while offering little more than promissory notes, especially when compared to the newly developing "physico-mathematical" and corpuscularian movements. His defence of the earth's diurnal motion, for example, was simply that it rotates on its axis in order to partake of the sun's light and heat, and it revolves around the sun so that it can partake in the seasons. This hardly engaged the natural-philosophical or astronomical issues seriously, and could not possibly have furthered the cause of Copernicanism. (Gaukroger 2006, p. 115)

---

supposed 'martyr for science'. It is true that he was burned at the stake in Rome in 1600, but the church authorities guilty of this action were almost certainly more distressed at his denial of Christ's divinity and alleged diabolism than at his cosmological doctrines." (Crowe 1999, p. 10)

Appendix B

Variability noise

B.1 Stellar leakage

One of the processes that make the output signal of a nulling interferometer nonzero is the so-called *stellar leakage.* It is an effect of the finite angular size of the stellar disk. With perfect optics, the instrument's on-axis transmission would be zero. This would be true only for perfectly on-axis beams, however. Let us call ϑ the angle between the axis and the line of sight to a given off-axis point. In a nulling interferometer, ϑ corresponds to the phase difference, i.e., to OPD.

Fig. B.1 shows the transmission of a two-aperture nulling interferometer as a function of ϑ. Since the fringe pattern is a enveloped sine curve, its behaviour around the minimum is quadratic:

$$I(\vartheta) \propto \vartheta^2. \tag{B.1}$$

With a stellar disk of a finite angular radius the spatially integrated flux from the star is a fraction *geom* of the total flux.

In addition, the instrument is not perfect and transmits a fraction *nl* of the on-axis flux. The stellar leakage generates a total photoelectron flux $F_{sl}(\lambda, \tau)$ at the wavelength λ and after the exposure time τ

$$F_{sl}(\lambda, \tau) = A\,F_{st}(\lambda)[geom(\lambda, \tau) + nl(\lambda, \tau)] \tag{B.2}$$

where

- A is a constant depending on telescope size, optics throughput, detector yield, etc.,
- $F_{st}(\lambda)$ is the incident stellar flux over a spectral bin centred around λ in photoelectrons per $\mathrm{m}^{-2}\mathrm{s}^{-1}$,
- *geom* is the geometrical nulling ratio due to the finite size of the stellar disk and the nonflat response of the interferometer around its axis (the ϑ^α response); considering perfect optics, $geom \ll 1$; and
- *nl* is the instrumental nulling ratio of the interferometer for an on-axis point source[1]; taking into account instrumental defects, $nl \ll 1$.

B.2 Shot noise

If the interferometer is optimised at a given wavelength for a planet position with a relative transmission of unity (the planet is on a bright fringe), after integration τ, the signal due to the planet is $AF_{pl}\tau$. Because the

---

[1] The laboratory experiments obviously measure *nl* with $geom \equiv 0$ because coherent light beams are used.

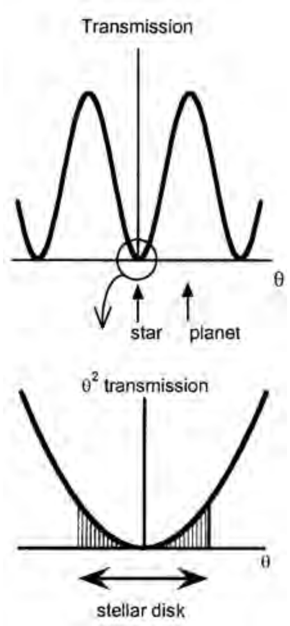

Figure B.1 - Transmission of a nulling interferometer with a ϑ^2 transmission around its axis. The finite size of the stellar disk leads to leaks with a relative intensity *geom*.

photon flux due to the planet is much weaker than that due to stellar leakage, the shot noise is given by the square root of the number of photoelectrons Nb_{sl}. The signal-to-noise ratio (SNR), if the shot noise were the only source of noise, would be

$$S/N_{sh} = \sqrt{\frac{A\tau}{F_{st}(\langle geom\rangle + \langle nl\rangle)}} \times F_{pl} \tag{B.3}$$

which improves with integration time as $\tau^{1/2}$.

Since the shot noise associated with $\langle geom\rangle$ is intrinsic to the interferometer design, it is reasonable to require that the instrument dependent noise associated with $\langle nl\rangle$ be somewhat smaller, so that the total shot noise would not be significantly increased by it. The actual requirement is dictated by the total SNR needed at the corresponding wavelength and depends on the planetary signal intensity and other sources of noises, e.g., the zodiacal and exo-zodiacal light, thermal background, etc.

At a given wavelength λ the first transmission maximum of a Bracewell interferometer with base B is at an angle $\vartheta = \lambda/(2B)$. This base can be selected so that the target planet is located at one of the transmission maxima. The angular separation of the Sun-Earth system at 20 pc (65 light years) is 0.05 arc sec. When one is observing at 7 μm, the planet is located on the first transmission maximum if the interferometer's baseline is $B = 14$ m. The geometrical stellar leakage due to the finite size of the stellar disk is then $geom = 1.8 \times 10^{-5}$. The most interesting target planets are located in the region where water can be liquid, i.e., in the habitable zone (HZ) of their stars (roughly 0.7–1.5 AU for the Sun, i.e., the zone between Venus and Mars). Most stars in the *Darwin*/TPF-I target lists are cooler than the Sun, and have a larger ratio between their angular size and the distance to their HZ. They produce larger leaks when a planet is searched for in their HZs. Therefore the preceding value for *geom* can be considered as the lowest one, and the condition derived thereafter for *nl* is the most severe.

A possible requirement for *nl* would be $\langle nl\rangle \leq 0.56\ \langle geom\rangle$, which corresponds to an increase in the total shot noise by 25%. For an interferometer with leakages similar to those of a Bracewell interferometer ($geom = 1.8\,10^{-5}$ for an Earth-Sun-like system) a sensible value for the mean instrumental leakage would then be

$$\langle nl\rangle_{7\mu\mathrm{m}} = 1.0\,10^{-5}. \tag{B.4}$$

For another interferometer design with more intrinsic leakages, the requirement on *nl* could be relaxed, but the required integration time for a given telescope collecting area would increase because of the shot noise associated with the larger value of *geom*.

B.3 Variability noise

Variability noise N_v is due to stochastic variations of the mean flux at the output of the (imperfect) nuller. It is proportional to the stellar flux and to the standard deviation of the mean of the instrumental nulling ratio $\langle nl \rangle$ over the integration time τ:

$$N_v = A\, F_{sl}(\lambda)\, \sigma_{\langle nl \rangle}(\tau)\, \tau, \tag{B.5}$$

where $\sigma_{\langle nl \rangle}(\tau)$ is obtained for each exposure time τ by calculating the standard deviation of the set of the mean values of *nl*, each of which corresponds to a moving window of the duration τ.

The resulting SNR is

$$S/N_v = \frac{F_{pl}}{F_{st}} \frac{1}{\sigma_{\langle nl \rangle}(\tau)}. \tag{B.6}$$

An analysis of the relationship between $\sigma_{\langle nl \rangle}(\tau)$ and the Power-Spectrum Density (PSD) of *nl* (Chazelas et al. 2006) shows that if the fluctuations of *nl* are white, i.e., $\mathrm{PSD}_{nl}(\nu)$ is constant, $\sigma_{\langle nl \rangle}(\tau)$ is proportional to $\tau^{-1/2}$ and S/N_v increases as $\tau^{1/2}$. If there are instrumental drifts, the PSD as a so-called $1/f$ component, i.e., the longer the time interval between two calibrations of the instrument, the more noise power there is at low frequency. Let T be the time separating two calibrations of the nuller. A possible model for this noise is

$$\mathrm{PSD}_{nl}(\nu) = \begin{cases} a\nu^{-1} + b & \text{for} \quad |\nu| > T^{-1} \\ aT + b & \text{for} \quad |\nu| \leq T^{-1} \end{cases} \tag{B.7}$$

In this model (Fig. B.2), if $a\tau \gg b$, the $1/f$ noise causes a very slow decrease of $\sigma_{\langle nl \rangle}(\tau)$ with the integration time τ. In the presence of dominating $1/f$ noise, the S/N_v is almost independent of integration time τ.

If $a\tau \ll b$, white noise dominates, $\sigma_{\langle nl \rangle}(\tau)$ is proportional to $\tau^{-1/2}$ and S/N_v increases as $\tau^{1/2}$. When the noises associated with the stellar leakage are dominant, e.g., at short wavelengths, a possible noise budget is

$$N_v = N_{sh} = \sqrt{\frac{1}{2}}\, N_{tot}. \tag{B.8}$$

To obtain spectroscopic information at different wavelengths, including the most difficult ones, the S/N_{tot} ratio must be sufficient in a maximum of 10 day integration, say $S/N_{tot} \sim 7$. The above equation implies that

$$S/N_v = \sqrt{2}\, S/N_{tot} \sim 10 \text{ in 10 days.} \tag{B.9}$$

At 7 μm the star-to-planet contrast is $4\,10^7$ for the Earth-Sun case. At other wavelengths the relation $F_{st}/F_{pl}(\lambda)$ can be estimated (Chazelas et al. 2006) using a simple power law curve $(\lambda/7\mu\mathrm{m})^{-3.37}$. The resulting requirement for the nuller stability is shown in Fig. B.3.

In the 7-20 μm domain, the required condition can be written as

$$\sigma_{\langle nl \rangle}(\lambda,\ 10\,\mathrm{days}) \leq 2.5\,10^{-9}\,(\lambda/7\mu\mathrm{m})^{-3.37}, \tag{B.10}$$

or

$$\sigma_{\langle nl \rangle}(\lambda,\ 10\,\mathrm{s}) \leq 7\,10^{-7}\,(\lambda/7\mu\mathrm{m})^{-3.37} + \text{ white noise.} \tag{B.11}$$

The condition “white noise” means that $1/f$-type noises, e.g., long-term drifts, must be small enough to permit an improvement in stability with integration time $\tau^{-1/2}$.

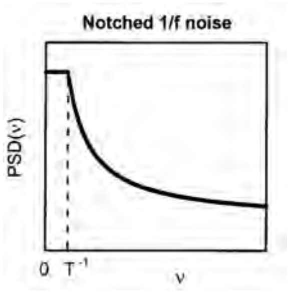

Figure B.2 **-** Mathematical model used to describe the $1/f$ noise. It has finite power, but this power grows with the time T separating two calibrations of the instrument.

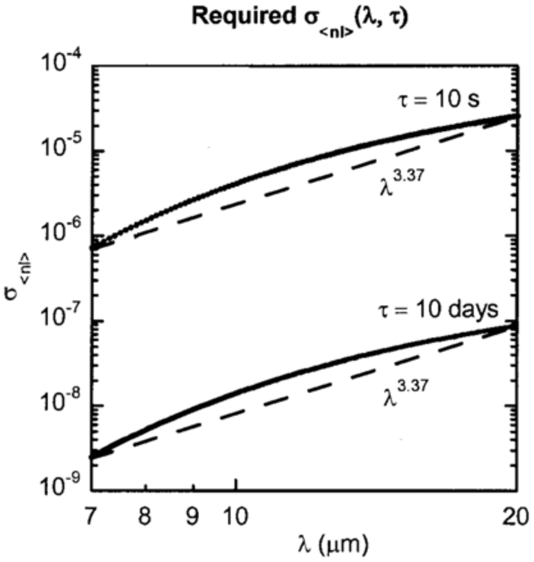

Figure B.3 **-** Required stability of the instrumental nulling function $nl(t)$ on time scales $\tau = 10$ s and 10 days.

Appendix C

Gaussian beams & parabolic mirrors

C.1 Paraboloid of Revolution

A paraboloid of revolution is the locus of points in space that are equally distant from a given plane (directrix) and from a given point (focus). The apex of the paraboloid is on the normal running from the focus to the plane. The distance f between the apex and the focus is called the focal length. The half-chord l passing through the focus parallel to the directrix is called the semilatus rectum.

By paraboloid's definition, $|FB| = |BD| = l = 2f$. The distance $r = |FP|$ from the focus F to an arbitrary point P on the paraboloid is, again by paraboloid's definition, equal to the distance $|PR|$ from the point P to the directrix. In Fig. C.1 it can be seen that $|PR| = 2f - |FQ|$, and that $|FQ| = r\cos\alpha$, where α is the angle AFP. Therefore, $r = 2f - r\cos\alpha$, which is the equation of the paraboloid in spherical coordinates:

$$r = \frac{2f}{1+\cos\alpha}$$

C.2 Gaussian Beam Encircled Power

A Gaussian beam has, in principle, non-zero flux values even very far from the beam axis. Neglecting the hyperbolic longitudinal behaviour of the beam, i.e., examining the behaviour at the beam waist, we express the electric field distribution at the radius r:

$$E(r) = \frac{1}{2\pi\sigma^2}\exp\left(-\frac{r^2}{2\sigma^2}\right)$$

where σ can be regarded as proportional to the beam's waist (we shall soon determine the proportionality factor). This formula is normalised as follows:

$$\int_0^{2\pi} \mathrm{d}\vartheta \int_0^{\infty} r\,\mathrm{d}r E(r) = 2\pi \int_0^{\infty} \frac{1}{2\pi\sigma^2}\exp\left(-\frac{r^2}{2\sigma^2}\right) r\,\mathrm{d}r = 1$$

calculate the flux I_0^r encircled within a radius r from the beam axis.

$$I_0^r = 2\pi \int_0^{r} \left[\frac{1}{2\pi\sigma^2}\exp\left(-\frac{t^2}{2\sigma^2}\right)\right]^2 t\,\mathrm{d}t = \frac{1}{4\pi\sigma^2}\left[1-\exp\left(-\frac{r^2}{\sigma^2}\right)\right]$$

And its complement I_r^∞:

$$I_r^\infty = 2\pi \int_r^{\infty} \left[\frac{1}{2\pi\sigma^2}\exp\left(-\frac{t^2}{2\sigma^2}\right)\right]^2 t\,\mathrm{d}t = \frac{1}{4\pi\sigma^2}\exp\left(-\frac{r^2}{\sigma^2}\right)$$

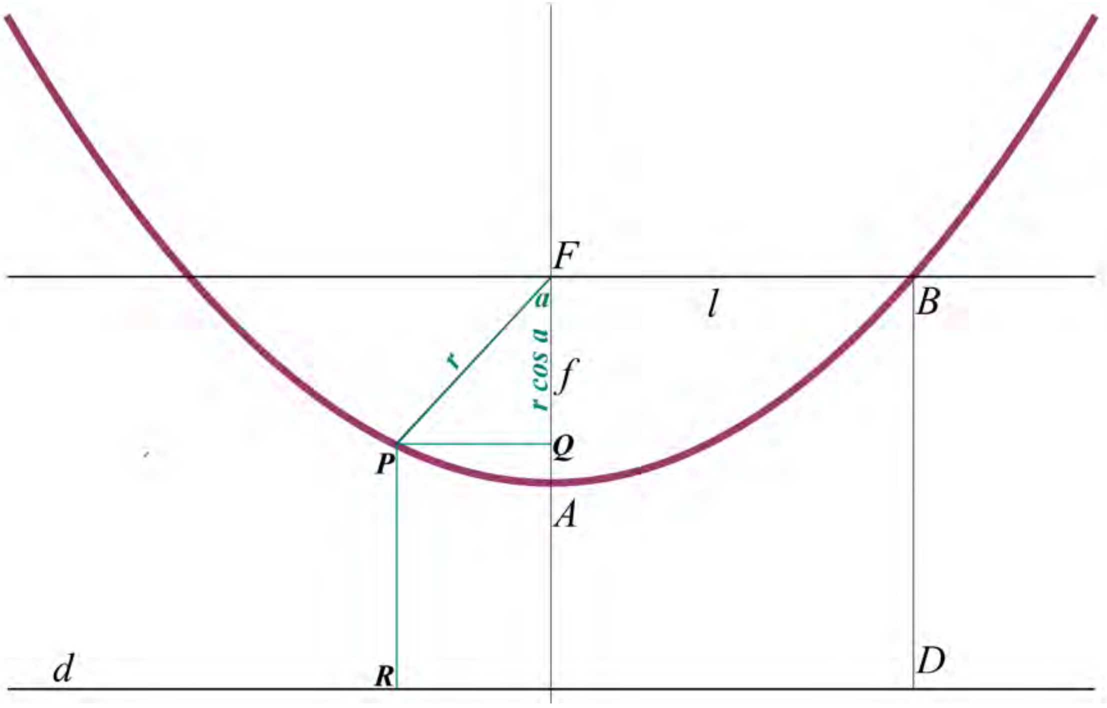

Figure C.1 **-** Parabola.

And the total flux I_0^∞:

$$I_0^\infty = 2\pi \int_0^\infty \left[\frac{1}{2\pi\sigma^2} \exp\left(-\frac{t^2}{2\sigma^2}\right)\right]^2 t \, \mathrm{d}t = \frac{1}{4\pi\sigma^2}$$

Let us now look at the expressions for the beam intensity $I(r)$ at the radius r and the maximum beam intensity $I(0)$ at the beam axis:

$$I(r) = \left[\frac{1}{2\pi\sigma^2} \exp\left(-\frac{r^2}{2\sigma^2}\right)\right]^2 = \left(\frac{1}{2\pi\sigma^2}\right)^2 \exp\left(-\frac{r^2}{\sigma^2}\right)$$

$$I(0) = \left(\frac{1}{2\pi\sigma^2}\right)^2$$

We can determine the relationship between our parameter σ and the conventional beam waist w_0 from these expressions for the beam intensity. If the waist w_0 is defined as the radius where flux is $1/e^2$ of the on-axis flux, then we obtain $w_0 = \sigma\sqrt{2}$, and therefore

$$I(r) = \left(\frac{1}{\pi w_0^2}\right)^2 \exp\left(-\frac{2r^2}{w_0^2}\right)$$

The proportion of the flux outside of the radius of r with respect to the total flux is therefore equal to the proportion of the beam intensity $I(r)$ at the radius r with respect to the maximum flux at beam axis $I(0)$:

$$\frac{I_r^\infty}{I_0^\infty} = \frac{I(r)}{I(0)}$$

C.3 Gaussian Beam Coupling

The formula we found in the literature and which we calculated independently using both the numerical and the symbolic-manipulation approach (Python and Mathematica) expresses the coupling efficiency η in

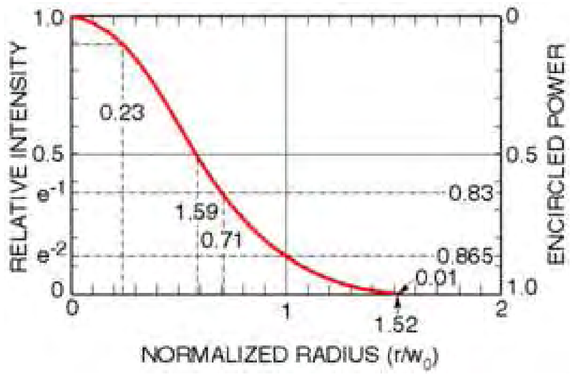

Figure C.2 - A linear-scale plot of the relative beam intensity $I(r)/I(0) = \exp(-2r^2)$ and encircled power I_0^r/I_0^∞ (or its complement I_r^∞/I_0^∞) vs. radius r given in units of w_0.

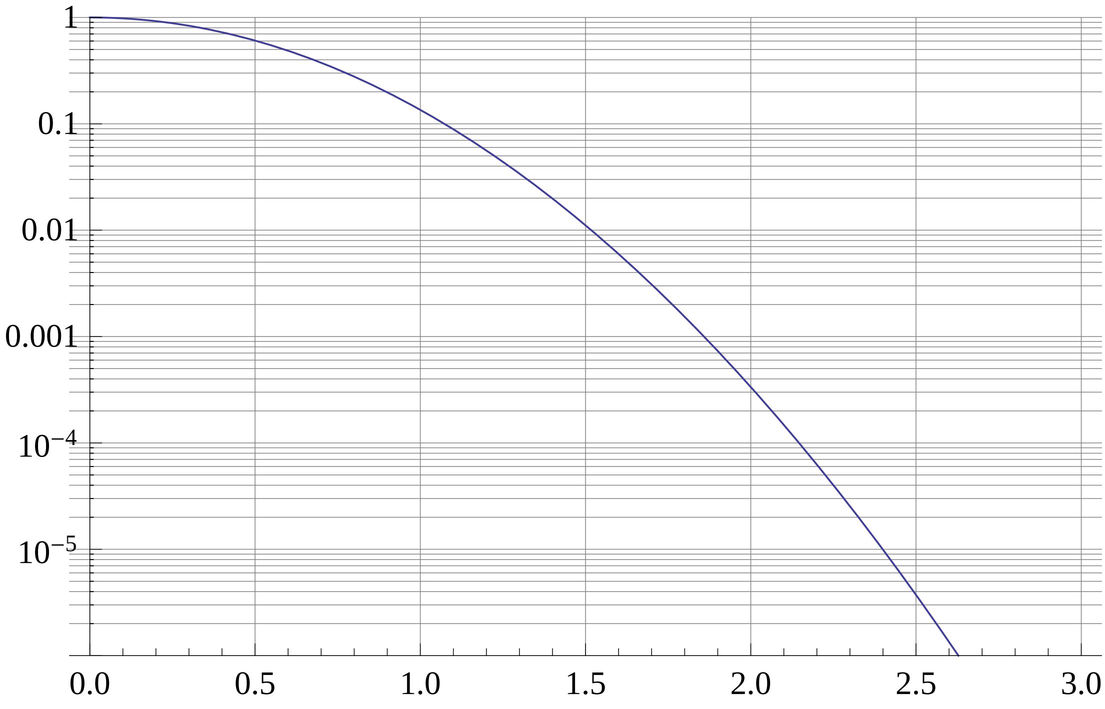

Figure C.3 - A semilogarithmic plot of the relative beam intensity $I(r)/I(0) = I_r^\infty/I_0^\infty = \exp(-2r^2)$ vs. radius r given in units of w_0.

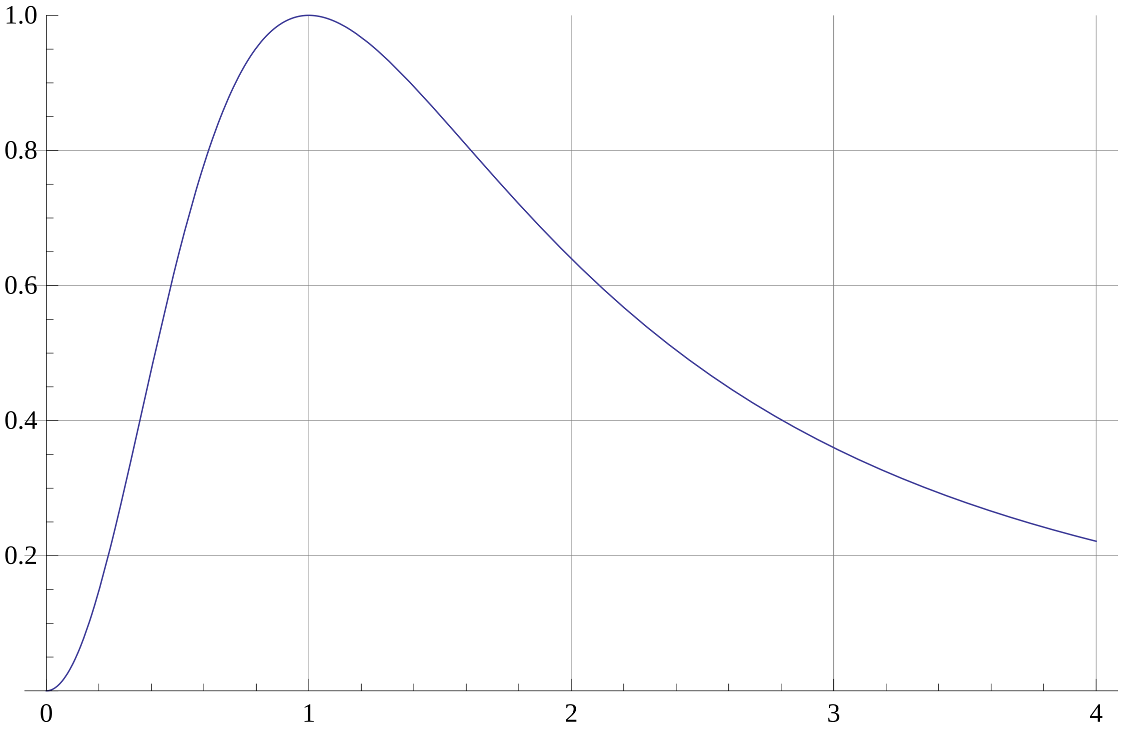

Figure C.4 **-** Coupling efficiency $\left(\frac{2\sigma}{\sigma^2+1}\right)^2$.

terms of the two beams' waists or MFDs, here denoted as σ and ρ:

$$\eta = \left(\frac{2\sigma\rho}{\sigma^2+\rho^2}\right)^2$$

The above result can be derived in the following way:

$$\frac{\int_{-\infty}^{\infty}\int_{-\infty}^{\infty}\frac{1}{2\pi\sigma^2}\exp\left[-\frac{x^2+y^2}{2\sigma^2}\right]\frac{1}{2\pi\rho^2}\exp\left[-\frac{x^2+y^2}{2\rho^2}\right]\mathrm{d}x\mathrm{d}y}{\sqrt{\int_{-\infty}^{\infty}\int_{-\infty}^{\infty}\left[\frac{1}{2\pi\sigma^2}\exp\left(-\frac{x^2+y^2}{2\sigma^2}\right)\right]^2\mathrm{d}x\mathrm{d}y}\sqrt{\int_{-\infty}^{\infty}\int_{-\infty}^{\infty}\left[\frac{1}{2\pi\rho^2}\exp\left(-\frac{x^2+y^2}{\rho^2}\right)\right]^2\mathrm{d}x\mathrm{d}y}} = \frac{2\sigma\rho}{\sigma^2+\rho^2}$$

Or, using cylindrical coordinates:

$$\frac{2\pi\int_{0}^{\infty}\frac{1}{2\pi\sigma^2}\exp\left[-\frac{t^2}{2\sigma^2}\right]\frac{1}{2\pi\rho^2}\exp\left[-\frac{t^2}{2\rho^2}\right]t\mathrm{d}t}{\sqrt{2\pi\int_{0}^{\infty}\left[\frac{1}{2\pi\sigma^2}\exp\left(-\frac{u^2}{2\sigma^2}\right)\right]^2 u\mathrm{d}u}\sqrt{2\pi\int_{0}^{\infty}\left[\frac{1}{2\pi\rho^2}\exp\left(-\frac{v^2}{2\rho^2}\right)\right]^2 v\mathrm{d}v}} = \frac{2\sigma\rho}{\sigma^2+\rho^2}$$

These integrals represent the electric field. In order to obtain the intensities, we have to square the above expression, obtaining our formula above.

Appendix D

Distance-Squared Law

We used a 12 V halogen bulb as an infrared source at a current of 2.5 A powered by a stabilised source. The lock-in amplifier was at 270 Hz chopping frequency with a time constant of 300 ms.

We measured the dependence of the detection system's response upon the distance from the source twice:

1. Placing the source close to the detector (a minimum distance of 45 cm was necessary so that we could neglect the geometric effects), we found a current corresponding to the maximum response of the detection system (≈ 1 V): 2.7 A and 2.2 V. Then we performed a series of measurements, while withdrawing the source from the detector until we reached the limit of 13.5 m (the size of our laboratory space).
2. At the farthest point from the detector we turned the current down until we reached a signal about an order of magnitude greater than the dark current, viz., 1.5 A at 0.5 V. Then we performed a series of measurements while bringing the source back to the detector, until we reached the same minimum distance as before (45 cm).

The results are presented in Figs. D.1, D.2) In the case of the first series of measurements was (with χ, the sum of squares of differences between the measured points and the fit):

$$I = \frac{1335.41}{(d - 4.94196)^2} + 3.38039\,10^{-3} \qquad \chi = 0.0453 \tag{D.1}$$

At the first glance it would seem that the two series of measurements are in good agreement with Bouguer's Law and that the putative non-linearity of the detection system's response is insignificant in the ranges 1–1000 mV and 0.02–10 mV. A closer look shows that the limitations of this conclusion, however.

Multiplying the maximum signal values by a factor 1.1 (the first points on the left) in both series of measurements and performing the fit on the modified data series, we obtain practically identical curves (no visual difference).

With the modified data series we obtained:

$$I = \frac{1338.45}{(d - 4.94226)^2} + 3.27240\,10^{-3} \qquad \chi = 0.0669 \tag{D.2}$$

In the case of the second series of measurements, the measured points were fitted with the curve:

$$I = \frac{15.3198}{(d - 7.00152)^2} + 4.60816\,10^{-6} \qquad \chi = 0.00027853 \tag{D.3}$$

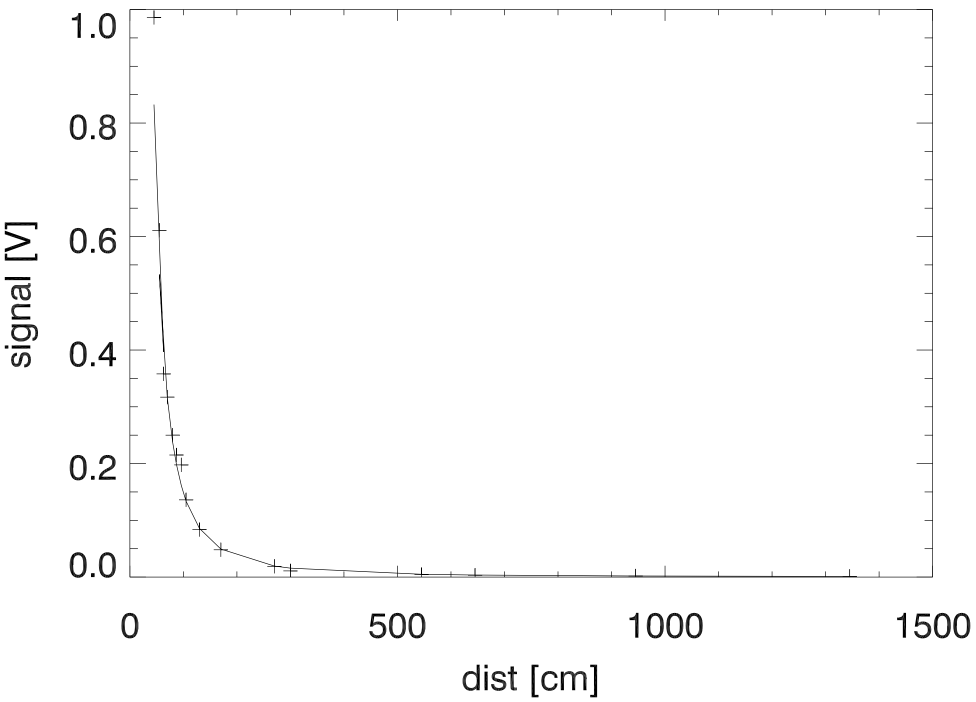

Figure D.1 - Measurement 1 – from the detector to the end of the laboratory. Measured points and the fit: $I = \frac{1335.41}{(d-4.94196)^2} + 3.38039\,10^{-3}$

And with the modified data:

$$I = \frac{15.3232}{(d-7.00146)^2} + 4.97863\,10^{-6} \qquad \chi = 0.000278395 \tag{D.4}$$

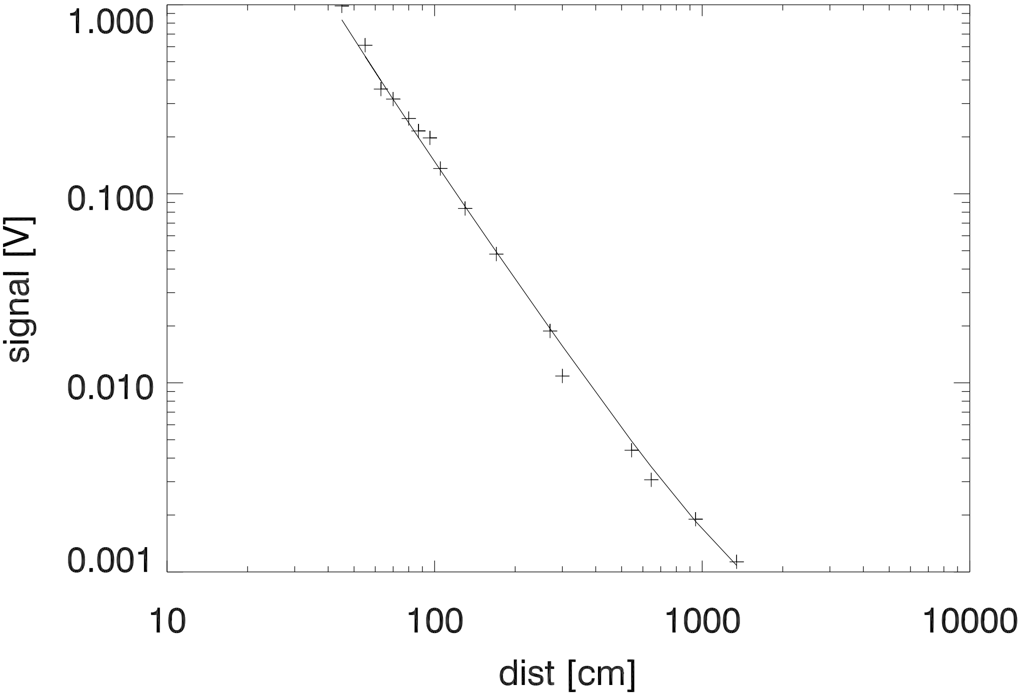

Figure D.2 **-** As the previous but in log-log.

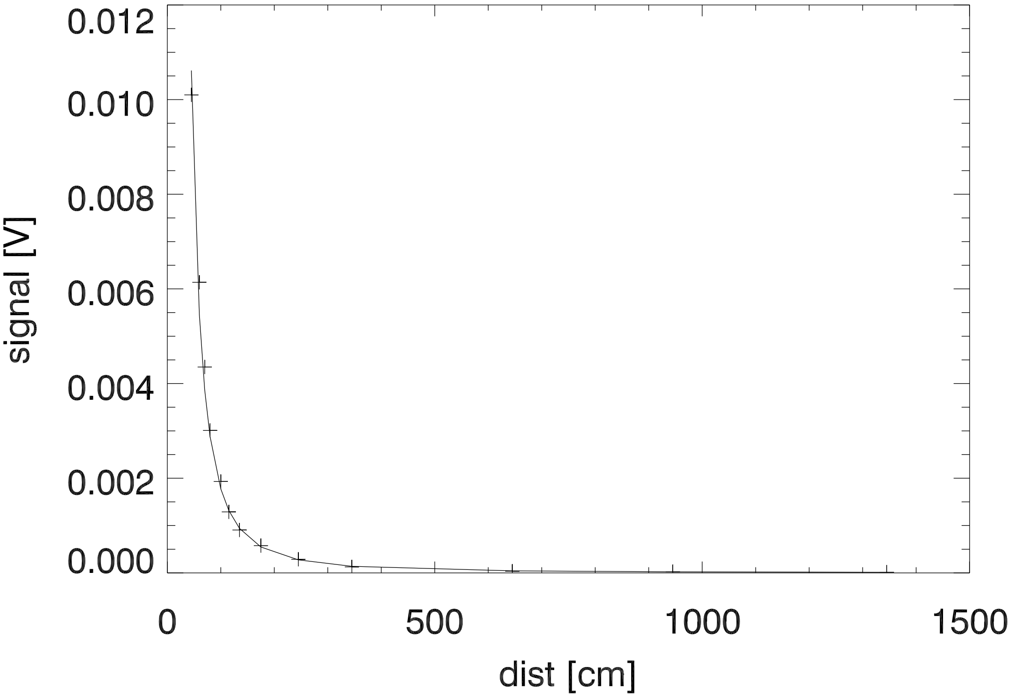

Figure D.3 **-** Measurement 2 - from the end of the room towards the detector. Measured points and the fit: $I = \frac{15.3198}{(d-7.00152)^2} + 4.60816\,10^{-6}$

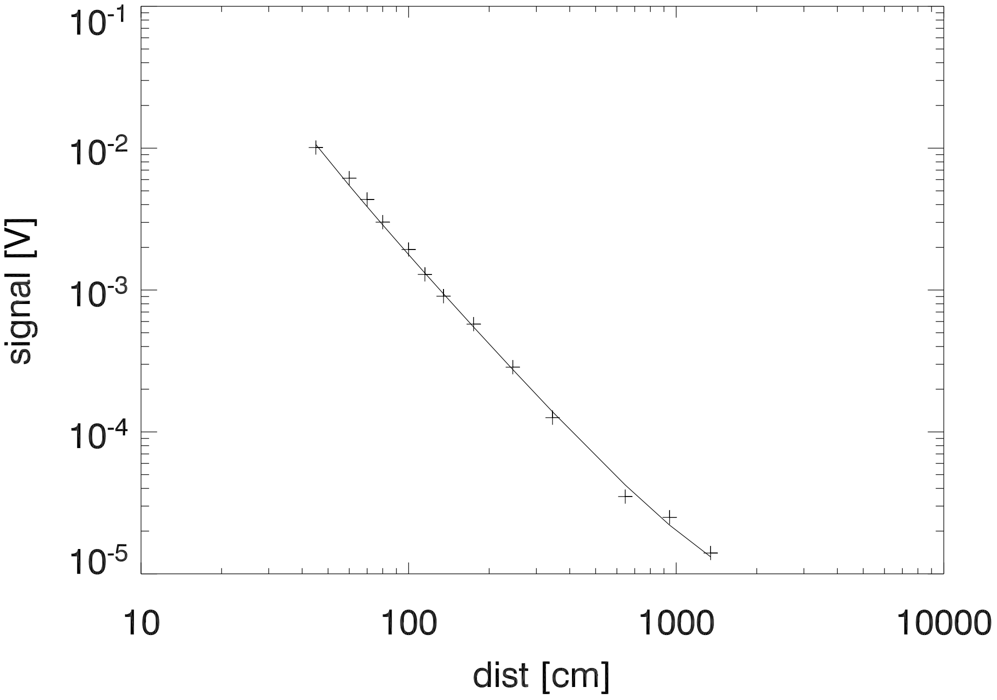

Figure D.4 **-** As the previous figure but in log-log.

Appendix E

Publications

We reported on our work in three papers:

- Gabor et al. *Astronomy & Astrophysics*, 483:365–369, May 2008.
- Gabor et al. *SPIE*, vol. 7013, p. 70131R.[1] (This paper is an update of the first one, reporting new results and otherwise only correcting several errors.)
- Gabor et al. *SPIE*, vol. 7013, p. 70134O.[2]

The first two papers, dealing with the OPD stabilisation, correspond to Chapter 4, which can be regarded as a corrected and updated version of the papers. Chapter 5 contains the material published in the third paper.

---

[1] Published in *Optical and Infrared Interferometry.* Edited by Schöller, Markus; Danchi, William C.; Delplancke, Françoise. Proceedings of the SPIE, Volume 7013, pp. 70131R-70131R-9 (2008).

[2] Published in *Optical and Infrared Interferometry.* Edited by Schöller, Markus; Danchi, William C.; Delplancke, Françoise. Proceedings of the SPIE, Volume 7013, pp. 70134O-70134O-11 (2008).

A&A 483, 365–369 (2008)
DOI: 10.1051/0004-6361:20077830

Astronomy
&
Astrophysics

Stabilising a nulling interferometer using optical path difference dithering

P. Gabor[1], B. Chazelas[1], F. Brachet[2], M. Ollivier[1], M. Decaudin[1], S. Jacquinod[1], A. Labèque[1], and A. Léger[1]

[1] Institut d'Astrophysique Spatiale, 91405 Orsay Cedex, France
e-mail: `pavel.gabor@ias.u-psud.fr`
[2] Centre National d'Études Spatiales, 3140 Toulouse Cedex 9, France

Received 9 May 2007 / Accepted 20 February 2008

Abstract

Context. Nulling interferometry has been suggested as the underlying principle for the *Darwin* and TPF-I exoplanet research missions.
Aims. There are constraints both on the mean value of the nulling ratio, and on its stability. Instrument instability noise is most detrimental to the stability of the nulling performance.
Methods. We applied a modified version of the classical dithering technique to the optical path difference in the scientific beam.
Results. Using only this method, we repeatedly stabilised the dark fringe for several hours. This method alone sufficed to remove the $1/f$ component of the noise in our setup for periods of 10 min, typically. These results indicate that performance stability may be maintained throughout the long-duration data acquisitions typical of exoplanet spectroscopy.
Conclusions. We suggest that further study of possible stabilisation strategies should be an integral part of *Darwin*/TPF-I research and development.

Key words. technique: interferometric – instrumentation: spectrographs – space vehicles: instruments – methods: laboratory

1. Nulling interferometry and exoplanet research

The method proposed for exoplanet research for the *Darwin* (Karlsson & Kaltenegger 2003, European Space Agency-SCI 12, 2000) and TPF-I (Coulter 2003, JPL Publ. 05-5, 2005) missions is based on nulling interferometry Bracewell (1978) designed to enable IR spectroscopic measurements of exoplanetary atmospheres as well as imagery of extrasolar planetary systems. The challenge is a daunting one with manifold sources of noise Lay (2004): every photon coming from the exoplanet has to be acquired and separated from the noise by all means available. This implies that strategies have to be designed to improve the signal-to-noise ratio (S/N) during the data acquisition stage, while developing efficient algorithms for work with the acquired data. This article comments on the former approach.

Experimental studies of nulling interferometer breadboards (Serabyn 2003; Schmidtlin et al. 2005; Ollivier et al. 2001; Vink et al. 2003; Alcatel 2004; Brachet 2005, etc.) show that even in simple setups, the interference pattern is unstable, drifting with time. Even interferometers breadboarded on an optical bench in the relatively well-controlled laboratory environment (a priori simpler than the actual *Darwin*/TPF-I, with its multiple telescopes rotating in space) display drifts.

Chazelas et al. (2006) suggest "that special attention be given to servo systems... for monitoring key quantities such as the optical path difference (OPD) because these systems [have to] be free of long-term drifts" to obtain the required performance throughout long integration times, e.g. 10 days. Their paper gives a quantitative summary of these effects, using data from Ollivier (1999); Alcatel (2004); Vink et al. (2003), and suggests that servo mechanisms, using the signal itself, be employed to control drifts.

Chazelas et al. (2006) find that the "quality of the null" at a given wavelength and at a given moment in time can be evaluated in terms of the contrast in intensity between two adjacent dark and bright fringes. It can be expressed as the "nulling ratio" (also referred to as "stellar leakage" because it represents the stellar flux that the interferometer tries to cancel) due to the nulling instrument

$$nl(\lambda, t) = \frac{I_{\min}}{I_{\max}}$$

where $I_{\min}$ and $I_{\max}$ stand for the intensity of the onaxis dark fringe and of the offaxis bright fringe, respectively. Chazelas et al. (2006) show that two types of requirements must be met: one requirement is imposed upon the mean value of the nulling ratio $nl(\lambda, t)$, and the other upon its stability.

Taking into account the wavelength dependence of the star/planet contrast, they estimate the required mean null as:

$$\langle nl \rangle (\lambda) = 1.0 \times 10^{-5} \left(\frac{\lambda}{7\,\mu\mathrm{m}} \right)^{3.37}.$$

If such performance in terms of the mean value is achieved, its required long-term stability (at 7 μm) can be expressed as:

$$\sigma_{\langle nl \rangle}(7\,\mu\mathrm{m}, 10\,\mathrm{days}) \leq 3 \times 10^{-9}.$$

In order to obtain such a high relative stability, an instrument with only white noise is desirable, so that instability is reduced with integration time τ as $\tau^{-1/2}$.

Courtesy of our colleagues (Ollivier 1999; Alcatel 2004; Vink et al. 2003; Brachet 2005), we were able to analyse their nulling-experiment data. Unfortunately, in all cases, the power spectral density (PSD) of the null output displays a strong peak

Article published by EDP Sciences

Stabilising a nulling interferometer using optical path difference dithering: an update

Pavel Gabor[a], Bruno Chazelas[b], Peter A. Schuller[a], Frank Brachet[c], Marc Ollivier[a], Michel Decaudin[a], Alain Labèque[a], Philippe Duret[a], Sophie Jacquinod[a], Alain Léger[a]

[a]Institut d'Astrophysique Spatiale, Université de Paris-Sud 11, Orsay, France;
[b]Observatoire de Genève, Genève, Switzerland;
[c]Centre National d'Etudes Spatiales, Toulouse, France

ABSTRACT

Nulling interferometry has been suggested as the underlying principle for an instrument which could provide direct detection and spectroscopy of Earth-like exo-planets, including searches for potential bio-signatures. This paper documents the potential of optical path difference (OPD) stabilisation with dithering methods for improving the mean nulling ratio and its stability. The basic dithering algorithm, its refined versions and parameter tuning, are reviewed. This paper takes up the recently presented results[1] and provides an update on OPD-stabilisation at significantly higher levels of nulling performance.

Keywords: Nulling interferometry - *Darwin*/TPF-I - optical path stabilisation - optical path difference dithering

1. NULLING INTERFEROMETRY AND EXOPLANET RESEARCH

The method proposed for exoplanet research for the *Darwin*[2] and TPF-I[3] missions is based on nulling interferometry[4] designed to enable IR spectroscopic measurements of exoplanetary atmospheres as well as imagery of extrasolar planetary systems. The challenge is a daunting one with manifold sources of noise:[5] every photon coming from the exoplanet has to be acquired and separated from the noise by all means available. This implies that strategies have to be designed to improve the signal-to-noise ratio (S/N) during the data acquisition stage, while developing efficient algorithms for work with the acquired data. This article comments on the former approach.

Experimental studies of nulling interferometer breadboards[6–11] show that even in simple setups, the interference pattern is unstable, drifting with time. Even interferometers breadboarded on an optical bench in the relatively well-controlled laboratory environment (a priori simpler than the actual *Darwin*/TPF-I, with its multiple telescopes rotating in space) display drifts.

Chazelas et al.[12] suggest "that special attention be given to servo systems... for monitoring key quantities such as the optical path difference (OPD) because these systems [have to] be free of long-term drifts" to obtain the required performance throughout long integration times, e.g. 10 days. Their paper gives a quantitative summary of these effects, using data from,[9,10,13] and suggests that servo mechanisms, using the signal itself, be employed to control drifts.

Chazelas et al.[12] find that the "quality of the null" at a given wavelength and at a given moment in time can be evaluated in terms of the contrast in intensity between two adjacent dark and bright fringes. It can be expressed as the "nulling ratio" (also referred to as "stellar leakage" because it represents the stellar flux that the interferometer tries to cancel) due to the nulling instrument

$$nl(\lambda, t) = \frac{I_{\min}}{I_{\max}}$$

Corresponding author: p.gabor@jesuit.cz; Institut d'Astrophysique Spatiale, bât. 121, Campus Scientifique, 91405 Orsay, France; phone +33 1 69 85 87 32.

Tests of achromatic phase shifters performed on the SYNAPSE test bench: a progress report

Pavel Gabor[a], Peter A. Schuller[a], Bruno Chazelas[b], Michel Decaudin[a], Alain Labèque[a], Philippe Duret[a], Yves Rabbia[c], Ralf Launhardt[d], Jean Gay[c], Zoran Sodnik[e], Marc Barillot[f], Frank Brachet[g], Thomas Laurent[h], Sophie Jacquinod[a], Denis Vandormael[i], Jérôme Loicq[i], Dimitri Mawet[j], Marc Ollivier[a], Alain Léger[a]

[a]Institut d'Astrophysique Spatiale, Univ. Paris-Sud 11, Orsay, France;
[b]Observatoire de Genève, Genève, Switzerland;
[c]Observatoire de la Côte d'Azur, Nice, France;
[d]Max-Planck-Institut für Astronomie, Heidelberg, Germany;
[e]European Space Agency, Nordwijk, Netherlands;
[f]Thales Alenia Space, Cannes La Bocca, France;
[g]Centre National d'Etudes Spatiales, Toulouse, France;
[h]Univ. Liège, Liège, Belgium;
[i]Centre Spatial de Liège, Liège, Belgium;
[j]Univ. Liège, Institut d'Astrophysique et de Géophysique, Liège, Belgium

ABSTRACT

The achromatic phase shifter (APS) is a component of the Bracewell nulling interferometer studied in preparation for future space missions (viz. *Darwin*/TPF-I) focusing on spectroscopic study of Earth-like exo-planets. Several possible designs of such an optical subsystem exist. Four approaches were selected for further study. Thales Alenia Space developed a dielectric prism APS. A focus crossing APS prototype was developed by the OCA, Nice, France. A field reversal APS prototype was prepared by the MPIA in Heidelberg, Germany. Centre Spatial de Liège develops a concept based on Fresnel's rhombs. This paper presents a progress report on the current work aiming at evaluating these prototypes on the SYNAPSE test bench at the Institut d'Astrophysique Spatiale in Orsay, France.

Keywords: Nulling interferometry, exoplanets, infrared spectroscopy, *Darwin*/TPF-I, achromatic phase shifters

1. NULLING INTERFEROMETRY AND ACHROMATIC PHASE SHIFTERS

Nulling interferometry, based on the concept suggested by Bracewell[1] in 1978, is one of the methods of future exoplanet research. It has been studied for the mission *Darwin*[2] proposed to ESA as well as for the mission TPF-I (Terrestrial Planet Finder - Interferometry)[3] proposed to NASA.

The basic performance parameter of a nulling interferometer is the "nulling ratio" (sometimes also referred to as "stellar leakage" although this term refers more properly to stray starlight due to the fact a star is not a point source) $nl(\lambda, t) = I_{\min}/I_{\max}$ where $I_{\min}$ and $I_{\max}$ stand for the intensity of the on-axis dark fringe and of the off-axis bright fringe, respectively.

The goal of *Darwin*/TPF-I is to perform infra-red ($6 - 18\,\mu$m) imagery of extrasolar planetary systems and spectroscopic observations of exoplanetary atmospheres in view of evaluating the presence of biomarkers. In order to reach this goal, the required nulling performance has been estimated[4] as $\langle nl \rangle (\lambda) = 1.0\,10^{-5}\ (\lambda/7\,\mu\mathrm{m})^{3.37}$, with a level of long-term stability expressed as $\sigma_{\langle nl \rangle}(7\,\mu\mathrm{m}, 10\,\mathrm{days}) \leq 3\,10^{-9}$.

Corresponding author: p.gabor@jesuit.cz; Institut d'Astrophysique Spatiale, bât. 121, Campus Scientifique, 91405 Orsay, France; phone +33 1 69 85 87 32.

List of Figures

List of Tables

Bibliography

Review and discussion of APS requirements, ESA AO/1-3946/02/NL/JA. Technical report, 2002.

Alcatel. private communication from Alcatel Space Industries (now Thales Alenia Space), 2004.

J. R. P. Angel and N. J. Woolf. An Imaging Nulling Interferometer to Study Extrasolar Planets. *Astrophysical Journal*, 475:373–+, January 1997. doi: 10.1086/303529.

P. Baudoz, Y. Rabbia, and J. Gay. Achromatic interfero coronagraphy I. Theoretical capabilities for ground-based observations. *Astronomy and Astrophysics*, 141:319–329, January 2000a.

P. Baudoz, Y. Rabbia, J. Gay, R. Burg, L. Petro, P. Bely, B. Fleury, P.-Y. Madec, and F. Charbonnier. Achromatic interfero coronagraphy. II. Effective performance on the sky. *Astronomy and Astrophysics*, 145:341–350, August 2000b.

C.A. Beichman, N.J. Woolf, and C.A. Lindensmith. *The Terrestrial Planet Finder (TPF), JPL 99-3*. NASA, 1999. URL `http://planetquest.jpl.nasa.gov/TPF/tpf_book/index.cfm`.

Matthieu Boffety and David Drugeon. Étude du déphasage introduit par un déphaseur achromatique. Master's thesis, École supérieure d'optique, 2006.

H. Bokhove, J. P. Kappelhof, H. J. P. Vink, L. L. A. Vosteen, and Z. Sodnik. Broadband nulling using a prism phase shifter. In *ESA SP-539: Earths: DARWIN/TPF and the Search for Extrasolar Terrestrial Planets*, pages 367–369, October 2003.

R. W. Boyd. Intuitive explanation of the phase anomaly of focused light beams. *Journal of the Optical Society of America (1917-1983)*, 70:877–+, 1980.

R. N. Bracewell. Detecting nonsolar planets by spinning infrared interferometer. *Nature*, 274:780–+, August 1978.

Frank Brachet. *Étude et développement d'un déphaseur achromatique pour l'interférométrie en frange noire*. PhD thesis, Paris XI, 2005.

C. Buisset, X. Rejeaunier, Y. Rabbia, and M. Barillot. Stable deep nulling in polychromatic unpolarized light with multiaxial beam combination. *Applied Optics*, 46:7817–7822, November 2007. doi: 10.1364/AO.46.007817.

Christophe Buisset. *Caractérisation et optimisation d'un interféromètre à frange sombre et à bande large*. PhD thesis, Nice, 2007.

B. Chazelas, F. Brachet, P. Bordé, B. Mennesson, M. Ollivier, O. Absil, A. Labèque, C. Valette, and A. Léger. Instrumental stability requirements for exoplanet detection with a nulling interferometer : variability noise is a central issue. *Applied Optics*, 45(5):984–992, 2006.

Bruno Chazelas. *Contribution à l'étude de l'interférométrie annulante pour la détection d'exo-planètes*. PhD thesis, Paris XI, 2007.

V. Coude Du Foresto, G. Perrin, C. Ruilier, B. P. Mennesson, W. A. Traub, and M. G. Lacasse. FLUOR fibered instrument at the IOTA interferometer. In R. D. Reasenberg, editor, *Society of Photo-Optical Instrumentation Engineers (SPIE) Conference Series*, volume 3350 of *Presented at the Society of Photo-Optical Instrumentation Engineers (SPIE) Conference*, pages 856–863, July 1998.

Michael J. Crowe. *The Extraterrestrial Life Debate, 1750–1900*. Dover Publications, 1999.

René Descartes. *Principia philosophiae*. 1644.

Steven J. Dick. *Plurality of Worlds: The Extraterrestrial Life Debate from Democritus to Kant*. Cambridge University Press, 1984.

Steven J. Dick. *Life on Other Worlds: The 20th Century Extraterrestrial Life Debate*. Cambridge University Press, 1996.

F. D. Drake. Project Ozma. *Physics Today*, 14:40–+, 1961.

Frank Drake and Dava Sobel. *Is Anyone Out There? The Scientific Search for Extraterrestrial Intelligence*. Delacorte Pr., New York, 1992.

G. Faure and T. Mensing. *Introduction to planetary science. The geological perspective*. Springer, 2007.

R. Flatscher, Z. Sodnik, K. Ergenzinger, U. Johann, and R. Vink. DARWIN nulling interferometer breadboard I: System engineering and measurements. In *ESA SP-539: Earths: DARWIN/TPF and the Search for Extrasolar Terrestrial Planets*, pages 283–291, October 2003.

Bernard le Bovier de Fontenelle. *Entretiens sur la pluralité des mondes*. 1686.

Fragment. From Anaxagoras quoted by Simplicius of Cilicia. B4a.

Fragment. From Simplicius of Cilicia quoted by Theophrastus, *Φυσικων Δοξαι*. Phys. opin. 4, 7.

P. Gabor, B. Chazelas, F. Brachet, M. Ollivier, M. Decaudin, S. Jacquinod, A. Labèque, and A. Léger. Stabilising a nulling interferometer using optical path difference dithering. *Astronomy & Astrophysics*, 483:365–369, May 2008a. doi: 10.1051/0004-6361:20077830.

P. Gabor, B. Chazelas, P. A. Schuller, F. Brachet, M. Ollivier, M. Decaudin, A. Labèque, P. Duret, S. Jacquinod, and A. Léger. Stabilising a nulling interferometer using optical path difference dithering: an update. In *Society of Photo-Optical Instrumentation Engineers (SPIE) Conference Series*, volume 7013 of *Society of Photo-Optical Instrumentation Engineers (SPIE) Conference Series*, July 2008b. doi: 10.1117/12.789222.

P. Gabor, P. A. Schuller, B. Chazelas, M. Decaudin, A. Labèque, P. Duret, Y. Rabbia, R. Launhardt, J. Gay, Z. Sodnik, M. Barillot, F. Brachet, T. Laurent, S. Jacquinod, D. Vandormael, J. Loicq, D. Mawet, M. Ollivier, and A. Léger. Tests of achromatic phase shifters performed on the SYNAPSE test bench: a progress report. In *Society of Photo-Optical Instrumentation Engineers (SPIE) Conference Series*, volume 7013 of *Society of Photo-Optical Instrumentation Engineers (SPIE) Conference Series*, July 2008c. doi: 10.1117/12.789269.

Pavel Gabor. Achromatic phase shifter performance stabilisation through optical path difference modulation. Master's thesis, Master Recherche (M2) Astronomie et Astrophysique, Université Paris VII, 2006.

R. O. Gappinger, R. T. Diaz, A. Ksendzov, P. R. Lawson, O. P. Lay, K. M. Liewer, F. M. Loya, S. R. Martin, E. Serabyn, and J. K. Wallace. Experimental evaluation of achromatic phase shifters for mid-infrared starlight suppression. *Applied Optics*, 48:868–+, February 2009. doi: 10.1364/AO.48.000868.

Stephen Gaukroger. *The emergence of a scientific culture. Science and the shaping of modernity, 1210–1685*. Oxford University Press, 2006.

Jean Gay and Yves Rabbia. *C.R. Acad.Sci. Paris*, IIb, 322:265, 1996.

A. Gelb and W. E. Vander Velde. *Multiple-Input Describing Functions and Nonlinear System Design*. McGraw-Hill, New York, 1968.

Anthony Gottlieb. *Particle Man.* A review of Rowland's *Giordano Bruno. Philosopher/Heretic*. New York Times, 19 Dec 2008.

G. Gouy. *C.R. Acad.Sci. Paris*, 110:1251, 1890.

Pierre Haguenauer and Eugene Serabyn. Deep nulling of laser light with a single-mode-fiber beam combiner. *Applied Optics*, 45(12):2749–2754, 2006. URL `http://ao.osa.org/abstract.cfm?URI=ao-45-12-2749`.

K. Houairi, F. Cassaing, J. M. Le Duigou, B. Sorrente, S. Jacquinod, and J. P. Amans. PERSEE, the dynamic nulling demonstrator: recent progress on the cophasing system. In *Society of Photo-Optical Instrumentation Engineers (SPIE) Conference Series*, volume 7013 of *Presented at the Society of Photo-Optical Instrumentation Engineers (SPIE) Conference*, July 2008. doi: 10.1117/12.789113.

Kamel Houairi. *Cophasage de téléscopes multi-pupilles sur point source : application à linterféromtre en frange noire Persée*. PhD thesis, Observatoire de Paris, oct. 2009.

E. M. Jones. Where is everybody? An account of Fermi's question. *Physics Today*, pages 11–13, Aug 1985.

Charles H. Kahn. *Anaximander and the origins of Greek cosmology*, page 52. Columbia Unversity Press, 1960.

L. Kaltenegger, W. A. Traub, and K. W. Jucks. Spectral Evolution of an Earth-like Planet. *Astrophysical Journal*, 658:598–616, March 2007. doi: 10.1086/510996.

A. Ksendzov, O. Lay, S. Martin, J. S. Sanghera, L. E. Busse, W. H. Kim, P. C. Pureza, V. Q. Nguyen, and I. D. Aggarwal. Characterization of mid-infrared single mode fibers as modal filters. *Applied Optics*, 46: 7957–7962, November 2007.

L. Labadie, E. Le Coarer, R. Maurand, P. Labeye, P. Kern, B. Arezki, and J.-E. Broquin. Mid-infrared laser light nulling experiment using single-mode conductive waveguides. *Astronomy and Astrophysics*, 471: 355–360, August 2007. doi: 10.1051/0004-6361:20067005.

Ralf Launhardt. Breadboarding an achromatic phase shifter for midinfrared nulling interferometry. volume 7013 of *To be presented at the Society of Photo-Optical Instrumentation Engineers (SPIE) Conference*, pages paper 7013–175, June 2008.

Thomas Laurent. Participaton à l'expérience d'interférométrie annulante SYNAPSE: validation des technologies de la mission spatiale Darwin. Master's thesis, Université de Liège, 2008.

P. R. Lawson, O. P. Lay, and C. A. Beichman. *Terrestrial Planet Finder Interferometer Science Working Group Report*. NASA, 2007.

P. R. Lawson, O. P. Lay, S. R. Martin, R. D. Peters, R. O. Gappinger, A. Ksendzov, and D. P. Scharf. Technology challenges for exoplanet detection with mid-IR interferometry. In *7th International Conference on Space Optics, 14-17 October, Toulouse, France*, October 2008.

Peter R. Lawson. Nulling interferometry and the detection of Earth-like planets. state of the art., 2009. URL `http://planetquest.jpl.nasa.gov/TPF-I/stateOfTheArt.cfm`.

P.R. Lawson and J.A. Dooley. *Technology Plan for the Terrestrial Planet Finder Interferometer, JPL 05-5*. NASA, 2005. URL `http://planetquest.jpl.nasa.gov/Navigator/library/tpfI414.pdf`.

O. P. Lay. Removing instability noise in nulling interferometers. In *Society of Photo-Optical Instrumentation Engineers (SPIE) Conference Series*, volume 6268 of *Society of Photo-Optical Instrumentation Engineers (SPIE) Conference Series*, July 2006. doi: 10.1117/12.670603.

O. P. Lay. Systematic errors in nulling interferometers. *Applied Optics*, 43:6100–6123, 2004.

J. Lazio, T. Bastian, G. Bryden, W. M. Farrell, J.-M. Griessmeier, G. Hallinan, J. Kasper, T. Kuiper, A. Lecacheux, W. Majid, R. Osten, E. Shklonik, I. Stevens, D. Winterhalter, and P. Zarka. Magnetospheric Emissions from Extrasolar Planets. *Astronomy*, 2010:177–+, 2009.

A. Léger, J-M. Mariotti, J-L. Puget, D. Rouan, and J. Schneider. *DARWIN: Mission concept for the ESA Horizon 2000+ program.* ESA, 1993.

A. Léger, M. Ollivier, K. Altwegg, and N. J. Woolf. *Astronomy and Astrophysics*, 341:304, 1999.

S. Martin, P. Szwaykowski, and F. Loya. Testing exo-planet signal extraction using the Terrestrial Planet Finder planet detection testbed. In D. R. Coulter, editor, *Society of Photo-Optical Instrumentation Engineers (SPIE) Conference Series*, volume 5905 of *Society of Photo-Optical Instrumentation Engineers (SPIE) Conference Series*, pages 70–79, August 2005. doi: 10.1117/12.615559.

S. R. Martin, R. O. Gappinger, F. M. Loya, B. P. Mennesson, S. L. Crawford, and E. Serabyn. Mid-infrared nuller for Terrestrial Planet Finder: design, progress, and results. In *Techniques and Instrumentation for Detection of Exoplanets. Edited by Coulter, Daniel R. Proceedings of the SPIE, Volume 5170, pp. 144-154 (2003).*, pages 144–154, November 2003a. doi: 10.1117/12.521312.

S. R. Martin, E. Serabyn, and G. Hardy. Deep nulling of laser light in a rotational shearing interferometer. In *Interferometry for Optical Astronomy II. Edited by Wesley A. Traub. Proceedings of the SPIE, Volume 4838.*, pages 656–667, February 2003b.

S. R. Martin, P. Szwaykowski, F. M. Loya, and K. Liewer. Progress in testing exo-planet signal extraction on the TPF-I planet detection testbed. In *Society of Photo-Optical Instrumentation Engineers (SPIE) Conference Series*, volume 6268 of *Society of Photo-Optical Instrumentation Engineers (SPIE) Conference Series*, July 2006. doi: 10.1117/12.672646.

J. Lewis McIntyre. *Giordano Bruno*. 1992.

B. Mennesson, M. Ollivier, and C. Ruilier. Use of single-mode waveguides to correct the optical defects of a nulling interferometer. *Optical Society of America Journal*, 19:596–602, March 2002.

B. Mennesson, S. L. Crawford, E. Serabyn, S. Martin, M. Creech-Eakman, and G. Hardy. Laboratory performance of the Keck Interferometer nulling beam combiner. In *ESA SP-539: Earths: DARWIN/TPF and the Search for Extrasolar Terrestrial Planets*, pages 525–528, October 2003.

B. Mennesson, A. Léger, and M. Ollivier. Direct detection and characterization of extrasolar planets: The Mariotti space interferometer. *Icarus*, 178:570–588, November 2005. doi: 10.1016/j.icarus.2005.05.012.

B. Mennesson, P. Haguenauer, E. Serabyn, and K. Liewer. Deep broad-band infrared nulling using a single-mode fiber beam combiner and baseline rotation. In *Society of Photo-Optical Instrumentation Engineers (SPIE) Conference Series*, volume 6268 of *Presented at the Society of Photo-Optical Instrumentation Engineers (SPIE) Conference*, July 2006. doi: 10.1117/12.672157.

R. M. Morgan, J. H. Burge, and N. J. Woolf. Final laboratory results of visible nulling with dielectric plates. In *Interferometry for Optical Astronomy II. Edited by Wesley A. Traub. Proceedings of the SPIE, Volume 4838, pp. 644-655 (2003).*, pages 644–655, February 2003.

M. Ollivier. *Coronographie interférentielle pour la mission Darwin*. PhD thesis, Université Paris XI, December 1999.

M. Ollivier, J.-M. Mariotti, A. Léger, P. Sékulic, J. Brunaud, and G. Michel. Interferometric coronography for the DARWIN space mission - Laboratory demonstration experiment. *Astronomy and Astrophysics*, 370:1128–1136, May 2001.

M. Perryman, O. Hainaut, D. Dravins, A. Léger, A. Quirrenbach, H. Rauer, F. Kerber, R. Fosbury, F. Bouchy, F. Favata, M. Fridlund, R. Gilmozzi, A. Lagrange, T. Mazeh, D. Rouan, S. Udry, and J. Wambsganss. Report by the ESA-ESO Working Group on Extra-Solar Planets. *ArXiv Astrophysics e-prints*, June 2005.

R. D. Peters, O. P. Lay, A. Hirai, and M. Jeganathan. Progress in deep broadband interferometric nulling with the adaptive nuller. In *Society of Photo-Optical Instrumentation Engineers (SPIE) Conference Series*, volume 7013 of *Presented at the Society of Photo-Optical Instrumentation Engineers (SPIE) Conference*, July 2008. doi: 10.1117/12.786845.

Robert D. Peters, Oliver P. Lay, and Muthu Jeganathan. Broadband phase and intensity compensation with a deformable mirror for an interferometric nuller. *Appl. Opt.*, 47(21):3920–3926, 2008. URL `http://ao.osa.org/abstract.cfm?URI=ao-47-21-3920`.

Michael Polanyi. *Personal Knowledge. Towards a Post-Critical Philosophy*. Harper, 1958.

Y. Rabbia, Y. Gay, and E. Bascou. Achromatic phase shifters for nulling interferometry. In *ICSO'2000 - Conférence Internationale d'Optique Spatiale, Toulouse, France, Dec. 5-7, 2000) CNES Eds.*, pages 389–400, 2000.

Y. Rabbia, Y. Gay, E. Bascou, and J. L. Schneider. Summary assessment report on achromatic phase shifters for space interferometry. Technical report, ESA ESTEC, Contract 14 398/00/NL/MV, 2001.

Y. Rabbia, J. Gay, B. Chazelas, A. Labèque, and J.-P. Rivet. Nulling interferometry : Lommel's integrals applied to a Fresnel's diffraction effect. In C. Aime and F. Vakili, editors, *IAU Colloq. 200: Direct Imaging of Exoplanets: Science & Techniques*, pages 265–270, 2006. doi: 10.1017/S1743921306009434.

Ingrid D. Rowland. *Giordano Bruno. Philosopher/Heretic*. Farrar, Strauss & Giroux, 2008.

Carl Sagan. *Cosmos*. Random House, 1980.

R. Samuele, J. K. Wallace, E. Schmidtlin, M. Shao, B. M. Levine, and S. Fregoso. Experimental progress and results of a visible nulling coronagraph. In *Proceedings of IEEE Aerospace Conference*. Institute of Electrical and Electronic Engineers, 2007.

N. C. Santos, G. Israelian, M. Mayor, R. Rebolo, and S. Udry. Statistical properties of exoplanets. II. Metallicity, orbital parameters, and space velocities. *Astronomy & Astrophysics*, 398:363–376, January 2003. doi: 10.1051/0004-6361:20021637.

E. Schmidtlin, J. K. Wallace, R. Samuele, B. M. Levine, and M. Shao. Recent Progress of Visible Light Nulling Interferometry and First 1 Million Null Result. In C Aime and F. Vakili, editors, *Direct Imaging of Exoplanets: Science and Techniques*, pages 353–360. IAU Colloquium No. 200, 2005.

F. Selsis, D. Despois, and J.-P. Parisot. *Astronomy and Astrophysics*, 388:985, 2002.

E. Serabyn. Nulling interferometry progress. In Wesley A. Traub, editor, *Interferometry for Optical Astronomy II. Proceedings of the SPIE, volume 4838*, pages 594–608, February 2003.

E. Serabyn. Nulling interferometry: symmetry requirements and experimental results. In P. Léna & A. Quirrenbach, editor, *Society of Photo-Optical Instrumentation Engineers (SPIE) Conference Series*, volume 4006 of *Society of Photo-Optical Instrumentation Engineers (SPIE) Conference Series*, pages 328–339, July 2000.

E. Serabyn and M. Colavita. Fully symmetric nulling beam combiners. *Applied Optics*, 40:1668, 2001.

E. Serabyn and M. M. Colavita. Fully Symmetric Nulling Beam Combiners. *Applied Optics*, 40:1668–1671, April 2001.

I. S. Shklovskii and C. Sagan. *Intelligent life in the universe*. Random House, 1966.

Daniel Špelda. *Astronomie v antice [Astronomy in Antiquity]*. Montanex, Ostrava, 2006.

J. Spronck, S. F. Pereira, and J. J. M. Braat. Chromatism compensation in wide-band nulling interferometry for exoplanet detection. *Applied Optics*, 45:597–604, February 2006. doi: 10.1364/AO.45.000597.

James Strick. Darwin and the origin of life: A historical perspective. *American Associaiton for the Advancement of Science*, Workshop “Exploring the Origin, Extent, and Future of Life: Philosophical, Ethical, and Theological Perspectives”, Feb 2003.

Leonard Susskind. *The Cosmic Landscape: String Theory and the Illusion of Intelligent Design*. Back Bay Books, 2006.

A. V. Tavrov, Y. Otani, T. Kurokawa, and M. Takeda. 3D common-path interferometer: achromatic nulling of on-axial light. In D. R. Coulter, editor, *Society of Photo-Optical Instrumentation Engineers (SPIE) Conference Series*, volume 5905 of *Society of Photo-Optical Instrumentation Engineers (SPIE) Conference Series*, pages 398–404, August 2005. doi: 10.1117/12.620027.

The Stanford encyclopedia of philosophy. The entry on Anaxagoras. 2007.

H. J. P. Vink, N. J. Doelman, R. Flatscher, and Z. Sodnik. DARWIN nulling interferometer breadboard II: design and manufacturing. In *ESA SP-539: Earths: DARWIN/TPF and the Search for Extrasolar Terrestrial Planets*, pages 641–645, October 2003.

L. L. A. Vosteen, H. J. P. Vink, H. van Brug, and H. Bokhove. Achromatic phase-shifter breadboard extensions. In D. R. Coulter, editor, *Society of Photo-Optical Instrumentation Engineers (SPIE) Conference Series*, volume 5905 of *Society of Photo-Optical Instrumentation Engineers (SPIE) Conference Series*, pages 91–101, August 2005. doi: 10.1117/12.614337.

J. K. Wallace, M. Shao, B. F. Lane, B. M. Levine, F. Loya, A. Azizi, B. Holmes, F. Aguayo, J. Negron, G. Sanchez, and R. O. Gappinger. Experimental results from the optical planet detector interferometer. In D. R. Coulter, editor, *Society of Photo-Optical Instrumentation Engineers (SPIE) Conference Series*, volume 5170 of *Society of Photo-Optical Instrumentation Engineers (SPIE) Conference Series*, pages 209–216, November 2003. doi: 10.1117/12.506356.

J. K. Wallace, V. Babtiwale, R. Bartos, K. Brown, R. Gappinger, F. Loya, D. MacDonald, S. Martin, J. Negron, T. Truong, and G. Vasisht. Mid-IR interferometric nulling for TPF. In *New Frontiers in Stellar Interferometry, Proceedings of SPIE Volume 5491. Edited by Wesley A. Traub. Bellingham, WA: The International Society for Optical Engineering, 2004., p.862*, pages 862–+, October 2004.

K. Wallace, G. Hardy, and E. Serabyn. Deep and stable interferometric nulling of broadband light with implications for observing planets around nearby stars. *Nature*, 406:700–702, August 2000.

Stephen Webb. *If the Universe is teeming with aliens... Where is everybody? Fifty solutions to the Fermi Paradox and the problem of extraterrestrial life*. Springer, 2002.

Valérie Weber. *Étude de l’interféromètre à frange noire MAII*. PhD thesis, Université de Nice-Sophia Antipolis, June 2004.

N. J. Woolf and J. R. P. Angel. Planet Finder Options I: New Linear Nulling Array Configurations. In *ASP Conf. Ser. 119: Planets Beyond the Solar System and the Next Generation of Space Missions*, pages 285–+, 1997.

Résumé

Les deux premiers chapitres introduisent le sujet. Le premier montre le contexte général de l'exobiologie, principalement dans une perspective historique, ainsi que l'étude récente des planètes extrasolaires. Le deuxième chapitre décrit le principe de l'interférométrie en frange noire. Le chapitre 3 est une description de Synapse et Nulltimate, le chapitre 4 continue la description, présentant en détail le système de stabilisation de la différence de marche optique. Les chapitres 5 et 6 contiennent les résultats. Le chapitre 5 présente les résultats en termes de taux d'extinction *nl* et sa stabilité σ, constatant une différence entre les taux d'extinction obtenus avec les sources laser et les autres sources. Le chapitre 6 liste nos études qui visaient une explication de ce phénomène. Le chapitre final est une prospective et conclusion.

Chapitre 1 : "Astrobiology and Exoplanetology"

Ancienne histoire

La première section de ce chapitre évoque une étude historique de la question du pluralisme cosmique (Somme-nous seuls dans l'Univers ?), présentée dans l'Annexe A. Il s'agit d'un travail qui a été présenté au congrès *Darwin's Impact on Science, Society, and Culture* qui a eu lieu à Braga (Portugal) du 9 au 12 septembre 2009. La question du pluralisme cosmique est ancienne, remontant peut-être à l'époque d'Anaximandre (c. 610–546 av. J.-C.).

La première forme historique de cette position est celle des atomistes et les épicuriens, pour qui il s'agit d'une pluralité des univers. Chez les anciens, un univers était constitué d'une terre et des corps célestes dans son entourage : des "planètes" (les corps célestes sujets aux mouvements sur la voûte céleste) et les "étoiles fixes". La deuxième forme du pluralisme cosmique est due à Nicolas de Cues (1401–1464) qui était le premier penseur à considérer que la terre était un corps céleste parmi d'autres. Dans son chef-d'oeuvre, *De docta ignorantia*, publié en 1440, il présente l'idée que, comme la terre ne diffère pas qualitativement des autres corps célestes, ceux-ci doivent être habités aussi bien que la terre. Nicolas de Cues suppose que tous les corps célestes sont habités, y compris le soleil, la lune, les planètes et les étoiles "fixes". Néanmoins, quant à la liste des corps célestes, il ne questionne pas le modèle de l'univers hérité de l'antiquité. L'apport de Giordano Bruno (1548 –1600) consiste à postuler que les étoiles "fixes" sont de même nature que le soleil. Par conséquent, en parallèle avec le soleil, chaque étoile "fixe" est entourée de planètes.

L'historiographie idéologisée des sciences, produite au 19^{e} siècle par des historiens positivistes, dit que, sur le chemin du progrès, le pluralisme cosmique a marqué un conflit clef entre la science et l'obscurantisme, avec le martyre d'un scientifique : Giordano Bruno, le seul martyr sanglant de cette lutte historique, brûlé vif parce qu'il a héroïquement refusé de renoncer à l'idée d'une infinité de mondes habités. Le chapitre 1 introduit deux arguments forts indiquant que cette version de l'histoire n'a pas de support dans les faits : (1) *De docta ignorantia* fut publié en 1440 et huit ans plus tard, son auteur, Nicolas de Cues, a été créé cardinal. Ses travaux ne furent jamais proscrits. (2) Le dossier du procès de Giordano Bruno a disparu suite à la prise de Rome par Napoléon. Sans le dossier, il est impossible de savoir quelles étaient les huit propositions auxquelles Bruno a “obstinément” refusé de renoncer. Pourtant, seize ans après l’exécution de Bruno, pendant le premier procès de Galilée, personne ne mentionne le procès de Bruno, ce qui serait normal si celui-ci constituerait précédent pour celui-là. Il est donc très probable que ni son pluralisme cosmique ni ses positions coperniciennes n’ont été décisives pour sa condamnation.

Développement récent

Dans la suite, mon manuscrit parcourt rapidement le paradoxe Fermi, l’équation de Drake, la discussion sur la vie identifiable par les moyens astronomiques et spatiaux, ainsi que les biosignatures spectroscopiques. SETI, l’exploration du système solaire (Mars, Titan, Europa) sont brièvement mentionnés.

Exoplanètes : détection et observation

Le chapitre continue avec une liste des défis et les techniques de la détection des exoplanètes : contraste entre l’étoile et la planète, la résolution angulaire, la lumière diffuse zodiacale et exo-zodiacale ; les techniques de détection indirecte (astrométrie, vélocimétrie radiale, transits, microlentilles gravitationnelles) et de l’observation directe (coronographie, observation avec un obturateur et interférométrie en frange noire).

A la fin du chapitre, il y a une description schématique d’un instrument spatial placé au point “deux” de Lagrange (L2) du système Soleil-Terre, consistant en quatre télescopes volant en formation avec une recombinaison des faisceaux “en frange noire”. Il s’agit des projets convergents *Darwin* (Agence Spatiale Européenne) et *Terrestrial Planet Finder Interferometer* (National Aeronautics and Space Administration). Les spécifications clefs d’une telle mission, en termes du taux d’extinction et de sa stabilité, sont données.

Chapitre 2 : “Nulling Interferometry”

Le principe et paramètres

L’interférométrie en frange noire, proposée déjà en 1978 par R. N. Bracewell, est basée sur la recombinaison destructive achromatique dans une bande passante donnée. Un interféromètre classique recombine deux faisceaux en phase, c’est-à-dire, le système de franges résultant d’un balayage de la différence de marche optique a un maximum au milieu de son enveloppe. La forme de l’enveloppe est donnée par le spectre de la lumière recombinée. Par définition, elle est symétrique autour de la différence de marche zéro. Les franges, inscrites dans l’enveloppe, sont des maxima et minima correspondant aux différences de marche de $k\lambda/2$, où k est pair pour le maxima et impair pour les minima. Un interféromètre constructif, encore une fois par définition, voit un maximum sur l’axe de l’enveloppe, c’est-à-dire, à la différence de marche zéro.

Dans le cas monochromatique, il est trivial de positionner, au milieu de l’enveloppe, un minimum : il suffit de changer la différence de marche de $\lambda/2$. Dans le cas d’une bande large, par contre, cette approche ne peut pas réussir, car $\lambda/2$ n’est pas constant. Pour cette raison, un interféromètre en frange noire a besoin d’un système qui change la phase d’un faisceau par rapport à l’autre d’une manière indépendante de la longueur d’onde : un déphaseur achromatique.

La première partie du chapitre 2 décrit le principe de l’interféromètre en frange noire et propose quelques quantités qui sont utilisées pour caractériser la performance de ces instruments. Il s’agit principalement du taux d’extinction et de son inverse, du taux de réjection, ainsi que de la stabilité de ces valeurs (une discussion plus détaillée de la stabilité est donnée dans l’Annexe A).

Déphaseurs achromatiques

La collaboration *Darwin* a étudié dix concepts différents de déphaseurs achromatiques (Annexe B) dont quatre ont été choisi pour une étude expérimentale. Trois parmi ces études ont abouti à la fabrication des prototypes qui ont été mis à la disposition du groupe *Darwin* de l'Institut d'Astrophysique Spatiale, pour des tests. Il s'agit des déphaseurs basés sur : (1) le passage par un foyer optique, (2) le retournement du champ électrique et (3) la dispersion dans des matériaux diélectriques.

A part les trois prototypes, le banc SYNAPSE utilise un quatrième déphaseur, réalisé comme deux paires de prismes diélectriques. Cet ensemble sert aussi de compensateur du chromatisme (pour équilibrer les épaisseurs du diélectrique traversées par les deux faisceaux). Le manuscrit contient une description plus détaillée du principe de ce déphaseur.

Qualité du front d'onde et la stabilité

Une brève discussion de deux autres points cruciaux est incluse dans le chapitre 2. Les interféromètres en frange noire sont très sensibles à la qualité du front d'onde, d'où le besoin d'un filtre soit spatial (trou d'épingle), soit modal (fibre monomode). Pour une opération fructueuse en termes de la détection et analyse spectrale de l'émission des exoplanètes, les interféromètres en frange noire ont besoin des longs temps d'intégration et donc d'une haute stabilité de performance.

L'état de l'art

Dans la dernière section du chapitre 2, un état de l'art concernant les bancs de test est présenté. Dans la version finale du manuscrit, nous prévoyons une étude plus concise de cette question. Pour l'instant, nous reprenons deux compilations réalisées par Bruno Chazelas et Peter R. Lawson. Il est clair que les taux d'extinction importants sont plus facilement accessibles par des expériences en bande passante étroite.

Chapitre 3 : "Description of SYNAPSE & NULLTIMATE"

Le chapitre 3, donnant une description détaillée du banc SYNAPSE, mais aussi du banc NULLTIMATE, vise un lecteur qui sent le besoin de comprendre non pas seulement une énumération des composants mais aussi la logique qui a guidé leur choix. Une description de l'électronique et du système informatique de contrôle des bancs est aussi inclue. Un passage important porte sur l'utilisation de la détection synchrone.

Chapitre 4 : "Stabilisation"

D'un côté, ce chapitre complète la description des bancs, car le système de stabilisation en fait partie importante. De l'autre, le chapitre ne contient pas seulement une description du système mais aussi un certain nombre de résultats de la stabilisation. Ces résultats ont fait l'objet de deux publications ajoutées en annexes (E et F). Le premier papier (publié en *Astronomy & Astrophysics*) contient les premiers résultats obtenus avec une source thermique (corps noir 2000 K), le deuxième (présentée au congrès SPIE à Marseille 2008) est une mise-à-jour du premier, apportant les résultats obtenus avec une source laser.

Le système de stabilisation implémenté, vise la différence de marche optique. Il est basé sur des mesures du signal recombiné, correspondant aux positions différentes de la ligne à retard fine. A la position du départ, la ligne à retard est placée sur une frange noire, proche de son minimum. Dans la suite, la ligne à retard fait deux excursions équidistantes de chaque côté de la position de départ. Les trois flux, correspondant aux trois positions, sont mesurés et une nouvelle position approximative du minimum interférométrique en est déduite. L'enregistrement des données s'effectue seulement quand la ligne à retard est dans les positions approximatives du minimum de la frange. Il s'agit donc d'un système où le signal scientifique fournit l'information métrologique. Il faut le distinguer des systèmes d'asservissement basés sur une modulation continue de la position de la lighe à retard, où le signal scientifique est enregistré continuellement. Dans le cas d'un système mécaniquement stable, un système comme le nôtre peut aider à obtenir des mesures reproductibles sans dégrader la performance et sans gaspiller trop le temps d'intégration.

Chapitre 5 : “SYNAPSE results update”

Le banc SYNAPSE a été commissionné vers la fin de l’année 2005. Les premiers résultats, obtenus par Frank Brachet, ont été mesurés avec une source thermique en bande K (2.0-2.5 µm). Le chapitre 5 résume la calibration du détecteur, la transmission du banc, la stabilité thermique et mécanique ainsi que les techniques de mesure proposées et le protocole expérimental utilisé.

En bande K, le taux d’extinction atteint était $nl \approx 3 \times 10^{-4}$. Des dérives considérables ont dû être stabilisées au niveau de la différence de marche (comme nous avons vu dans le chapitre précédent). Avec une source laser (3.39 µm), le taux d’extinction était $nl \approx 1 \times 10^{-5}$. La différence importante entre ces résultats, bande large versus monochromatique, faisaient l’objet de nombreuses études et tests. En été 2008, plusieurs raisons ont mené au passage du banc SYNAPSE au banc NULLTIMATE (principalement une volonté de clore un contrat, mais aussi l’espoir, sur NULLTIMATE d’une stabilité mécanique et thermique ainsi qu’un flux plus important). Le chapitre 5 est essentiellement une mise-à-jour d’un article (présentée au congrès SPIE à Marseille 2008 ; annexe G), qui fait l’état des lieux des travaux expérimentaux sur SYNAPSE au moment de ce passage vers NULLTIMATE.

Le chapitre conclut avec trois points :

1. Le prototype du déphaseur basé sur le passage par un foyer optique ne limite pas la performance du banc.
2. La présence des polariseurs améliore le taux d’extinction.
3. Il y a une différence difficile à expliquer entre la performance du banc en lumière monochromatique et en bande large.

Chapitre 6 : “Error budget”

Le dernier chapitre avant la conclusion apporte un survol des estimations théoriques et des mesures expérimentales des effets qui nuisent à la performance du banc : non-linéarité du détecteur, vignettage, déformation du profil de faisceau, polarisation différentielle, des effets chromatiques latéraux et angulaires introduits par la dispersion, multiplicité de points dans l’espace (*e*, ddm) où le système des franges parat symétrique, défauts des traitements optiques, inhomogénéités des éléments en transmission, déséquilibre spectral entre les deux bras de l’interféromètre, la qualité du front d’onde. Comparant les estimations théoriques avec les mesures expérimentales, plusieurs de ces effets ont été clairement éliminés comme explication possible de la différence entre les performances du banc en bande large et en lumière monochromatique sur le banc SYNAPSE. Pourtant, certains effets ont été retenus pour une investigation sur le banc NULLTIMATE. Il s’agit

- des mesures avec une bande étroite (FWHM de 16 nm autour de 2.3 µm),
- une comparaison entre des mesures en cette bande étroite et des mesures avec une diode laser strictement monochromatique (2.32 µm),
- une comparaison entre les mesures avec deux sources monochromatiques (2.32 et 3.39 µm)
- mesures de la dépendance du taux d’extinction et de la position de la frange noire en fonction de la polarisation.

Chapitre 7 : “Conclusions and perspectives”

Par rapport aux travaux sur le banc SYNAPSE, la construction et mise en service du banc NULLTIMATE représente la prospective immédiate. Le chapitre 7 résume l’état de ces travaux, ainsi qu’un plan de mesures intéressantes à effectuer avec le nouvel instrument. Dans ce cadre, il est rassurant que le banc NULLTIMATE promet un fonctionnement nettement plus stable mécaniquement et thermiquement que le banc SYNAPSE. Son architecture plus simple donne l'espoir d'une facilité plus grande quant à la comparaison entre les attentes théoriques et les résultats obtenus. Le manuscrit suggère quatre études qui peuvent apporter des résultats intéressants pour la communauté scientifique :

- une étude de l'extinction en lumière polarisée,
- tests des prototypes des déphaseurs achromatiques,
- développement d'un système de stabilisation de l'équilibre des flux entre les bras de l'interféromètre et
- passage à la bande passante autour du 10 μm.

Ensuite, le chapitre essaie placer ces travaux dans un contexte plus large, de la préparation d'un projet d'un interféromètre spatial (*Darwin*/TPF-I) pour étudier les exoplanètes telluriques spectroscopiquement. Dans l'avenir, les objectifs scientifiques d'une telle mission constitueront une étape inéluctable pour la planétologie et pour l'astrobiologie. Les défauts techniques devant l'interférométrie spatiale sont triples : (1) cryogénique des optiques et des détecteurs, (2) vol en formation et (3) l'architecture optique de l'interféromètre. Les deux premiers de ces points seront développés indépendamment des aléas du projet *Darwin*/TPF-I, notamment, dans le contexte de la préparation de plusieurs autres missions spatiales. Quant au troisième point, la plupart des questions techniques sera abordée par les équipes qui préparent des interféromètres en frange noire au sol, dans l'Antarctique et dans l'espace. Pourtant, aucun de ces projets ne vise pas toutes les spécifications nécessaires pour la réalisation d'une mission comme *Darwin*/TPF-I, notamment, aucun ne prévoit de développement d'un système de filtration du front d'onde pour la bande passante entière 6-18 μm. Pour ne pas fermer la porte vers *Darwin*/TPF-I, nous conluons qu'il faut continuer la recherche et développement de ce sous-système critique.

Il y a trois ans, nous nous sommes mis au travail avec deux objectifs en vue : tester les différents prototypes de déphaseurs achromatiques et stabiliser le banc. Nous avons implémenté une méthode améliorée de la stabilisation en différence de marche basée sur la voie scientifique, effectuant des excursions autour de la position correspondant au taux d'extinction optimal. Nous avos pu démontrer l'efficacité de cette méthode et partager les résultats avec la communauté scientifique (Gabor et al., 2008).

Les expériences menées sur le banc SYNAPSE nous ont permis de mieux comprendre les facteurs limitant ses performances et nous avons contribué à la construction du nouveau banc, NULLTIMATE, en vue d'une amélioration. Ce banc, pour lequel nous avons développé l'architecture informatique, est sur le point de donner des résultats intéressants dans les années à venir.

Si nous devions formuler un message pour la conception d'une future mission du type *Darwin*/TPF-I, nous dirions qu'il faut prévoir, non pas seulement une métrologie externe, mais aussi une possibilité d'un asservissement basé sur le signal scientifique.

Title: *A study of the performance of a nulling interferometer testbed preparatory to the Darwin mission*

Preparations for a future interferometric flagship space mission (Darwin, TPF-I) are under way in order to study Earth-like extrasolar planets in the habitable zones of their parent stars, and more particularly to estimate the proportion of such exoplanets with atmospheric compositions suggesting the presence of biotic photosynthesis.

Nulling interferometry operating in the spectral band between 6 and 18 µm may allow distinguishing the emissions of the exoplanet from those of its star and the ambient diffuse sources. The thesis summarises the experimental work performed on the Synapse test bed at the *Institut d'Astrophysique Spatiale in Orsay.* The bench was tested in the K band, from 2.0 to 2.5 µm, as well as with a laser at 3.39 µm. The results confirm the trend observed by other research groups, viz., the performance is better in monochromatic light than in broadband (nulling ratios of 10^{-5} monochromatic, and 3×10^{-4} broad band). Extensive experimental study of this phenomenon is described.

In addition to these efforts aiming at a better grasp of nulling interferometry as such, we tested an Achromatic Phase Shifter prototype (a key element in broadband nulling) based on the through-focus principle.

We developed a technique of optical path difference stabilisation, where interferometrically combined flux is measured while dithering the optical path difference. We reached stability levels comparable to those required for the future space mission.

Titre: *Etude des performances d'un banc interférométrique en frange noire dans le cadre de la préparation de la mission Darwin*

Une future mission spatiale (Darwin, TPF-I) est en préparation pour étudier les planètes extrasolaires telluriques dans les zones habitables respectives de leurs étoiles, notamment, pour établir combien, parmi ces exoplanètes, ont une composition atmosphérique indiquant la présence de la photosynthèse biotique.

Travaillant dans la bande spectrale de 6 à 18 m, l'interférométrie en frange noire doit permettre de distinguer le flux lumineux de l'exoplanète de celui de son étoile ainsi que des sources diffuses. La thèse résume les travaux expérimentaux conduits sur le banc Synapse à l'Institut d'Atrophysique Spatiale à Orsay. Le banc a été testé dans la bande K, de 2.0 à 2.5 µm, ainsi qu'avec une source laser à 3.39 µm. Les fibres optiques monomodes sont employées comme filtres du front d'onde. Le banc utilise deux paires (une dans chacun des deux bras) de prismes dispersifs qui servent de compensateur du chromatisme et de déphaseur achromatique. Les résultats confirment la tendance observée par d'autres équipes : les performances sont meilleures en lumière monochromatique qu'en bande large (taux d'extinction : 10^{-5} monochromatique et 3×10^{-4} bande large). Des études expérimentales extensives de ce phénomène sont décrites.

A part ces travaux portant sur le principe de l'interférométrie en frange noire, nous avons testé un prototype du déphaseur achromatique basé sur le passage par un foyer optique.

Nous avons développé une technique pour stabiliser la différence de marche, mesurant le flux recombiné en modulant la différence de marche. Nous avons obtenu des niveaux de stabilité comparables à ceux qui sont nécessaires pour la future mission spatiale.